DETONATION MODELLING OF NON-IDEAL HIGH EXPLOSIVES

BY

CHARLES BASENGA KIYANDA

DISSERTATION

Submitted in partial fulfillment of the requirements
for the degree of Doctor of Philosophy in Theoretical and Applied Mechanics
in the Graduate College of the
University of Illinois at Urbana-Champaign, 2010

Urbana, Illinois

Doctoral Committee:

Associate Professor Mark Short, Chair & Director of Research
Associate Professor Dimitrios Kyritsis
Assistant Professor Joanna Austin
Assistant Professor Carlos Pantano-Rubino

Abstract

High explosives (HE) are used in many fields where the energy liberated by the combustion process is used to perform useful work. High explosives normally burn via a detonation; a supersonic wave consisting of a shock wave coupled to chemical energy release. Detonations in conventional HE (CHE) propagate with a typical velocity of 6–8 km/s. Insensitive HE (IHE) and non-ideal HE (NIHE) are of particular interest as they are harder to initiate and thus safer to store and transport. Detonations in IHEs and NIHEs are characterized by longer reaction time and length scales than detonations in CHE. NIHEs are typically characterized by their porous, granular structure. Detonations in NIHEs have lower detonation velocities (4–6 km/s) than those in CHEs or IHEs due to their lower initial densities.

The short time scales ($O(ns-\mu s)$), length scales ($O(\mu m-mm)$) and the opaque nature of HEs and their products make experimental observations, required to calibrate detonation models for reaction flow modelling, challenging. Currently used reactive burn models assume a two component, mechanically equilibrated mixture of reactants and products. Individual components are modelled with an empirical equation of state (EOS). The set of relations which uniquely determine the mixture-averaged state in terms of the states of the mixture constituents, the mixture closure conditions, are also often of a pressure-temperature equilibrium form. The chemical reaction rate law(s) are mostly based on preconceptions of how a detonating HE burns. Typically, such engineering style models are complex and contain a large number of fitting parameters that are calibrated in some form to a limited set of experimental data. Minimal attention has been devoted to the physical and mathematical implications of the fitting process and reactive burn model structure (such as the choice of closure condition) to issues such as detonation stability and interacting oblique shock structure. For a well-posed reactive burn model, such properties should be understood.

A majority of this thesis research is devoted to formulating and studying the shock and detonation properties of reactive burn models based on the use of stiffened-gas (SG) equations of state. A SG model allows an appropriate initial sound speed of a material to be set, an important improvement over ideal gas models when applied to condensed phase reactive burn models. Due to its relative simplicity, a semi-analytical understanding of reactive burn models based on the use of SG EOS models for its constituent components

can be obtained. Furthermore, changes in physical aspects of the reactive burn model, such as detonation stability and interacting oblique shock structure, with changes in calibrated fitting parameters, can be better understood. In this context, we establish the ability of SG EOS models to reasonably formulate a reactive burn model for the IHE PBX 9502. The model is designed to capture the fast and slow reaction stages inherent in PBX 9502 detonation using a two-stage reaction model. Different mixture closure conditions are examined, namely the classical pressure-temperature equilibrium assumption and a constant solid entropy closure condition. The stability characteristics of SG EOS based detonation models are examined in the context of varying EOS properties of the reactants and products, as well as closure conditions. The SG EOS based structure of oblique shock and detonation waves are also examined. Finally, in a separate exercise, the implementation and results of a series of large cylindrical rate-stick experiments with the NIHE ammonium nitrate-fuel oil (ANFO) is reported. A detonation-shock-dynamics calibration to the detonation front curvature data obtained from experiments is also presented.

To my parents who have always pushed me to achieve more.

(Until my third year of Ph.D., that is, when they just started asking "When will you stop studying?")

To Julie, for providing me with love and constant encouragement.

To Unilever UK, for providing me with PG Tips. (Sorry Honey.)

Acknowledgments

The author wishes to thank many people. The staff of the LANL DE-9 group who have shown interest and helped in the course of this work. Most particularly the researchers and engineers Tariq Aslam, Terry Salyer, John Morris, John Bdzil, Larry Hill and Scott Jackson. DE-9 group leader David Robbins was instrumental in the support he provided. Brad Clements, Ralph Menikoff and Sam Shaw from the theoretical division must also be thanked for their support and collaboration. Obviously, none of this would have been possible without the supervision of Dr. Mark Short. Finally, heartfelt gratitude is due to all the parents and friends who have been supportive and have had to endure much complaining.

Most of the work in this thesis was supported by the DOE ASC HE program. The ANFO rate-stick experiments were funded through the DOE NCT program.

Table of Contents

List of Tables

List of Figures

List of Abbreviations

AMR	Adaptive mesh refinement
AMRITA	Adaptive mesh refinement interactive teaching aid
AN	Ammonium nitrate
ANFO	Ammonium nitrate and fuel oil
BSG	Blended stiffened-gas (EOS)
CHE	Conventional high explosive
CJ	Chapman-Jouguet
CL	Centerline
CS	Contact surface
DE	Differential evolution
DNS	Direct numerical simulation
DSD	Detonation shock dynamics
EM	Electromagnetic
EOS	Equation of state
EXN	Expan
FGM	Fragmax
FO	Fuel oil
GB	Gigabyte
GHz	Gigaghertz
GPa	Gigapascal
GR	Guderley reflection
HC	Heat transfer, convective
HE	High explosive
HME	Homemade explosive
HMX	octogen, cyclotetramethylene-tetranitramine

IHE	Insensitive high explosive
IN	Inflow (boundary)
IR	Irregular reflection
JWL	Jones-Willkinson-Lee
KCl	Potassium chloride
LANL	Los Alamos National Laboratory
LAPACK	Linear algebra package
LiF	Lithium Fluoride
LSQ	Least-square fit
MR	Mach reflection
NIH	National Institute of Health
NIHE	Non-ideal high explosive
NR	No reflection
ODE	Ordinary differential equation
PBX	Plastic bonded explosive
PETN	Pentaerythritol tetranitrate
PM	Prandtl-Meyer (expansion)
PMMA	Polymethylmetacrylate
PS	Post-shock (state)
RAM	Random access memory
RB	Reactive burn
RHE	Regular high explosive (grade ANFO)
RE	Reflection (boundary)
RR	Regular reflection
SG	Stiffened-gas (EOS)
SSE	Sum of square of error
SSG	Single stiffened-gas (EOS)
SO	Solid obstacle
ST	Shock tracker (gauge)
TATB	Triaminotrinitrobenzene
TOA	Time of arrival
TR	Transmissive (boundary)
UTSDE	Unsteady transonic small disturbance equation

vNR	von Neumann reflection
VN	Von Neumann (state)
WENO	Weighted essentially non-oscillatory
WSD	Wescott-Stewart-Davis
ZND	Zel'dovich-von Neumann-Döring

List of Symbols

Certain sections use different variable definitions from those given below. These sections are self-contained, the meaning of variables in those sections is given in the text and only the meaning of variables appearing elsewhere in the text and which are necessary for an overall comprehension are given here. The sections containing unlisted variables are 1.3, 2.3.2–2.3.3 (and by extension section A.2), 3.7.1–3.7.2 and 6.5.3.

Subscripts and Superscripts

$_b$	Pertaining to the denominator (for Φ_b)
$_H$	Along the Hugoniot curve (unless defined otherwise, e.g. the heat transfer time constants of chapter 2)
$_n$	Normal direction (velocities in chapter 5)
$_p$	Pertaining to products (except for N_p)
$_r$	Pertaining to reactants
$_{\text{ref}}$	Reference state
$_R$	Along the Rayleigh line
$_S$	Along an isentrope
$_t$	Transverse velocities in chapter 5 (except for Φ_t which is described in the text)
*	Base (ZND) problem in chapter 4, Critical state for BSG in chapter 2
$'$	Perturbations (used in chapter 4)
$_{\text{CJ}}$	Chapman-Jouguet state
$_{\text{VN}}$	von Neumann state

Derivative Notation

ζ	A random variable
$\zeta_{1,\zeta_2} = d\zeta_1/d\zeta_2$	Derivatives
$\dot{\zeta} = d\zeta/dt$	Time derivative

Symbols and Variables

A	Stiffened-Gas EOS pressure offset
$a = A/\rho D^2$, $a = A/\rho u^2$	Non-dimensionalized stiffened-gas EOS pressure offset
B	$\approx c_g^2 - c_0^2 \Gamma_g/\Gamma_r - \Gamma_g Q$
$\boldsymbol{C_0}$, $\boldsymbol{C_1}$, $\boldsymbol{C_2}$	Matrices arising in the derivation of the perturbed flow problem
C_i	Constant (except for the specific heat)
C_p	Specific heat at constant pressure
C_v, C_{vs}, C_{vg}	Specific heat at constant volume (general, solid phase, gaseous phase)
c	Speed of sound
D_0, D_n, D_{CJ}	Steady detonation propagation velocity, local normal wave velocity, CJ wave velocity
$e = e(P, v)$	Specific internal energy
$\overline{e}_0$	Initial specific internal energy
F	Function
$f = M^2/M_{\mathrm{CJ}}^2$	Overdrive
f_q	Ratio of heat releases between reaction steps
$f_r = k_{II}/k_I$	Ratio of rate constants between reaction steps
$\boldsymbol{f}_\alpha$, $\boldsymbol{f}_0$	Vectors arising in the derivation of the perturbed flow problem
G	Fundamental derivative
g	Non-dimensional ...
h	Specific enthalpy
K	Heat conductivity
k, k_i	Arbitrary constant, reaction rate constant
L/D	Charge aspect ratio (in chapter 6)
$L_{\mathrm{induction}}$, L_{reaction}	Induction and reaction length scales
L_r	Reaction length scale
$l = D/D_{\mathrm{CJ}} - 1$	Normalized velocity decrement
l_{eng}	Engineering length scale
M	Mach number
N	Number of species in model
N_g	Number of generations (in DE algorithm)
N_m	Number of atoms in a molecule
n	Exponent of pressure in reaction rate

P	Pressure
P_c	BSG crossover pressure
Q	Heat release
R	Charge radius
R_c	Radius of curvature
R_s	Specific gas constant
$\hat{r}$	Radial coordinate (in the derivation of the nozzle equation in cylindrical coordinates)
r_i, r_I, r_{II}	Reaction rates
S	Entropy
T	Temperature
T_m, T_b, T_o	Center, bottom and outside temperatures (in ANFO experiments)
t	time
$\boldsymbol{u} = \{u, w\}$	Velocity vector
v	Specific volume
W	Switch function (except in chapter 6 where it denotes weights in a cost function)
x	Axial distance along detonation wave thickness (except in discussions of shock Hugoniot or DE algorithm)
$x = v/v_0$, x_c	Compression ratio, compression ratio at the crossing point (in discussions of shock Hugoniot)
y	Mass fraction (except in discussions of shock Hugoniot)
$y = P/P_0$	Pressure ratio (in discussions of shock Hugoniot)
z	Shock shape coordinate along charge axis
α	Eigenvalue (in chapter 4)
α_s	Thermal diffusivity of the solid phase
Δ, Δ_{ZND}	Detonation reaction zone thickness
$\Delta_{1/2}$	Half reaction zone thickness
δ	Deflection angle
$(\Delta H)_{\mathrm{comb}}$	Heat of combustion
$\eta = 1 - u^2/c^2$	Sonic parameter
ϵ	Small number
γ, $\overline{\gamma}$	Adiabatic index, constant part thereof
Γ	Grüneisen Gamma
κ, κ_s	Local curvature

κ_T	Local total curvature
Λ	Eigenfunctions of the associated matrix problem (collocation method)
λ	Reaction progress variable
ν, μ	Reaction order
Ω	Shock angle (in shock and detonation polar calculations)
Ω_{TP}	Triple point track angle
ϕ, ϕ_e	Shock normal angle, edge angle (in discussions of DSD)
ϕ	Thermicity
Ψ_0	Small number (order of the perturbations in linear stability analysis)
ρ	Density
τ_R, τ_H, τ_{HC}	Time scale for reaction, heat transfer, convective heat transfer
θ	Activation energy
$\xi_1(P)$, $\xi_2(P, y_s)$	Functions used with the P-T equilibrium condition
χ	$= C_{vs}/C_{vg}$

Non-Dimensional Groups

Fo	Fourier number
Ra	Rayleigh number

Chapter 1

Introduction

A high explosive (HE) is a reactive substance, liquid or solid, which can burn via the detonation process. A detonation wave is a supersonic mode of combustion in which chemical reactions support the propagation of a shock wave through the material. The traveling shock wave compresses the reactant material to high pressures ($\sim$ 40 GPa) and to temperatures ($\sim$ 2000 K), which in turn trigger the onset of chemical reactions at very high rates, when compared to other, slower, modes of combustion. The chemical energy released serves to prevent the decay of the leading shock wave, resulting in a steady phenomenon propagating at a natural velocity, the Chapman-Jouguet (CJ) detonation velocity. The CJ velocity occurs when the flow velocity at the end of the reaction in a frame of reference traveling with the shock is identically sonic.

There are several classes of HE, conventional HE (CHE), insensitive HE (IHE), non-ideal HE (NIHE), improvised HE (or home-made explosive, HME), each with varying uses. IHEs are high energy, yet safe to store and transport making them attractive for a range of applications where safety is critical. NIHEs are easy to prepare in large quantities from non-explosive components. For example, ANFO is made of ammonium nitrate (AN), a fertilizer, and diesel fuel. This makes NIHEs especially attractive for improvised explosive devices.

There is an interest in modelling the behaviour of IHE and NIHE for a large range of uses and conditions.

1.1 Classification of Explosives

The boundaries between a sensitive and an insensitive HE or between an ideal and a non-ideal HE (NIHE) can be sometimes arbitrary and ill-defined. This work centers around the IHE PBX 9502 and the NIHE ANFO. The definition of sensitive and insensitive HE as well as ideal and non-ideal are reviewed below.

1.1.1 Sensitivity of Explosives

Solid explosives can be categorized according to the level of effort required into initiating reaction in the material. Several experimental tests involving different stressors have been devised, generally using frictional

heating, impact through a weight drop and conductive, convective and radiative heating over a period of time. Such tests serve to empirically categorize explosives, in order of reduced sensitivity, as primary, secondary or tertiary (blasting agents) explosives (See [26] for a review of explosive classification). The division between primary and secondary explosives is the granular solid explosive pentaerythritoltetranitrate (PETN), which is by definition the most sensitive secondary explosive. Explosives more sensitive are termed primary explosives while those less sensitive are termed secondary explosives. Blasting agents are explosive materials extremely difficult to initiate. One such example is the mixture of ammonium nitrate and fuel oil, ANFO, discussed in more detail in chapter 6.

The denomination *insensitive high explosive* (IHE) refers to very insensitive explosives based on secondary HEs. Mostly, these explosives are formulated by using the insensitive powder explosive triaminotrinitrobenzene (TATB), as in the case of PBX 9502, pressed with a polymer binder. Hence the name plastic bonded explosive (PBX).

1.1.2 Ideal and Non-Ideal High Explosives

Ideal and non-ideal explosives are distinguished by their detonation properties. Non-ideal explosives exhibit lower detonation velocities (as low as 4-5 km/s) and lower densities than CHE or IHE. One non-ideal explosive of interest in this work is the granular blasting agent ANFO, which has detonation velocities as low as 3.5 km/s and a density of only 0.8-1.1 g/cc (half that of the IHE PBX 9502, for example, at about 1.89 g/cc). Non-ideal explosives also have longer reaction zones which make the detonation wave much more susceptible to changes in the geometry and the dynamics of their confinement. This greater dependence results in larger velocity deficits when non-ideal HEs are detonated in cylindrical charges of small diameter. In fig 1.1, the diameter effect curves of X-0219 (an ideal TATB based explosive similar to PBX 9502) and heavy ANFO (an ANFO mixture using porous prills and an AN-water emulsion) are shown. The diameter effect curve is a plot of the steady detonation propagation velocity in a cylindrical charge vs. the inverse charge diameter. Here, the propagation velocity is normalized by the infinite-diameter charge velocity, D_{CJ}, and the charge diameter is normalized by the failure diameter. The failure diameter is the smallest diameter charge for a given explosive in which a detonation will propagate at a steady velocity. Ideal explosives, like X-0219, exhibit much "flatter" diameter effect curves with small velocity deficits up to the failure diameters. Non-ideal explosives, like heavy ANFO, exhibit much larger velocity deficits of more than 50% until the detonation is unable to propagate.

For each explosive type, there is substantial interest in being able to model detonation initiation, propagation and failure, and to calculate the work done on surrounding material by high pressure gases. To date,

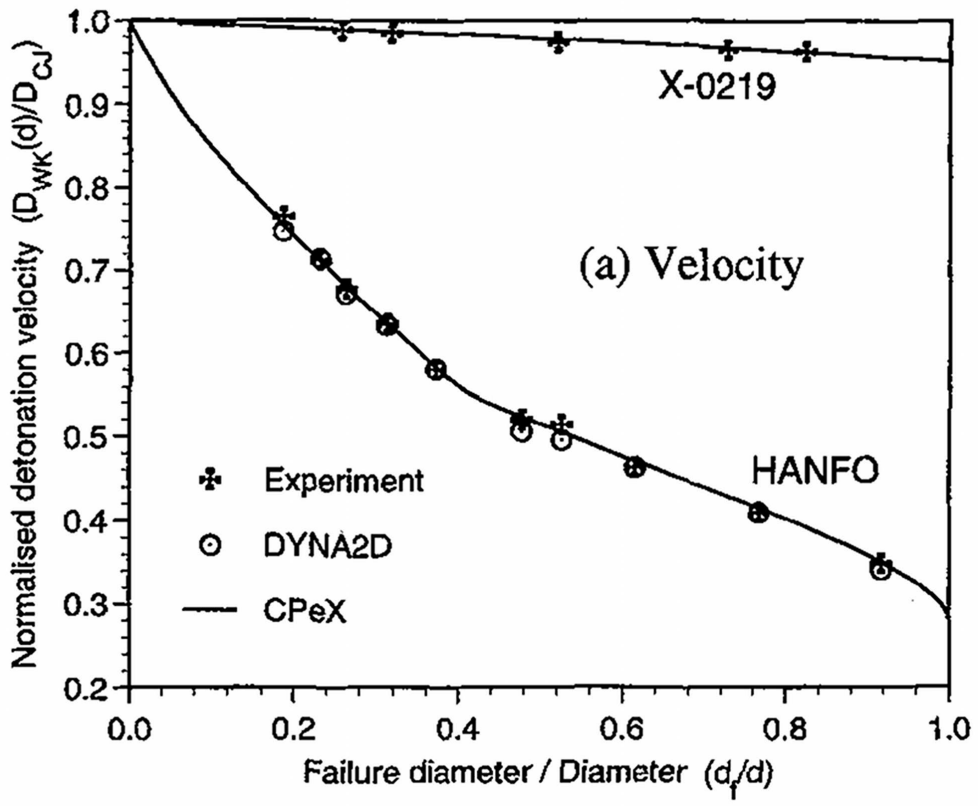

Figure 1.1: Figure 1 from [2] showing the normalized diameter effect curves of X-0219 (TATB based ideal HE, 90% TATB 10% Kel-F 800) and heavy ANFO (a proprietary mixture of porous AN prills, fuel oil and an AN/water-in-oil emulsion). X-0219 has a D_{CJ} of 7.63 mm/μs while heavy ANFO has a D_{CJ} of 5.807 mm/μs. The failure diameters are 14 mm and 46 mm respectively.

simulations of HE detonation have been conducted for "engineering", phenomenological models.

1.2 Simulation Approaches

There are two approaches to simulating the behaviour of HE devices. The *program burn* methodology does not resolve the detonation wave structure, whereas the *reactive burn* methodology does.

1.2.1 Program Burn

In the program burn methodology, the detonation reaction zone is not resolved. The detonation wave is instead replaced by a surface with an associated evolution equation. The solution of this evolution equation describes the path of the detonation and the post-detonation state. This solution is used as an input to a hydrodynamic solution of only the detonation products (see for example [27]). Two underlying assumptions of this methodology are that

1. the detonation reaction zone thickness Δ is thin compared to the engineering scale of the device, $\Delta/l_{\text{eng}} \ll 1$,

2. the reaction time of a particle through the detonation is short so that no work is done on the engineering scales.

Such assumptions are, by definition, better suited to ideal HEs. A strong advantage of the program burn methodology is the relatively short computation time required. On the other hand, this approach hinges on an accurate description of the detonation propagation (known as timing) and of the post-detonation thermodynamic state. Two solution methods are used to model the detonation: one is the Huygen's construction and the other detonation shock dynamics (DSD).

Huygen's Construction

In the Huygen's construction, the normal detonation propagation speed is fixed at a constant value. From its initial shape, the detonation wave propagates locally in a direction normal to its current surface. The state of a computational cell is switched to the post-detonation state based on the Huygen's construction timing.

Detonation Shock Dynamics

The DSD model is a rational asymptotic solution to the detonation wave, which assumes the radius of curvature of the detonation wave R_c is much larger than the detonation wave reaction thickness

$$R_c \gg \Delta. \tag{1.1}$$

Based on this, an evolution equation can be derived for the propagation of the detonation wave as a function of its curvature, which at leading order states

$$D_n = D_n(\kappa), \tag{1.2}$$

where D_n is the normal wave velocity at a point on the surface where its curvature is κ [25, 28]. Higher order DSD surface propagation laws can also be derived that include for instance shock acceleration $D(D_n)/Dt$ and transverse flow variation. Such higher-order laws tend to be ad-hoc [29, 30], for instance

$$\kappa_s + \frac{\sin\phi}{r} = F(l) - A(l)\frac{Dl}{Dt} + B(l)\frac{\partial^2 l}{\partial \xi}, \tag{1.3}$$

$$\tag{1.4}$$

where $l = D/D_{\mathrm{CJ}} - 1$ and $\kappa_s + \sin\phi/r$ is the curvature in a cylindrical geometry.

The DSD model is calibrated to a particular explosive typically from break-out times in rate-stick experiments. In such experiments, a cylindrical charge of explosive is detonated and the steady detonation propagation velocity is recorded as a function of charge diameter as well as the steady wave-shape. A set of rate-stick experiments and a DSD calibration are reported for ANFO in chapter 6. Because the DSD solution takes into account the velocity deficit exhibited by curved detonation waves, the solution is a significant improvement over the Huygen's construction, which assumes a constant detonation velocity regardless of the wave shape.

Comparison of Huygen's Construction and DSD Methods

The DSD method offers good agreement with DNS calculations as well as an improved agreement when compared to the Huygen's construction method [3, 4]. Figures 8 (a) and (b) from Bdzil and Stewart [3] are reproduced in fig 1.2 and show the comparison between a higher-order DSD calculated detonation shape and one calculated by direct numerical simulation for a detonation wave in an arc-shaped charge. The detonation model used in this case was a polytropic model with a detonation velocity of 8 km/s. Two figures from page 16 of [4] are reproduced in fig 1.3. The wave shape is compared between a Huygen's construction and three different experiments using the explosive PBX 9502. The Huygen's construction is seen to substantially precede the experimental measurements. The breakout shape (the shape of the detonation wave as it reaches the end of the sample) from this same experiments is compared with a first-order DSD result showing near perfect agreement over most of the sample size with the largest discrepancy at the edges of the charge.

The program burn method, using either the Huygen's construction or DSD, cannot accurately represent explosives with a thick reaction zone and problems in which local extinction occurs. In this case, one needs a complete, time-dependent, description of the detonation wave structure.

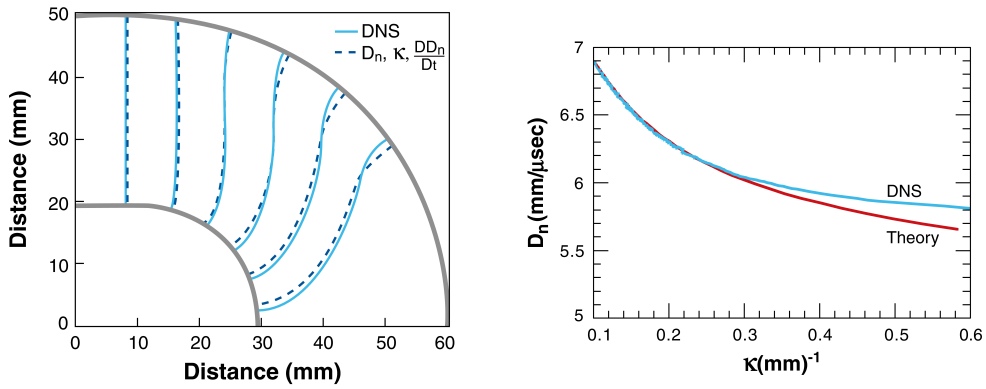

(a) Detonation Wave Shape.

(b) Calculated $D_n - \kappa$ Curve.

Figure 1.2: Figure 8 from [3] showing the comparison of the solution of a higher-order $\dot{D}_n$–D_n–κ DSD method and a direct numerical simulation. The model used is a typical polytropic EOS tuned to give a detonation velocity of 8 km/s.

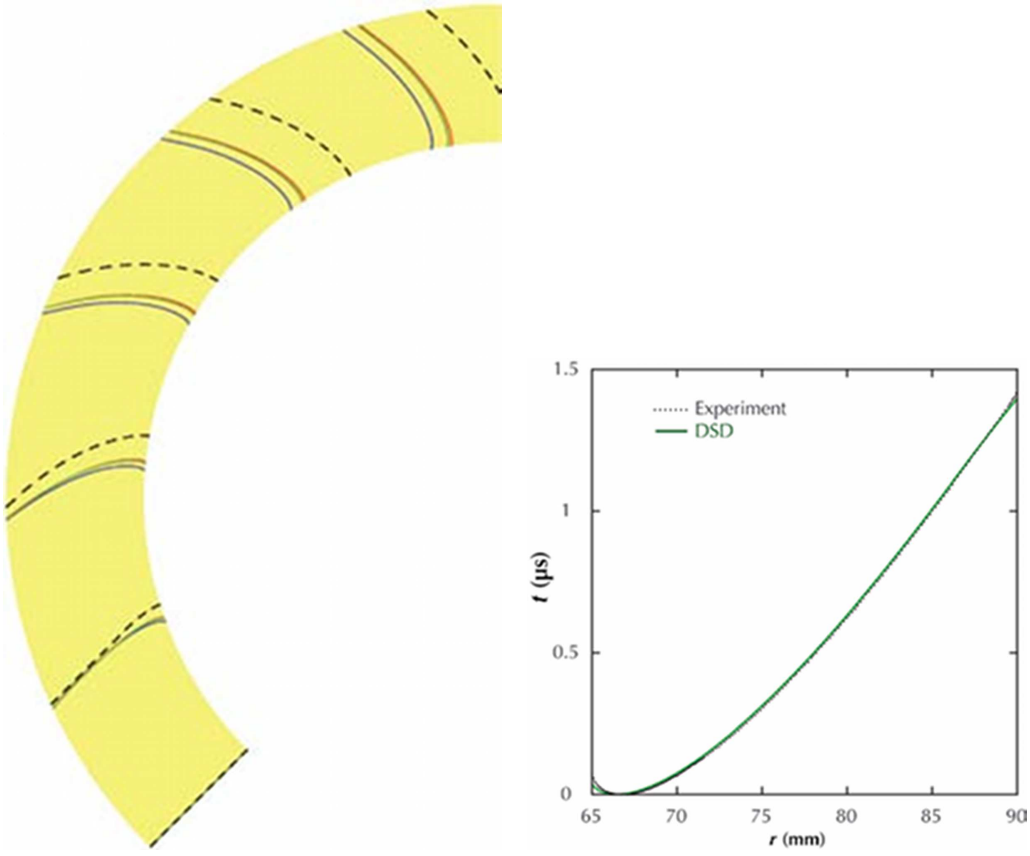

(a) Detonation Wave Shape.

(b) Breakout Shape.

Figure 1.3: Figures from [4](page 16) showing (a) the comparison of the Huygen's construction (dashed line) with three different experiments (solid colored lines). The breakout shape of a first-order DSD calculation is compared to experimental measurements (b), showing good agreement with the largest deviations at the edges.

1.2.2 Reactive Burn

In the reactive burn approach, the simulation domain includes the reaction zone and, and requires that the detonation structure be resolved computationally. Such simulations are computationally more intensive than the program burn approach. In the IHE PBX 9502, for example, the bulk of the reaction zone has a thickness of about 20 μm. Capturing the correct detonation speed typically requires a resolution of 20-60 grid points in the reaction zone. The spatial resolution must therefore typically by less than 1 μm. One clear advantage of reactive burn models is their ability to capture the interaction between the geometry and the detonation wave. Specifically, for NIHEs where the size of the reaction zone is not small when compared to the engineering scale, such interactions can influence the propagation of the detonation wave. The ability to perform reactive burn simulations depend in great part on the ability to accurately describe the hydrodynamic and chemical processes taking place inside the detonation reaction zone. A detonation model suitable to the particular material under consideration is necessary. Such detonation models are normally composed of one equation of state (EOS) for each component, a mixture rule between components, closure condition and a chemical kinetic rate scheme. Typically, in the high pressure regime encountered in HE (O(10s of GPa)), detonating solids and shocked solids can be treated as fluids, and thus shear stresses can be neglected. Consequently, all current widely used HE detonation models are fluid models.

Equation of State (EOS)

The caloric EOS relates the internal energy e of a substance with its thermodynamic state. If the chemical processes only depend on the pressure, P, and specific volume, v, then all that is needed is an incomplete EOS of the form $e = e(P, v)$. If the temperature or the entropy appears in the closure condition or the reaction rates, then a complete EOS is required, of the form $e = e(S, v) = e(T, v)$, etc [31].

In different models, different species or different phases of the mixture may have different thermodynamic properties (i.e. a different EOS). In such models, a different EOS form or different values of the EOS parameters can be specified for the different species. In the context of fluid models, the mixture-averaged internal energy and specific volume are given by

$$e_{\text{mixture}} = \sum_{i=1}^{N} e_i y_i, \tag{1.5}$$

$$v_{\text{mixture}} = \sum_{i=1}^{N} v_i y_i, \tag{1.6}$$

where e_i and v_i are the internal energy and specific volume of species i, y_i is its mass fraction and the mass fractions sum to unity, i.e. $\sum_i y_i = 1$.

An often used way to specify the internal energy of a substance is the Mie-Grüneisen EOS form, which consists of a first order expansion of an incomplete caloric EOS from a reference curve. For a general reference curve, the Mie-Grüneisen EOS is

$$P(v, e) = P_{ref}(v) + \frac{\Gamma(v)}{v} \left[e - e_{ref}(v) \right]. \tag{1.7}$$

A consistent model is formulated by specifying a reference curve, $P_{ref}(v)$ and a consistent internal energy along this reference curve, $e_{ref}(v)$. The reference energy is normally obtained by integrating the energy along an isentrope, $(de/dv)_s = -P$. This form is widely used with models of the Hugoniot curve, $P_H(v)$, such as the linear the Jones-Wilkinson-Lee (JWL) EOS.

Closure Condition

For a multi-component model with N individual components in a mixture, there are $2(N-1)$ supplemental independent variables. Consider, for example, an N component mixture, each component with its own incomplete EOS $e_i = f(P_i, v_i)$. Instead of a single pressure, P, there are N different pressures, P_1 through P_N. Similarly, there are N specific volumes, v_1 through v_N, instead of the single specific volume v. To determine the system and be able to solve for the mixture-averaged state, P, v, one needs $2(N-1)$ compatibility equations, referred to as the closure condition. The most often used closure condition is the pressure and temperature equilibrium

$$P = P_1 = P_2 = P_i = P_N, \tag{1.8}$$

$$T = T_1 = T_2 = T_i = T_N. \tag{1.9}$$

This condition closes the set uniquely has it replaces the N pressures with a single pressure, P, and N temperatures with a single temperature, T. Note that here only two state variables are independent and one must specify a thermodynamically consistent temperature for each species, $T_i = T_i(P_i, v_i)$. Other closure conditions exist, among others pressure equilibrium combined with the isentropic expansion of one of the phases, which is also explored in this thesis,

$$P = P_i, \forall i, \tag{1.10}$$

$$\frac{DS_i}{Dt} = 0, \text{ for a single } i. \tag{1.11}$$

The above is sufficient for a two species model. In the case where $N > 2$, one could assume all remaining species to be in temperature equilibrium, thereby specifying the required $2(N-1)$ closure conditions.

Chemical Kinetic Rate scheme

The remaining component of a detonation model is a chemical kinetic rate model, which specifies the rate at which one species of the mixture reacts to become a different species. Unlike the detailed, realistic chemical kinetic mechanisms which have been developed for reactive gaseous mixtures, the kinetic models used in HE modelling are abstracted and simple. Given the high pressures, high temperatures and the rapidity of the phenomenon, essentially no kinetics can be determined. For a single component, such a model may take the form of a reaction progress variable, λ, which varies according to a law

$$\frac{D\lambda}{Dt} = k\lambda^{\nu} f(P, v, T). \tag{1.12}$$

An extra heat release term would then be present in the caloric EOS to mimic the change in enthalpy of formation, such as

$$e = e(P, v) - \lambda Q. \tag{1.13}$$

For an N component mixtures, $N-1$ rate equations akin to eqn 1.12 are necessary since $\sum_i y_i = 1$. One or more heat release terms are also then present in the EOS.

1.3 Review of the Standard Models of High Explosives

Current widely used reactive flow models for IHEs and NIHEs are phenomenological, typically treating the explosive as a homogeneous mixture of two or more components under a number of flow equilibrium restrictions. Typically, velocity, pressure and temperature equilibrium is assumed. The models probably most employed for detailed numerical simulations of HE today are the Ignition and Growth (I&G), Wescott-Stewart-Davis (WSD) and CREST models. Two of those models, I&G and CREST, were initially developed with the intent of modelling the detonation initiation process. The WSD model has structural similarities

to the I&G model, but has a pressure switch function that selects the exponent of pressure terms present in the rate laws according to the shock strength, whether it is an initiation or propagation problem.

In the current models, equations of state for each component are obtained by fitting empirical EOS forms to available Hugoniot, and other, data. Unsurprisingly, the current generation of reactive burn models have limited predictive ability beyond conditions in which the flow models are directly calibrated. Their phenomenological nature and empirical formulation limits our ability to analyze the dependence of the different model parameters on physical quantities.

1.3.1 Ignition and Growth (I&G)

One well known and often used HE model is the I&G model. It has been extensively used in calibrating several different HE to different experimental conditions. It was originally developed to model the detonation initiation process [32, 33, 34, 35, 36]. The model has been applied outside the range of detonation initiation to detonation propagation [37, 38, 7, 39] and failure [40, 41].

Equations of State

The equation of state for both reactants and products is the Jones-Wilkinson-Lee (JWL) EOS. The JWL EOS is, in fact, an empirical relation of $P(v)$ along an isentrope. An incomplete EOS is normally obtained by using the Mie-Grüneisen formalism (described next). The form of the JWL EOS is

$$P(v) = B_1 e^{-R_1(v/v_0)} + B_2 e^{-R_2(v/v_0)} + B_3 \left(v/v_0\right)^{-(B_4+1)}, \tag{1.14}$$

where R_1, R_2 and B_1–B_4 are fitting parameters. The same EOS form is used for both the reactants and the products, with each species calibrated independently.

Closure Condition

The closure condition used is the pressure-temperature equilibrium, $P_r = P_p = P$, $T_r = T_p = T$.

Chemical Kinetic Rate

A single kinetic rate law is used to describe the conversion of reactants into products. This single rate is comprised of three components, from which the model derives its name. One component is an ignition term aimed at representing the number of hot-spots ignited by the shock, the second is a growth term representing the rate of spread of hot-spots into unreacted material and the third is a carbon coagulation term representing a slow reaction tail that is present in PBX 9502. Combined this gives the rate law

$$\frac{d\lambda}{dt} = I(1-\lambda)^b(\rho/\rho_0 - 1 - a)^x H(\lambda_{igmax} - \lambda) + G_1(1-\lambda)^c\lambda^d P^y H(\lambda_{G_1max} - \lambda) + G_2(1-\lambda)^e\lambda^g P^z H(\lambda - \lambda_{G_2min}), \quad (1.15)$$

where λ is the reaction progress variable, $I, G_1, G_2, a, b, c, d, e, g, x, y$ and z are calibration constants, λ_{igmax}, λ_{G_1max} and λ_{G_2min} are switch points in the form of the reaction rate and H is the Heavyside function.

1.3.2 Wescott-Stewart-Davis (WSD)

The WSD model is described in the Ph.D. thesis of Wescott [42] and in a subsequent paper [8].

Equations of State

The equations of state for the reactants and the products both consist of Mie-Grüneisen forms where the pressures along an isentrope is specified. The resulting EOS for the products is the wide-ranging EOS of Davis [31]

$$E_p(p,v) = E_p^s(v) + \frac{f}{\Gamma_p(v)}\left[p - p_p^2(v)\right], \quad (1.16)$$

$$p_p^s(v) = p_c\frac{\left[\frac{1}{2}(v/v_c)^n + \frac{1}{2}(v/v_c)^{-n}\right]^{a/n}}{(v/v_c)^{k+a}}\frac{k-1+F(v)}{k-1+a}, \quad (1.17)$$

$$F(v) = \frac{2a(v/v_c)^{-n}}{(v/v_c)^n + (v/v_c)^{-n}}, \quad (1.18)$$

$$\Gamma_p(v) = k - 1 + (1-b)F(v), \quad (1.19)$$

$$E_p^s(v) = E_c\frac{\left[\frac{1}{2}(v/v_c)^n + \frac{1}{2}(v/v_c)^{-n}\right]^{a/n}}{(v/v_c)^{k-1+a}}, \quad (1.20)$$

$$E_c = \frac{p_c v_c}{k-1+a}, \quad (1.21)$$

where the parameters p_c, v_c, a, k, n and b are calibration parameters. The EOS for the reactants is based on a cubic fitting form

$$
\begin{aligned}
E_r(p,v) &= E_r^s(v) + \frac{v}{\Gamma_r(v)}\left[p - p_r^s(v)\right], && (1.22)\\
p_r^s(v) &= \hat{p}\left[\sum_{j=1}^{3}\frac{(4By)^j}{j!} + C\frac{(4By)^4}{4!}\,\frac{y^2}{(1-y)^4}\right], && (1.23)\\
E_r^s(v) &= v_0\int_0^y p_r^s(\overline{y}d\overline{y} + E_0, && (1.24)\\
\Gamma_r(y) &= \Gamma_{r,0} + Zy, && (1.25)\\
\Gamma_r^0 &= \beta c_0^2/C_p, && (1.26)\\
Z &= (\Gamma_{sc} - \Gamma_r^0)/y_{max}, && (1.27)\\
y_{max} &= \frac{2}{\Gamma_p(y_{max}) + 2}. && (1.28)
\end{aligned}
$$

Closure Condition

Two different closure conditions were examined in [8]:

1. pressure and temperature equilibrium,
2. pressure equilibrium and fixed solid entropy.

Although both closure conditions were examined, only the P–T equilibrium condition was used to calibrate the reactive burn model.

Chemical Kinetic Rate

The chemical kinetic rate of the WSD model is a modification of the I&G chemical kinetic rate and is given by

$$
\begin{aligned}
r &= r_I S_I(\lambda) + r_G S_G(\lambda) + \left[1 - S_G(\lambda)\right] r_B, && (1.29)\\
r_I &= k_I\left(\frac{\rho}{\rho_0} - 1 - a\right)^7 (1-\lambda)^{2/3} H\left(\frac{\rho}{\rho_0} - 1 - a\right), && (1.30)\\
r_G &= \left\{r_{IG} W(\rho_{SH}) + r_{DG}\left[1 - W(\rho_{SH})\right]\right\}, && (1.31)\\
r_{IG} &= k_I G\left(\frac{P}{P_{CJ}}\right)^{4.5} \lambda^{1/3}(1-\lambda), && (1.32)\\
r_{DG} &= k_{DG}\left(\frac{P}{P_{CJ}}\right)^{2} \lambda^{1/3}(1-\lambda), && (1.33)\\
r_B &= k_B\left(\frac{P}{P_{CJ}}\right)(1-\lambda)^{1/2}. && (1.34)
\end{aligned}
$$

The functions S_I and S_G are equivalent to Heaviside functions, but are instead based on hyperbolic tangent functions

$$S_i(\lambda) = \frac{1}{2}\left\{1 - \tanh\left[\xi_{1,i}\left(\lambda - \xi_{2,i}\right)\right]\right\}, \tag{1.35}$$

with $\xi_{1,I} = 200, \xi_{2,I} = 0.025$ and $\xi_{1,G} = 30, \xi_{2,G} = 0.9$. The function $W(\rho_{SH})$ is also a representation of a step function based on a hyperbolic tangent

$$W(\rho_{SH}) = \frac{1}{2}\left\{1 - \tanh\left[50\left(\frac{\rho_{SH}}{\rho_c} - 1\right)\right]\right\}. \tag{1.36}$$

The modifications from the classical I&G rate function are

1. the use of the $W(\rho_{SH})$ function to switch between the two pressure exponents depending on the strength of the shock a specific particle experienced,
2. the use of hyperbolic tangent based step function representations instead of Heavyside functions,

Item 1 switches between a pressure exponent suited to initiation problems and one suited to reproduce propagation problems, but forces the implementation to track a Lagrangian quantity–the strength of the shock which a particle first experienced. Item 2 makes the reaction rate function continuously differentiable, making analysis easier [8].

1.3.3 AWE's CREST

The CREST model is originally a detonation initiation model which tries to avoid the additional 'desensitization' that is required for models to properly capture the initiation of explosives subjected to multiple shocks instead of single shocks [5]. The model assumes a two component system, one being the solid reactants and the other the gaseous products.

Equations of State

The equation of state of the reactants is a Mie-Grüneisen EOS form with a reference pressure given in finite-strain form [43]. The energy on the reference isentrope, in finite-strain from, is

$$e_i(v) = \frac{9}{2} v_{0s} K_{0s} f^2 F(f), f = \frac{1}{2}\left[\left(v_{0s}/v\right)^{2/3} - 1\right]. \tag{1.37}$$

where f is the finite strain. The associated pressure on this same reference isentrope is then

$$p_i(v) = 3K_{0s} f (2f+1)^{5/2} \left(F(f) + \frac{fF'}{2} \right). \tag{1.38}$$

The equation of state of the products is a JWL EOS.

Closure Condition

The closure condition enforced is pressure equilibrium, $P_r = P_p = P$ and fixed solid entropy,

$$\left(\frac{DS_r}{Dt} \right)_{\text{particle}} = 0. \tag{1.39}$$

Aside from forcing the tracking of Lagrangian particle, one unfortunate consequence of such a choice of closure condition is that shock waves internal to the reaction wave cannot be accurately represented as they would yield a second entropy rise behind the lead shock wave. Other implementation difficulties presented by the model are described in [44].

Chemical Kinetic Rate

The kinetic rate for is based on observations from initiation gauge data that reaction wave profiles are solely dependent on the entropy of a particle at its shocked state.

$$\frac{D\lambda}{Dt} = m_1 \dot{\lambda}_1 + m_2 \dot{\lambda}_2, \tag{1.40}$$

$$\frac{D\lambda_1}{Dt} = \left[-2b_1 \ln (1-\lambda_1) \right]^{1/2} (1-\lambda_1), \tag{1.41}$$

$$\frac{D\lambda_2}{Dt} = \left[2b_2 \left(\frac{b_2 \lambda_1}{b_1} - \ln (1-\lambda_2) \right) \right]^{1/2} \lambda_1 (1-\lambda_2), \tag{1.42}$$

$$b_1 = c_0 S_s^{c_1}, \tag{1.43}$$

$$b_2 = c_2 S_s^{c_3}, \tag{1.44}$$

where λ_i are reaction progress variables. The weighting functions, m_1, m_2 are given by

$$m_1 = \frac{c_6}{\sqrt{b1}\,(1-\lambda)}, \tag{1.45}$$

$$m_2 = \frac{c_8 S_s^{-c_9} + c_{10} S_s^{c_{11}}}{\sqrt{b_2}\,(1-\lambda)}. \tag{1.46}$$

The variables c_0–c_{11} are fitting parameters. It should also be noted that limits are imposed in the implementation of the CREST model to ensure that b_1 and b_2 remain below a value of 4000 and m_2 does not exceed 10 [5].

1.4 Limitations of Current Models and Methodology

1.4.1 Effectiveness of Models in the Detonation Propagation Regime

The reactive burn models most used currently to model detonation often perform poorly in describing detonation phenomena outside of their calibration range. This is specifically the case for the I&G and CREST models. These two models were formulated specifically as initiation models. In the initiation range, such models perform adequately. For example, in fig 1.4(a) (fig 4 in ref [5]), the calculations of the CREST model for a shock initiated (via a flyer plate) explosive is compared to experimental measurements. Here, the Lagrangian velocity, measured as a function of time at different locations in the explosive sample, are shown for a projectile with a velocity corresponding to a shock pressure of 2.76 GPa in the test explosive EDC-37 (an explosive similar to PBX 9501). When the models are used outside their calibration range, their performance is significantly lower. In fig 1.4(b), the same explosive EDC-37 is modeled using the CREST model. In this case, the input pressure was 10.8 GPa and the input shock transitions to a detonation within the size of the sample. The CREST model is seen to perform adequately during the initiation stage, but significantly over-predicts the particle velocity in the detonation propagation range.

Another test of the ability of a model to adequately capture the detonation propagation regime is the calculation of the diameter effect curve. In this case, the steady-state shape and velocity of a detonation traveling in a right cylindrical geometry is calculated. The detonation velocity is seen to decrease with increasing charge diameter due to the lateral expansion of the reaction zone and detonation products. In fig 1.5(a), the diameter effect curve is calculated for the IHE PBX 9502 (symbols), for three different grid resolutions. In the case of fig 1.5(a), the curvature of the diameter effect curve is wrong, the failure diameter is too large and the velocity deficit for small diameter charges are too great. Similarly in fig 1.5(b), three different I&G calculations are shown and either the failure diameter is correctly reproduced or the velocity deficit for larger charges is correct. Both cannot be reproduced at the same time. Both calculations are for a TATB based explosive like PBX 9502.

The WSD model shows a similar behaviour to the CREST and I&G models in that it reproduces the initiation behaviour of a calibrated explosive very well, but not the propagation behaviour. As an example, fig 1.6 shows figures 8 and 10 from [8]. Fig 1.6(a) shows the particle velocity records from Lagrangian

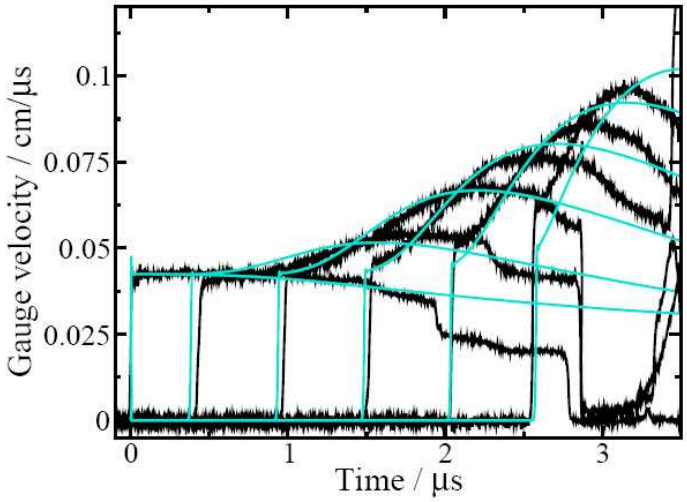

(a) Figure 4 from ref [5], initiation of EDC-37.

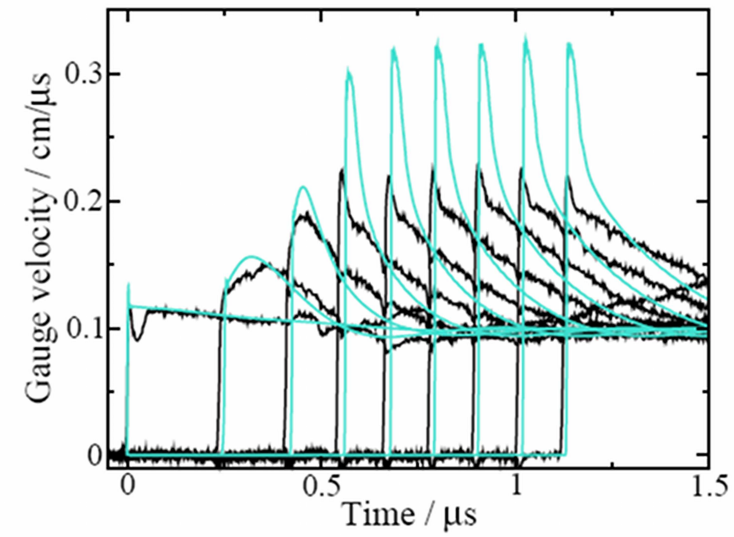

(b) Figure 7 from ref [5], initiation of EDC-37.

Figure 1.4: Figures 4 & 7 from ref [5] showing the initiation of EDC-37 with flyer plates driving shocks with an input pressure of (a) 2.76 GPa and (b) 10.8 GPa.

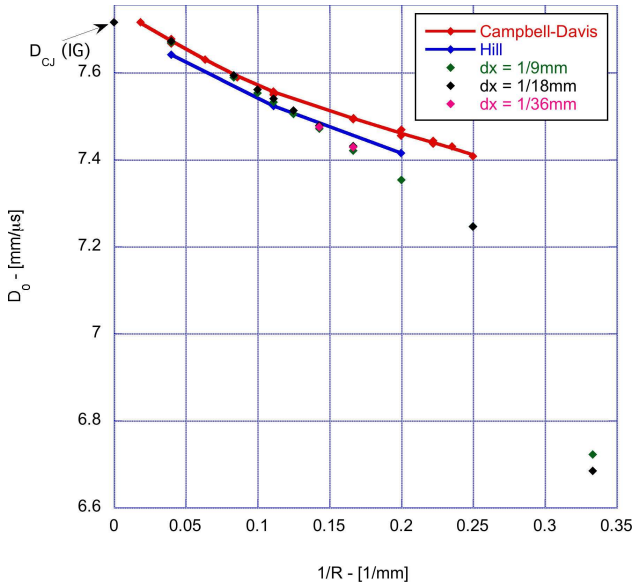

(a) Diameter effect curve calculated by Aslam [6].

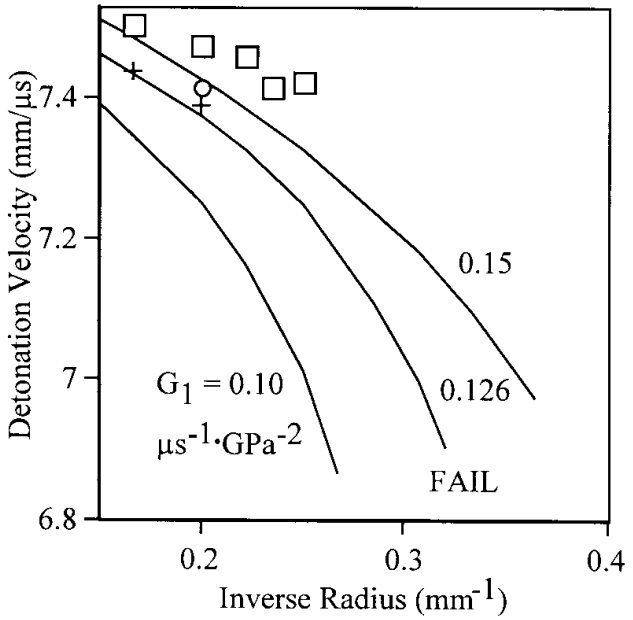

(b) Diameter effect curve calculated in [7].

Figure 1.5: Diameter effect curves for the I&G model as calculated by T.Aslam [6] and [7].

gauges embedded in a sample of PBX 9502 and the profiles simulated using a WSD model. The initiation behaviour shows very good agreement, but a slight overestimation of the peak particle velocity is observed. This overestimation could be attributed to the incapacity of the gauges used in experiments to resolve a very short duration spike in particle velocity, such that the measured maximum particle velocity measured by any one gauge is, in fact, lower than its true value. Fig 1.6(b) shows the diameter effect curve of the explosive PBX 9502 and the calculated curves using the WSD model. Here, the simulations agree relatively well with the experiments, although it should be pointed that this happens only for the finer mesh resolution and there is no evidence that the solution is, in fact, convergent under mesh resolution. This pairing of a model with *a particular grid resolution* is a standard method employed by several researchers in which a particular model calibration is paired with a particular grid spacing which reproduces additional experimental results not used in the model calibration. Such a method obviously does not ensure that the underlying model does, in fact, reproduce the relevant processes examined.

1.5 Outline of Thesis

The main problem of the current generation of HE models is their phenomenological nature. EOS models and rate laws are either ad-hoc fitting forms or based on a preconception of HE dynamics and chemistry not rooted in an understanding of the underlying physical principles. In all cases, the current models are complex and involve many fitting parameters. The model complexity prevents systematic attempts at analyzing their basic behaviour: detonation structure, stability, etc. For example, the P–T equilibrium closure condition is widely used in HE modelling despite the understanding that heat transfer rates between the solid and gaseous phases are probably not fast enough to equilibrate the temperature. The implications of changing the closure condition of an HE model has not been studied systematically. As a result, current models lack predictive capability.

There is a growing interest and need for a new generation of engineering style reactive burn HE models which adequately capture physical processes at play and are simple enough to be integrated into the available engineering calculation tools. The next generation of predictive models will need to exhibit lower complexity and fitting parameters which can be easily related to physical characteristics of the material. Developing these new engineering models requires a deeper understanding of the implications of model design choices. A strong candidate to explore this new class of predictive models is the stiffened-gas (SG) EOS model. The SG EOS is an extension of the ideal gas EOS but incorporates a pressure offset. This simple extension allows the EOS to capture a much wider range of physical behaviour relevant to HEs and an engineering model

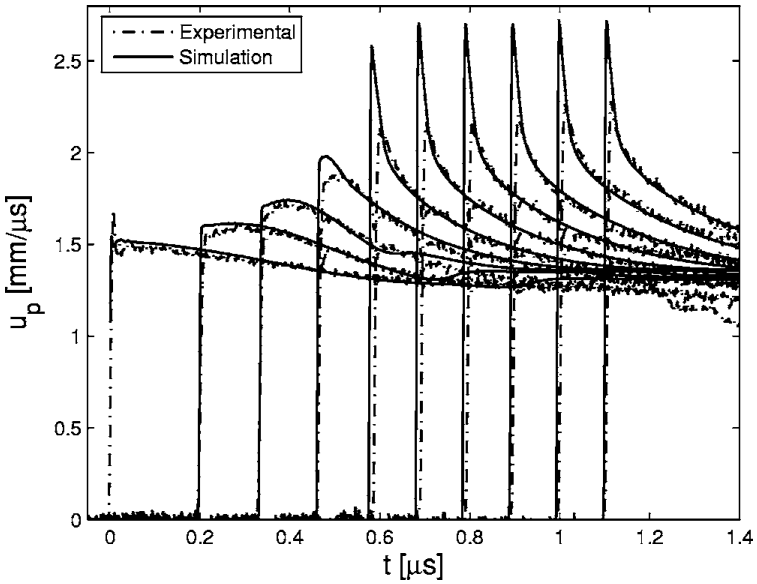

(a) Figure 8 from [8] showing the initiation by a flyer plate and propagation of a detonation.

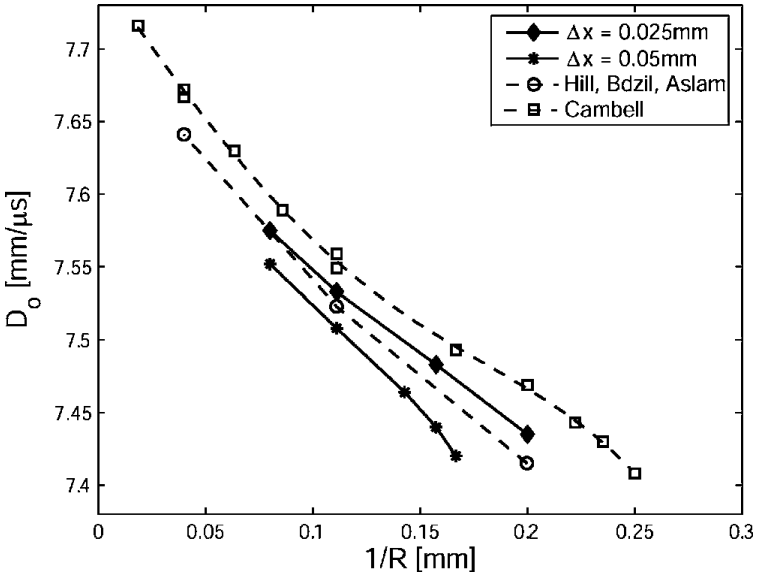

(b) Figure 10 from [8] showing the diameter effect curve for the explosive PBX-9502.

Figure 1.6: Figures 8 (initiation and propagation) and 10 (diameter effect curve) from [8] for the explosive PBX 9502 and the simulations with a calibrated WSD model.

based on the SG EOS is amenable to having for example its stability characteristics and detonation shock structure studied. The implications of different model changes, such as substituting the closure condition, can be studied independently.

The basis of this thesis is to formulate a reactive burn model that is flexible enough to capture the characteristics of the IHE PBX 9502, yet analytically tractable so that individual model components and the implications of a change in one of those components can be studied systematically. Although there are limitations to using the SG EOS when fitting Hugoniot data, those limitations are balanced by the possibility of systematic study of the model characteristics.

The present work is divided into 5 chapters. Chapter 2 covers the derivation of a mathematically tractable, SG based reactive burn model. In chapter 3, this model is calibrated to the IHE PBX 9502 using experimental data relevant to detonation propagation. Two different closure conditions are considered in the fitting process. A new approach utilizing a genetic algorithm is used to fit the chemical parameters. In the following two chapters, basic properties of this reactive burn model are explored. In chapter 4, the linear stability of Zel'dovich-von Neumann-Döring (ZND) detonation waves is formulated for a general EOS and reaction rate model. This general formulation is solved using a pseudo-spectral (collocation) approach and this framework is used to study the stability of multi-component EOS in the context of the SG EOS. The implications of changes in the model parameters as well as changes in the closure condition are examined. In chapter 5, the 2D non-linear structure of detonation waves is investigated in the context of the SG EOS. Shock polar analysis and numerical simulations are utilized to determine the detonation structure when the SG EOS does not allow the classical Mach reflection structure. Finally, in chapter 6, new unconfined rate-stick experiments of the NIHE mixture ANFO are reported and results from the DSD calibration of these experiments are also reported.

Chapter 2

A Tractable Model for Insensitive High Explosives

2.1 Introduction

The goal is to formulate models which are flexible enough to capture the dynamics of propagating detonations, simple enough to be analytically tractable and physically rather than phenomenologically based. One tractable model that has been used is the idealized condensed phase model which uses an ideal gas EOS with an adiabatic $\gamma = 3$. A major drawback of modeling condensed explosives, such as PBX 9502, with an ideal fluid EOS is the low initial sound speed. Combined with the high detonation velocities observed in most solid explosives, this results in very high (near infinite) detonation Mach numbers. The main purpose of deriving the stiffened-gas EOS is to make the initial sound speed of the material higher, i.e. on the order of the detonation sound speed as is the case for PBX 9502 with $c_0 \approx 2$ km/s and $D_{\mathrm{CJ}} = 7.706$ km/s. Two models are described here; both are based on a stiffened-gas (SG) EOS. The SG EOS is similar to the ideal gas EOS, but its sound speed is controlled through a pressure offset. Two closure conditions are considered: pressure & temperature equilibrium and constant solid entropy. The reaction scheme is a two step chemical kinetic reaction to capture the two stages of heat release that are typical in IHEs.

2.2 Stiffened-Gas EOS

2.2.1 Incomplete EOS Definition

The SG incomplete EOS is an extension of the ideal condensed phase model [45], having the property that the sound speed is finite as $P \to 0$. An incomplete EOS is of the form $e = e(P, v)$ involving only pressure and specific volume, but not temperature. The accompanying thermal EOS is described later. The sound speed and adiabatic index γ are related as

$$\gamma = -\left(\frac{d(\ln P)}{d(\ln v)}\right)_S = -\frac{v}{P}\left(\frac{dP}{dv}\right)_S \frac{d\rho}{dv} = \frac{c^2}{Pv}. \tag{2.1}$$

For a constant adiabatic index, γ, the sound speed $c^2 \to 0$ as $P \to 0$. To obtain a finite sound speed at low pressures, the requirement that $\gamma \sim 1/P$ when $P \to 0$ is imposed. As the simplest possible EOS, a model with an adiabatic index

$$\gamma = \overline{\gamma} + \frac{A}{P}, \tag{2.2}$$

is proposed, where $\overline{\gamma}$ and A are both constants. With such a choice, for $P_0 \sim 0$, the initial sound speed becomes $c_0^2 \sim Av_0$, as desired. From the first law of thermodynamics, $Tds = de + Pdv$, the sound speed can be derived for an arbitrary EOS as

$$c^2 = v^2 \frac{P + e_{,v}}{e_{,P}}. \tag{2.3}$$

The Grüneisen Gamma is defined as $\Gamma = v/(e_{,P})_v$. Substituting for $e_{,P}$ and c^2, the derivative of internal energy with pressure is found

$$(e_{,v})_P = \frac{kP + A}{\Gamma}, \tag{2.4}$$

where $k = \overline{\gamma} - \Gamma$. The simplest form of the Grüneisen Gamma is to assume a constant, leading to the stiffened-gas EOS

$$e - e_0 = \frac{kP + A}{\Gamma} v - \frac{kP_0 + A}{\Gamma} v_0, \tag{2.5}$$

with k constant. The above can be rewritten, for clarity, as

$$e - e_0 = \frac{P + (A/k)}{(\Gamma/k)} v - \frac{P_0 + (A/k)}{\Gamma/k} v_0, \tag{2.6}$$

from which it is obvious that the constant k acts as an arbitrary scale factor on the two constants A and Γ and, without loss of generality, $k = 1$ is selected. Eqn 2.2 then yields the adiabatic gamma

$$\gamma = \Gamma + 1 + \frac{A}{P}. \tag{2.7}$$

The sound speed for the SG EOS, eqn 2.3, becomes

$$c^2 = \left[(\Gamma + 1)\, P + A\right] v. \tag{2.8}$$

2.2.2 Definition of Temperature and Caloric Equation of State

The SG EOS, eqn 2.6, is an incomplete EOS of the form $e = e(P, v)$. If the temperature of the material appears in either the closure condition or the chemical rate law, a complete EOS or an accompanying thermal EOS $T = T(P, v)$ is required. Using the first law of thermodynamics for a reversible process and the differential of energy, the thermodynamic temperature is defined as

$$\begin{aligned} TdS &= de + Pdv, && (2.9)\\ de &= \left(\frac{\partial e}{\partial P}\right)_v dP + \left(\frac{\partial e}{\partial v}\right)_P dv. && (2.10) \end{aligned}$$

Upon substituting and rearranging, one obtains

$$T = \left(\frac{\partial e}{\partial P}\right)_v \frac{dP}{dS} + \left[\left(\frac{\partial e}{\partial v}\right)_P + P\right]\frac{dv}{dS}. \tag{2.11}$$

Using Maxwell's relations

$$\begin{aligned} \left(\frac{\partial P}{\partial S}\right)_T &= -\left(\frac{\partial T}{\partial v}\right)_P, && (2.12)\\ \left(\frac{\partial v}{\partial S}\right)_T &= \left(\frac{\partial T}{\partial P}\right)_v, && (2.13) \end{aligned}$$

it is possible to relate the temperature, T, the pressure, P, and specific volume, v, of a substance through the caloric EOS, $(\partial e/\partial v)_P$ and $(\partial e/\partial P)_v$, and two different processes represented by the differentials $(\partial T/\partial P)_v$ and $(\partial T/\partial v)_P$. Considering each of the processes independently, we find that

$$\frac{dT}{T} = \frac{dP}{(\partial e/\partial v)_P + P} = -\frac{dv}{(\partial e/\partial P)_v}. \tag{2.14}$$

Applying this to the stiffened-gas EOS one obtains

$$\frac{dT}{T} = \frac{\Gamma dP}{P(\Gamma + 1) + A} = -\Gamma\frac{dv}{v}, \tag{2.15}$$

and integration yields

$$\ln T = \frac{\Gamma}{\Gamma + 1}\ln\left(\frac{\Gamma + 1}{\Gamma}P + \frac{A}{\Gamma}\right) + \ln C_1 = -\Gamma \ln v + \ln C_2 \tag{2.16}$$

or equivalently

$$T\left[\frac{\Gamma+1}{\Gamma}P+\frac{A}{\Gamma}\right]^{-\frac{\Gamma}{\Gamma+1}} = C_1, \tag{2.17}$$

$$Tv^{\Gamma} = C_2, \tag{2.18}$$

$$\left[\frac{\Gamma+1}{\Gamma}P+\frac{A}{\Gamma}\right]^{\frac{\Gamma}{\Gamma+1}} v^{\Gamma} = \frac{C_2}{C_1}. \tag{2.19}$$

These reduce, for the case of $A = 0$, to the isentropic relations for an ideal gas. Using eqns 2.17-2.19, if a reference temperature, T_{ref} is known in some region of space $(P_{\text{ref}}, v_{\text{ref}})$, then the temperature, T, can be calculated along all the isentropes which intersect that section of space. Using the above relationships, the incomplete EOS can be written as a function of temperature,

$$e(T) - e_0 - \frac{(P_0+A)v_0}{\Gamma} = \frac{1}{\Gamma+1}\frac{C_2^{1/\Gamma}}{C_1^{(\Gamma+1)/\Gamma}}T + \frac{AC_2^{1/\Gamma}}{\Gamma+1}T^{-1/\Gamma}. \tag{2.20}$$

The specific heat at constant volume, assumed to be a constant in the remainder of this work, is defined by $C_v = \frac{1}{\Gamma+1}\frac{C_2^{1/\Gamma}}{C_1^{(\Gamma+1)/\Gamma}}$. The complete EOS is then

$$e(T,v) - (e_0 - \overline{e}_0) = C_vT + \frac{A}{\Gamma+1}v = \frac{P+A}{\Gamma}v, \tag{2.21}$$

which simplifies to the perfect gas result in the case of $A = 0$. The constant $\overline{e}_0$ corresponds to the internal energy of the fluid at the reference state, i.e. $\overline{e}_0 = (P_0 + A)v_0/\Gamma$. The assumption of the form of C_v specifies the relationship between P, v and T. Using eqns 2.17-2.19, and defining the arbitrary reference state, $(P_{\text{ref}}, v_{\text{ref}}, T_{\text{ref}})$, it can be shown that

$$C_v = \frac{1}{\Gamma(\Gamma+1)}\frac{[(\Gamma+1)P_{\text{ref}} + A]\, v_{\text{ref}}}{T_{\text{ref}}}. \tag{2.22}$$

In the case of the ideal gas law, $A = 0$, and $\Gamma = \gamma - 1$, the expected EOS is obtained,

$$(\gamma-1)C_vT = Pv. \tag{2.23}$$

The subscript $_{\text{ref}}$ has been dropped as the above must hold for *any* reference state and is therefore valid in the entire state space. For a SG EOS, the corresponding thermal EOS is

$$\Gamma(\Gamma+1)C_vT = [(\Gamma+1)P + A]\, v. \tag{2.24}$$

An alternate derivation of the same EOS is presented in section A.1.

2.2.3 Shock Behaviour and Stability

A parameter of interest is the fundamental derivative, G, [45, 46]. The incomplete stiffened-gas EOS, $e(P, v)$, can be rewritten as

$$P(e, v) = \frac{\Gamma \left[e - (e_0 - \overline{e}_0) \right]}{v} - A. \tag{2.25}$$

It follows that the quantity of interest is

$$G = \frac{v^3}{2c^2} \left(\frac{d^2 P}{dv^2} \right)_s = \frac{\Gamma + 2}{2}. \tag{2.26}$$

This result is independent of A and identical to that obtained using a perfect gas EOS. As $G > 0$, "normal" behaviour is expected, i.e. compression waves steepen into shock waves and expansion shock waves are impossible. Fowles and Swan [47, 48, 49, 50] have analyzed the stability of shock waves extensively, following and reviewing the early work of D'iakov and Kontorovich. The issue of shock stability is also extensively discussed in Menikoff and Plohr [51]. A sufficient criterion for stable shock waves is

$$\Gamma \leq \gamma - 1. \tag{2.27}$$

From 2.7, it is easily shown that for $A \geq 0$, this stability criterion is always satisfied and shock waves are stable.

2.2.4 Shock Hugoniot

For a generic, non-reacting fluid, starting from the steady conservation laws in integral form

$$\frac{u_0}{v_o} = \frac{u_1}{v_1}, \tag{2.28}$$

$$P_0 + \frac{u_0^2}{v_0} = P_1 + \frac{u_1^2}{v_1}, \tag{2.29}$$

$$h_0 + \frac{u_0^2}{2} = h_1 + \frac{u_1^2}{2}, \tag{2.30}$$

an equation relating the enthalpy, h, the specific volume, v, and the pressure, P can be written

$$h_1 - h_0 = \frac{1}{2}\left(P_1 - P_0\right)\left(v_0 + v_1\right). \tag{2.31}$$

For a stiffened-gas EOS, the enthalpy becomes

$$h = e + Pv = \frac{(P + A)v}{\Gamma} + Pv + e_0 = \frac{((\Gamma + 1)P + A)v}{\Gamma} + e_0. \tag{2.32}$$

Substituting, the Hugoniot curve for a fluid with a stiffened-gas EOS is obtained

$$\frac{2(\Gamma + 1)}{\Gamma}\left[\left(\frac{P_1}{P_0} + \frac{A}{(\Gamma + 1)P_0}\right)\frac{v_1}{v_0} - \left(1 + \frac{A}{(\Gamma + 1)P_0}\right)\right] = \left(\frac{P_1}{P_0} - 1\right)\left(\frac{v_1}{v_0} + 1\right). \tag{2.33}$$

This links the initial state of a fluid, $_0$, with its final shocked state, $_1$.

Characteristics of the $P - v$ Hugoniot

For clarity, the substitution $y = P_1/P_0$, $x = v_1/v_0$ is used and solving eqn 2.33 for the pressure ratio the Hugoniot then becomes

$$y = \frac{\Gamma + 2 + 2A/P_0 - (\Gamma + 2A/P_0)\,x}{2(\Gamma + 1)x - (x + 1)\,\Gamma}. \tag{2.34}$$

There are two limits of interest. The first is the minimum specific volume ratio, $x_{\min}$, at which the pressure ratio becomes infinite, $y \to \infty$.

$$x_{\min} = \frac{\Gamma}{\Gamma + 2}. \tag{2.35}$$

The second limit is the maximum specific volume ratio, $x_{\max}$, at which the pressure ratio becomes null, $y = 0$.

$$x_{\max} = \frac{\Gamma + 2 + 2A/P_0}{\Gamma + 2A/P_0} \tag{2.36}$$

These two limits define the range between which the Hugoniot curve has physical meaning. A shock of infinite strength would bring the pressure ratio to infinity, $y \to \infty$, and the specific volume ratio to its minimum value, $x \to x_{\min}$. An expansion to a vacuum would bring the pressure ratio to zero, $y \to 0$ and the specific volume to its maximum value, $x \to x_{\max}$. Ultimately, the behaviour of the EOS is of concern only between those two bounds.

2.2.5 u_p-u_s curve

One of the most important experimental diagnostics is the particle-shock velocity plot for a given material. Starting, again from the conservation laws in integral form, eqns 2.28–2.30, but eliminating the pressure P and density ρ and retaining the two velocities, u_0 and u_1, one can express the same Hugoniot relationship in the "$u_s - u_p$" plane. Note that, in the frame of reference of the shock, the incoming velocity is the shock velocity, $u_0 = u_s$, and the exit velocity is related to the particle velocity, $u_1 = u_s - u_p$. Solving for the particle velocity gives

$$u_p = \frac{2}{\Gamma + 2}\left[u_s - \frac{(\Gamma+1)P_0 + A}{\rho_0}\frac{1}{u_s}\right] = \frac{2}{\Gamma+2}\left[u_s - \frac{c_0^2}{u_s}\right]. \tag{2.37}$$

The term containing the reciprocal of the shock velocity can be rewritten as $u_s - c_0^2/u_s = u_s(1 - 1/M_s^2)$, i.e. the non-linearity in the shock Hugoniot is on the order of the inverse square of the shock Mach number. For solid explosives in the range of interest, $u_s \sim D_{\mathrm{CJ}} \sim 6-8$ km/s and $c_0 \sim 1-3$ km/s and $1.5\% \lesssim 1/M_s^2 \lesssim 25\%$. As expected, the u_p–u_s curve is thus mostly linear. The u_s–u_p curve corresponding to the SG EOS has a positive curvature, most pronounced for low particle velocities. As will be shown later, this limits our ability to fit Hugoniot data for solid PBX 9502. The implication of the SG EOS's positive curvature is discussed in chapter 3. (See fig 3.8 for an example of the SG EOS Hugoniot compared to experimental data.)

2.3 Blended Pressure Offset EOS

As is shown in chapter 3, the shock Hugoniot of a single phase stiffened-gas (SSG) EOS has the opposite curvature when compared to the experimentally determined Hugoniot (u_s–u_p) of PBX 9502. The Hugoniot of this explosive also appears to have an inflexion point around $u_p \sim 1$ km/s. To capture this feature, an EOS which consists of two "blended" SG (BSG) EOS is developed.

2.3.1 EOS Definition

The incomplete EOS is given by blending the energy functions such that

$$e(P,V) - e_0 = \frac{(P+A_1)v}{\Gamma_1}W(P) + \frac{(P+A_2)v}{\Gamma_2}(1-W(P)) - \frac{(P_0+A_1)v_0}{\Gamma_1}W(P_0) - \frac{(P_0+A_2)v_0}{\Gamma_2}(1-W(P_0)). \tag{2.38}$$

The function $W(P)$ exhibits a rapid transition around $P = P_c$, so that

$$W(P) \to 1,\ P << P_c, \tag{2.39}$$

$$W(P) \to 0,\ P >> P_c. \tag{2.40}$$

Some choices of $W(P)$ include a Heaviside function or a well-crafted hyperbolic tangent function. In the present section, the function is assumed to be a Heaviside function $W(P) = H(1-P/P_c)$. Assuming $P_0 < P_c$, the final incomplete EOS is

$$e(P,v) - e_0 = \frac{(P+A_1)v}{\Gamma_1}W(P) + \frac{(P+A_2)v}{\Gamma_2}(1-W(P)) - \frac{(P_0+A_1)v_0}{\Gamma_1}. \tag{2.41}$$

2.3.2 Temperature

The temperature is, again, defined by integrating along the isentrope from a reference state, $P_{\text{ref}}, v_{\text{ref}}, T_{\text{ref}}$, using eqn 2.15. There are three different cases depending on whether the cross-over pressure, P_c, lies outside or inside the interval defined by the reference pressure and the pressure at which the temperature is desired, (P_{ref}, P). In the first case, the isentropic relations are identical to those of a single SG EOS and the material parameters are chosen accordingly.

Case $P_c \notin (P_{\text{ref}}, P)$

If the pressure P_c is not within the range (P_{ref}, P) the definition of temperature is identical to that of a single SG EOS, eqns 2.17-2.19. If $P_c \geq P_{\text{ref}} > P$ or $P_c \geq P > P_{\text{ref}}$, the material properties are defined by $A = A_1$ and $\Gamma = \Gamma_1$. If $P_c \leq P_{\text{ref}} < P$ or $P_c \leq P < P_{\text{ref}}$, the material properties are defined by $A = A_2$, $\Gamma = \Gamma_2$.

Case $P_c \in (P_{\text{ref}}, P)$

In the case where $P_{\text{ref}} < P_c < P$ or $P < P_c < P_{\text{ref}}$, the integration of eqn 2.15 must be carried over the discontinuity in the caloric EOS. First, an equation relating temperature and pressure can derived by integrating

$$\int_{T_{\text{ref}}}^{T} \frac{dT}{T} = \ln\frac{T}{T_{\text{ref}}} = \int_{P_{\text{ref}}}^{P} \frac{dP}{e_{,v}+P} = C, \tag{2.42}$$

where C is a constant. From the definition of the caloric EOS, the integration along pressure can be broken down into two parts

$$C = \int_{P_{\text{ref}}}^{P_c} \frac{\Gamma_1 dP}{(\Gamma_1 + 1)\, P + A_1} + \int_{P_c}^{P} \frac{\Gamma_2 dP}{(\Gamma_2 + 1)\, P + A_2}. \tag{2.43}$$

The final result is a relationship between (T, T_{ref}) and (P, P_{ref})

$$\frac{T}{T_{\text{ref}}} = \frac{\left[(\Gamma_2 + 1)\, P + A_2\right]^{\Gamma_2/(\Gamma_2+1)}}{\left[(\Gamma_1 + 1)\, P_{\text{ref}} + A_1\right]^{\Gamma_1/(\Gamma_1+1)}} \frac{\left[(\Gamma_1 + 1)\, P_c + A_1\right]^{\Gamma_1/(\Gamma_1+1)}}{\left[(\Gamma_2 + 1)\, P_c + A_2\right]^{\Gamma_2/(\Gamma_2+1)}}. \tag{2.44}$$

A relationship between pressure and volume can also be obtained by integrating

$$\int_{P_{\text{ref}}}^{P} \frac{dP}{e_{,v} + P} = -\int_{v_{\text{ref}}}^{v} \frac{dv}{e_{,P}}. \tag{2.45}$$

This integral is possible because for the present choice of EOS, $e_{,P} = vF(P)$, making the problem separable

$$\int_{P_{\text{ref}}}^{P} \frac{(e_{,P}/v)dP}{e_{,v} + P} = -\int_{v_{\text{ref}}}^{v} \frac{dv}{v} = -\ln \frac{v}{v_{\text{ref}}} = C. \tag{2.46}$$

The integral along pressure is described in section A.2. The result is

$$\left[\frac{(\Gamma_1 + 1)P_c + A_1}{(\Gamma_1 + 1)P_{\text{ref}} + A_1}\right]^{\frac{1}{\Gamma_1+1}} \left[\frac{(\Gamma_2 + 1)P + A_2}{(\Gamma_2 + 1)P_c + A_2}\right]^{\frac{1}{\Gamma_2+1}} e^{\Phi_g(P_c)} = \left(\frac{v}{v_{\text{ref}}}\right)^{-1}, \tag{2.47}$$

where $\Phi_g(P_c)$ is a function of $\Gamma_1, \Gamma_2, A_1, A_2$ and P_c (eqn A.14). For the present work, it is assumed that in the context of a propagation model, $P = P_c$ occurs only within the lead shock, and $P > P_c$ can be assumed within the reaction zone. The definition of temperature for the case $P_c < P_{\text{ref}} < P$ can be assumed and the temperature does not have to be defined for pressures lower than P_c.

2.3.3 Shock Stability

In a general fashion, the shock stability criterion can be written as

$$\gamma = \frac{v\,(P + e_{,v})}{P e_{,P}} = \Gamma\left(\frac{e_{,v}}{P} + 1\right) \geq \Gamma + 1. \tag{2.48}$$

From the definition of the caloric EOS, the criterion becomes

$$\frac{(1 + A_1/P)\Gamma_1^{-1} W(P) + (1 + A_2/P)\Gamma_2^{-1}(1 - W(P))}{W(P)\Gamma_1^{-1} + (1 - W(P))\Gamma_2^{-1} + \left[(P + A_1)\Gamma_1^{-1} - (P + A_2)\Gamma_2^{-1}\right] W'(P)} \geq 1. \tag{2.49}$$

Case $P \neq P_c$

In this case, the EOS behaves essentially as a single phase EOS and the stability criterion yields $A_1 > 0$ for stable shocks with $P < P_c$ and $A_2 > 0$ for stable shocks with $P > P_c$

Case $P = P_c$

This analysis is restricted to the case of

$$W(P) = H\left(1 - \frac{P}{P_c}\right), \tag{2.50}$$

$$W'(P) = -\frac{1}{P_c}\delta\left(1 - \frac{P}{P_c}\right). \tag{2.51}$$

The value of the numerator and denominator at $P = P_c$ is found by evaluating, for each function,

$$\Phi(P_c) = \lim_{\epsilon \to 0} \frac{1}{2P_c\epsilon} \int_{P_c(1-\epsilon)}^{P_c(1+\epsilon)} \phi(P) dP. \tag{2.52}$$

The numerator is written as

$$\begin{aligned} \Phi_t &= \int_{P_c(1-\epsilon)}^{P_c(1+\epsilon)} \left[\frac{W}{\Gamma_1} + \frac{A_1}{\Gamma_1 P} W + \frac{1-W}{\Gamma_2} + \frac{A_2}{\Gamma_2 P}(1-W)\right] dP = \\ &\int_{P_c(1-\epsilon)}^{P_c} \left[\frac{1}{\Gamma_1} + \frac{A_1}{\Gamma_1 P}\right] dP + \int_{P_c}^{P_c(1+\epsilon)} \left[\frac{1}{\Gamma_2} + \frac{A_2}{\Gamma_2 P}\right] dP, \end{aligned} \tag{2.53}$$

and the result of the integration is

$$\Phi_t = \int_{P_c(1-\epsilon)}^{P_c(1+\epsilon)} \phi_t(P) dP = \frac{A_1}{\Gamma_1} \ln \frac{1}{(1-\epsilon)} + \frac{P_c\epsilon}{\Gamma_1} + \frac{P_c\epsilon}{\Gamma_2} + \frac{A_2}{\Gamma_2} \ln \frac{(1+\epsilon)}{1}. \tag{2.54}$$

Similarly, the denominator is written as

$$\begin{aligned} \Phi_b &= \int_{P_c(1-\epsilon)}^{P_c(1+\epsilon)} \left[\frac{W}{\Gamma_1} + \frac{1-W}{\Gamma_2}\right] dP - \left(\frac{P_c}{\Gamma_1} + \frac{A_1}{\Gamma_1} - \frac{P_c}{\Gamma_2} - \frac{A_2}{\Gamma_2}\right) = \\ &\int_{P_c(1-\epsilon)}^{P_c} \frac{dP}{\Gamma_1} + \int_{P_c}^{P_c(1+\epsilon)} \frac{dP}{\Gamma_2} - \left(\frac{P_c}{\Gamma_1} + \frac{A_1}{\Gamma_1} - \frac{P_c}{\Gamma_2} - \frac{A_2}{\Gamma_2}\right). \end{aligned} \tag{2.55}$$

The result of the integration is

$$\Phi_b = \int_{P_c(1-\epsilon)}^{P_c(1+\epsilon)} \phi_b(P)dP = \frac{P_c\epsilon}{\Gamma_1} + \frac{P_c\epsilon}{\Gamma_2} - \frac{P_c}{\Gamma_1} - \frac{A_1}{\Gamma_1} + \frac{P_c}{\Gamma_2} + \frac{A_2}{\Gamma_2}. \tag{2.56}$$

The stability criterion can thus be evaluated at $P = P_c$

$$\frac{\phi_t(P_c)}{\phi_b(P_c)} = \frac{\lim_{\epsilon\to 0}\Phi_t(2P_c\epsilon)^{-1}}{\lim_{\epsilon\to 0}\Phi_b(2P_c\epsilon)^{-1}} = \frac{\Gamma_1^{-1} + \Gamma_2^{-1} + A_1(\Gamma_1 P_c)^{-1} + A_2(\Gamma_2 P_c)^{-1}}{\Gamma_1^{-1} + \Gamma_2^{-1}} \geq 1. \tag{2.57}$$

This last result is true since $A_1 > 0$, $A_2 > 0$, $\Gamma_i > 0$, $P > 0$. Shock waves are therefore stable with the present choice of EOS.

2.3.4 Shock Hugoniot

Pressure-volume Hugoniot

The difference in enthalpy between the pre- and post-shock states is

$$h - h_0 = \frac{(P + A_i)v}{\Gamma_i} + Pv - \frac{(P_0 + A_1)v_0}{\Gamma_1} - P_0v_0 = \frac{(\Gamma_i + 1)P + A_i}{\Gamma_i}v - \frac{c_0^2}{\Gamma_1}, \tag{2.58}$$

where $i = 1$ if $P < P_c$ and $i = 2$ if $P > P_c$. The $P - v$ Hugoniot can be written, similar to the single SG case, as

$$y = \frac{(2/\Gamma_1)(1 + a_1) - 2a_i x/\Gamma_i + 1 - x}{2x/\Gamma_i + x - 1}, \tag{2.59}$$

where $a_i = A_i/P_0$. The minimum specific volume ratio (maximum compression) is

$$x_{\min} = \frac{\Gamma_2}{2 + \Gamma_2} \tag{2.60}$$

and the intersection of the Hugoniot with the $P = 0$ axis is, as for the single SG EOS,

$$x_{\max} = \frac{(2/\Gamma_1)(1 + a_1) + 1}{2a_1/\Gamma_1 + 1}. \tag{2.61}$$

Shock-Particle Velocity Hugoniot

The $u_s - u_p$ Hugoniot is found by eliminating P and v from the conservation laws. From the conservation of mass and momentum, the specific volume and pressure are expressed as

$$v = \left(1 - \frac{u_p}{u_s}\right) v_0, \tag{2.62}$$

$$P = P_0 + \frac{u_p u_s}{v_0}. \tag{2.63}$$

Upon substituting the above in the conservation of energy, the following is obtained

$$\frac{1}{\Gamma_1}\left[(\Gamma_1+1)P_0 + A_1\right] v_0 = \left\{\frac{1}{\Gamma_i}\left[(\Gamma_i+1)P_0 + A_i\right] v_0 + \frac{\Gamma_i + 1}{\Gamma_i} u_p u_s\right\}\left(1 - \frac{u_p}{u_s}\right) + \frac{u_p^2}{2} - u_s u_p. \tag{2.64}$$

Two sound speeds are defined. The actual initial sound speed of the material, $c_0^2 = \left[(\Gamma_1+1)P_0 + A_1\right] v_0$ and an initial sound speed based on the post-shock material properties, $\overline{c}_0^2 = \left[(\Gamma_i+1)P_0 + A_i\right] v_0$. If the post-shock pressure is lower than P_c, $i = 1$ and $\overline{c}_0^2 = c_0^2$. If the post-shock pressure is higher than P_c, $\overline{c}_0^2 \neq c_0^2$. The above can be solved for u_p,

$$u_p = \frac{1}{\Gamma_i + 2}\left[\left(u_s - \frac{c_i^2}{u_s}\right) \pm \sqrt{\left(u_s - \frac{c_i^2}{u_s}\right)^2 + 2\left(\Gamma_i + 2\right)\left(c_i^2 - \frac{\Gamma_i}{\Gamma_1} c_1^2\right)}\right]. \tag{2.65}$$

2.3.5 Continuity of the Caloric EOS and its Derivatives

The continuity of the caloric EOS is related to the choice of the cross-over pressure, P_c, presented in the next section. For an arbitrary choice of P_c, the resulting internal energy, $e(P, v)$ is not guaranteed to be continuous around the set of states (P_c, v). To ensure the energy function is continuous, i.e.

$$e_1(P_c, v) = \frac{P_c + A_1}{\Gamma_1} v = e_2(P_c, v) = \frac{P_c + A_2}{\Gamma_2} v, \tag{2.66}$$

the transition pressure must be given by

$$P_c = \left(\frac{A_2}{\Gamma_2} - \frac{A_1}{\Gamma_1}\right) \frac{\Gamma_1 \Gamma_2}{\Gamma_2 - \Gamma_1}. \tag{2.67}$$

Forcing the energy to be continuous results in only three of the four parameters, Γ_1, Γ_2, A_1 and A_2 being imposed independently. Moreover, even with a continuous internal energy function, the derivatives of the internal energy,

$$e_{,P} = e_{1,P}W(P) + e_{2,P}(1 - W(P)) + (e_1 - e_2)W'(P), \tag{2.68}$$

$$e_{,v} = e_{1,v}W(P) + e_{2,v}(1 - W(P)), \tag{2.69}$$

are only guaranteed to be continuous if $e_{1,v} = e_{2,v}$ and $e_{1,P} = e_{2,P}$. From this restriction follows that $\Gamma_1 = \Gamma_2$ and $A_1 = A_2$ and the EOS reverts to the SG EOS derived previously. Outside of the trivial case, it is thus impossible to craft a blended EOS of the proposed type and ensure continuity of the internal energy, e as well as that of its derivatives, $e_{,P}$ and $e_{,v}$.

A non-continuous caloric EOS at the cross-over pressure, P_c results in a model behaviour akin to a non-thermally neutral phase change. Depending on the selection of the parameters, $\Gamma_1, \Gamma_2, A_1, A_2$ and P_c, there is a sudden endo- or exo-thermic process taking place at $P = P_c$ corresponding to the phase change.

2.3.6 Selection of the Cross-Over Pressure, P_c

For the present purpose, the transition pressure is selected to have a resulting continuous Hugoniot. The transition pressure is set to be the intersection point of the Hugoniots curves corresponding to e_1 and e_2.

$$P_c = \rho_0 u_s^* u_p^*, \tag{2.70}$$

where u_s^*, u_p^* corresponds to the intersection point of the Hugoniots in $u_s - u_p$ space. The four parameters, Γ_1, Γ_2, A_1 and A_2 are therefore selected to match the experimental Hugoniot data below and above the transition point. The transition pressure, P_c, is selected to correspond to the intersection of the shock Hugoniots of e_1 and e_2, according to equation 2.70. For PBX 9502, this transition point is in the vicinity of

$$u_s^* \sim \frac{5}{8} D_{\mathrm{CJ}}, u_p^* \sim \frac{1}{8} D_{\mathrm{CJ}}, \tag{2.71}$$

corresponding to

$$P_c \sim 0.078 \rho_0 D_{\mathrm{CJ}}^2. \tag{2.72}$$

If the local pressure everywhere inside the detonation reaction zone is above P_c, then the discontinuity in the energy and its derivatives only occurs within the lead shock wave.

2.4 Species Composition of Mixture Model

One of the characteristics of PBX 9502, is the two step chemical conversion from reactants to products. First, the solid reactants (A) are converted to a mixture of mostly hot gaseous products and some solid carbon (B). This step accounts for most of the heat release. A second step is carbon coagulation [10], in which small solid carbon particles coalesce to form larger complexes and ultimately yield the final products (C). This second step occurs on a much slower scale and accounts for a smaller amount of the heat release. This two step process, involving three chemical species, calls for a three component model, in which

$$A \rightarrow B \rightarrow C. \tag{2.73}$$

Ideally, species A, B and C would each be represented by a separate EOS, reflecting their thermodynamic behaviour

$$\begin{aligned} e_{\text{mixture}} &= e_A^{\triangleright}(P_A, v_A)y_A + (\overline{e}_{0A} - e_{0A})y_A + e_B^{\triangleright}(P_B, v_B)y_B + (\overline{e}_{0B} - e_{0B})y_B + \\ & \quad e_C^{\triangleright}(P_C, v_C)y_C + (\overline{e}_{0C} - e_{0C})y_C. \end{aligned} \tag{2.74}$$

For clarity, the EOS have been written in two parts corresponding to the sensible enthalpy and the enthalpy of formation, $e_i^{\triangleright} = e_i(P_i, v_i) - (e_{0i} - \overline{e}_{0i})$. There is no thermodynamic data on the intermediate B. The thermodynamic characteristics of the species B and C are thus assumed to be identical, yet a release of heat is associated with the conversion from B to C. The mixture model thus consists of three species represented by mass fractions y_A, y_B, y_C, each with its own EOS. The EOS parameters of species B and C are assumed to be identical, thus $e_B^{\triangleright} = e_C^{\triangleright}$. Species A is the solid reactant and mixtures B and C behave like the gaseous products, thus $y_s = y_A$ and $y_g = y_B + y_C$, where the subscripts $_s$ and $_g$ correspond to the properties of the solid (reactant) and gaseous (product) phases respectively. Two heat release terms correspond to the main, first step and slow, second step heat releases.

$$e_{\text{mixture}} = e_s^{\triangleright}(P_s, v_s)y_s + e_g^{\triangleright}(P_g, v_g)y_g + (\overline{e}_{0A} - e_{0A})y_A + (\overline{e}_{0B} - e_{0B})y_B + (\overline{e}_{0C} - e_{0C})y_C. \tag{2.75}$$

The last three terms containing the enthalpies of formation of the different species are replaced by two heat release terms, such that $(\overline{e}_{0A} - e_{0A})y_A + (\overline{e}_{0B} - e_{0B})y_B + (\overline{e}_{0C} - e_{0C})y_C = -y_B Q_{(A\rightarrow B)} - y_C Q_{(A\rightarrow C)}$. The passage from the 6 parameters e_{0i} and $\overline{e}_{0i}$ to the two parameters $Q_{(A\rightarrow B)}$ and $Q_{(A\rightarrow C)}$ conserves the number

of free parameters. The reference sensible energy of each species, $\overline{e}_{0i}$ is defined by the arbitrary reference state (P_0, v_0). The enthalpy of formation, e_0, is defined with respect to the reference sensible energy. There is therefore only a single free parameter per species, $\Delta_i = \overline{e}_{0i} - e_{0i}$. Moreover, similar to setting the enthalpy of formation of stable species to zero, we can set one of the parameters Δ_i to an arbitrary value. There are therefore only two independent parameters. If we redefine the heat release terms with $Q = Q_{(A\to C)}$ and $f_q = Q_{(B\to C)}/Q$, then the energy and specific volume of the mixture are given by

$$e_{\text{mixture}} = e_s(P_s, v_s)y_s + e_g(P_g, v_g)y_g - Q\left[1 - y_A - y_B f_q\right], \tag{2.76}$$

$$v_{\text{mixture}} = v_s y_s + v_g y_g. \tag{2.77}$$

The specific forms of e_s and e_g are selected independently and fitted to Hugoniot data and detonation properties (see chapter 3). For the gaseous phase, only a single SG EOS is used. For the solid (reactant) phase, both the single SG EOS and the blended SG EOS are used. The state variables of the different species (P_s, v_s), (P_g, v_g) are related to the mixture state (P, v) using the closure conditions.

2.5 Closure Conditions

The model developed here ultimately contains 3 species: the solid reactants (A), the gaseous products (C) and an intermediate species (B) close in composition to the final products. Because of the lack of data relevant to the intermediate species, the intermediate species and the products are assumed everywhere to have the same EOS, the same thermodynamical response (i.e. the same EOS parameters) and to be in pressure and temperature equilibrium at all times. This yields a mixture with only two distinguishable phases, a solid phase (reactant) and a gaseous phase (intermediate and product). The closure condition of the model therefore consists of only two conditions relating the solid and gaseous phases.

2.5.1 $P - T$ equilibrium

The pressure and temperature equilibrium closure condition,

$$P_g = P_s = P,\ T_g = T_s = T, \tag{2.78}$$

assumes that both phases are thoroughly mixed and the time scale for heat transfer between the different species is much shorter than the acoustic and reaction time scales. Estimates of the heat transfer time

scales are shown in the next section to be, in fact, longer than reaction time scales and the assumption of thermal equilibrium is incorrect for detonating HE. Given the ubiquity of the temperature equilibrium assumption in current models, this closure condition is examined in the current work. From equation 2.21, the temperatures of the different phases are

$$T_s = \left[\frac{P+A_s}{\Gamma_s}v_s - \frac{A_s}{\Gamma_s+1}v_s\right]\frac{1}{C_{vs}}, \tag{2.79}$$

$$T_g = \left[\frac{P+A_g}{\Gamma_g}v_g - \frac{A_g}{\Gamma_g+1}v_g\right]\frac{1}{C_{vg}}. \tag{2.80}$$

The above result is correct for both the single SG EOS and the blended SG EOS. For the latter EOS, the temperature is defined by assuming that $P > P_c$ everywhere in the reaction zone. As a result, the temperature is only defined for $P > P_c$ and no information is needed about the implicit phase change of the model, yielding $A_s = A_2$ and $\Gamma_s = \Gamma_2$. Imposing thermal equilibrium, v_s is found to be

$$v_s = \frac{C_{vs}\Gamma_s(\Gamma_s+1)}{C_{vg}\Gamma_g(\Gamma_g+1)}\frac{(A_g+P+P\Gamma_g)}{(A_s+P+P\Gamma_s)}v_g = \xi_1(P)v_g. \tag{2.81}$$

Using the definition of the mixture volume, 2.77, and the above result, 2.81, the specific volume of gaseous and solid phases versus the mixture averaged specific volume can be expressed as

$$v_g = \frac{v}{1-y_s+\xi_1 y_s} = \frac{v}{\xi_2(P,y_s)}, \tag{2.82}$$

$$v_s = \frac{\xi_1}{\xi_2}v. \tag{2.83}$$

Using 2.82 and 2.83 into 2.76, the final result is an energy formulation in terms of mixture averaged properties, P and v, the mixture fractions, y_i, and the different parameters of the two phases, Γ_s, Γ_g, A_s, A_g, C_{vs}, C_{vg}

$$\begin{aligned} e(P,v) + Q\left[1-y_A-y_B f_q\right] &= \\ (1-y_s)\frac{(P+A_g)}{\Gamma_g}\frac{v}{\xi_2} + y_s\frac{(P+A_s)}{\Gamma_s}\frac{\xi_1}{\xi_2}v &\quad . \end{aligned} \tag{2.84}$$

Upon setting $A_s = A_g = 0$ and $f_q = 0$, the EOS is that of a two phase ideal gas with $\Gamma_s \neq \Gamma_g$ and differing heat capacities

$$e(P,v) - e_0 = \frac{Pv}{\overline{\Gamma}} - y_g Q, \tag{2.85}$$

where

$$\frac{1}{\overline{\Gamma}} = \frac{C_{vs}(1-y_g) + (y_g)C_{vg}}{C_{vs}\Gamma_s(1-y_g) + C_{vg}\Gamma_g y_g}. \tag{2.86}$$

If in addition $\Gamma_s = \Gamma_g$ and $C_{vs} = C_{vg}$, the calorically perfect gas EOS is recovered.

2.5.2 Solid Entropy Closure Condition

The solid entropy closure condition considered consists of

$$P_g = P_s = P, \tag{2.87}$$

$$\frac{dS_s}{dt} = \frac{\delta Q}{T}, \tag{2.88}$$

where δQ is the heat transfer rate between the gas and solid phases of the mixture. The condition of pressure equilibrium between the different species assumes again mechanical equilibrium between the different phases. The entropy condition is a measure of the heat transfer between the two different species, which can consist of conductive, convective and/or radiative heat transfer, $\delta Q = \delta Q_{\text{cond}} + \delta Q_{\text{conv}} + \delta Q_{\text{rad}}$. For any of these heat transfer mechanisms to be relevant the time scale for heat transfer τ_{H} must be less than the reactive time scale of the flow, $\tau_{\text{R}} \lesssim 300$ns. The rate of conductive heat transfer between the solid particles and the gaseous products is estimated by the Fourier number

$$\text{Fo} = \frac{\alpha_s \tau_{\text{HC}}}{L_{\text{R}}^2}, \tag{2.89}$$

$$\alpha_s = \frac{K}{\rho C_p}. \tag{2.90}$$

Estimating the Fourier number for PBX 9502 yields a convective heating timescale $\tau_{\text{HC}} \sim 3.61 - 81.6$ ms, much longer than the reaction time scale. Convective heat transfer can be dominated by forced or free convection. Free convection is described by the Rayleigh number, which has a cubic dependence on the length scales of the problem and for small length scales (on the order of a grain size) is not expected to play a significant role. Forced convection is directly dependent on the existence of a velocity difference between the two phases. In a detonation wave, the bulk of the flow acceleration occurs via the lead shock wave which accelerates a mixture of initially only solid reactants and not a multi-phase mixture. The presence of gaseous inclusions through chemical reactions occurs while the bulk explosive is moving with a uniform velocity. Only insignificant velocity differences are expected between the two phases and convection can also

be neglected. Finally, the importance of radiative heat transfer is estimated by comparing it to the energy released through combustion

$$\frac{Q_{rad}}{Q_{react}} = \frac{\sigma A(T_g^4 - T_s^4)\tau_R}{\rho\,(\Delta H)_{\text{comb}}\,V}, \tag{2.91}$$

where σ is the Stefan-Boltzmann constant, A is the surface area, V is the volume and $(\Delta H)_{\text{comb}}$ is the heat of combustion. Assuming spherical particles and reaction zone temperatures in the range of 3000–6000 K, the error generated by ignoring radiative heat transfer is on the order of 0.01 %. The final result is that there is no heat transfer between the solid and gaseous phases and the solid reactants can indeed be considered isentropic throughout the reaction zone and

$$\frac{DS_s}{Dt} = 0 \tag{2.92}$$

is valid. (A more detailed description of the estimates is given in appendix B.) An isentropic relation involving pressure and specific volume, eqn 2.19, has already been derived. Together with pressure equilibrium, the closure condition becomes

$$\left(P + \frac{A_s}{1+\Gamma_s}\right) v_s^{1+\Gamma_s} = \left(P^* + \frac{A_s}{1+\Gamma_s}\right) v_s^{*(1+\Gamma_s)} = F(S^*), \tag{2.93}$$

where the * superscript corresponds to the conditions each particle experienced when subjected to the initial lead shock wave. $F(S^*)$ is a function of the solid entropy of each particle at the lead shock conditions. In this form, one of the main drawbacks of this type of condition becomes apparent. The conditions of every particle when undergoing the initial shock process, a Lagrangian property, need to be tracked throughout the flow.

2.6 Chemical Kinetic Model

An important feature of PBX 9502 that one would want to investigate with regards to the stability of the wave is the occurrence of two different time scales for heat release. The proposed chemical kinetic model is of the form

$$A \rightarrow B \tag{2.94}$$

$$B \rightarrow C \tag{2.95}$$

where the first step represents the bulk burning of the solid explosive (A) to gaseous species and particulates (B) and the second step is the coagulation of particulates (carbon clusters) to form the final (mostly gaseous) product mixture (C). Both stages are exothermic with the first step accounting for the most part of the total heat release. The kinetic rates of the two different reactions can be tuned to represent a fast, bulk burn reaction and a slow carbon coagulation. Evidence of two disparate scales in the reaction zone can be seen in the velocity–curvature relationship of the explosives described further in chapter 3.

2.6.1 Bulk Burn

Pressure dependent reaction rates are often employed for bulk burning of solid explosives. The current model includes both a pressure dependence and an Arrhenius like temperature dependence

$$\frac{Dy_s}{Dt} = -r_I = -k_I y_s^{\nu} P^n e^{-\theta/C_{vs}T_s}. \tag{2.96}$$

Both the pressure and temperature dependence are included in this model as only a pressure dependence is incorrect. For example, in diamond anvil cell static compression experiments (see [52] for example) samples of explosives are pressurized to $P > 10$ GPa and yet there is no indication the material starts to undergo reaction.

2.6.2 Carbon Clustering

Close to the CJ point, the particle velocity is expected to be related to the reaction progress variable, $u \propto \lambda$. The rate of clustering of carbon (and therefore the heat release from the process) is expected to be proportional to $t^{-1/3}$ [10]. Shown in fig 2.1, this rate form is compared to the release isentropes of PBX 9502 [53], which shows good agreement. The release isentropes shown are the measured free surface velocity of a cylindrical charge as the detonation wave emerges at its end (colored lines). The result of the calculations are shown by the $\times$ symbol. Given the time dependence of velocity, $\lambda \propto u \propto t^{-1/3}$ can be differentiated, which yields

$$\frac{D\lambda}{Dt} \propto t^{-4/3} = \left(t^{-1/3}\right)^4 = \lambda^4. \tag{2.97}$$

The second kinetic step in this model is thus taken to be pressure independent and of the form

$$r_{II} = f_r k_I y_B^4. \tag{2.98}$$

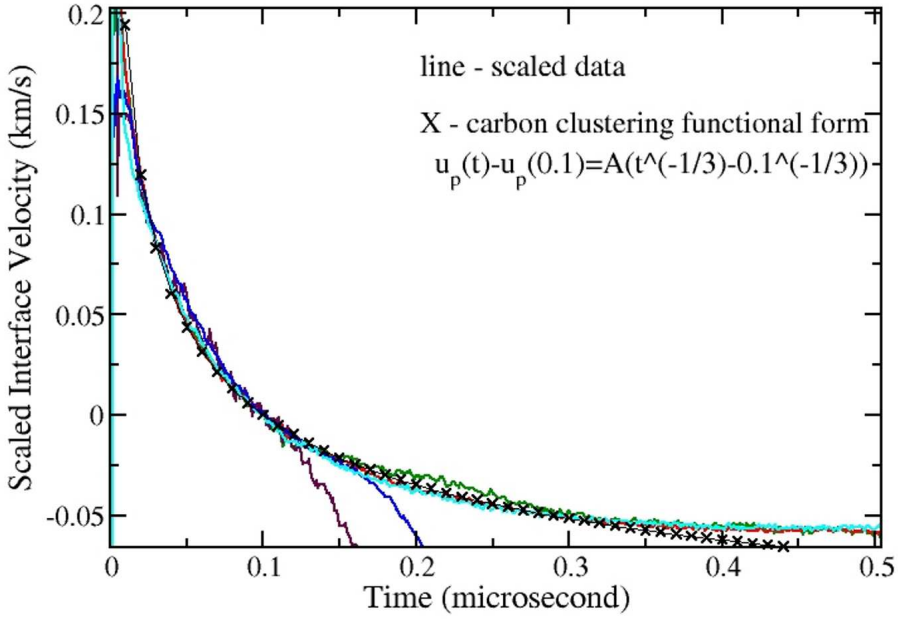

Figure 2.1: Comparison of experimental release isentropes from [9] with the $t^{-1/3}$ dependence of carbon coagulation predicted by Shaw [10]. The experimental data has been shifted to set $t = 0$ as the time of arrival of the shock. The sudden drop-offs in velocity for the different traces corresponds to the arrival of the expansion wave due to the finite sample thickness.

The kinetic rates associated with y_B and y_C are

$$\frac{Dy_B}{Dt} = r_I - r_{II}, \frac{Dy_C}{Dt} = r_{II}. \tag{2.99}$$

The pre-exponential term of r_{II} is defined as $k_{II} = f_r k_I$ and the ratio of time-scales between the two steps can be specified directly.

2.7 Chapman-Jouguet Detonation Solution

This section parallels [54, sections 2A and 2B1(up to page 20)]. The conservation laws, in integral form, applied through a detonation wave are

$$\rho_0 D = \rho(D-u), \tag{2.100}$$

$$P - P_0 = \rho_0 D u, \tag{2.101}$$

$$e(P,v,\lambda=1) + \frac{P}{\rho} + \frac{(D-u)^2}{2} = e_0(P_0,v_0,\lambda=0) + \frac{P_0}{\rho_0} + \frac{D^2}{2}. \tag{2.102}$$

The Rayleigh line equation is identical to that for the perfect gas case,

$$P - P_0 = -\left(\rho_0 D\right)^2 (v - v_0)\,. \tag{2.103}$$

The Hugoniot curve, in its general form is also identical to the perfect gas case

$$e(P,v,\lambda=1) - e_0(P_0,v_0,\lambda=0) = \frac{1}{2}(P+P_0)(v_0-v)\,. \tag{2.104}$$

The Chapman-Jouguet condition requires that the Rayleigh line, Hugoniot curve and isentrope be tangent at the CJ point

$$\left(\frac{dP}{dv}\right)_R = \left(\frac{dP}{dv}\right)_H = \left(\frac{dP}{dv}\right)_s = \frac{-(P-P_0)}{v_0 - v} \tag{2.105}$$

(See [54] or section A.3). The relationship between pressure and specific volume along an isentrope for a fluid following a single SG EOS, eqn 2.19, has already been expressed. Differentiating yields

$$\left(\frac{dP}{dv}\right)_s = -\frac{(\Gamma_g+1)P + A_g}{v} = -\frac{\gamma P}{v}. \tag{2.106}$$

Equating following the criterion in eqn 2.105 and using the Rayleigh line, eqn 2.103, one obtains an equation for the CJ pressure

$$P = \frac{\rho_0 D^2}{\Gamma_g + 2 + A_g/P - P_0/P} = \frac{\rho_0 D^2}{\gamma_{g,\mathrm{CJ}} + 1 - P_0/P}, \tag{2.107}$$

where now $\gamma_{g,\mathrm{CJ}}$ refers to the adiabatic gamma for the gas phase at the CJ state and is given by

$$\gamma_{g,\mathrm{CJ}} = \Gamma_g + 1 + A_g/P_{\mathrm{CJ}}. \tag{2.108}$$

The specific volume and particle velocity can be expressed as functions of the CJ pressure

$$\frac{v}{v_0} = \frac{\gamma_{g,\mathrm{CJ}}}{\gamma_{g,\mathrm{CJ}} + 1 - P_0/P}, \tag{2.109}$$

$$\frac{u}{D} = \frac{1}{\gamma_{g,\mathrm{CJ}} + 1 - P_0/P}. \tag{2.110}$$

These define the CJ state as a function of the eigenvalue velocity, D, the CJ detonation velocity.

The Hugoniot curve can be written as

$$\frac{(P + A_g)v}{\Gamma_g} - Q - \frac{(P_0 + A_s)v_0}{\Gamma_s} = \frac{1}{2}(P + P_0)(v_0 - v), \tag{2.111}$$

where the constants A_g and Γ_g refer to the parameters of the single SG EOS fitted to the products. The constants A_s and Γ_s refer to the EOS parameters of the solid phase. In the case of the blended SG EOS, $A_s = A_1$ and $\Gamma_s = \Gamma_1$. After some manipulation, the following form

$$P\left(1 + \frac{P_0}{P}\right)\left(1 - \frac{v}{v_0}\right) = \frac{2P(1 + A_g/P)v/v_0}{\Gamma_g} - \frac{2Q}{v_0} - \frac{2P(P_0/P + A_s/P)}{\Gamma_s} \tag{2.112}$$

is obtained. A standard approximation for solid explosives is that $P_0/P \to 0$, implying that the CJ pressure is much higher than the initial pressure of the material. In all cases of interest, this is indeed the case. The result is then

$$P\left(1 - \frac{v}{v_0}\right) = \frac{2P(1 + A_g/P)v/v_0}{\Gamma_g} - \frac{2Q}{v_0} - \frac{2A_s}{\Gamma_s}, \tag{2.113}$$

allowing one to solve for the detonation velocity, D,

$$D^2 = \frac{2(\gamma_{g,\mathrm{CJ}} + 1)^2(Q\Gamma_g + A_s v_0(\Gamma_g/\Gamma_s)) - 2\gamma_{g,\mathrm{CJ}}(\gamma_{g,\mathrm{CJ}} + 1)A_g v_0}{2\gamma_{g,\mathrm{CJ}} - \Gamma_g}. \tag{2.114}$$

A verification of the validity of the above is that, upon setting $A_g = A_s = 0$ and $\Gamma_g = \Gamma_s = \Gamma = \gamma - 1 =$ constant, the expression for the detonation velocity of a constant specific heat ratio ideal gas is recovered, namely

$$D^2 = 2\left(\gamma^2 - 1\right)Q. \tag{2.115}$$

There is one unbounded term in the above solution of the CJ velocity of the two stiffened-gas model. This unbounded term causes problems for the limit of $\Gamma_s \to 0$. Indeed, the term $A_s v_0 \Gamma_g/\Gamma_s$ diverges in that limit, for $\Gamma_g \neq \Gamma_s$. For a practical model, $\Gamma_s > 0$ and this unbounded term poses no problem. Interestingly, this

model also allows for propagating detonations even if the heat release Q is zero or negative. This is easily noticed if one examines the expression of detonation velocity in the case of $A_g = 0$

$$D^2 = \frac{2(\gamma_{g,\mathrm{CJ}} + 1)^2 (Q\Gamma_g + A_s v_0 (\Gamma_g/\Gamma_s))}{2\gamma_{g,\mathrm{CJ}} - \Gamma_g}. \tag{2.116}$$

It is clear that even for $Q = 0$, the term $A_s v_0 (\Gamma_g/\Gamma_s)$ still allows a non-zero, positive detonation velocity. This raises an important concern regarding blindly fitting a phenomenological EOS model to limited experimental data without understanding the *physical* consequences of such fitting. This, however, is the norm in fitting phenomenological models to condensed-phase explosives. Part of the aim of this thesis is to derive a simplified model for which the consequences of various fitting can be understood while retaining some reasonable ability to fit real condensed-phase data.

2.8 Variation in von Neumann State

Here, the detonation velocity is specified, in this case $D_{\mathrm{CJ}} = 7.706$ km/s, as well as the CJ pressure and the von Neumann state is plotted as a function of both Γ_s and A_s. for a fixed D_{CJ}, the VN state is independent of the CJ pressure, but its value will influence the value of the gas phase parameters, Γ_g and A_g, and the heat release, Q. The VN state is given by:

$$\frac{u_{\mathrm{VN}}}{D_{\mathrm{CJ}}} = \frac{2}{\Gamma_s + 2}\left[1 - \frac{c_0^2}{D_{\mathrm{CJ}}^2}\right], \tag{2.117}$$

$$P_{\mathrm{VN}} = P_0 + \rho_0 D_{\mathrm{CJ}}^2 \frac{u_{\mathrm{VN}}}{D_{\mathrm{CJ}}}, \tag{2.118}$$

$$\frac{v_{\mathrm{VN}}}{v_0} = 1 - \frac{u_{\mathrm{VN}}}{D_{\mathrm{CJ}}}, \tag{2.119}$$

$$M_{\mathrm{CJ}} = \frac{D_{\mathrm{CJ}}}{c_0}, \tag{2.120}$$

$$c_0^2 = \frac{(\Gamma_s + 1)P_0 + A_s}{\rho_0}. \tag{2.121}$$

Figs 2.2–2.4 show the variation of $u_{\mathrm{VN}}/D_{\mathrm{CJ}}$, P_{VN} and M_{CJ}. A large range of conditions can be achieved using a SG EOS. The almost exclusive dependence of the detonation Mach Number on the pressure offset, A, is to be expected. Since the initial pressure is low (essentially zero), the detonation Mach number can be well approximated by

$$M_{\mathrm{CJ}} = \frac{D_{\mathrm{CJ}}}{A/\rho_0}. \tag{2.122}$$

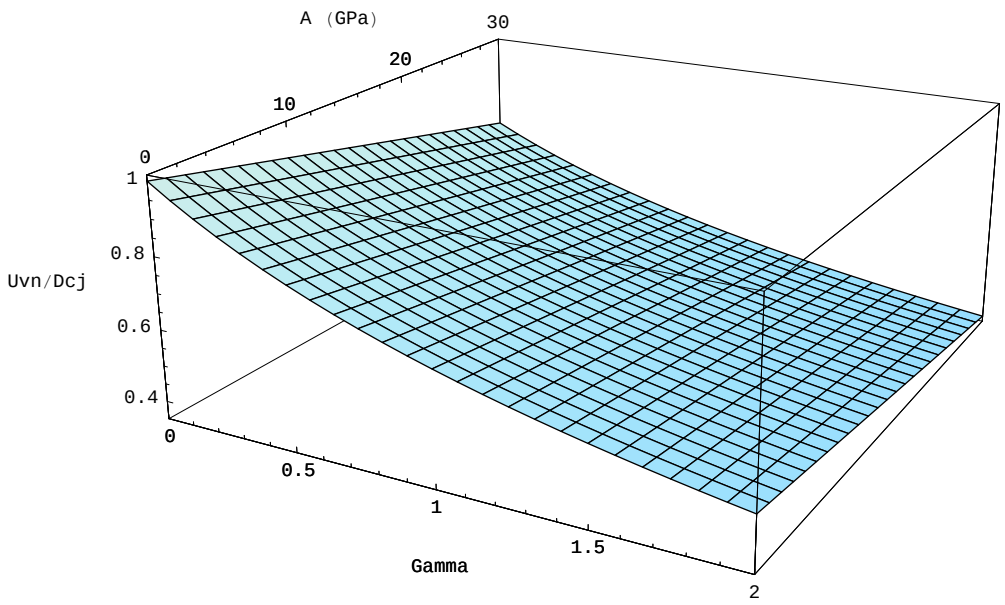

Figure 2.2: Von Neumann velocity as a function of the Grüneisen gamma, Γ, and the pressure offset, A. The pressure offset is given in units of GPa, while the von Neumann velocity is normalized by the detonation velocity.

2.8.1 Intersection of the Reactant and Product Hugoniot Curves

Physically, one would expect the reactant and product Hugoniots not to cross over the entire state space. It is however difficult to ensure such a condition is met for an arbitrary EOS. For a particular model restricted to modelling detonation waves, it is sufficient to ask that if the Hugoniot curves do cross, they only do so at a high pressure (equivalent to a high shock and particle velocity). How high of a pressure is high enough for the intersection of the Hugoniots is a matter open to argument. For a steady ZND wave, the highest pressure encountered in the wave is P_{VN}. The pressure at the lead shock is related to the Mach number of the wave, thus relating the critical Hugoniot crossing pressure to the maximum overdrive of a detonation wave one can model

$$\frac{P_{cross}}{P_{VN,CJ}} = \frac{P_{VN,MAX}}{P_{VN,CJ}} = f\left(\frac{M_{0,MAX}}{M_{\mathrm{CJ}}}\right). \tag{2.123}$$

Knowing if/when the Hugoniots of the reactants and the products intersect is vital to determining the range of applicability of the model. Using the mixture definition of the incomplete EOS, eqn 2.76, the reactant and product Hugoniot curves are

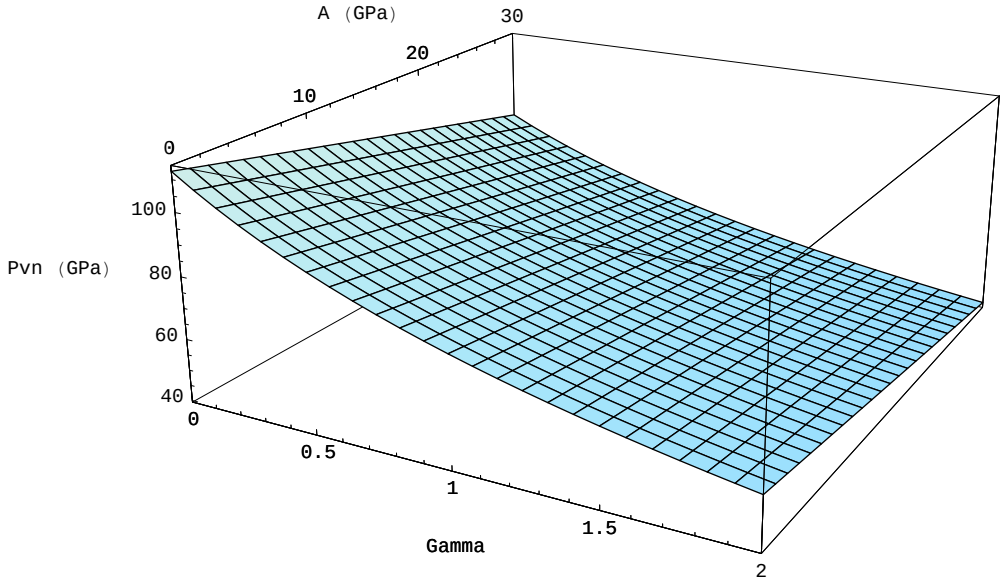

Figure 2.3: Von Neumann pressure as a function of the Grüneisen gamma, Γ, and the pressure offset, A. The von Neumann pressure and pressure offset are given in units of GPa.

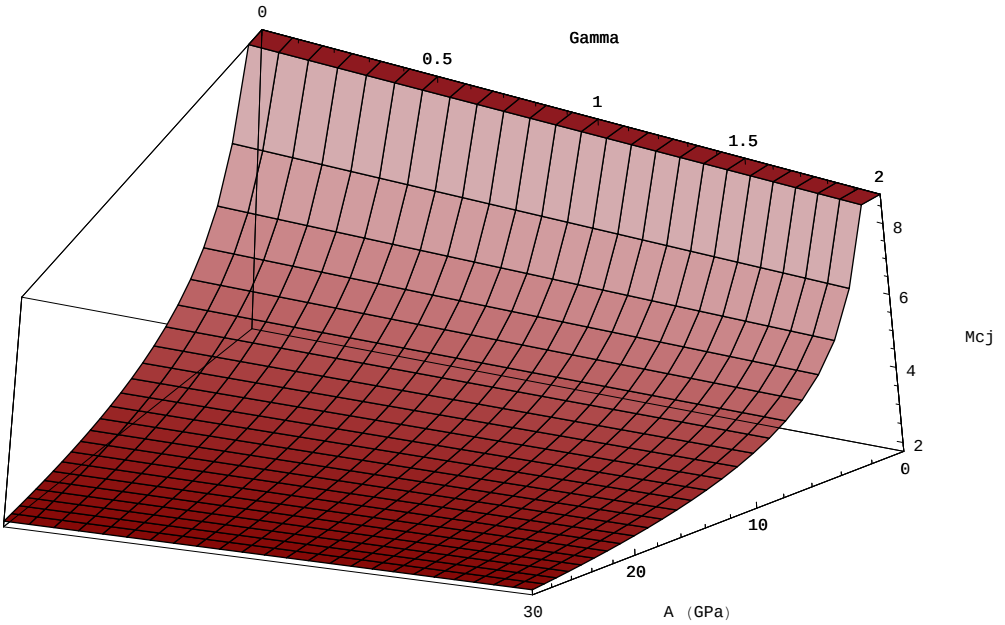

Figure 2.4: Detonation Mach number as a function of the Grüneisen gamma, Γ, and the pressure offset, A. The pressure offset is given in units of GPa.

$$\frac{(P+A_s)v}{\Gamma_s} - \frac{(P_0+A_s)v_0}{\Gamma_s} = \frac{1}{2}(P+P_0)(v_0-v), \tag{2.124}$$

$$\frac{(P+A_g)v}{\Gamma_g} - Q - \frac{(P_0+A_s)v_0}{\Gamma_s} = \frac{1}{2}(P+P_0)(v_0-v). \tag{2.125}$$

For HE, the initial pressure P_0 can be neglected and the Hugoniots can be expressed in the form of $P(x)$ where $x = v/v_0$ is the compression ratio. The Hugoniots are

$$P \approx \frac{2A_s(1-x)}{2x-\Gamma_s(1-x)} \quad \text{and} \quad P \approx \frac{2(A_s\Gamma_g/\Gamma_s + \Gamma_g\rho_0 Q - A_g x)}{2x-\Gamma_g(1-x)} \tag{2.126}$$

for the reactants and products respectively. The above Hugoniots are formulated for the single SG EOS. If the reactant EOS is the BSG, the product Hugoniot is unchanged except for the transformation $\Gamma_s \to \Gamma_1$ and $A_s \to A_1$. The reactant Hugoniot becomes

$$P \approx \frac{2A_1\Gamma_2/\Gamma_1 - 2A_2 x}{2x-\Gamma_2(1-x)}, \tag{2.127}$$

for pressures above the switch pressure. The possibility of crossing points is first explored for the SSG EOS and similar results can be obtained for the BSG EOS with the different scenarios being defined by the relative values of Γ_g and Γ_2.

Similarly to the behaviour of the CJ speed, the sound speed mismatch between reactants and products allows positive values of Q to result in a pressure decrease for a constant volume combustion. The requirement that constant volume combustion with positive values of Q result in a pressure increase yields

$$\rho_0 Q > \frac{A_g}{\Gamma_g} - \frac{A_s}{\Gamma_s}. \tag{2.128}$$

The crossing point of the Hugoniots (P_c, v_c) is given by the solution to

$$\frac{A_s(1-x_c)}{2x_c-\Gamma_s(1-x_c)} = \frac{A_s\Gamma_g/\Gamma_s + \Gamma_g\rho_0 Q - A_g x_c}{2x_c-\Gamma_g(1-x_c)}. \tag{2.129}$$

The three possible scenarios, based on the relative values of Γ_s and Γ_g, are examined.

Case SSG: $\Gamma_g = \Gamma_s$

Assuming $\Gamma_g = \Gamma_s = \Gamma$ and restricting Q to have physical behaviour yields

$$\frac{A_s(1-x_c)}{\Gamma_g} + \frac{A_g x_c}{\Gamma_g} - \frac{A_s}{\Gamma_s} = \rho_0 Q > \frac{A_g}{\Gamma_g} - \frac{A_s}{\Gamma_s} \tag{2.130}$$

or

$$x_c > 1 \tag{2.131}$$

always. Hence, there can be no intersection of the reactant and product Hugoniots if $\Gamma_s = \Gamma_g$.

Case SSG: $\Gamma_g < \Gamma_s$

This case is simplest. The minimum compression ratio, corresponding to an infinite pressure ratio is independent of A and given by

$$x_{\min} = \frac{\Gamma}{2+\Gamma}. \tag{2.132}$$

Hence, if $\Gamma_g < \Gamma_s$ then $x_{\min,\mathrm{g}} < x_{\min,\mathrm{s}}$. By definition, the zero crossing of the reactant Hugoniot is $x_s^* = 1$. The restriction on Q means the zero crossing of the product Hugoniot is $x_g^* > 1$. The solid (reactant) Hugoniot therefore acts as a separatrix and there must be exactly 1 crossing point for $\Gamma_g < \Gamma_s$.

Case SSG: $\Gamma_g > \Gamma_s$

Given this choice of parameters, the product Hugoniot lies to the right of the reactant Hugoniot for both $x \to x_{\min}$ and $x \to 1$. There could technically be two crossing points or one tangency point and the location of those critical points must satisfy

$$x_c^2 F_1 - x_c(F_1 + \Gamma_g^2 F_2) + F_2 > 0, \tag{2.133}$$

where

$$F_1 = (\Gamma_s + 2)A_g - (\Gamma_g + 2)A_s, \tag{2.134}$$

$$F_2 = \frac{A_g}{\Gamma_g} - \frac{A_s}{\Gamma_s}. \tag{2.135}$$

It will be seen in chapter 3 that proper fits involve $\Gamma_g < \Gamma_s$ and a single point of intersection of the Hugoniot is expected.

Case BSG: $\Gamma_g < \Gamma_2$

This simplest case is considered first. Using the reactant Hugoniot of the BSG, physical values of Q are restricted to

$$\rho_0 Q > \frac{A_g}{\Gamma_g} - \frac{A_1}{\Gamma_1}. \tag{2.136}$$

For $\Gamma_g < \Gamma_2$, the product Hugoniot has a minimum compression ratio smaller than that of the reactant Hugoniot yet its pressure at $x = 1$ is higher than that of the reactants. Hence the Hugoniots must have a crossing point, as with the SSG. This case is also the relevant one for the fits of chapter 3 and Hugoniots are expected to cross.

Case BSG: $\Gamma_G = \Gamma_2$

Following the same argument as with the SSG, the crossing point of the Hugoniots satisfies

$$x_c > \frac{A_g - A_1\Gamma_g/\Gamma_1}{A_g - A_2}. \tag{2.137}$$

In chapter 3, potential BSG fits are only found for $A_2 = 0$ and a crossing point exists in that region.

Case BSG: $\Gamma_g > \Gamma_s$

Equation the product and reactant pressures at the crossing point yields

$$\frac{A_1\Gamma_g/\Gamma_1 + \Gamma_g\rho_0 Q - A_g x_c}{A_1\Gamma_2/\Gamma_1 - A_2 x_c} = \frac{2x_c - \Gamma_g(1-x_c)}{2x_c - \Gamma_2(1-x_c)} < 1. \tag{2.138}$$

Restricting to the case of $A_2 = 0$ again, the inequality

$$\frac{A_1}{\Gamma_1}(\Gamma_g - \Gamma_2) - A_g x_c < -\Gamma_g\rho_0 Q < A_1\frac{\Gamma_g}{\Gamma_1} - A_g \tag{2.139}$$

is obtained which yields

$$x_c > 1 - \frac{A_1\Gamma_2}{A_g\Gamma_1} \tag{2.140}$$

and crossing points are found to be possible.

Chapter 3

Fitting of Simplified Models

3.1 Introduction

The models described in chapter 2 provide a balance between the desire to have analytically tractable models and the need to fit actual data for PBX 9502. Analytically tractable models provide insight into the consequences of fitting parameter choices and about the stability of the wave and other shock dynamic behaviour. A single SG (SSG) EOS is used to represent the gaseous products while the solid reactants are modeled using both the SSG EOS and a blended SG (BSG) EOS. The SG based EOS models are fitted to thermodynamic data pertinent to detonation propagation in the explosive PBX 9502. The chemical kinetic fitting is performed with both the $P-T$ equilibrium and constant solid entropy closure conditions, $DS_s = 0$. Results for a single phase, ideal gas, single step model are also presented as a reference.

First, the available experimental data is reviewed. This includes, for the explosive PBX 9502, the shock Hugoniot data of the solid reactants, overdriven Hugoniot data, $D_n - \kappa$ data, diameter effect curve and velocity gauge data. The EOS parameters of the solid reactant phase are fitted to reactant shock Hugoniot data. The EOS parameters of the gaseous product phase and the heat release, Q, are fitted to the overdriven Hugoniot data. The chemical kinetic parameters are fitted to the $D_n - \kappa$ data through iteratively solving the ZND detonation structure with a divergence term. The fitting employs a genetic algorithm based approach, a new strategy employed in the fitting of condensed phase explosives to engineering style reaction flow models.

3.2 Review of Experimental Data for PBX 9502

The main objective of the reactive burn models developed in the present work is to model propagating detonations. These models are thus calibrated against data relevant to the propagation regime. The data available for PBX 9502 and selected to fit the current models consists of

- shock Hugoniot data of the reactants,
- overdriven shock Hugoniot data,

- $D_n - \kappa$ data.

There is also data available not directly relevant to detonation propagation and hence not reviewed here, namely

- Pop-plot (initiation) data,
- isothermal compression data.

3.2.1 Hugoniot Data

The shock Hugoniot data is obtained from several sources and covers both the unreacted shock Hugoniot and overdriven Hugoniot of PBX 9502. Two basic techniques are used. One is the wedge test method in which a detonation propagates in an HE sample with a triangular shape. In those experiments, the shock velocity is tracked by a streak camera looking at the breakout point of the shock along the inclined surface. In all three studies [11, 12, 13], the shock is explosively driven and the free surface velocity of the driver is measured. Using the free surface velocity, the particle velocity is found by constructing consecutive iterations of the shock Hugoniot. The second technique uses a gas-gun launched flyer plate which drives a shock by impacting a cylindrical charge of explosive. In addition to the wedge test, [11] uses this method as well. The particle velocity of the material is measured directly using electro-magnetic (EM) gauges embedded inside the HE charge. An EM field is produced around the charge and the movement of the metallic EM gauges inside the field produces a measurable voltage. In [11], two such gauges are used and the difference in the time of arrival (TOA) of the signal at the two gauges is used to infer the shock velocity. In [15], EM gauges are used to measure the particle velocity at different locations and, in addition to the EM gauge, a "shock tracker" (ST) gauge is used to measure the shock position as a function of time. The ST gauge consists of multiple EM gauges multiplexed on the same package. An ST gauge can be embedded inside an HE charge and provides TOA measurements of the shock at various locations.

The experiments of [16] are gas-gun experiments with thick, high-velocity flyer plates. The input shock strength is above the CJ pressure, causing a prompt reaction of the HE charge. The overdriven Hugoniot experiments of [16] thus provide a measure of the reacted Hugoniot of PBX 9502. Recent data was published in 2009 by Jensen and Byers [17] and was not available when the fits of this study were produced. Shown in fig 3.3 is a comparison of this data set with that of Tang et al. The overdriven Hugoniot data of Jensen and Byers is only in the low pressure region of the overdriven Hugoniot and agrees with that of Tang et al. The inclusion of this data set in the current fits would not change the conclusions of this work.

A summary of the openly available data sets is given in table 3.1. The reactant Hugoniot data is shown

in figure 3.1, the overdriven Hugoniot data is shown in figure 3.2(a) and both unreacted and overdriven shock Hugoniot data are shown in figure 3.2(b). Some key points to note about the shock Hugoniot data are that

- there are variations in initial density between the different data sets and within the different individual experiments of each data sets. The scatter in the experimental measurements is greater than the influence of the variation of the density;
- the variation between the cold and ambient temperature experiments of [15] shows little effect of cooling the material to -55°C on the Hugoniot curve (greatest effect is in initiation pop-plot data);
- the experiments at higher initial temperatures [13] indicate a stronger dependence of the shock Hugoniot on temperature when the material is heated rather than cooled, although more data would be required to be conclusive. This model does not explicitly take the initial temperature of the material into account and the data from heated samples is discarded for the calibration process, although they may be shown in plots as a reference;
- there appears to be a turning point in the shock Hugoniot for particle velocities around 1 km/s. For lower particle velocities, the Hugoniot is quasi-linear with a high slope and a slight, seemingly positive curvature. For higher particle velocities, the Hugoniot is again quasi-linear, but with a slight negative curvature.

3.2.2 $D_n - \kappa$ Data and Diameter Effect Curve

The curvature data is obtained from steady-state rate sticks and/or cylinder tests experiments providing a measure of the mechanisms at play in detonation propagation. In both types of experiments, a detonation is initiated and propagates axially down a straight cylinder of a given diameter until it attains a steady-state velocity. The difference between the two types of experiments resides in the diagnostics used. In a cylinder test experiment, the diagnostics consist of TOA pins along the length of the charge and a measurement of the charge wall expansion. The goal of cylinder tests is to provide information about the product EOS. The measurement of detonation velocity, D_n, for a given charge diameter, R, is also a product of cylinder tests. In a rate stick, the shape of the detonation at the charge end is recorded along with the propagation velocity, recorded via TOA pins. For PBX 9502, the breakout of the wave is typically measured via light extinction. The end of the charge is polished and used to reflect incident light from a source onto the slit of a streak camera. The emerging detonation wave disrupts the polished surface, leading to the extinction of

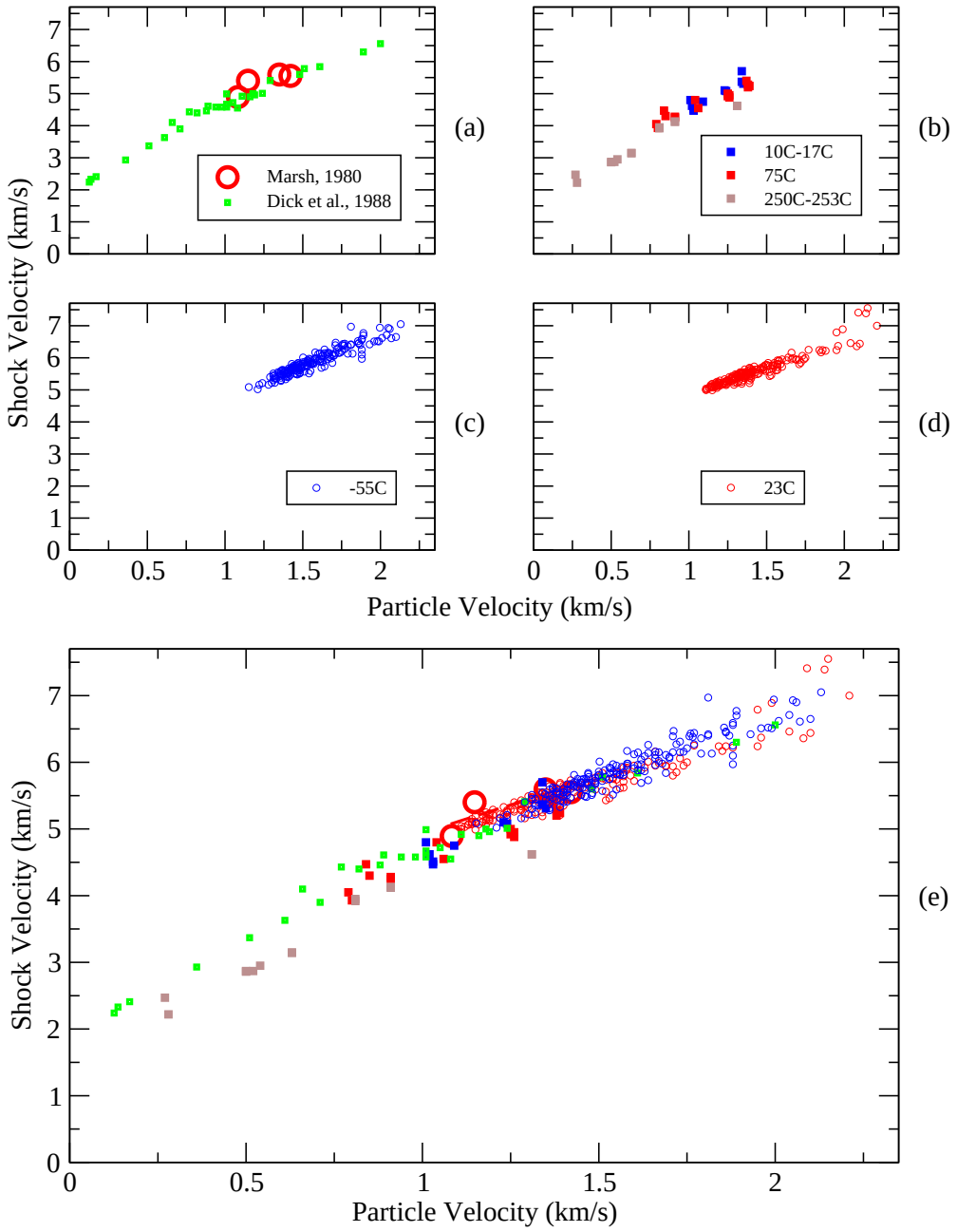

Figure 3.1: The available reactant shock Hugoniot data. In (a), the data of Dick et al. [11] and Marsh [12], in (b) the data of Dallman & Wackerle [13] at the 3 tested temperatures, in (c), the data of Gustavsen [14] at -55°C and in (d), the data of Gustavsen et al. [15] at 23°C. In (e), the 7 data sets are shown together.

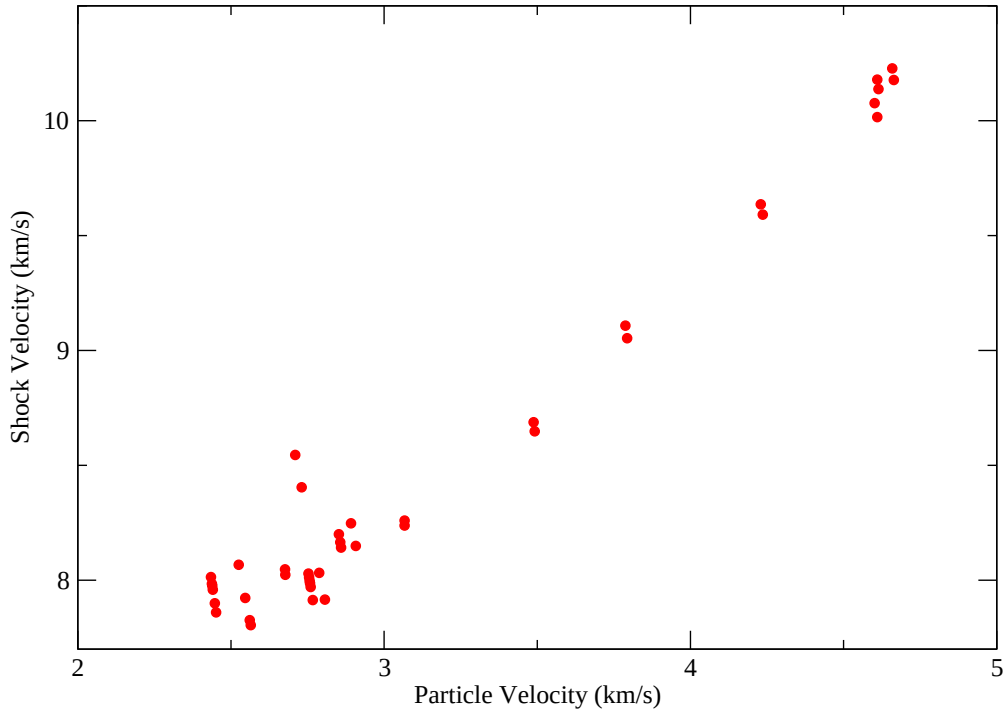

(a) Overdriven Shock Hugoniot Data.

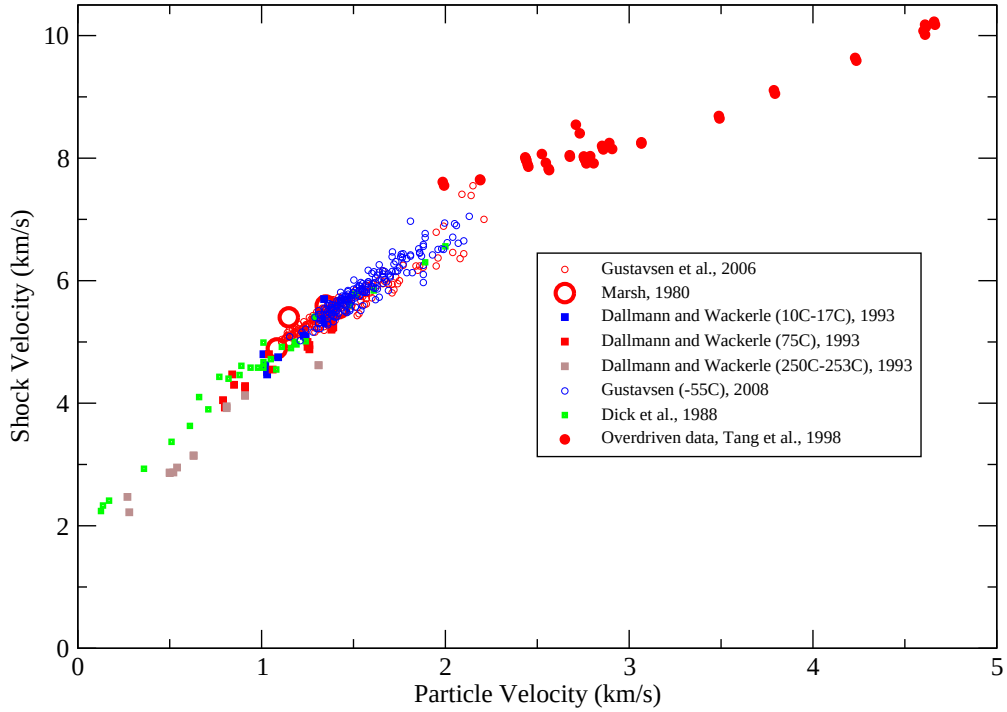

(b) Reactant shock Hugoniot data and overdriven Hugoniot data.

Figure 3.2: The (a) overdriven Hugoniot data of Tang et al. [16] and (b) both the reactant shock Hugoniot data and the overdriven Hugoniot data.

Reference	Year	Description	Notes
Gustavsen et al. [15]	2006	reactant	• Gas-gun experiments • high-pressure • ambient (23°C) and cold (-55°C) temperature • points near the CJ velocity show evidence of reaction
Dick et al. [11]	1988	reactant	• No repeat experiments • low pressure • ambient temperature
Dallman et al. [13]	1993	reactant	• low pressure • cold (10-17°C), ambient (25°C) and hot (250°C) temperatures
Marsh et al. [12]	1980	reactant	• only 4 data points • linear fit given in [55]
Tang et al. [16]	1998	product	• outliers near the CJ point
Jensen and Byers [17]	2009	product	• Low pressure region of the overdriven Hugoniot • Not used in the present fitting

Table 3.1: Sources and notes on the available shock Hugoniot data

the light on the streak record and tracing out the breakout time vs. radial position. This breakout record can be transformed into a relationship between the normal wave velocity, D_n, and the local curvature, κ. Such tests were also performed for a different explosive, ANFO, in the course of the present work and more details are given in chapter 6 on the specific experimental methods and analysis procedures related to rate stick experiments in general (See fig 6.5 for a representation of the experimental setup). Rate sticks thus provide, in addition to a data point along the $D_n(R)$ curve, one $D_n(\kappa)$ curve for a given diameter. The most complete source for the diameter effect curve is the 1984 work of Campbell [18]. $D_n(\kappa)$ data was obtained at LANL over the course of various studies and was summarized in a 2006 paper [20].

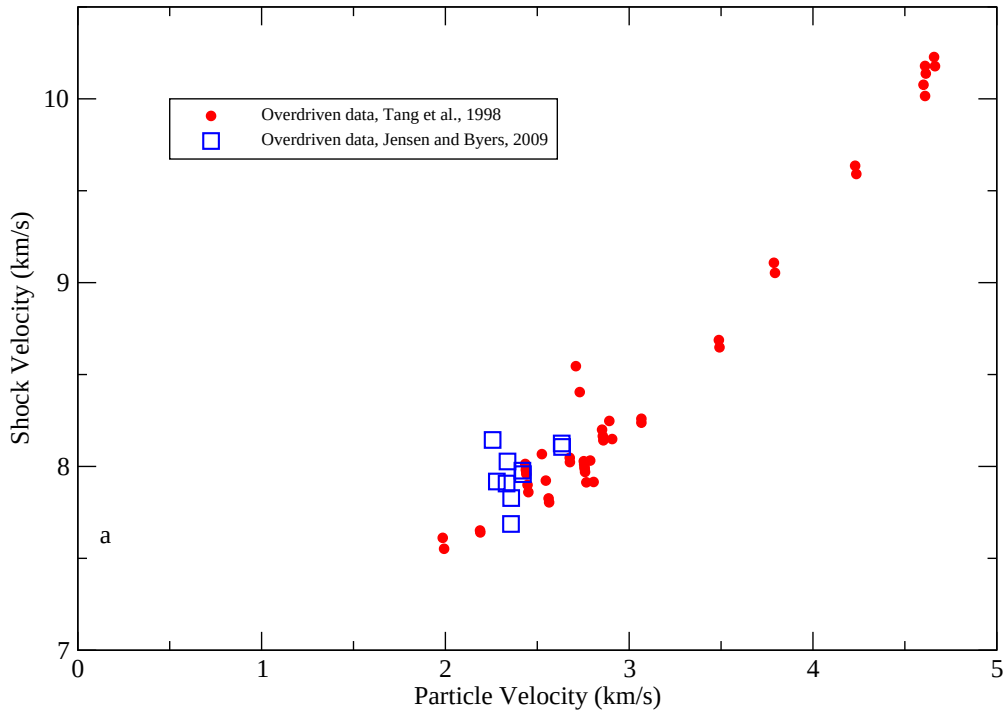

Figure 3.3: Comparison of the data by Tang et al. [16] and the more recent data by Jensen and Byers [17].

Relationship Between the Different Curvature Measurements

For a bare charge, the diameter of the cylindrical charge controls the shape of the detonation front and its velocity and, at a given charge diameter, the detonation exhibits a particular velocity decrement, $D_{\mathrm{CJ}} - D_n$. The CJ velocity D_{CJ} is the *infinite charge diameter* velocity. The relationship between the observed velocity D_n and the charge diameter (typically plotted as the inverse radius, $1/R$) is the diameter effect curve $D(1/R)$. Shown in fig 3.4 is the diameter effect curve at room temperature of Campbell [18]. In this same work, the diameter effect curve is also measured at -55°C and 75°C, although the current calibrations are limited to room temperature data. The curvature data is obtained from the measurements of the shock shape (these measurements were not made by Campbell). The local, total curvature is inferred from the shape of the lead shock as a function of radius along the charge diameter $\kappa(r)$. The local, normal propagation velocity is also inferred from this shock shape as a function of radius along the charge diameter $D_n(r)$. This defines the parametric curve for a given charge diameter, $D_n(\kappa)$. Shown in fig 3.5 is data from [19]. The behaviour of the $D_n(\kappa)$ curve can be used as a gauge of the "ideality" of an explosive. For ideal explosives, the $D_n(\kappa)$ curves of different diameters overlap, while the opposite is true for non-ideal explosives. For example, compare the behaviour of the data shown in fig 3.5 with that of ANFO data shown in fig 6.14. The calibrations obtained in this chapter use an approximate solution of the reaction zone structure which is most valid along the charge

axis where transverse flow velocity is minimal. If we designate $\kappa_0 = \kappa(r = 0)$, where $r = 0$ corresponds to the charge central axis, the reference data for the calibration is therefore $D_n(\kappa_0)$. The available data, from [20], is shown in fig 3.6. This data is available for three different lots of the explosive PBX 9502 (three different production runs of this explosive) designated here as lot 136, lot 008 and lot 007. Lot 136 is a recycled lot from 1985. Recycled lots are produced by pressing new material with left-over material from previous pressings. Lot 008 is a virgin lot, which means it was only produced from fresh material. Lot 007 is an early virgin lot known to have poor performance [20] and its associated data are not used in the present calibrations.

Since so much data is available from [18], it is tempting to try and relate the central curvature of the wave with the charge radius and seek a universal relationship. Unfortunately, there is substantial scatter in the data available and this avenue was not pursued. Yet, it is instructive to look at the relationship between the on-axis curvature and the charge radius. Shown in fig 3.7 is the relationship between the product $R\kappa_0$ and the charge radius, R. A spherical wave would yield $R\kappa_0 = 2$, independent of R, which is not the case here. The curvature is also much smaller than that expected for a spherical wave. A self-similar shock shape, i.e. $z/R = f(r/R)$ only, where z is the shock shape coordinate along the charge axis, would yield $R\kappa_0 =$ constant, which is also not the case here.

3.3 Fitting of Solid Phase Parameters

The single SG EOS (SSG) and blended SG EOS (BSG) are fitted to the reactant Hugoniot data. Some restrictions on the possible fits apply. As this model is aimed at detonation propagation, a higher importance is ultimately given to fitting the Hugoniot data near the CJ velocity of PBX 9502 ($D_{\text{CJ}} = 7.706$ km/s). The initial sound speed of the material should represent the sound speed of the unreacted HE, $c_0 \approx 1.85$ km/s [11]. The reactant Hugoniot should not intersect the product (overdriven) Hugoniot data. Because of the positive curvature of the reactant Hugoniot predicted by the SG EOS in the $u_s - u_p$ plane, satisfying all these requirements simultaneously is difficult. Nonetheless, the choice of such simple EOS models is attractive as they are analytically tractable.

3.3.1 Single SG EOS

The reactant shock Hugoniot data, presented in section 3.2.1, is fitted using the SSG EOS. The theoretical shock Hugoniot predicted by this EOS is given by eqn 2.37. First, two least-square fit (LSQ) are produced by minimizing the sum of the square of the error on the shock velocity u_s. The first least-square fit, fig 3.8, uses

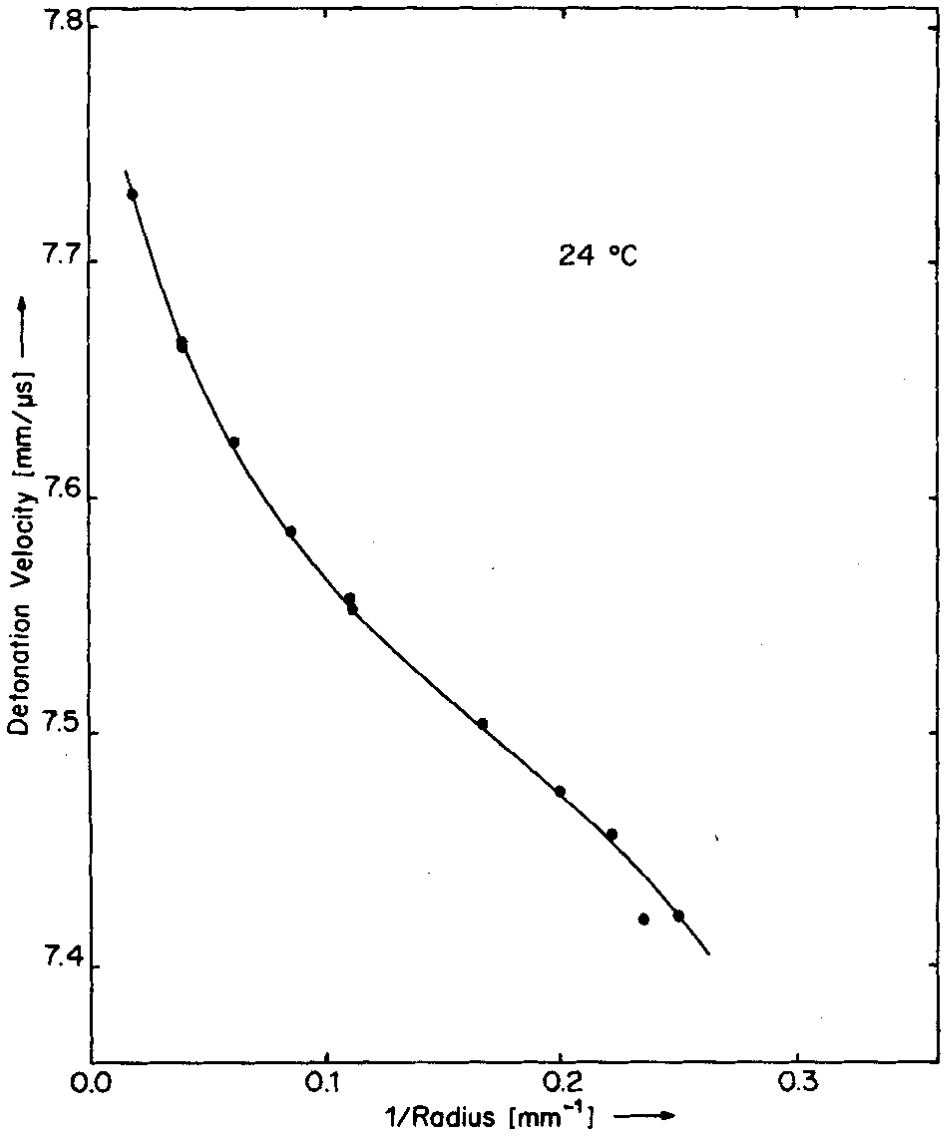

Figure 3.4: Diameter effect curve from Campbell [18].

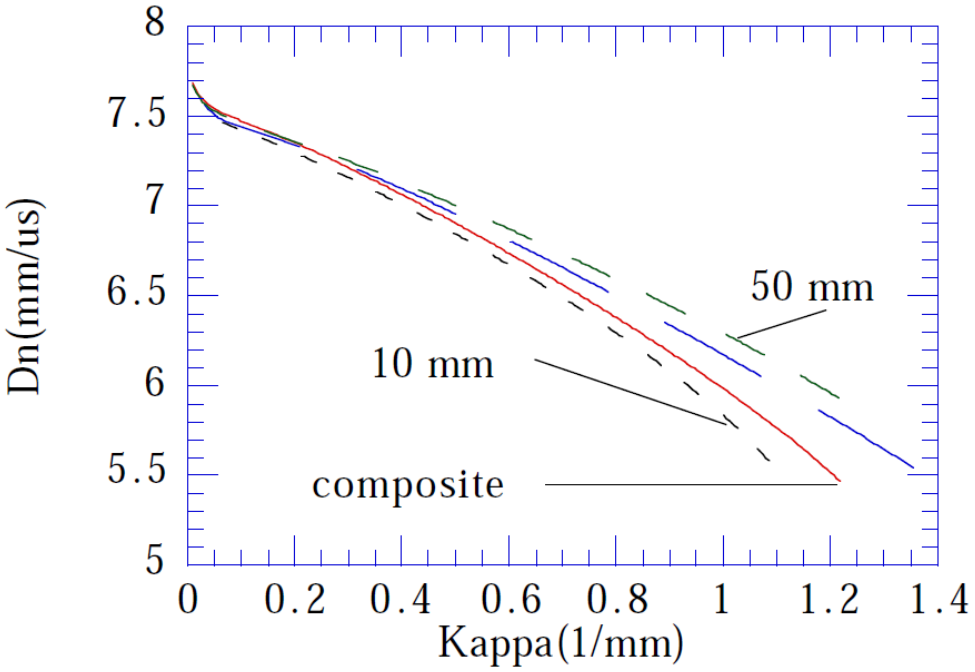

Figure 3.5: $D_n - \kappa$ data from [19] for three charge diameters (black, blue and green lines) and a composite of the three measurements (red).

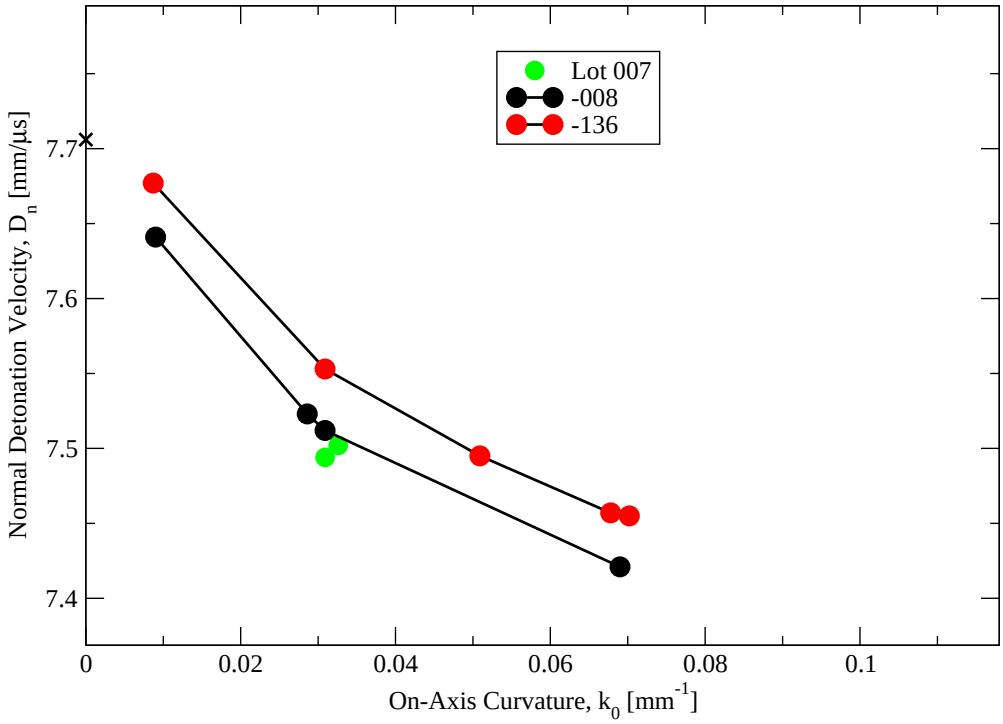

Figure 3.6: Curvature data $D_n(\kappa)$ along the charge axis from [20]. The three different lots are lot 007, an early virgin lot (meaning only from new material), lot 136, a recycled lot (manufactured from new material mixed with scraps from previous production runs) and lot 008, a virgin lot from 1988.

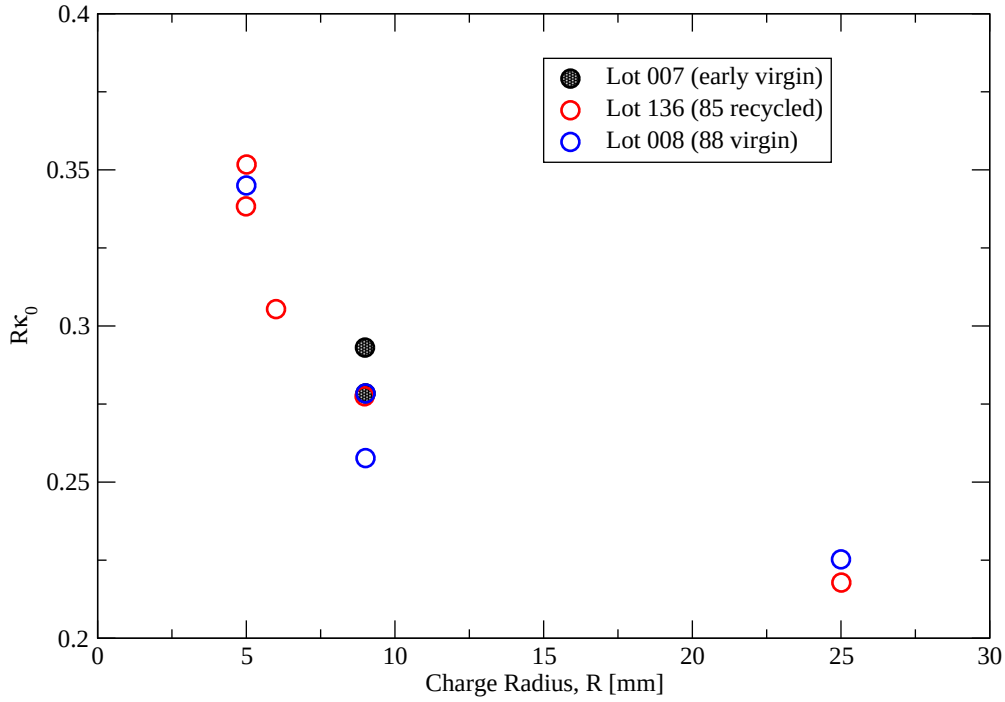

Figure 3.7: Relationship between the curvature at the charge center multiplied by the charge radius, $R\kappa_0$, and the charge radius, R. The data is from [20]

.

the entire set of data available for the reactant Hugoniot. Only the data sets of Dallmann and Wackerle [13] at 75°C and 250-253°C are excluded because of the temperature dependence. This least-square fit represents reasonably well the Hugoniot data, however, the intersection with the overdriven data is at the CJ point and the predicted initial sound speed is high at $c_0 = 2.65161$.

A second least-square fit, shown as a dashed line in fig 3.9, is produced. Only the data from shocks with velocity $u_s > 4.5$ km/s are used. The change in slope occurring at this value of shock speed is possibly indicative of a phase change in the material, justifying this demarcation point. The intersection point with the overdriven Hugoniot data is again too close to the CJ point. The initial sound speed is also much higher at $c_0 = 3.10421$ km/s.

A final fit is produced, this time by visual inspection. The parameters are chosen so that the model is in line with the lower edge of the cloud of data for $u_s > 4.5$ km/s and the intersection point with the overdriven data is at $u_s = 9$ km/s. This final fit is shown as a solid line in fig 3.9 and is used as the appropriate SSG EOS fit for PBX 9502. The current calibration effort is aimed at producing a detonation propagation model, so an accurate reproduction of the shock response at low pressures is not required. The high initial sound speed of the model will result in a lower detonation Mach number. The parameters of the different fits generated are shown in table 3.2.

Type of Fit	Least-Squares Fit		Non-intersecting
Data Range	Whole Data Set	$u_s > 4.5$ km/s	Visual Inspection
Γ	3.99157	3.378	1.8
$c_0 = \sqrt{A/\rho_0}$ (km/s)	2.65161	3.10421	4

Table 3.2: Parameters of the three different generated fits for the single SG EOS.

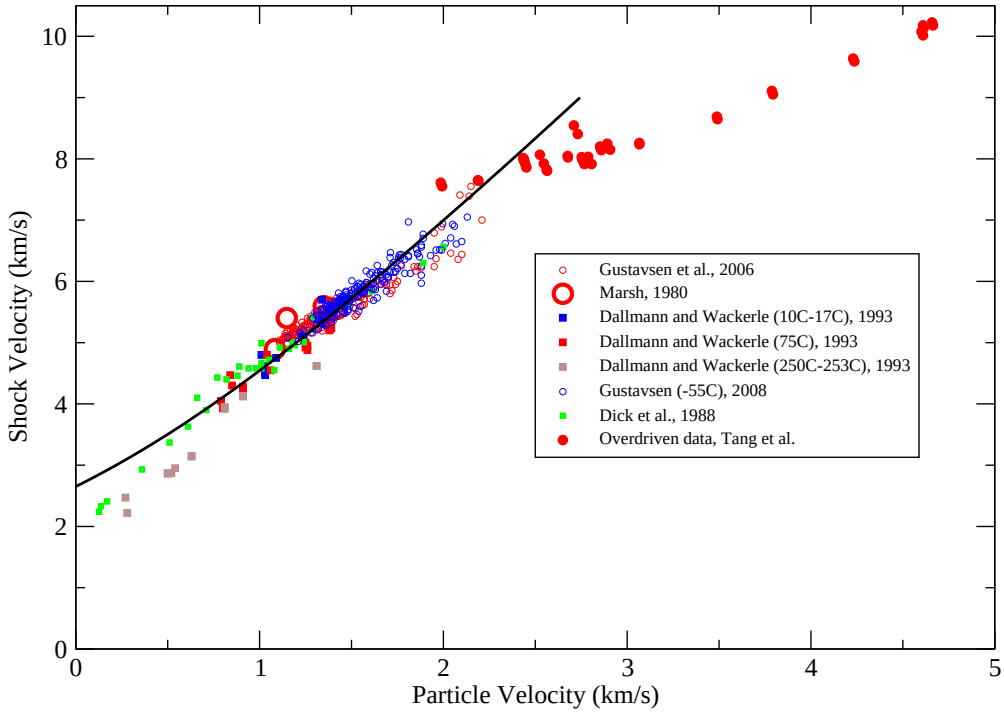

Figure 3.8: Least-square fit of the entire reactant Hugoniot data set using the single SG EOS.

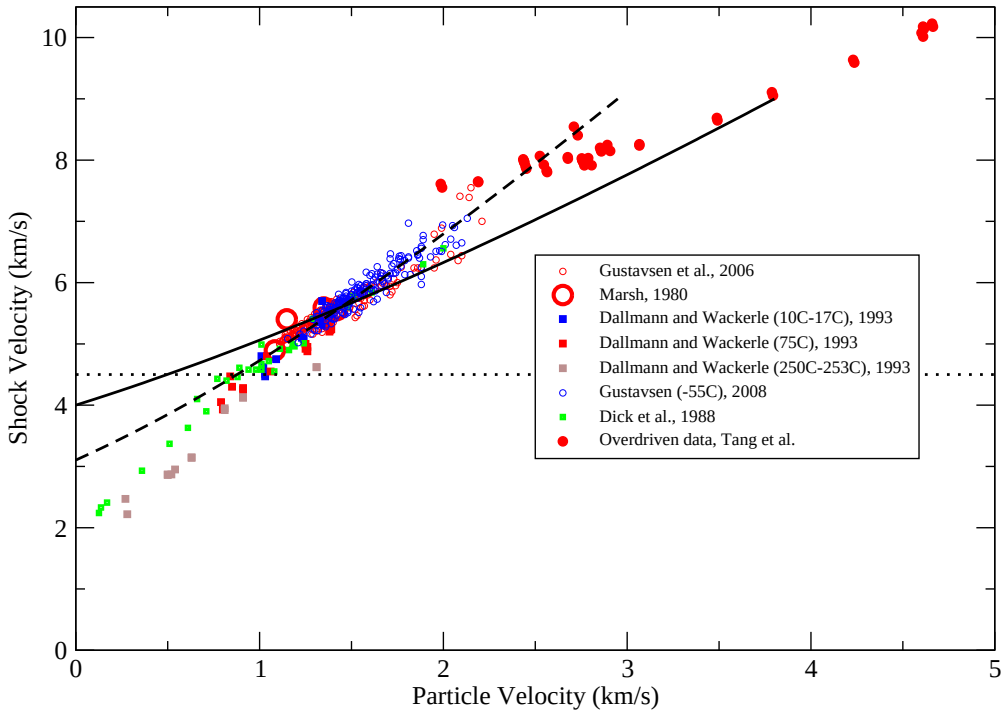

Figure 3.9: Least-square fit of the reactant Hugoniot data set, for $u_s > 4.5$ km/s using the single SG EOS (dashed curve). The solid curve corresponds to an ad-hoc fit for which the resulting fit does not cross the overdriven Hugoniot data below $u_s < 9.0$ km/s. The dotted horizontal line indicates $u_s = 4.5$ km/s.

3.3.2 Blended SG EOS

The blended SG EOS (BSG) is fitted in two steps using the Hugoniot derived in chapter 2 (eqn 2.65). First the data in the range $u_s < 4.5$ km/s is fitted using the parameters Γ_1 and $c_1 = \sqrt{A_1/\rho_0}$ (the low-pressure fit). Once these parameters are fitted, the data in the range $u_s > 4.5$ are fitted using the parameters Γ_2 and $c_2 = \sqrt{A_2/\rho_0}$ (the high pressure fit). The priority here is to capture the initial sound speed of the material c_0. For detonation waves in PBX 9502, $u_s > 4.5$ km/s and the parameter from the low pressure fit relevant to the full reactive burn model is the initial sound speed.

Low Pressure Fit

Three least-square fits to the $u_s < 4.5$ km/s range of the Hugoniot are shown in fig 3.10. Fit 1 is obtained by allowing both c_1 and Γ_1 to vary and minimizing the deviation. Fits 2 and 3 are obtained by fixing the initial sound speed at values respectively lower and higher than that predicted by the least-square fit. The initial sound speed of fit 2 is $c_1 = 1.85$ km/s (from [11]) and the initial sound speed of fit 3 is $c_1 = 2.2$ km/s. The resulting values of Γ_1 are shown in table 3.3.

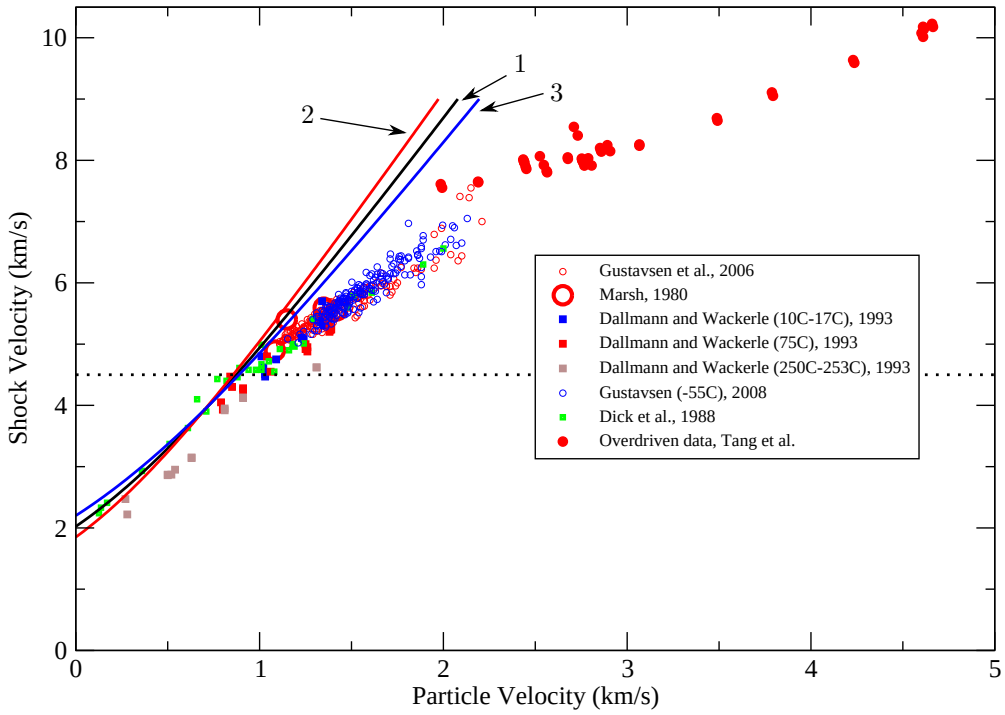

Figure 3.10: Fits of the reactant Hugoniot data for the $u_s < 4.5$ km/s range. Three least-square fit are shown. One where both c_1 and Γ_1 are fitted (1), one where $c_1 = 1.85$ km/s is forced (2) and one where $c_1 = 2.2$ km/s is forced.

	Both c_1 and Γ_1 free	c_1 forced and Γ_1 free	
	Fit 1	Fit 2	Fit 3
Γ_1	6.22257	6.73677	5.7111
$c_1 = \sqrt{A_1/\rho_0}$ (km/s)	2.02394	1.85 (forced)	2.2 (forced)

Table 3.3: Parameters of the three least-square fit of the $u_s < 4.5$ km/s range using the blended SG EOS.

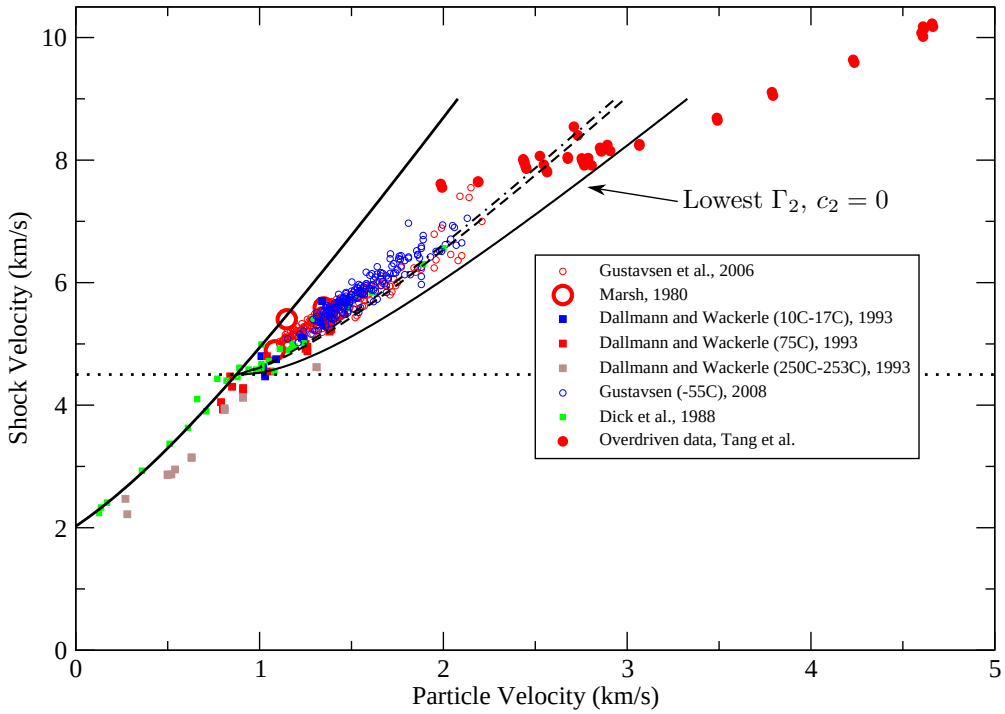

Figure 3.11: High pressure fits (A_2, Γ_2) corresponding to fit 1. Increasing values of Γ_2 result in a steeper Hugoniot. Three such Hugoniots are shown. The minimum $\Gamma_2 = 3.047$ fit (solid), $\Gamma_2 = 3.6$ fit (dashed) and the $\Gamma_2 = 3.7$ fit (dash-dot). The values of c_2 are selected to yield the same transition pressure, corresponding to $u_s^* = 4.5$ km/s.

High Pressure Fit

The resulting model Hugoniot is required to be continuous. If the Hugoniots are continuous, then so must be the internal energy at the transition pressure, hence $e_1(P_s, v_s) = e_2(P_s, v_s)$. Criterion (2.67) is used to relate c_2 and Γ_2 as a function of c_1, Γ_1 and the transition point. Fixing the transition point at $u_s^* = 4.5$ km/s, two properties of the high pressure fits become apparent. As seen in fig 3.11, a higher value of Γ_2 results in a steeper slope of the Hugoniot. For a given low pressure fit and transition point, there exists a minimum value of Γ_2, for which $c_2^2 = 0$ and thus $c_2 = 0$. For lower values of Γ_2, $c_2^2 < 0$ giving $A_2 < 0$ and shock stability is no longer ensured. In fig 3.11, three high pressure fits corresponding to the low pressure fit 1 are shown. The solid line originating at $u_p = 1$ km/s is the fit corresponding to the lowest value of Γ_2 possible. The dashed and dash-dotted lines are examples of fits with higher values of Γ_2.

Varying the transition point between the low and high pressure fits of the BSG EOS shows that the value of Γ_2 controls the slope of the Hugoniot at high pressure. In fig 3.12, the $\Gamma_2 = 3.6$ fits corresponding to fit 1 are both seen to asymptote to the same slope for $u_s^* = 4.5$ and $u_s^* = 5$. Based on this behaviour of the blended SG EOS, the high pressure fits corresponding to the lowest value of Γ_2 ($c_2 = 0$) and a crossing point

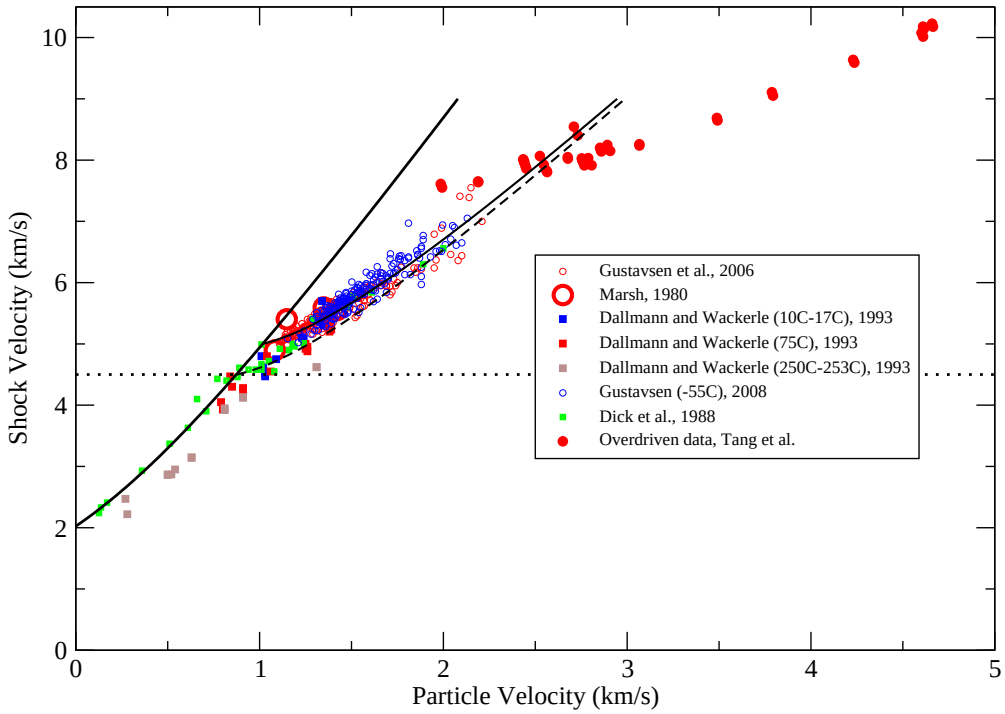

Figure 3.12: High pressure fits corresponding to fit 1. $\Gamma_2 = 3.6$ in both cases and the crossing point of the low and high pressure parts of the blended SG EOS is varied from $u_s^* = 4.5$ to $u_s^* = 5$ km/s.

	Fit 1	Fit 3
Γ_1	6.22257	5.7111
$c_1 = c_0 = \sqrt{A_1/\rho_0}$ (km/s)	2.02394	2.2
Γ_2	3.047	2.5831
$c_2 = \sqrt{A_2/\rho_0}$ (km/s)	0	0
u_s^* (km/s)	4.5	4.5

Table 3.4: Summary of the parameter values of the retained blended SG EOS fits.

of $u_s^* = 4.5$ km/s are selected. These three fits are shown in fig 3.13. In the case of fit 3 ($c_1 = c_0 = 2.2$ km/s), the crossing point of the model reactant Hugoniot with the overdriven Hugoniot data occurs at $u_s \approx 9$ km/s, but the EOS exhibits lower shock speed values than expected from experiments. In the case of fits 1 and 2, the predicted shock speeds are closer to experimental data, but the crossing point with the overdriven Hugoniot data is too low. Only fits 1 and 3 are retained in the rest of this chapter since the crossing point of fit 2 with the overdriven data is too low. The parameters of these two fits are shown in table 3.4. It is worth repeating that the shape of the Hugoniot for the SG model is a trade-off in retaining a simpler theoretical structure.

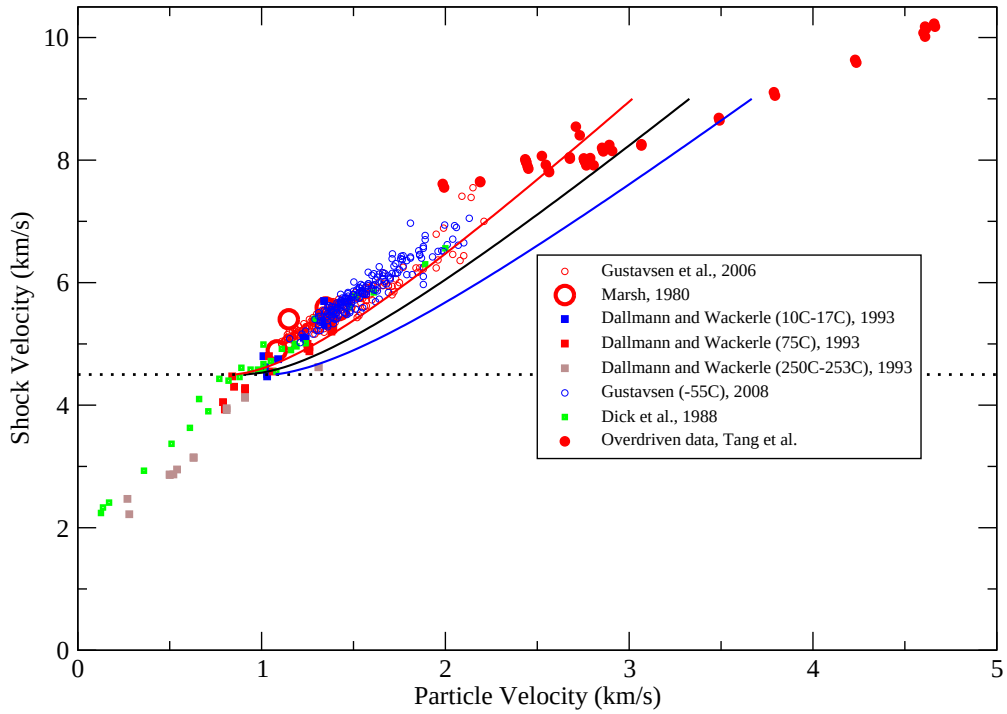

Figure 3.13: High pressure fits corresponding to $c_2 = 0$ for the three low pressure fits and a crossing point of $u_s^* = 4.5$ km/s.

Single-Valued and Multi-Valued Solutions of the Blended SG EOS

The Hugoniot corresponding to the high pressure part of the blended SG EOS is not monotonic. The constant term $c_2^2 - (\Gamma_2/\Gamma_1)c_1^2$ is akin to a heat release term in the SG EOS. As a result, the Hugoniot is upwards concave in the $u_p - u_s$ plane. If the section of the Hugoniot corresponding to the low pressure part of the EOS crosses the high pressure section of the Hugoniot on the upwards branch (i.e. to the right of the minimum point), the resulting Hugoniot is single-valued. If the crossing point is on the downwards branch (i.e. to the left of the minimum point), the resulting Hugoniot is multi-valued near the transition point. In the case of fit 3, the solution is multi-valued, but the problematic region is confined to a region near the transition point. Single-valued solutions are easily obtained by raising the transition shock velocity, as shown in fig 3.14. In this case, the intersection of the high pressure section of the Hugoniot with the reacted data also moves closer to the CJ point. Since the multi-valued region is confined to a region near the transition point and the states encountered within the reaction zone of *propagating detonations* are above the transition region, the multi-valued fit is preferred over one which intersects the reacted data too close to the CJ state. A multi-valued Hugoniot would become problematic in initiation scenarios, which are not considered here.

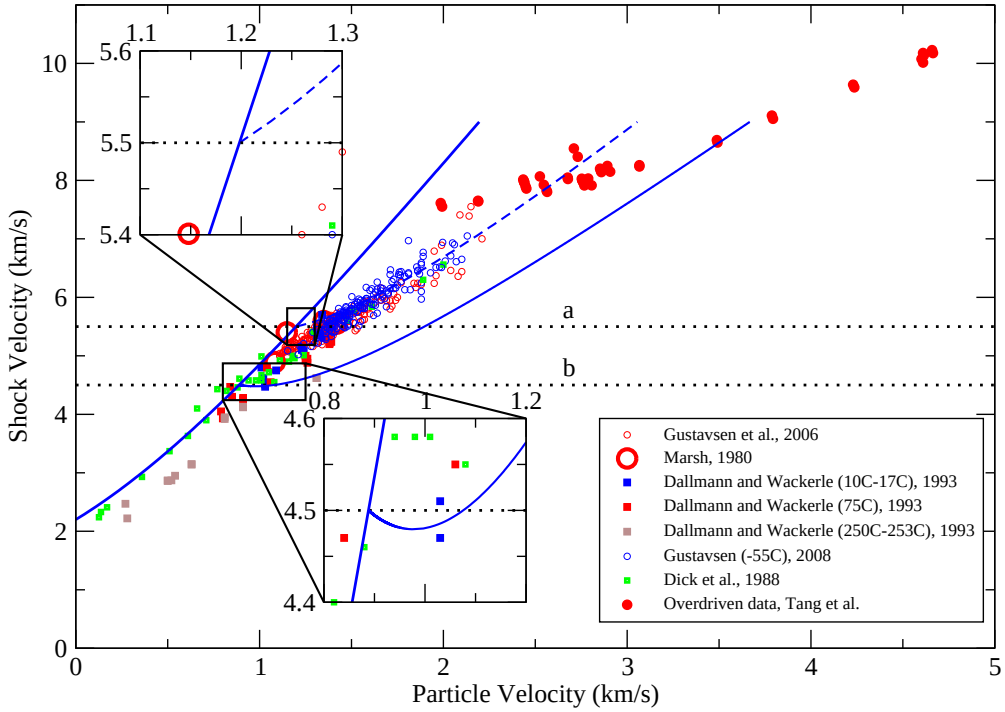

Figure 3.14: Details of the transition point for the lowest Γ_2 solutions ($c_2 = 0$) corresponding to fit 3 and transition points of $u_s^* = 4.5$ (solid, multi-valued) and 5.5 km/s (dashed, single-valued).

3.3.3 Von Neumann Particle Velocity, u_{VN}

The particle velocity behind the leading shock of the detonation has been measured experimentally. Data collected using the dual Fabry-Perot interferometer technique in [1] shows that $u_{\mathrm{VN}} \simeq 2.25 - 3.25\mathrm{mm}/\mu\mathrm{s}$. This range of velocities corresponds to measurements done with windows of different materials and corresponds to the entire variation of three different measurements, shown in table 3.5. The over/under-match description refers to the impedance matching of the observation window. From the available data, one would expect u_{VN} to be closer to the 2.80–3.00 km/s range. Using eqn. 2.37 for the single SG EOS and eqn 2.65 for the blended SG EOS, the von Neumann particle velocities can be calculated for a shock speed of $u_s = D_{\mathrm{CJ}} = 7.706$ km/s. The resulting velocities are shown in table 3.6 and the discrepancy is given with respect to the average of the three experimental results, $(u_{\mathrm{VN}})_{exp} = 2.75$ km/s. The "non-intersecting SSG" fit (only referred to as SSG fit from now on) and the BSG EOS fit 1 perform adequately, while the BSG EOS fit 3 predicts a von Neumann particle velocity which is too high.

Window Material	u_{VN} (km/s)	Impedance Match
LiF	2.25	Strong Overmatch
KCl	2.75	Slight Overmatch
PMMA	3.25	Strong Undermatch

Table 3.5: Particle velocity behind the lead shock of the detonation for different window materials, as reported in [1].

	Single SG EOS	Blended SG EOS	
		Fit 1	Fit 3
u_{VN} (km/s)	2.96	2.77	3.05
Error	7.64%	0.73%	10.91%

Table 3.6: Particle velocity at the von Neumann point for the three selected reactant fits.

3.4 Gas phase parameters fitting

Only a single SG EOS is used for the detonation products, such that

$$e_g(P, v_g) = \frac{(P + A_g)v_g}{\Gamma_g} \tag{3.1}$$

Three parameters thus remain to be fitted, namely, A_g, Γ_g (the material properties of the reaction products) and Q (the total heat released in converting the reactants to the final products). In the context of the current models, the heat release is treated as a fitting parameter and is not calculated from enthalpies of formation. The shock Hugoniot for the detonation products is given by

$$u_p = \frac{1}{\Gamma_g + 2}\left[u_s - \frac{c_g^2}{u_s} \pm \sqrt{\left(u_s - \frac{c_g^2}{u_s}\right)^2 + 2(2 + \Gamma_g)B}\right], \tag{3.2}$$

where

$$c_g^2 = [(\Gamma_g + 1)\,P_0 + A_g]\,v_0, \tag{3.3}$$

$$B = P_0 v_0\left(1 - \frac{\Gamma_g}{\Gamma_r}\right) + A_g v_0 - A_r v_0 \frac{\Gamma_g}{\Gamma_r} - \Gamma_g Q. \tag{3.4}$$

In the above, $\Gamma_r = \Gamma_1$ and $A_r = A_1$ when the reactants are modeled using the BSG EOS. When the reactants are modeled using the SSG EOS, $\Gamma_r = \Gamma_s$ and $A_r = A_s$. The shock Hugoniot is only dependent on the model of the reactants through the parameter B, thus Γ_g and A_g are independent of the reactant fitting and only the heat release, Q, depends on the details of the reactant behaviour. Since $P_0 \approx 0$, $A_g v_0 \approx c_g^2$ and $A_r v_0 \approx c_r^2 = c_0^2$. The parameter B can be rewritten as

$$B \approx c_g^2 - \frac{\Gamma_g}{\Gamma_r} c_0^2 - \Gamma_g Q. \tag{3.5}$$

There are two approaches to select the parameters of the product EOS. The first approach consists of fitting the overdriven Hugoniot data with the product Hugoniot (3.2) to obtain fitted values of Γ_g, c_g and B. From c_g, the value of A_g is obtained and from B, the value of Q is obtained for each of the reactant fits outlined in section 3.3. The second approach consists of forcing a particular value of D_{CJ} and P_{CJ}. With those two quantities fixed, c_g and B can be expressed as functions of Γ_g, $c_g(\Gamma_g)$ and $B(\Gamma_g)$. Varying the single remaining free parameter, the product Hugoniot is matched as closely as possible to the overdriven Hugoniot data. Both of these approaches are examined next.

3.4.1 Direct Least-Squares Fitting of Γ_g, A_g and Q

In this method, the value of Γ_g, A_g and Q are determined from fitting the overdriven Hugoniot data directly. No other experimental data is used. Overdriven shock Hugoniot data is available from [16]. Three fits were obtained, namely fits of:

1. the entire data set,
2. the entire data set without two outlying data points,
3. the data set with only the data points for which $u_p > 3$.

The two data points eliminated in dataset 2 appear to be experimental scatter. Dataset 3 consists of the region for which experimental scatter is visibly lower. Without determining the accuracy of each experiments, the comparison of fits to the three subsets of data specified provides an estimate of the variability due to scatter in the experimental data. The least-square fits corresponding to the three data sets are shown in fig 3.15 and their parameters are given in table 3.7. By specifying the reactant fit, the value of Q is calculated from the fitting parameters, Γ_g, c_g and B. The value of the heat release is also shown in table 3.7. One value of the heat release is negative. This occurs for the combination of the single SG EOS reactant fit and the product fit LSQ3. The adiabatic exponent at the CJ point, $\gamma_{g,\mathrm{CJ}}$, the detonation velocity, D_{CJ}, and the detonation pressure, P_{CJ}, are given by

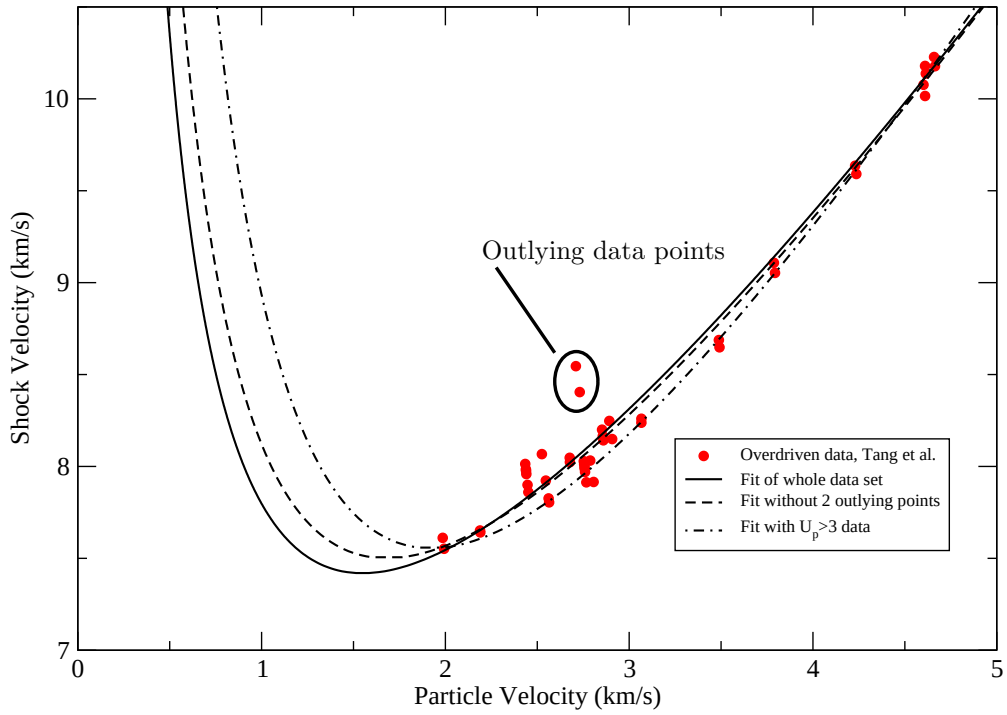

Figure 3.15: u_p-u_s overdriven Hugoniot curve for the explosive PBX 9502 with fits to the data. The two outlying data points that were removed for one of the fits (dashed) are circled.

$$\gamma_{g,\mathrm{CJ}} = (\Gamma_g + 2)\left[\frac{D_{\mathrm{CJ}}^2}{D_{\mathrm{CJ}}^2 - c_g^2}\right], \tag{3.6}$$

$$P_{\mathrm{CJ}} = \rho_0\left[\frac{D_{\mathrm{CJ}}^2 - c_g^2}{\Gamma_g + 2}\right], \tag{3.7}$$

$$D_{\mathrm{CJ}}^2 = \frac{2\left(\gamma_{g,\mathrm{CJ}} + 1\right)^2\left(Q\Gamma_g + c_0^2\Gamma_g/\Gamma_s\right) - 2\gamma_{g,\mathrm{CJ}}\left(\gamma_{g,\mathrm{CJ}} + 1\right)c_g^2}{2\gamma_{g,\mathrm{CJ}} - \Gamma_g}. \tag{3.8}$$

The above system is solved and the results are reported in table 3.8. The error between the predicted detonation velocity and the experimentally measured detonation velocity of $D_{\mathrm{CJ}} = 7.706$ km/s [12] is also reported. While the fits exhibit a relatively small error when predicting the detonation velocity ($< 4\%$), there is enough flexibility in the model to force the CJ state, leading to the second fitting approach.

3.4.2 Enforcement of CJ Pressure and Velocity

The SG EOS has enough flexibility to allow both the CJ pressure and velocity to be enforced as well as to allow a least-square fit to the overdriven Hugoniot data. A best fit is sought for which the unsupported detonation velocity is $D_{\mathrm{CJ}} = 7.706$ km/s [55]. The pressure at the CJ state is estimated to be about

		Γ_g	c_g	$A_g = \rho_0 c_g^2$
Entire data set (LSQ1)		1.27035	4.17845	33.08564714
Data set without outliers (LSQ2)		1.31806	3.80067	27.37345019
Data set restricted to $u_p > 3$ (LSQ3)		1.52445	2.42677	11.16005794
	B	Q for the various reactant fits		
		SSG	BSG1	BSG3
Entire data set (LSQ1)	-3.92303	7.943066401	16.17365283	15.98448282
Data set without outliers (LSQ2)	-4.68308	5.623479629	13.85406606	13.66489605
Data set restricted to $u_p > 3$ (LSQ3)	-6.51254	-0.753658062	7.476928369	7.28775836

Table 3.7: Fits to the overdriven shock Hugoniot data. A_g is given for an initial density of $\rho_0 = 1.895$ g/cc.

	$\gamma_{g,\mathrm{CJ}}$	D_{CJ}	Error	P_{CJ}
Entire data set	3.789718308	7.418885461	3.73%	21.775922904
Data set without outliers	3.464329568	7.500581113	2.67%	23.880464902
Data set restricted to $u_p > 3$	2.929941795	7.554933415	1.96%	27.522278046

Table 3.8: CJ properties of the three least-square fit of the product data.

$P_{\mathrm{CJ}} \approx 28.5$ GPa [56]. Since P_{CJ} is not well known, its value is varied between $25 \leq P_{\mathrm{CJ}} \leq 35$ GPa and the effect of changing P_{CJ} is investigated. From equation 2.107 and assuming $P/P_0 \to 0$, one obtains

$$\gamma_{g,\mathrm{CJ}} = \frac{\rho_0 D_{\mathrm{CJ}}^2}{P_{\mathrm{CJ}}} - 1 \sim 2.948. \tag{3.9}$$

From the definition of the sound speed, eqn 2.8, and the definition of the adiabatic gamma, eqn 2.7, the pressure offset, A_g, can be expressed as a function of Γ_g

$$\frac{A_g}{\rho_0} = c_g^2 = \left(\gamma_{g,\mathrm{CJ}} - \Gamma_g - 1\right) \frac{P_{\mathrm{CJ}}}{\rho_0}. \tag{3.10}$$

To satisfy the Kontorovich criterion, eqn 3.10 imposes an upper limit of $\Gamma_g \leq \gamma_{g,\mathrm{CJ}} - 1 = 1.948$. Enforcing the CJ velocity and following equation 2.114, one obtains

$$-B = \frac{D^2\left(2\gamma_{g,\mathrm{CJ}} - \Gamma_g\right) + 2\gamma_{g,\mathrm{CJ}}\left(\gamma_{g,\mathrm{CJ}} + 1\right) c_g^2}{2\left(\gamma_{g,\mathrm{CJ}} + 1\right)^2} - c_g^2, \tag{3.11}$$

where the parameters c_g^2 and B have been expressed as a function of Γ_g. The value of Γ_g is determined as the best fit to the overdriven Hugoniot data. Again, fits to the overdriven Hugoniot data are independent of the reactant fits. The different reactant fits only change the numerical value of Q.

Shown in fig 3.16 are three fits to the shock Hugoniot data for $P_{\mathrm{CJ}} = 28.5$ GPa. The upper limit of $\Gamma_g = 1.948$ corresponds to the $c_g = 0$ solution. All other values of Γ_g result in a Hugoniot lying "to the right" of this limiting case and with a shallower slope. This behaviour is characteristic of all values of P_{CJ}

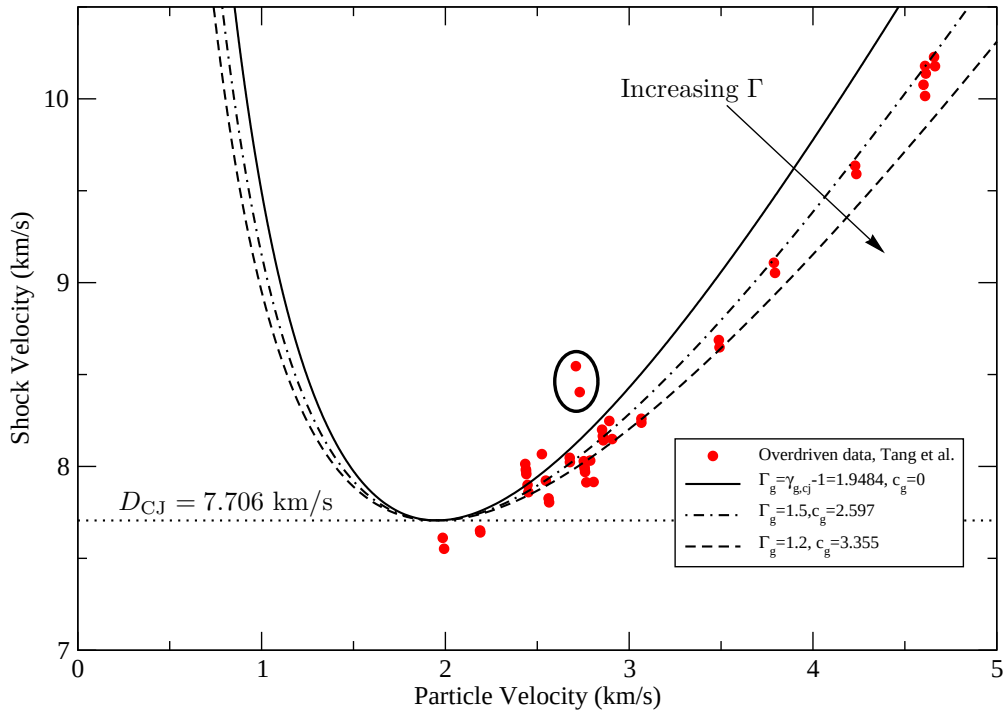

Figure 3.16: Variation of the predicted overdriven Hugoniot with increasing Γ_g for a fixed CJ pressure, $P_{\rm CJ} = 28.5$ GPa, and velocity, $D_{\rm CJ} = 7.706$ km/s. The fit corresponding to $c_g = 0$ is the furthest "left".

considered. For values of $P_{\rm CJ} \lesssim 31$ GPa, a best fit to the Hugoniot data can be found via a least-square minimization. For values of $P_{\rm CJ} \gtrsim 31$ GPa, the best fit possible is the solution corresponding to $c_g = 0$ i.e. $\Gamma_g = \gamma_{g,\rm CJ} - 1$. In fig 3.17, best fits to the entire set of the Hugoniot data are shown for pressures varying between 25 and 35 GPa. The black curves correspond to $P_{\rm CJ} < 31$ GPa and the red curves correspond to the $c_g = 0$ solutions for $P_{\rm CJ} \geq 31$ GPa. Results of the least-square fitting using the three subsets of the overdriven Hugoniot data defined earlier in this section are shown in figs 3.18-3.20. The variation of the value of Γ_g as a function of the CJ pressure, $P_{\rm CJ}$, for all three data sets is shown in fig 3.18. The sharp transition at $P_{\rm CJ} \approx 31$ GPa corresponds to the minimum value of CJ pressure above which $c_g = 0$ is always the best fit. The corresponding variations in c_g and B are shown in fig 3.19. The R-squared value for every data set as a function of the CJ pressure is shown in fig 3.20. In all three cases, an optimal CJ pressure can be identified for which the fit to the overdriven Hugoniot data has the value of R-squared closest to unity. These three optimal fits are shown in fig 3.21 and constitute the best fits to the overdriven Hugoniot data with a fixed CJ velocity and pressure. The optimal CJ pressures found through this method are all close to the $P_{\rm CJ} = 28.5$ GPa estimate first considered. The values of the parameters Γ_g, c_g and B are shown in table 3.9 along with the value of Q for the different reactant fits.

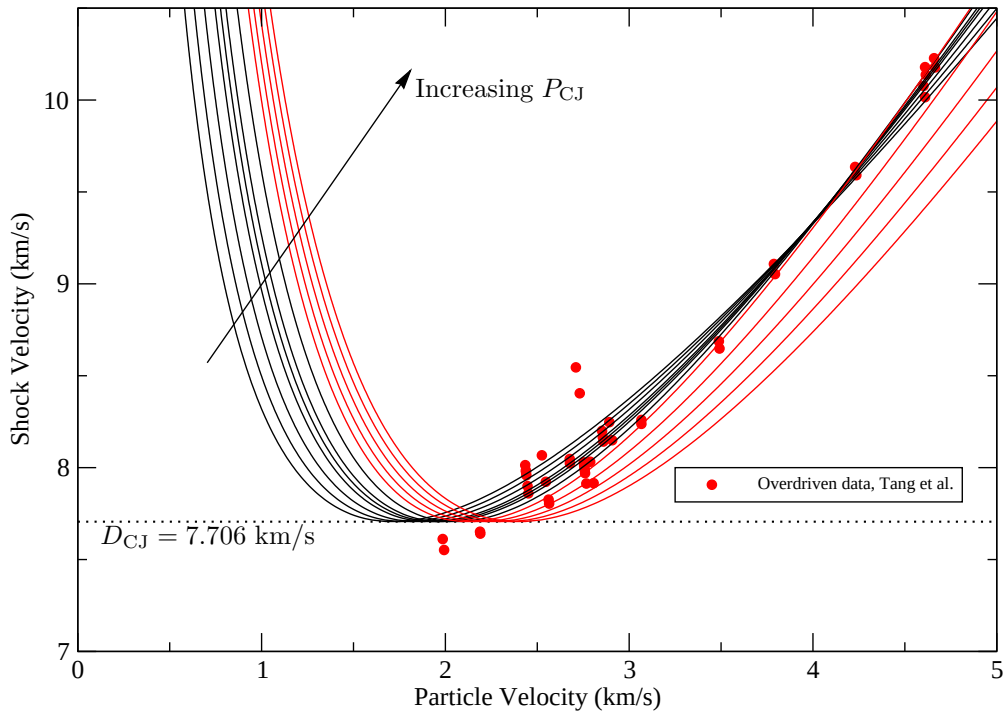

Figure 3.17: u_s-u_p overdriven Hugoniot curve for the explosive PBX 9502. Model curves use a single SG EOS for the products and are independent of the reactant fits. Black curves are fits for which $P_{\mathrm{CJ}} \leq 30$ GPa. For these values of the CJ pressure, an optimal least-square fit can be found. Red curves correspond to fits for which $P_{\mathrm{CJ}} \geq 31$ GPa. In this case, an optimal fit would correspond to $c_g^2 < 0$ and the Kontorovich criterion is no longer satisfied. In this case, the $c_g = 0$ fit is the best fit shown.

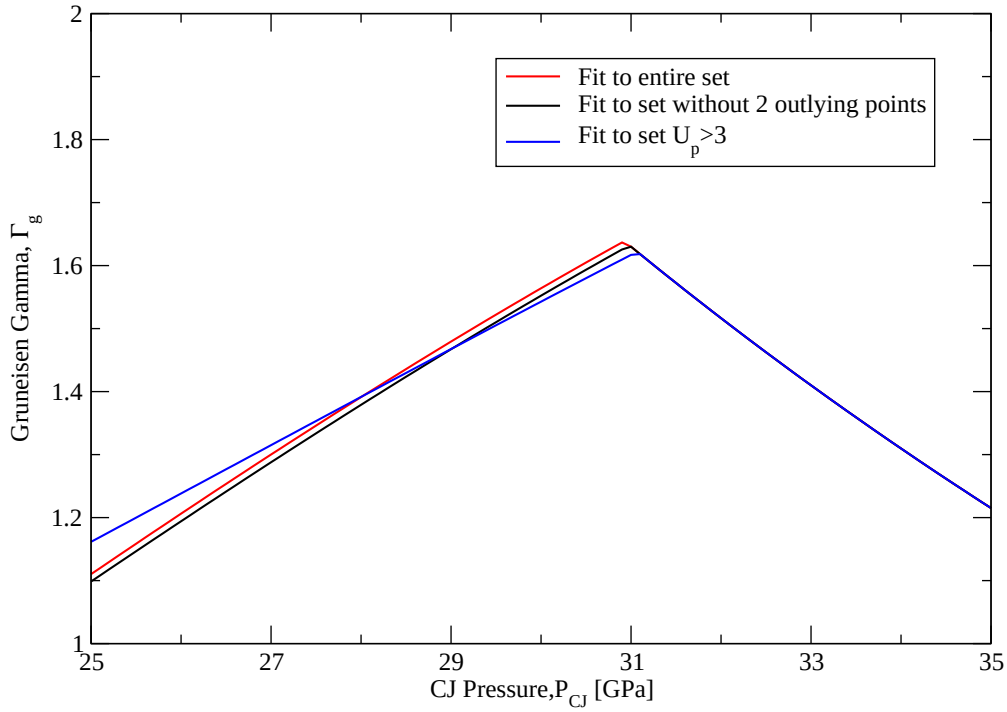

Figure 3.18: Variation of Γ_g with P_{CJ}.

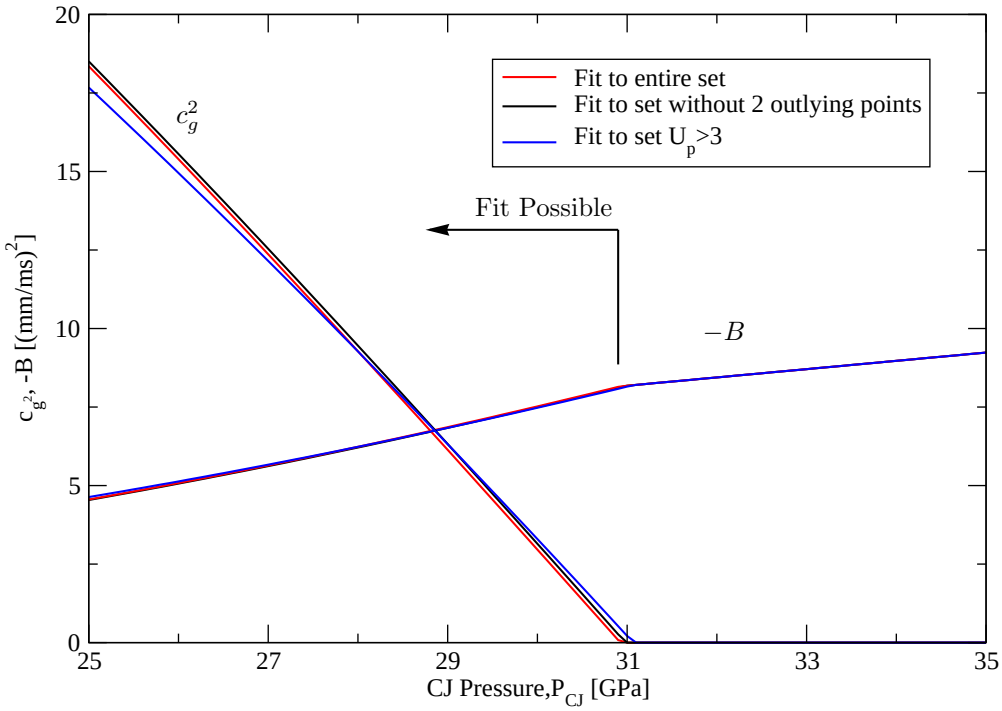

Figure 3.19: Variation of $-B$ and c_g^2 with P_{CJ}.

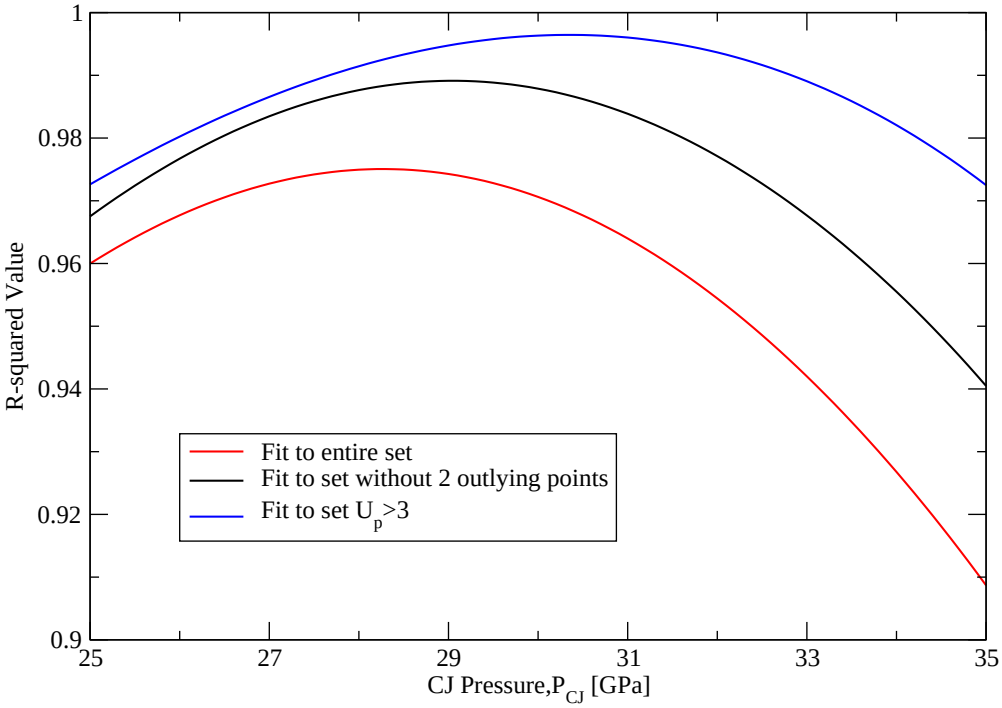

Figure 3.20: Variation of the R-squared value with P_{CJ}.

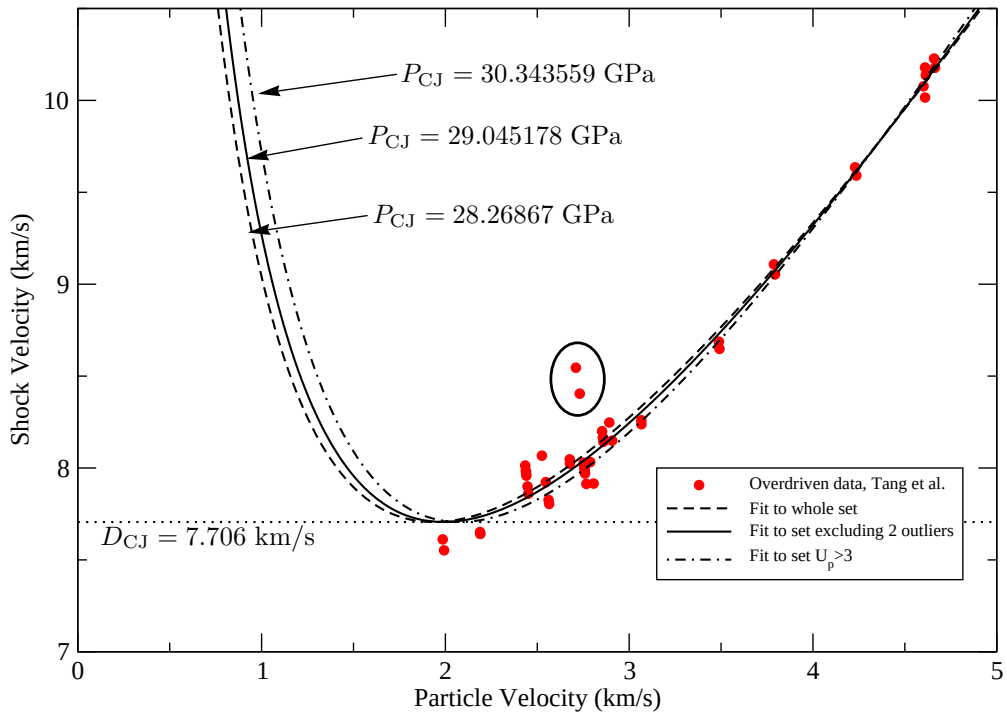

Figure 3.21: Best fits to the three subsets of the overdriven Hugoniot data using P_{CJ} as a fitting parameter.

		Γ_g	c_g	$A_g = \rho_0 c_g^2$
Entire data set		1.4152799	2.904306	15.9816047
Data set without outliers		1.471171	2.485730	11.7089276
$u_p > 3$		1.568385	1.497970	4.25221726
	$-B$	Q for the different reactant fits		
		SSG1	BSG1	BSG3
Entire data set	6.399271	1.592617	9.823203	9.634033
Data set without outliers	6.866220	-0.021753	8.208834	8.019664
$u_p > 3$	7.703681	-2.546317	5.684270	5.495100

Table 3.9: Model parameters for the CJ state forced fits of the overdriven Hugoniot. The value of A_g is for an initial density of $\rho_0 = 1.8905$ g/cc.

Parameter	Value
Γ_s	1.8
c_s (km/s)	4
$A_s = \rho_0 c_s^2$ (GPa)	30.32
Γ_g	1.415
c_g (km/s)	2.904
$A_g = \rho_0 c_g^2$ (GPa)	15.982
$-B$	6.399
Q	1.593
P_{CJ} (GPa)	28.269
D_{CJ} (km/s)	7.706

Table 3.10: Model parameters for the SSG1 fit combined with the CJ state forced product fit. The CJ pressure is optimized to give the best fit to the entire overdriven Hugoniot data.

3.5 Summary of Hugoniot Fitting

The SSG model exhibits a reasonable ability to fit the unreacted Hugoniot data in the high pressure, high shock speed ($u_s > 4.5$ km/s) region while also only intersecting the reacted Hugoniot data at a high shock speed ($u_s \gtrsim 9$ km/s). Because its curvature is reversed when compared to experimental data, the SSG model is however unable to simultaneously capture the initial sound speed of unreacted PBX 9502. The BSG model, on the other hand, is able to capture the initial sound speed of the material, although it is difficult with such a model to ensure a quantitative fit to the unreacted shock Hugoniot while intersecting the reacted Hugoniot data at a high enough shock speed.

The SSG model also exhibits enough flexibility to force a value of the CJ pressure and velocity and still obtain an accurate fit of the overdriven Hugoniot experimental data. When combined with the SSG1 reactant fit, the value of the heat release, Q, is seen to be negative for certain fits. As noted before in section 2.7, $Q < 0$ solutions are allowable using the SG EOS. Nonetheless, fits with $Q > 0$ are favored in this work over those with an unphysical, negative value of heat release. The final selection of a SG-type fit to PBX 9502 consists of the SSG1 fit and the CJ state forced product fit using the entire data set. For an initial density of $\rho_0 = 1.895$ g/cc, the final parameters are shown in table 3.10.

3.6 Specific heat at constant volume

There are no accurate experimental measurements of temperature for detonating PBX 9502 or an equivalent explosive such as LX-17. At room temperature, the specific heat at constant pressure is about $C_p \approx$ 1100J/Kg.K [55]. The two specific heats are related by

$$C_p - C_v = \frac{\alpha^2 T}{\rho \beta_T}, \tag{3.12}$$

with α the volumetric dilation coefficient and β_T the isothermal bulk compressibility and $C_v \leq C_p$. From [57], $\alpha = 150\text{x}10^{-6}$ K^{-1}. Also, $T/\rho \approx 158$ kg.m^3/kg. An estimate is needed for β_T as there is no data. Looking at a range of $\beta_T \sim O(10^{-3} - 10^{-8})$ yields a specific heat in the vicinity of $C_v \sim 1000$ J/kg.K. For high temperature estimates of the solid and gaseous phases C_v, the Debye limit at high temperature (Dulong-Petit law) [58]

$$C_v = 3N_m R_s, \tag{3.13}$$

is used. N_m is the number of atoms in a molecule and R_s is the specific gas constant. The molar mass of PBX 9502 is 258.18 [55] and there are 24 atoms in one TATB molecule. The specific heat at high temperatures can therefore be approximated as

$$C_{vs} \approx 2318 \frac{\text{J}}{\text{Kg.K}}. \tag{3.14}$$

The composition of the products is unknown. It is mostly gaseous, although agglomerates of solid carbon particles can exist. If we use the same Dulong–Petit limit, for a range of molar masses (resulting in $R \approx 40$–550) and atom counts ($N \approx 3$–10) specific heats in the range $C_{vg} \sim 1000 - 5000$ J/kg.K are found.

For the present models the issue is side-stepped. The Arrhenius activation energy is rescaled with the specific heat such that $r \propto e^{(-\theta/C_{vs}T_s)}$. Also, for P–T equilibrium, only the ratio of the specific heats is required and not the absolute values. The $DS_s = 0$ closure is independent of temperature, and the caloric EOS, being incomplete, the specific heats of the solid and the gas are not needed. In the chemical fitting procedure using P–T equilibrium, the ratio of the specific heats is allowed to vary in the range of 0.3–3.0.

3.7 Chemical Kinetic Fitting

There are up to 8 free parameters in the current reaction model. Six parameters are associated directly with the reaction rates given in eqn 2.96 and 2.98: k_I, f_r, ν, n, θ and μ. Two more parameters are associated with the EOS model, but could not be determined from fitting to Hugoniot data namely the ratio C_{vs}/C_{vg} (relevant only to the P–T equilibrium condition) and the fraction of heat released by the second reaction f_q. The value of the exponent of y_B in the second rate was given as $\mu = 4$ in chapter 2 although it is allowed to vary within a range here to account for possible variance in the accuracy of that determination. Those

8 chemical kinetic parameters are determined by comparing the detonation structure resulting from the nozzle assumption with rate-stick data along the axis center line. The nozzle assumption solves the reaction zone profile with a constant flow divergence term in the continuity equation (for example, see [54]). The solution is then optimized over the vector of possible chemical parameters. For each set of possible solution parameters, the master equation (eqn 3.27 derived in section 3.7.3) is integrated through the reaction zone at the curvature values of the available experimental data. The reaction zone integration is performed using a backwards gear method. A normalized sum of the square of the error (SSE) is calculated for each set of curvature and a global optimization is performed.

Because of the large number of parameters in the proposed model, simpler methods (such as a carpet search) would be time-consuming and a robust optimization method with a fast convergence rate is necessary. This requirement would be even more apparent if more complex reaction rate models were involved, such as I&G or CREST. To address this issue, a differential evolution (DE) algorithm [59, 60] is used. DE is a genetic or evolutionary algorithm formulated for the optimization of continuous variables. It has been used in various fields and has proven to be robust and exhibit high convergence rates.

3.7.1 Overview of the Differential Evolution Algorithm

The differential evolution (DE) algorithm is a global, evolutionary optimization algorithm, which minimizes the cost function $F(\boldsymbol{x})$, where $\boldsymbol{x} = \{x_1, x_2, \ldots, x_m\}$ is a vector of m unknown parameters. In the present case, the cost function used is the SSE of the calculated detonation velocity, $D_n(\kappa)$ compared to that of experimental points. Given here is a condensed description of the DE algorithm and the justification for the parameter choices. For a detailed description of DE and of its convergence characteristics, see [60].

DE starts by generating an initial set of N_p random vectors, $P_0 = \left\{\boldsymbol{x}_{1,0}, \boldsymbol{x}_{2,0}, \ldots, \boldsymbol{x}_{N_p,0}\right\}$, that lie within user-defined bounds. The cost function is calculated for each trial vector in the initial population, $f_{i,0} = F(\boldsymbol{x}_{i,0})$. This initial distribution of parameter vectors, called the initial generation, is then iterated to produce the subsequent generations. This iteration is conducted from every generation j to the next generation $j+1$ in three steps. First, mutated individuals, $\boldsymbol{v}_{i,j}$, are created from the current generation P_j. Second, a random crossover phase between the mutated individuals $\boldsymbol{v}_{i,j}$ and their associated target vector $\boldsymbol{x}_{i,j}$ creates new trial vectors, $\boldsymbol{y}_{i,j}$. Finally, a contest determines which of the new trial vectors $\boldsymbol{y}_{i,j}$ and the members of the current generation $\boldsymbol{x}_{i,j}$ are best suited. These individuals then becomes the members of the $j+1$ generation, $\boldsymbol{x}_{i,j+1}$.

Mutation

For every $\boldsymbol{v}_{i,j}$, three individuals in the current generation are randomly selected and denoted $\boldsymbol{x}_{r1}$, $\boldsymbol{x}_{r2}$ and $\boldsymbol{x}_{r3}$. The mutated individual is created using arithmetic operations as $\boldsymbol{v}_{i,j} = \boldsymbol{x}_{r3} + C_M\left(\boldsymbol{x}_{r1} - \boldsymbol{x}_{r2}\right)$, where C_M is a scaling factor. Different strategies can be used to select the random vectors and the scaling factor C_M. For the present purpose, the three vectors are selected such that $\boldsymbol{x}_{r1} \neq \boldsymbol{x}_{r2} \neq \boldsymbol{x}_{r3}$. Additionally, there are ultimately N_p mutated vectors generated and each individual in the current generation, $\boldsymbol{x}_{i,j}$ serves as the "base vector" $\boldsymbol{x}_{r3}$ only once. The scale factor is held constant for all parameters, all individuals in a generation and all generations. A value of $C_M = 0.8$ was used.

Crossover

The crossover phase creates the new trial vector, $\boldsymbol{y}_{i,j}$. A random starting point within the new trial vector, m_{start} is selected and the value of that parameter is copied from the mutated vector, such that $y_{i,j,m_{start}} = v_{i,j,m_{start}}$. For each of the other parameters composing the individual, a random number, R_m, is generated. If this random number is less than a threshold, $R_m \leq C_{Cr}$, the parameter is copied from the mutated individual, $y_{i,j,m} = v_{i,j,m}$ and conversely. There are also different methods to select the value of the crossover threshold. In the present case, this value was constant, $C_{Cr} = 0.9$.

Contest

Once a trial vector is generated, $\boldsymbol{y}_{i,j}$, it is compared with the corresponding individual of the current generation, $\boldsymbol{x}_{i,j}$. If $F(\boldsymbol{y}_{i,j}) \leq F(\boldsymbol{x}_{i,j})$, the trial vector becomes the i-th member of the $j+1$ generation, $\boldsymbol{x}_{i,j+1} = \boldsymbol{y}_{i,j}$. Otherwise, the current individual is retained,$\boldsymbol{x}_{i,j+1} = \boldsymbol{x}_{i,j}$. Because trial vectors are generated in sequence and compared only to a single individual of the j-th generation, the contest is pair-wise and ensures the best individual is always retained in the current generation.

End of the Optimization

The final "best" solution is selected either when the cost function is lower than a user-defined value, $F(\boldsymbol{x}_{best}) < \epsilon$ or when the maximum number of generations is reached, $j = N_g$. In this case, $\epsilon = 10^{-16}$ is selected to force the DE algorithm to iterate to the maximum number of generations N_g.

3.7.2 DE Cost Function

The DE optimization algorithm is based on the evaluation of a cost function, $F(\boldsymbol{x})$, associated with a particular set of parameters, $\boldsymbol{x}$. Here, the set of parameters correspond to the unknown chemical kinetic

parameters; activation energy, rate constants, reaction orders, etc. The cost function is a normalized SSE of the calculated $D_n(\kappa)$ curve compared to the experimental data available

$$F(\boldsymbol{x}) = \frac{\sum_{i=1}^{N_{exp}} \left[D_{n,calc}(\kappa_i) - D_{n,exp}(\kappa_i)\right]^2}{\sum_{i=1}^{N_{exp}} \left[D_{n,exp}(\kappa_i) - \overline{D_n}_{,exp}\right]^2}, \tag{3.15}$$

where $\overline{D_n}_{,exp}$ is the average of the experimental D_n values. Calculating the cost function thus involves calculating N_{exp} values of D_n corresponding to the different experimental points available. Calculating each value of D_n involves integrating the nozzle equations for a particular value of κ_i and iterating on D_n until the sonic point criterion is satisfied. The iteration on D_n is performed via a bisection method.

3.7.3 Nozzle Equations

The description of the nozzle equations follows the derivation of Fickett & Davis [54]. The nozzle equations solve the quasi-1D steady detonation structure with front curvature, along the central axis of a cylindrical charge. This approximate solution assumes

1. radial velocity component is small (i.e. all fluid velocity is along the charge axis), and
2. the curvature is small.

The equations of conservation for mass, momentum and energy can be expressed in cylindrical coordinates and specialized for a steady, axisymmetric process. A set of N rate equations corresponding to N components of the mixture as well as a caloric EOS are also specified.

$$\rho\frac{du}{dx} + u\frac{d\rho}{dx} + \frac{1}{\hat{r}}\left[\frac{d\rho}{d\hat{r}}w\hat{r} + \rho\hat{r}\frac{dw}{d\hat{r}}\right] = 0, \tag{3.16}$$

$$\rho u\frac{du}{dx} + \frac{dP}{dx} = 0, \tag{3.17}$$

$$u\frac{dw}{dx} + w\frac{dw}{d\hat{r}} + \frac{dP}{d\hat{r}} = 0 \tag{3.18}$$

$$u \cdot \bigtriangledown e + Pu \cdot \bigtriangledown v = 0, \tag{3.19}$$

$$u\frac{dy_i}{dx} = r_i, \tag{3.20}$$

$$e = e(P, v, y_i). \tag{3.21}$$

Along the charge axis, there is no radial motion (the first assumption of the solution), i.e. $w(\hat{r} = 0, x) = 0$. Also, $\rho w/\hat{r} \rightarrow \rho w_{,\hat{r}}$ along $\hat{r} = 0$. The internal energy of the mixture can be expressed in terms of (P, v, y_i) and its derivatives. The component of momentum in the radial direction result in $P_{,\hat{r}} = 0$ or $P = P(x)$ only. The result is

$$\rho\frac{du}{dx} + u\frac{d\rho}{dx} + 2\rho\frac{dw}{d\hat{r}} = 0, \tag{3.22}$$

$$\rho u\frac{du}{dx} + \frac{dP}{dx} = 0, \tag{3.23}$$

$$\frac{de}{dP}\frac{dP}{dx} + \left(\frac{de}{d\rho} - Pv^2\right)\frac{d\rho}{dx} + \sum_i \left(\frac{de}{dy_i}\frac{dy_i}{dx}\right) = 0. \tag{3.24}$$

The above derivatives are expressed in terms of du/dx and an expression for the velocity derivative, the master equation, is obtained.

$$\frac{dv}{dx} = \frac{v}{u}\left[2\frac{dw}{d\hat{r}} + \frac{du}{dx}\right], \tag{3.25}$$

$$\frac{dP}{dx} = -\frac{u}{v}\frac{du}{dx}, \tag{3.26}$$

$$\frac{du}{dx} = \frac{\phi}{\eta}, \tag{3.27}$$

$$\eta = 1 - \frac{u^2}{c^2}, \tag{3.28}$$

$$\phi = -\frac{v}{c^2 e_{,P}}\sum_i \left[e_{,y_i} r_i\right] - 2w_{,\hat{r}}. \tag{3.29}$$

The behaviour of $w_{,\hat{r}}(r = 0)$ is found by assuming that the curvature at the axis center is small. To within an order of $1/R_c$ where R_c is the radius of curvature of the wave at the center of the charge, $w_{,\hat{r}} \approx (1/R_c)\,(D_n - u(0))$, where $u(0)$ is the post-shock velocity at the center of the wave and D_n is the propagation velocity along the charge axis [54]. In a rate-stick, the total curvature $\kappa_T = 2/R_c$ and $2w_{,\hat{r}} = \kappa_T(D - u(0))$. Note that to within $1/R_c$, the curvature along the central axis of the charge is constant throughout the reaction zone.

Sonic Point Criterion

The correct detonation velocity D_n for a given curvature value κ_i corresponds to a wave in which, at the end of the reaction zone, $\eta = 0$ along with $\phi = 0$. The curvature term acts similarly to an endothermic reaction. (Despite the initial negative sign, the thermicity component of ϕ is positive for all the models considered here.)

3.7.4 Chemical Fitting Results

The $D_n - \kappa$ data was fitted using the SSG model and both closure conditions, P-T equilibrium and isentropic reactants $DS_s = 0$. The best fits identified after 3 runs are shown in fig 3.22 corresponding to $N_g = 25$, 50 and 100 generations. For both closure conditions, the population size was fixed at $N_p = 80$. The parameters of the best solutions are given in table 3.11.

In both cases, the three best solutions corresponding to the three different number of generations correspond to very different parameters, yet the calculated $D_n - \kappa$ are very similar. Certain parameters vary by a large amount, notably f_q. The fraction of heat release was constrained between $0.05 < f_q < 0.25$ and in most cases, the algorithm hit either one of those bounds. Despite those large variations in f_q, the reaction zone structure is similar, as will be shown later. The case of the $DS_s = 0$ closure condition shows the least variation in SSE with a maximum deviation of 0.74% above the mean SSE of the three solutions. When using the P-T equilibrium closure condition, the maximum deviation of the SSE is 5.95% about the mean of the three corresponding solutions. Since large variations in the parameter sets correspond to relatively small deviations in the SSE, it is possible the current models allow enough flexibility to fit more types of data related to detonation chemistry such as initiation data (pop-plot), etc. An EOS with a larger validity range would be necessary, such that for example the thermodynamic state corresponding to weaker shocks could be accurately described.

The variation of the reaction zone thickness with curvature, $\Delta(\kappa)$, is shown in fig 3.23. Here, the reaction zone thickness is defined as the point at which $\phi, \eta \leq 10^{-5}$, at which point the integration was stopped. Most of the variation occurs in calculating $\Delta(0)$ which varies from 2-10 mm. Regardless of the actual value of Δ, its behaviour is qualitatively similar for all the models. There is an initial, sharp drop in Δ, followed by a relative plateau. This behaviour shows the current models accurately capture the two timescale behaviour of PBX 9502. The detonation wave consists of a first, fast reaction followed by a second, slow reaction.

3.8 Reaction Zone Structure

The structure of the detonation reaction zone for the best solution found by the $N_g = 100$ minimization is shown for $\kappa_0 = 0$ in figs 3.24-3.26. The variation of pressure is shown in fig 3.24 where the VN spike has been identified by a symbol. The difference in record length is due to the longer Δ_{ZND} predicted by using the $DS_s = 0$ closure condition.

The temperature variation is shown in fig 3.25. Here, the value of the product $C_{vi}T_i$ is shown since the exact values of C_{vs} and C_{vg} are both unknown and unnecessary for the calculation of the reaction

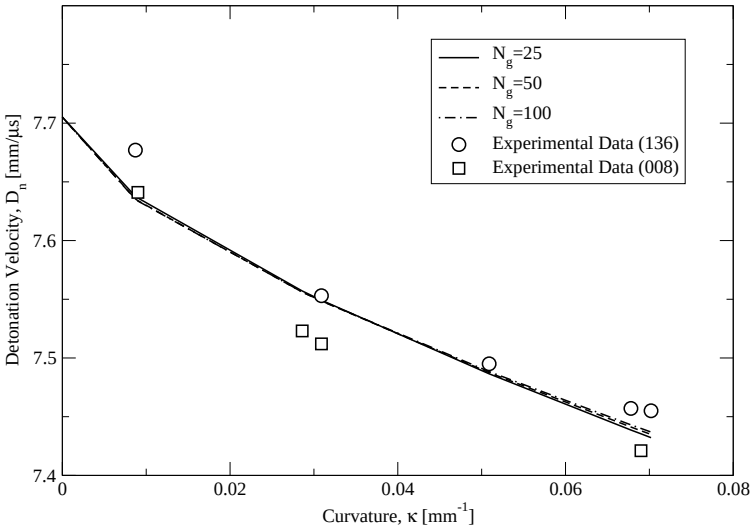

(a) $DS_s = 0$ closure condition.

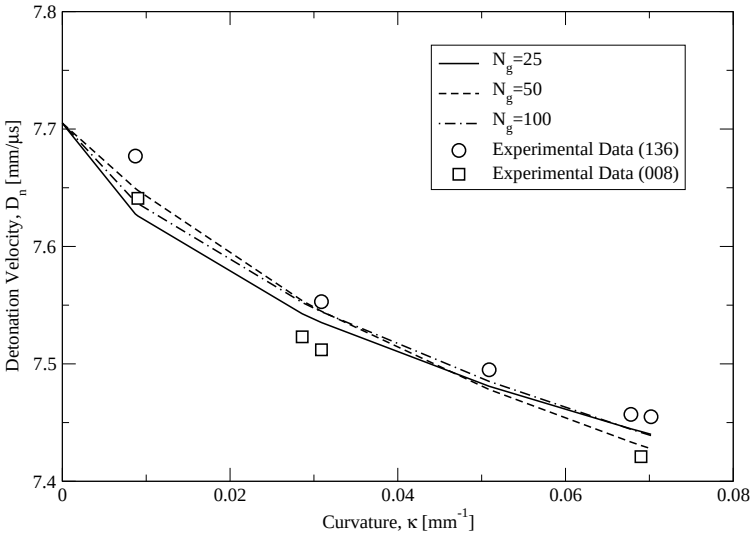

(b) P-T equilibrium closure condition.

Figure 3.22: $D_n(\kappa_0)$ relationships of the fitted models for the $DS_s = 0$ (a) and P-T equilibrium (b) closure conditions. Each curve is the result of a minimization using 80 individuals in the population and N_g generations.

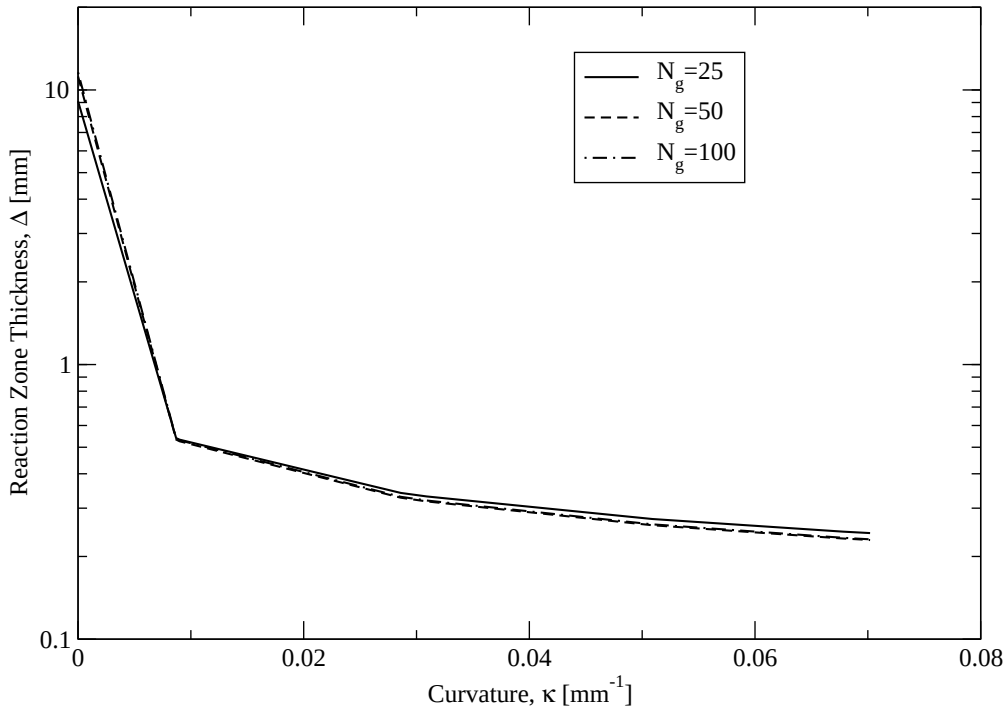

(a) $DS_s = 0$ closure condition.

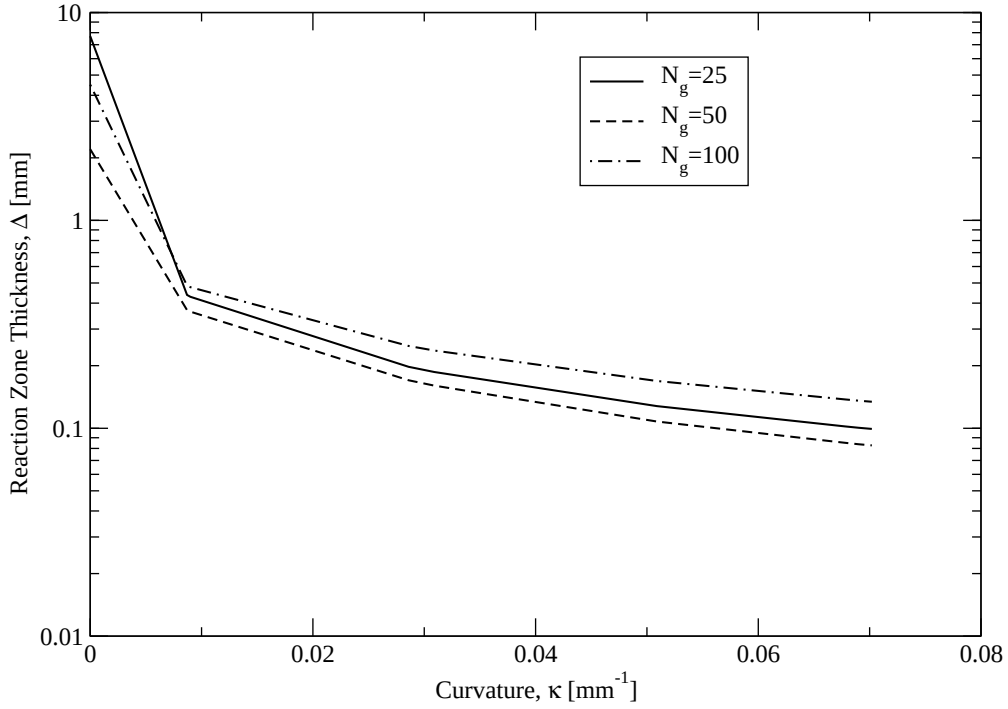

(b) P-T equilibrium closure condition.

Figure 3.23: Thickness of the reaction zone, Δ, versus the wave curvature, κ_0 for the SG EOS model with both the $DS_s = 0$ and P-T equilibrium closure conditions. The thickness, Δ, is defined as the point at which $\phi, \eta = 10^{-5}$

Parameter	$P-T$ Equilibrium			$DS_s = 0$		
	$N_g = 25$	$N_g = 50$	$N_g = 100$	$N_g = 25$	$N_g = 50$	$N_g = 100$
C_{vg}/C_{vs}	0.3	0.3	0.349	N/A	N/A	N/A
k_1 ($\times 10^{-5}$)	1	1	0.768	0.167	0.297	0.170
$f_r = k_2/k_1$ ($\times 10^{-4}$)	1.92	10	8.24	1.681	7.686	9.857
n	2.335	3.646	1.178	0	0	0.0665
ν	1.056	0.690	0.971	1.446	1.521	1.523
μ	4.501	5	4.264	3	3.673	4.571
f_q	0.25	0.05	0.25	0.25	0.0659	0.05
θ	34.103	40.482	34.253	41.542	45.037	41.049
SSE ($\times 10^2$)	5.602	5.201	5.058	5.978	5.932	5.892

Table 3.11: Chemical fitting parameters for the SSG EOS model using both the P-T equilibrium and $DS_s = 0$ closure conditions. The reference pressure was arbitrarily fixed at $P_n = 10$ GPa.

zone structure. For the P-T equilibrium closure condition, only the product $C_{vs}T_s$ is shown. Although the product $(C_{vg}T_g)_{P-T}$ is different than its solid counterpart, the gas temperature must be equal to the solid temperature and the information is redundant. The heat capacities do not appear in the caloric EOS for the $DS_s = 0$ closure condition and only the solid heat capacity C_{vs} appears in the reaction rates. Both $C_{vs}T_s$ and $C_{vg}T_g$ are therefore shown here. The horizontal dotted lines show the maximum temperature for the gas and solid phases. This maximum temperature, for both models, occurs at the shock front and the maximum solid temperature is equal for both closure conditions. Two temperature scales are given, assuming values of heat capacity of $C_v = 2000$ J/kg.K and $C_v = 5000$ J/kg.K respectively. For a solid heat capacity of 2000 J/kg.K, both closure conditions predict a von Neumann temperature of $T \approx 5000$ K. The variation of temperature through the reaction zone is much greater for the P-T equilibrium closure condition with a final CJ temperature of $T \approx 1800$ K. The temperature variations through the reaction zone for the $DS_s = 0$ closure condition are more modest and the final solid temperature is $T_s \approx 4000$ K for the same assumed value of heat capacity. Given the uncertainty in the final product heat capacity, a range is reported here for heat capacities between $2000 < C_{vg} < 5000$ K. The initial gas temperature is then $T_g = 2400 - 6000$ K and the final gas temperature, $T_g = 1800 - 4900$ K.

The ability of the SG model to capture the two timescales of reaction is seen easiest when examining the variation of the species mass fractions and of the fraction of heat released through the reaction zone, as shown in fig 3.26. The mass fraction $y_1 = y_s$ represents the fraction of unreacted solid, while y_2 is the intermediate species. The fraction of the total heat released, $Q(x)/Q = (1 - y_1 - y_2 f_q)$ is also plotted. Two vertical lines identify the point where $q \approx 90\%$. For both closure conditions, 90% of the heat is released within 100 microns and the remaining 10% is released over a space of 1-10 mm. This two scale structure is true regardless of the large variations in the parameter f_q. This behaviour is possible because the two reactions occur concurrently. Only for sequential reactions (where reaction 2 only starts when reaction has

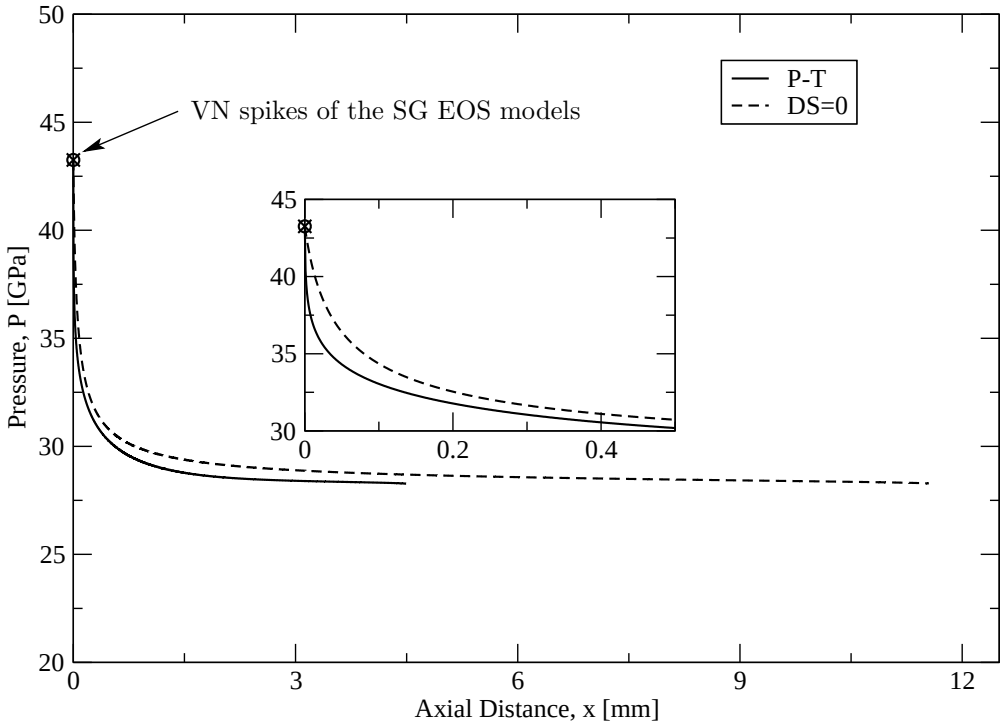

Figure 3.24: Variation of pressure for both closure conditions.

terminated) would f_q be the exact amount of heat released in the second, slow reaction zone.

3.9 Summary

The current calibrations show the SG EOS is flexible enough to capture the characteristics of propagating detonation waves. The EOS model was able to simultaneously reproduce the detonation velocity, CJ pressure as well as the VN spike. Only the response to shocks of lower pressures and the initial sound speed could not be captured adequately. However, the low shock pressure regime is relevant more to problems of detonation initiation and not so much for problems of detonation propagation. Given its simplicity, the SG EOS represents an acceptable compromise between a thermodynamic model that is flexible enough to capture the main characteristics of detonations, yet is sufficiently tractable to determine properties of the reaction flow model in a meaningful fashion. Moreover, when supplemented with a 2 step reaction scheme, there was enough flexibility in the resulting reactive burn model to allow *several* acceptable fits to the $D_n(\kappa_0)$ data. Substituting the SG EOS used to model the reactants with a more complex one, such as a Birch-Murnaghan EOS might allow this model to capture both initiation and propagation properties of PBX 9502, however this is not the purpose of the present work.

The reactive burn model which was calibrated here to detonation propagation data could now be used

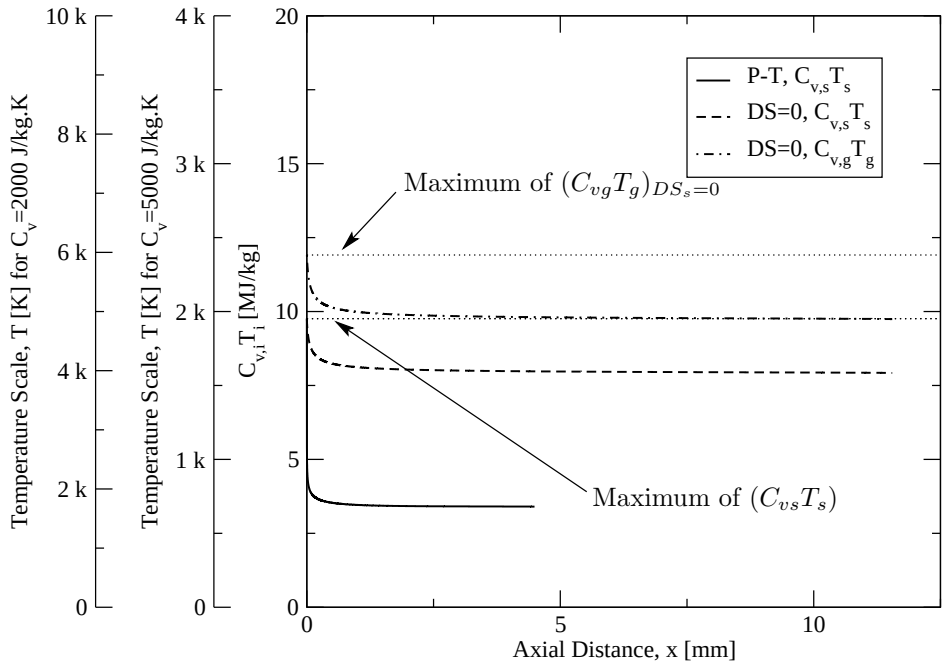

(a)

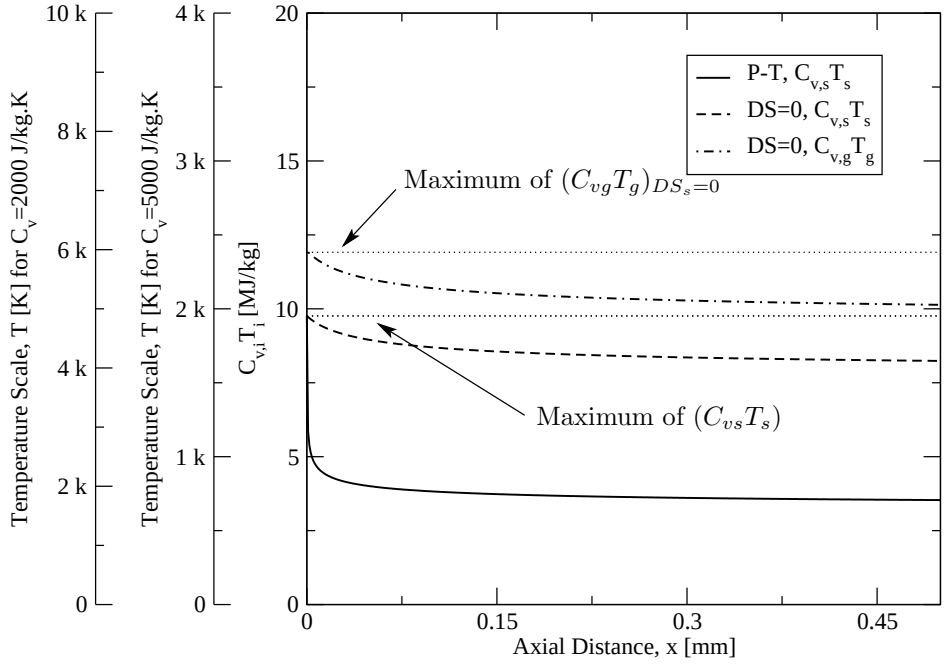

(b)

Figure 3.25: Variation of temperature for both closure conditions. The variation shown is that of $C_{vi}T_i$ and two temperature scales are given assuming two different values of $C_{vi} = 2000, 5000$ J/kg.K. Only a single curve is shown for the $P-T$ equilibrium closure as the resulting temperatures are equal by definition. The dotted lines are the maximums, in this case at the shock front, of $(C_{vg}T_g)_{DS_s=0}$ and $(C_{vs}T_s)$. The curves corresponding to the solid temperature for both closure conditions have the same maximum. Shown in (b) is a closeup of (a) near the lead shock.

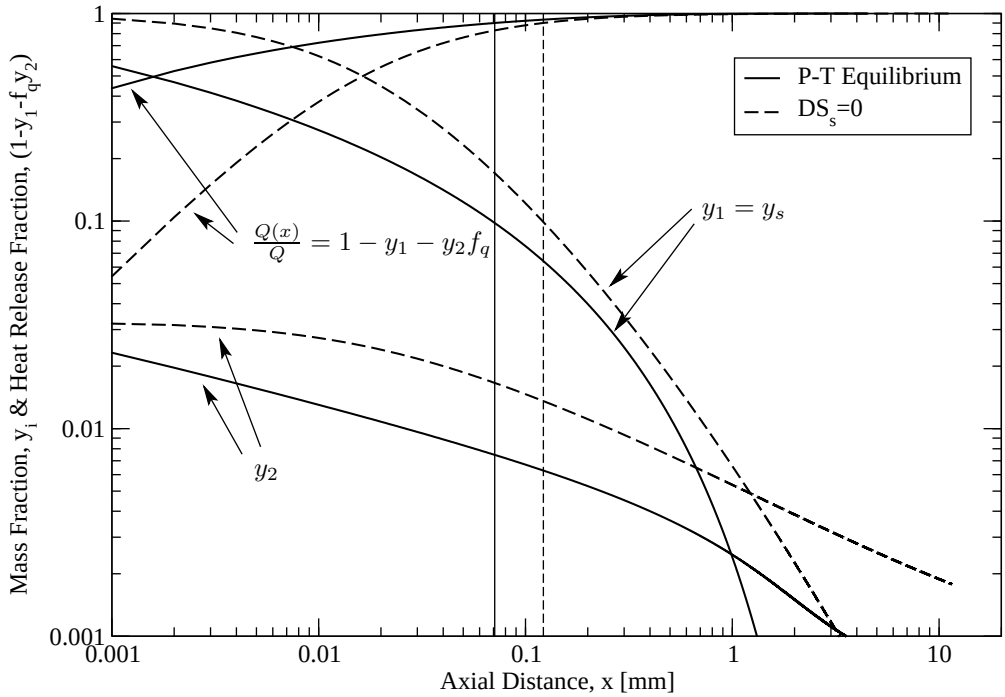

Figure 3.26: Variation of the species mass fraction, $y_1 = y_s$ and y_2, as well as the percentage of the total heat released, $Q(x)/Q = 1 - y_1 - y_2 f_q$ through the reaction zone. The thin vertical lines indicate the position at which $Q(x)/Q \approx 90\%$.

to calculate, say, the $D_n(1/R)$ curve. We focus this work though on some of the properties of detonation stability and structure which can be inferred using this model. Such properties ideally need to be considered when formulating and fitting a model.

Chapter 4

Linear Stability Analysis of Multi-Component Detonation Models

4.1 Introduction

The linear stability analysis of a steady, planar ZND detonation wave yields the linear behaviour of infinitesimal disturbances. Starting with a traveling detonation wave, disturbances (of order $\Psi_0 << 1$, where Ψ_0 is a small number) are superimposed on the steady reaction wave structure. The linear decomposition of the resulting unsteady perturbation problem via a normal-mode method yields an eigenvalue problem for the growth or decay of disturbances. Solving this eigenvalue problem subject to constraints on the spatial boundedness of the eigenfunctions yields the discrete unstable modes of the detonation wave.

In this chapter, the first general formulation of the linear detonation stability problem is presented that is valid for general EOSs and an arbitrary number of reversible reaction rates, limited to pressure and velocity equilibrium between components. The first results are presented for two-component EOS models with different EOSs. Also, the first results are presented for mixtures not in thermal equilibrium. A pseudo-spectral collocation method is used to solve the eigenvalue problem. This method's main advantage is its ability to return at least all the problem's eigenvalues without the need for appropriate initial guesses, as required by shooting methods. Such a behaviour is desirable when analyzing the stability spectrum of new detonation models. The stability characteristics of the SG EOS model derived in the previous chapters are investigated

4.2 Literature Review

Most of the work on the linear stability of detonation waves has been focused on models applicable to gas phase explosives. Ever since the discovery of the cellular structure of gas detonations in the 50's and 60's [61, 62, 63, 64], predicting whether a particular mixture yields a stable or unstable wave has been a central topic of detonation research. Erpenbeck [65] first solved the linear stability problem for single step Arrhenius kinetics of a single phase ideal gas using a Fourier transform approach. The issue was revisited by Buckmaster

[66] in the limit of infinite activation energy. Later, the normal-mode approach was utilized and the ideal gas model was studied with single step kinetics [67] as well as three step kinetics [68]. Multidimensional perturbations have been considered [69, 70, 71]. Attempts were also made at linking the linear stability analysis to the non-linear cellular structure [72, 73]. More recently, the linear stability of fluid reactive burn models applicable to solid explosives has been investigated. The classical $\gamma = 3$ ideal-gas EOS and the single phase SG EOS have been examined [74, 75]. For the SG EOS, an increasing pressure offset a was seen to stabilize the wave. The effect of having two different reaction length scales was also studied and it was found that the presence of a slow reaction zone had a destabilizing effect on the wave.

The algorithms to solve the normal-mode detonation stability formulation have seen recent attention. The traditional shooting method was replaced by a pseudo-spectral (or collocation) method in which the eigenfunctions are discretized as a sum of basis functions instead of using a finite difference integration scheme of the ODE set [76, 77]. The shooting method requires a guess of each eigenvalue from which it converges and improper guesses can lead to missed eigenvalues, whereas the pseudo-spectral method requires no a priori knowledge about the eigenvalues of the system. Collocation methods have the distinct advantage of returning at least all the eigenvalues of a problem when the grid is refined enough. This method has been applied to an ideal gas with single step Arrhenius kinetics [78, 79].

4.3 General Formulation of the Linear Stability of Detonation Waves

The linear stability problem is derived by linearizing the reactive Euler equations around a base flow corresponding to the one-dimensional ZND flow. In this section, the Euler equations have been non-dimensionalized using the DSD scaling, such that

$$P = \tilde{P}/\rho_0 D_{\mathrm{CJ}}^2,\ v = \rho_0 \tilde{v},\ \boldsymbol{u} = \tilde{\boldsymbol{u}}/D_{\mathrm{CJ}}^2, \tag{4.1}$$

where the˜quantities are in the physical scales and $\boldsymbol{u} = \{u, w\}$. The different variables, $\boldsymbol{z} = (v, P, u, w, y_1, y_2, \ldots, y_N)^T$ respectively the specific volume, pressure, longitudinal and transverse velocity and species mass fractions, are expressed as the sum of the time-invariant ZND base flow and a perturbation of small order

$$\boldsymbol{z}(x,t) = \boldsymbol{z}^*(x) + \Psi_0 \boldsymbol{z}'(x) e^{\alpha t + ky}, \tag{4.2}$$

where the * superscript denotes the time-invariant, one-dimensional ZND solution, k is the transverse wave number of a 2D disturbance and α is the complex eigenvalue of the eigenfunctions $\boldsymbol{z}'$. The frame of reference is changed to one where the shock location is fixed. Once linearized, the equations for the base flow (which are the equations of a one-dimensional ZND detonation) and the first order perturbation problem can be solved. The only restriction imposed on the detonation model at this point is that of mechanical equilibrium, i.e. all phases share a single pressure P and a single velocity $\boldsymbol{u}$.

4.3.1 Base-Flow (ZND) Problem

The zeroth-order terms in Ψ_0 yield the base flow, the one-dimensional ZND problem

$$
\begin{aligned}
u v_{,x} - v u_{,x} &= 0, && (4.3)\\
u u_{,x} + v P_{,x} &= 0, && (4.4)\\
e_{,P} P_{,x} + (P + e_{,v})\, v_{,x} + \sum_i e_{,v_i} y_{i,x} &= 0, && (4.5)\\
u y_{i,x} &= r_i, && (4.6)\\
e = e(P, v, y_i), && (4.7)
\end{aligned}
$$

from which follows the derivative of velocity with respect to space

$$
\begin{aligned}
u_{,x} &= -\frac{v \sum_i e_{,y_i} r_i}{c^2 \eta e_{,P}}, && (4.8)\\
\eta &= 1 - u^2/c^2. && (4.9)
\end{aligned}
$$

This set of equations is supplemented by appropriate initial conditions. For these four 1$^{\text{st}}$ order differential equations, four boundary conditions are needed. These conditions correspond to the von Neumann conditions, the conditions immediately after the lead shock. The initial state is given by

$$
\begin{aligned}
u_0 &= -\sqrt{f}, && (4.10)\\
v_0 &= 1, && (4.11)\\
P_0 &= \frac{\tilde{P}_0 \tilde{v}_0}{\tilde{D}_{\mathrm{CJ}}^2}, && (4.12)\\
y_{i0} &= 0, && (4.13)
\end{aligned}
$$

where $f = D_0^2/D_{\rm CJ}^2$ is the overdrive. The post-shock state is given by

$$
\begin{aligned}
u(0) + \sqrt{f}v(0) &= 0, && (4.14)\\
u(0)\left(u(0) + \sqrt{f}\right) + v(0)\left(P(0) - P_0\right) &= 0, && (4.15)\\
w(0) &= 0, && (4.16)\\
\left(e(0) + \frac{u(0)^2}{2} + v(0)P(0)\right) - \left(e_0 + \frac{f}{2} + P_0\right) &= 0, && (4.17)\\
y_i(0) &= y_{i0}, && (4.18)
\end{aligned}
$$

where the location $x = 0$ is at the shock front. The superscript * has been dropped and the above is understood to apply to the base flow. A reaction progress variable can be used as an independent variable instead of the physical space coordinate x (see for example [67, 75]). For even simple systems, for example a single step Arrhenius gas, the extent of the reaction zone can be finite or infinite depending on the choice of the reaction order [75]. Using a reaction progress variable, which goes to completion at the end of the wave, eliminates this problem. However, the choice of reaction progress variable must be tailored, to a certain degree, to the problem at hand. For example, the two-step models developed in chapter 2, cannot be adequately treated by using a single species concentration as a reaction progress variable. For these models, we have a three species, two reaction kinetic scheme. At the start of the reaction zone, the chemical composition is $(y_1, y_2, y_3)_0 = (1, 0, 0)$. The rate of change of the products $(\mathrm{D}y_3/\mathrm{D}t)_0 \propto (y_2^\mu)_0 = 0$. Hence x is multivalued when $y_3 = 0$. Similarly, at the end of the reaction zone, $(y_1, y_2, y_3)_\infty = (0, 0, 1)$ and $(\mathrm{D}y_1/\mathrm{D}t)_\infty \propto (y_1^\nu)_\infty = 0$. Hence, $x(y_1)$ is equally problematic. Because $(y_2)_0 = (y_2)_\infty$ the intermediate species mass fraction is non-monotonic and y_2 is also not a suitable choice of independent variable.

Any linear combination of the chemical composition is also inadequate to serve as a reaction progress variable. A better approach for complex systems is to find a non-linear function of the chemical composition which can act as a reaction progress variable. Non-linear functions of the chemical composition which can be conveniently used are the state variables and functions P, v, u, e, h, etc. If any one of those functions is monotonic, then it can serve the role of reaction progress variable. The correct choice guaranteed to always be monotonic is the mixture entropy, S. The second law of thermodynamics guarantees that, for a closed system, entropy must increase as time passes (or equivalently in this case, through the reaction zone). Unfortunately, the entropy does not appear explicitly in the problem formulation and not all models are formulated such that a simple expression for S can be easily evaluated. An easier choice is to use one of the variables already appearing in the problem, namely P, v or u. Generally, such a choice restricts the

types of chemical models that can be analyzed. From the formulation of the steady ZND problem, it is easy to show that P and v are linearly related to u and, consequently, to each other. As a result, if one varies monotonically, then all vary monotonically and all three choices are equivalent. The criterion under which the velocity variation is monotonic is given by the master equation (eqn 4.8). Both P and v are always positive. Depending on the frame of reference, u is also always positive or negative (but never switches sign). The condition for a monotonic variation of u is therefore a monotonic variation of the thermicity. At first glance, such a condition seems overly restrictive as it precludes, for example, problems with endothermic reaction zones. However, most models of detonations in solid explosives developed so far, including the models of concern in this work, exhibit a monotonic thermicity, thus ensuring that the choice of u as an independent variable is applicable for problems involving solid explosives. The transformation to u-space is as expected for an arbitrary function ζ

$$\frac{d\zeta}{dx} = \frac{du}{dx}\frac{d\zeta}{du}. \tag{4.19}$$

It is important to bear in mind that the restriction of monotonic heat release in the reaction is only an *implementation restriction* and not an inherent restriction of the current formulation. For instance, implementing the linear stability problem as formulated here but using entropy as an independent variable would lift the restriction on the thermicity.

4.3.2 Perturbed Flow Problem

Collecting the first order terms in Ψ_0 in the linearized Euler equations yields the perturbation problem

$$\alpha \boldsymbol{C}_0 \boldsymbol{z}' + \boldsymbol{C}_1 \boldsymbol{z}'_{,u} + \boldsymbol{C}_2 \boldsymbol{z}' - \alpha \boldsymbol{f}_\alpha - \boldsymbol{f}_0 = 0, \tag{4.20}$$

where

$$\boldsymbol{C}_0 = \boldsymbol{I}_{N+4\times N+4}, \tag{4.21}$$

$$\boldsymbol{C}_1 = \begin{bmatrix} uu_{,x} & -vu_{,x} & 0 & 0 & \boldsymbol{0}_{1\times N} \\ 0 & uu_{,x} & 0 & vu_{,x} & \boldsymbol{0}_{1\times N} \\ 0 & 0 & uu_{,x} & 0 & \boldsymbol{0}_{1\times N} \\ 0 & (c^2/v)u_{,x} & 0 & uu_{,x} & \boldsymbol{0}_{1\times N} \\ \boldsymbol{0}_{N\times 1} & \boldsymbol{0}_{N\times 1} & \boldsymbol{0}_{N\times 1} & \boldsymbol{0}_{N\times 1} & uu_{,x}\boldsymbol{I}_{N\times N} \end{bmatrix}, \tag{4.22}$$

$$\boldsymbol{C}_2 = \begin{bmatrix} -u_{,x} & (v/u)u_{,x} & -ikv & 0 & \boldsymbol{0}_{1\times N} \\ -(u/v)u_{,x} & u_{,x} & 0 & 0 & \boldsymbol{0}_{1\times N} \\ 0 & 0 & 0 & ikv & \boldsymbol{0}_{1\times N} \\ a_v & -(u/v)u_{,x} & ikc^2/v & a_P & \boldsymbol{a}_y \\ -\boldsymbol{r}_{i,v} & \boldsymbol{r}_i/u & \boldsymbol{0}_{N\times 1} & -\boldsymbol{r}_{i,P} & -\boldsymbol{M}_y \end{bmatrix}, \tag{4.23}$$

$$\boldsymbol{f}_\alpha = \{ \ \tfrac{v}{u}u_{,x} \quad u_{,x} \quad 0 \quad -\tfrac{u}{v}u_{,x} \quad \boldsymbol{r}_i/u \ \}^T, \tag{4.24}$$

$$\boldsymbol{f}_0 = \{ \ 0 \quad 0 \quad -ikuu_{,x} \quad 0 \quad \boldsymbol{0}_{1\times N} \ \}^T, \tag{4.25}$$

with the following definitions

$$\boldsymbol{r}_i = \left\{ \ r_1 \quad r_2 \quad \dots \quad r_N \ \right\}^T \tag{4.26}$$

$$\boldsymbol{M}_y = \begin{bmatrix} r_{1,y_1} & r_{1,y_2} & \dots & r_{1,y_N} \\ r_{2,y_1} & \ddots & \ddots & r_{2,y_N} \\ \vdots & \ddots & \ddots & \vdots \\ r_{N,y_1} & r_{N,y_2} & \dots & r_{N,y_N} \end{bmatrix}, \tag{4.27}$$

$$a_v = u_{,x}\left[\frac{c^2}{v^2} - \frac{e_{,Pv}u^2}{ve_{,P}} + \frac{ve_{,vv}}{e_{,P}}\right] + \frac{1}{e_{,P}}\sum_i \left(e_{,y_i}r_{i,v} + e_{,y_iv}r_i\right), \tag{4.28}$$

$$a_P = u_{,x}\left[-\frac{e_{,PP}u^2}{ve_{,P}} + \frac{v(1+e_{,Pv})}{e_{,P}}\right] + \frac{1}{e_{,P}}\sum_i \left(e_{,y_i}r_{i,P} + e_{,y_iP}r_i\right), \tag{4.29}$$

$$a_{y_i} = u_{,x}\left[-\frac{e_{,Py_i}u^2}{ve_{,P}} + \frac{ve_{,y_iv}}{e_{,P}}\right] + \frac{1}{e_{,P}}\sum_j \left(e_{,y_j}r_{j,y_i} + e_{,y_jy_i}r_j\right). \tag{4.30}$$

$$\tag{4.31}$$

The sound speed is the frozen sound speed $c^2 = v^2(P + e_{,v})/e_{,p}$ and the internal energy is a general function $e = e(P, v, y_i)$. Again, this formulation applies for multi-component mixture with models allowing different EOS between components, provided the mixture is in mechanical equilibrium, i.e. pressure and velocity equilibrium.

4.3.3 Shock Boundary Conditions

A set of boundary conditions on the perturbation quantities, v',u',w',P' and y_i' is necessary. Linearizing the shock conditions results in the shock boundary conditions on $\boldsymbol{z}'$

$$v'(0) = \alpha \frac{u(0) + \sqrt{f} - a_u}{f}, \quad u'(0) = \alpha \frac{a_u}{\sqrt{f}}, \quad w'(0) = -ik\left(u(0) + \sqrt{f}\right), \\ P'(0) = \alpha\left(u(0) + \sqrt{f} + a_u\right), \quad y_i'(0) = 0, \tag{4.32}$$

where

$$a_u = \frac{\left(f e_{,P} + e_{,v} + P_0\right)\left(u(0) + \sqrt{f}\right)}{e_{,v} + P(0) - f e_{,P}}. \tag{4.33}$$

4.3.4 Radiation and CJ Boundary Condition

One more condition is required for the determination of α. This is the compatibility condition. Substantial work has been done on the formulation. For overdriven waves, the compatibility condition is a statement that no information can be propagated from the back of the wave. This radiation condition is obtained from the linear stability analysis of the subsonic, non-reactive flow beyond the end of the reaction zone and is independent of the EOS and reaction rate model. The overdriven condition is nonlinear in α and can only be applied with the collocation method for the one-dimensional case $k = 0$.

$$u' + MF(\eta, k, \alpha)p' - \frac{iku}{\alpha}w' = 0, \tag{4.34}$$

$$\tag{4.35}$$

where

$$F(\eta, k, \alpha) = \sqrt{1 - \eta\frac{k^2}{\alpha^2}}, \tag{4.36}$$

and M is the Mach number. This overdriven compatibility condition is only applicable to irreversible reactions. The SG models considered here only involve irreversible reactions.

Short et al. [75] showed that the CJ closure condition obtained through a boundedness analysis of the different modes at the CJ plane is equivalent to the linearization of an equation describing forward traveling plane waves in the shock frame. The result of this linearization is a CJ compatibility condition which is linear in the eigenvalue α

$$\alpha(p' + u') - ikuw' + 2u_{,x}(u' - \alpha) + b_p p' + b_v v' + \sum_{i=1}^{n} b_{y_i} y_i' = 0, \tag{4.37}$$

where

$$b_p = -uu_{,x}(1 - e_{,pp} + e_{,vp})/e_{,p} + \sum_{i=1}^{n}(e_{,y_i} r_{i,p} + r_i e_{,y_i p}) - e_{,pp} \sum_{i=1}^{n} e_{,y_i} r_i / e_{,p}^2, \tag{4.38}$$

$$b_v = (-uu_{,x}(e_{,vv} - e_{,pv} - 2e_{,p}c^2/u^3) + \sum_{i=1}^{n}(e_{,y_i} r_{i,v} + r_i e_{,y_i v}) - e_{,pv} \sum_{i=1}^{n} e_{,y_i} r_i / e_{,p})/e_{,p}, \tag{4.39}$$

$$b_{y_i} = (-uu_{,x}(e_{,vy_i} - e_{,py_i}) + \sum_{j=1}^{n} e_{,y_j} r_{j,y_i} + \sum_{j=1}^{n} r_j e_{,y_j y_i} - e_{,py_i} \sum_{j=1}^{n} e_{,y_j} r_j / e_{,p})/e_{,p}. \tag{4.40}$$

4.4 Multi-Phase Equations of State

The 2 phase SG EOS model with P–T equilibrium and $DS_s = 0$ closure conditions were written as a function of mixture-averaged properties, P and v. The resulting descriptions were then differentiated analytically.

4.4.1 P–T equilibrium

The two phase SG EOS was already written down for the P–T equilibrium closure condition in the closed form $e = e(P, v, y_i)$ (eqn 2.84). This formulation makes use of eqns 2.81 and 2.82 to define the two functions $\xi_1(P)$ and $\xi_2(P, y_s)$. In this form, the internal energy function can be directly differentiated.

4.4.2 $DS_s = 0$ closure

For this closure condition, the solid phase follows the isentropic relation (2.93). The entropy level of the fluid is calculated at the post-shock conditions using

$$F(S_0) = P_{\text{shock}} + \frac{a_s}{1 + \Gamma_s} v_{\text{shock}}^{1+\Gamma_s}, \tag{4.41}$$

where $F(S_0)$ is a function of the entropy at the shock state and $v_{\text{shock}} = (v_s)_{\text{shock}}$ since no reaction occurs within the shock. The specific volume of the solid phase can be expressed as a function of pressure for any point in the flow

$$v_s = \left(\frac{F(S_0)}{P + a_s/(1+\Gamma_s)} \right)^{(1/(1+\Gamma_s))}. \tag{4.42}$$

Using the definition of the mixture average specific volume (2.77), the internal energy can be expressed as $e = e(P, v, v_s(P), y_i)$

$$e - e_0 = (1-y_p)\frac{P+a_s}{\Gamma_s} v_s + \frac{P+a_g}{\Gamma_g}(v - (1-y_p)v_s) - (y_p Q_1 + y_B Q_2) \tag{4.43}$$

where y_p and y_B are the mass fractions of products and intermediate, respectively. The above is for a two step reaction although the simplification to a single step reaction is trivial. The derivatives with respect to the state variables are directly calculated from the above. One important consequence of the $DS_s = 0$ closure condition concerns the solid temperature of the solid. For a SG EOS, the temperature is

$$C_{vs} T_s = v_s \frac{P(\Gamma_s + 1) + a_s}{\Gamma_s(\Gamma_s + 1)}. \tag{4.44}$$

For the $DS_s = 0$ closure, $v_s = v_s(P)$ only, leading to $C_{vs}T_s = F(P)$ only. In a ZND wave, the pressure decreases through the reaction zone and, as a result, so does the temperature. Any reaction rate dependent on temperature alone will have its maximum at the shock front. It is worth noting this result is not a characteristic of the SG EOS per se even though the SG EOS can, for some parameters, exhibit this behavior. Rather, the $DS_s = 0$ closure condition leads to a temperature maximum at the shock regardless of the underlying EOS of the different phases.

The reaction rates are formulated as defined in section 2.6 and again the reduction to a single step solid phase is trivial. It is worth repeating that since thermal equilibrium no longer applies, the Arrhenius dependence of the kinetic rates depends on T_s and not T_g

$$r \propto e^{-\theta/C_{vs}T_s}. \tag{4.45}$$

This choice is in accordance with the basic assumption behind the $DS_s = 0$ closure, namely the absence of heat transfer between the products and reactants.

4.5 Implementation of the Pseudo-Spectral Method to the Linear Stability Analysis of Detonations

As noted, the stability problem has traditionally been calculated using a shooting method. A guess for α is taken, the eigenfunctions eqns are integrated from the shock to the reaction termination point. The solution is iterated using the residues of the compatibility condition. The residues for solid EOS are large and the method requires good initial guesses. The spectral collocation method (or pseudo-spectral method) is used instead here to solve the stability problem with a general EOS and reaction rate. The formulation here follows the work of Tumin and Chiquete [78, 79] where the stability problem was solved for an ideal gas with 1 step Arrhenius kinetics. The reasoning behind using the collocation method was to build a framework which could accept any detonation model (notwithstanding the restrictions imposed in previous sections) and return the discrete spectrum without a priori knowledge of the spectrum. An approach which requires no previous knowledge of the stability of an explosive has value when studying new detonation models and/or an as of yet unexplored range of model parameters. This approach contrasts the more conventional shooting method approach which requires a guess of each eigenvalue in order to converge on a root. Eigenvalues can be "missed" in the event either the search grid is not refined enough or if the residual function near a root is too steep.

4.5.1 Description of the Collocation Method with Chebyshev Polynomials

The basic theory of the collocation method and of spectral and pseudo-spectral methods can be found in several references, for example Canuto et al. [76, 77]. For a more practical approach, one can consult the reference by Boyd [80]. Finally, Schmid and Henningson [81], while specifically targeting applications relevant to shear flows, gives valuable information on practical implementations of the collocation method. In the collocation method, the unknown functions are discretized using a set of basis functions, in this case the Chebyshev polynomials

$$\boldsymbol{z}' = \sum_n \boldsymbol{z}'_n T_n(\xi) \tag{4.46}$$

where the vector $\boldsymbol{z}'$ is the vector of unknown eigenfunctions. The problem has therefore been changed, as in most numerical methods, from a problem of finding unknown functions to a problem of finding unknown coefficients of functions. The different derivatives of the above expansion can be found by directly differentiating the basis functions. Were the stability problem a homogeneous eigenvalue differential equation, the solution

would be simpler. The n-term expansion of $\boldsymbol{z}'$ would be substituted in the 1st order problem 4.20 and the resulting matrix equation solved. However, the stability problem is an inhomogeneous eigenvalue differential equation system, owing to the presence of the terms $-(\alpha \boldsymbol{f}_\alpha + \boldsymbol{f}_0)$. The solution is to augment $\boldsymbol{z}'$ with a pseudo-variable σ. The vector of eigenfunctions is then $\boldsymbol{z}' = \{v', P', u', w', y_i', \sigma\}^T$. This pseudo-variable is in fact an arbitrary constant which rescales 4.20 as $\sigma = 1$ returns the original problem. The pseudo-variable is discretized using Chebyshev polynomials also, but truncated after a single term, such that

$$\sigma = \sigma_0 T_0(\xi), \tag{4.47}$$

as $T_0(\xi) = 1$ by definition. Solutions which return $\sigma_0 = 0$ are discarded as they solve the homogeneous problem and not the complete problem. Any other value of σ_0 is used to rescale the eigenfunctions $\boldsymbol{z}'$. Once this pseudo-variable σ has been defined, the rest of the implementation follows the same method as that described in standard references. The ODE set is evaluated at a number of points, the Gauss-Lobatto points. The differentiation matrices, for the derivatives of $T_n(\xi)$ at the collocation points, can be evaluated in a number of ways. The differentiation matrices were evaluated here by direct differentiation and the use of a recursive relation for the derivatives of the Chebyshev polynomials. A clear description of the procedure is found in [81]. A standard mapping was used to go from the non-dimensional variable ξ to the independent variable of the problem u^* [80]. Finally, a multi-domain approach was implemented. In this case, a 3 domain approach was used in which the problem is discretized into 3 domains, the eigenfunctions in each domain are represented by an N_i-term Chebyshev expansion. Continuity and smoothness conditions are applied at the boundary of the domains. A thorough presentation of the collocation method using multi-domain methods and complex geometries can be found in [77]. Following [78], the three domain method with 50-200 points per domain was mainly used in the present work.

Regardless of the number of domains used or of the procedure selected to obtain the differentiation matrices, the result of the collocation method is an eigenvalue matrix problem of the form

$$\alpha \boldsymbol{A} = \Lambda \boldsymbol{E}, \tag{4.48}$$

where $\boldsymbol{A}$ and $\boldsymbol{E}$ are obtained through the spectral collocation method, α is the same eigenvalue as in the original problem and Λ is a vector of the eigenfunction coefficients. The solution is found using standard solving tools, in this case the QR/QZ algorithm from the standard LAPACK routines is used to solve for the eigenvalues and eigenfunctions.

4.5.2 Drawbacks of the Collocation Method and its Current Implementation

Several issues arise when using the collocation method. The most noticeable characteristic is the presence of spurious modes. For a given calculation of an eigenvalue problem using a collocation method with N collocation points, the method returns N eigenvalues. For a system which has an infinite number of eigenvalues, a useful rule-of-thumb is that only about half of all the eigenvalues found by the collocation method are proper solutions of the system [80]; the other eigenvalues are spurious eigenvalues, typically those with the highest frequencies. However, the detonation stability problem has a finite number of unstable modes and all other eigenvalues are spurious eigenvalues. Discerning between the proper and the spurious eigenvalues is a task in itself, especially for nearly stable waves. The accuracy of a given solution is dependent on the number of collocation points used. As a result, it is difficult to limit the number of spurious modes returned by the method without affecting also the precision of the calculation method.

The precision of the scheme is also not adaptive. The overall accuracy of the solution is dictated by the number of collocation points and the local accuracy by the exact distribution of the collocation points. The 3 domain method was suggested in [78] as a method to ensure more collocation points were located near the lead shock and the end of the reaction zone, where most rapid fluctuations in the eigenfunctions occur. The distribution of the collocation points is fixed at the beginning of the calculation and cannot be changed as the solution is computed. This is in contrast to iterative solution methods where the eigenfunctions are calculated via a finite-difference integration. By employing adaptive integration methods, iterative solutions can adapt to the precision required by the eigenfunctions being calculated. A related issue is that the collocation method for a problem with a fixed number of eigenvalues (and not an infinite number of eigenvalues) can still "miss certain modes" if the solution is under-resolved. The resulting eigenvalue map is increasingly difficult to distinguish from that of a stable case as only spurious eigenvalues are present.

Only eigenvalue systems which are linear in the eigenvalue α can be implemented using the collocation method. The radiation condition for 2D waves cannot be implemented directly. Tumin and Chiquete [78] force the eigenfunctions of 2D overdriven waves to independently go to zero at the end of the reaction zone as an alternate compatibility condition. For a reaction rate order greater than or equal to one, this is the correct spatial boundedness structure of the eigenfunctions provided one is sufficiently close to the end of the reaction zone, an irregular singular solution of the ODE system governing the eigenfunction behavior. Typically, the enforcement of the condition $\boldsymbol{z}' \to 0$ gives eigenvalues that are highly sensitive to resolution [82] and do not converge rapidly to results obtained using the radiation condition. Due to this restriction, 2D overdriven ZND wave stability behavior was not considered here with a collocation method. Reliable 2D results thus require a switch to an ODE shooting method calculation. Given the considerable amount

of attention given to designing a general EOS and reaction rate collocation method, all results shown below address one-dimensional instability. This is sufficient to address the trends in stability behavior resulting from varying reactant and product EOSs, and equilibrium closure conditions.

A second observation of the author while using the present implementation of the collocation method was that CJ waves and near stable waves would demand a higher number of collocation points in order to obtain good accuracy. In addition, a larger number of spurious modes would appear near the $\alpha = 0$ point, which is where the relevant eigenvalues are located when they exist. The full extent of this behaviour was not investigated thoroughly in the course of this work.

Drawbacks of the current implementation are mostly related to the execution speed and could be partially mitigated by using a more thoughtful code design. The current implementation requires from 5–30 minutes of calculations whereas some of the execution times quoted by Tumin and Chiquete [78] are on the order of minutes albeit for a simpler ideal gas model with one-step kinetics. It should be noted that the nature of the irregular singular structure of the eigenfunction system near the end of the reaction zone (or internal sonic point) is more severe for non-ideal equations of state [74]. It is possible gains in run time could be made by selecting a more appropriate language. The current implementation was written using an interpreted language, which is always slower than compiled languages. A more careful code design would also limit the number of function calls necessary, thereby speeding up execution time. There is a limit to how much minimization of function calls one can attain. For a framework designed to solve a general EOS, quantities such as the sound speed, the internal energy and its derivatives, etc. will have to require a minimum number of function calls.

4.5.3 Performance of the Collocation Implementation

The ideal gas model with a single Arrhenius reaction and $\gamma = 1.2$, $f = 1.2$, $\gamma\tilde{Q}/c_0^2 = 50$, $\gamma\tilde{E}_a/c_0^2 = 50$ has been studied extensively. It was used here (as in [78]) to verify the collocation method with the general equation of state and reaction kinetic formulation (4.20–4.30) as well as to characterize the pseudo-spectral scheme. The full eigenvalue map resulting from the 3-domain calculation with 100 collocation points per domain is shown in fig 4.1(a). The detail of the map in the vicinity of $\alpha = 0$ and showing the physically relevant eigenvalues, is shown in fig 4.1(b). The eigenvalues were calculated using the 1, 2 and 3 domain methods with an equivalent total number of collocation points and all three methods are in agreement. For the 3-domain method, the convergence of α is shown in fig 4.2 for $N = 25, 50, 75, 100, 125$ points per domain. The $N = 125$ points is the reference solution for the calculation of the error in fig 4.2. The wall time for those same 3-domain calculations is shown in fig 4.3 as it was run on a single intel Xeon 3.80GHz core with

2GB of RAM.

4.6 Linear Stability of the SG EOS

The goal is to study the effects of individual changes in the EOS in a multi-phase EOS setting. A choice is made to reduce the problem to the two species SG EOS model with 1 step Arrhenius kinetics and to study the behaviour of 1D instabilities starting from the thoroughly studied case, $Q = E = 50$ (in the Erpenbeck scaling), $\Gamma_s = \Gamma_g = \Gamma = \gamma - 1 = 0.2$, $f = 1.2$ and $a_s = a_g = a = 0$. Variations in the value of a_s, a_g, Γ_s, Γ_g, C_{vs}/C_{vg} and a change in the closure condition are studied independently in the course of this study. The variation of a_s, a_g, Γ_s, Γ_g and C_{vs}/C_{vg} is investigated using the P–T equilibrium closure condition. While the reference problem is applicable to gas phase rather than to solid phase, insight into the behaviour of the EOS model is still realized and this choice of parameters has the advantage of studying the model in a range where the collocation solving method performs well.

The stability problem is solved in the DSD scaling and specified such that when $a_s = 0$, the activation energy is equivalent to $E = 50$ *in the Erpenbeck scaling.* The activation energy E is held constant in the DSD scaling. The two scales give activation energies

$$(E)_{\text{Erpenbeck}} = \frac{\gamma \tilde{E}}{c_0^2}, (E)_{\text{DSD}} = \frac{\tilde{E}}{D_{\text{cj}}^2}. \tag{4.49}$$

The question which is asked here is "Given a particular explosive with a particular activation energy, CJ detonation speed and high initial sound speed, what do different models predict in terms of stability for that particular explosive?" Holding the activation energy constant in the DSD scales is equivalent to specifying a constant value of D_{CJ} in addition to a constant activation energy.

4.6.1 Global Variation in Pressure Offset $a_s = a_g = a$

First, the value of both a_s and a_g is varied in a range of $a = 0$ to 0.03 while enforcing $a_s = a_g = a$ and $\Gamma_s = \Gamma_g = 0.2$. The results are then those of a single SG EOS. The eigenvalue map of fig 4.4 shows the growth rate of each of the 5 modes decreasing as a is increased. Three of the modes become stable for high values of a. The ZND profiles are shown in fig 4.5. Figs 4.5(a)–4.5(c) show the variation of pressure, specific volume and velocity respectively through the wave. The temperature profile is shown in fig 4.5(d) along with the variation of the reaction rate normalized by its maximum $r/r_{\max}$. The temperature profile shifts from lower to higher values for increasing values of a. For a fixed activation energy, this shift in temperature raises the initial value of $e^{-\theta/T}$ over the entire profile. The result is an higher reaction rate at the front and

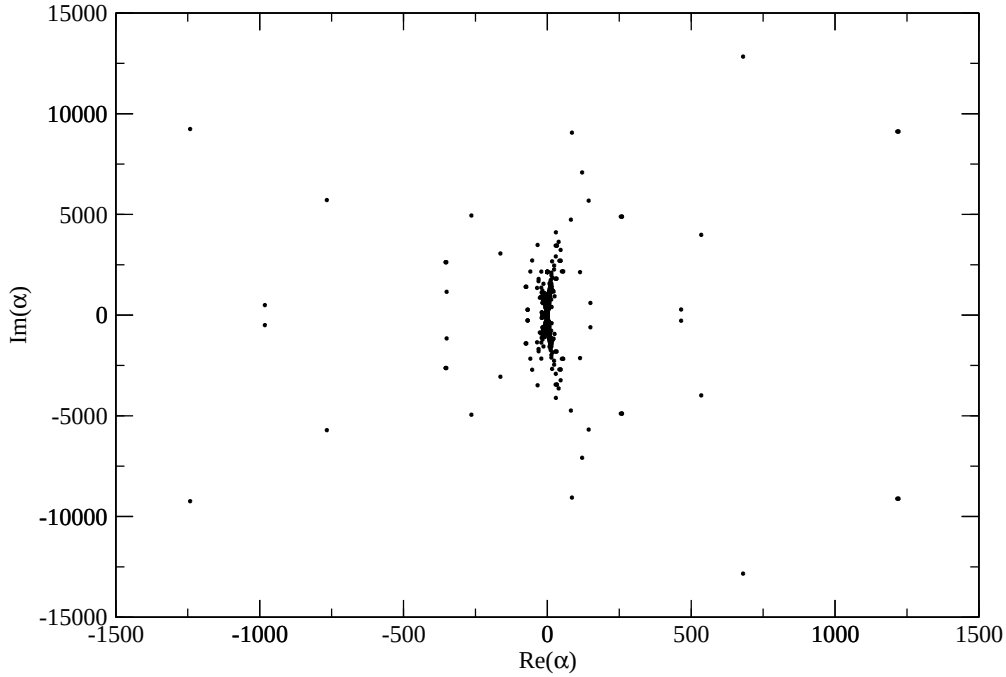

(a) Full eigenvalue map showing all the calculated eigenvalues.

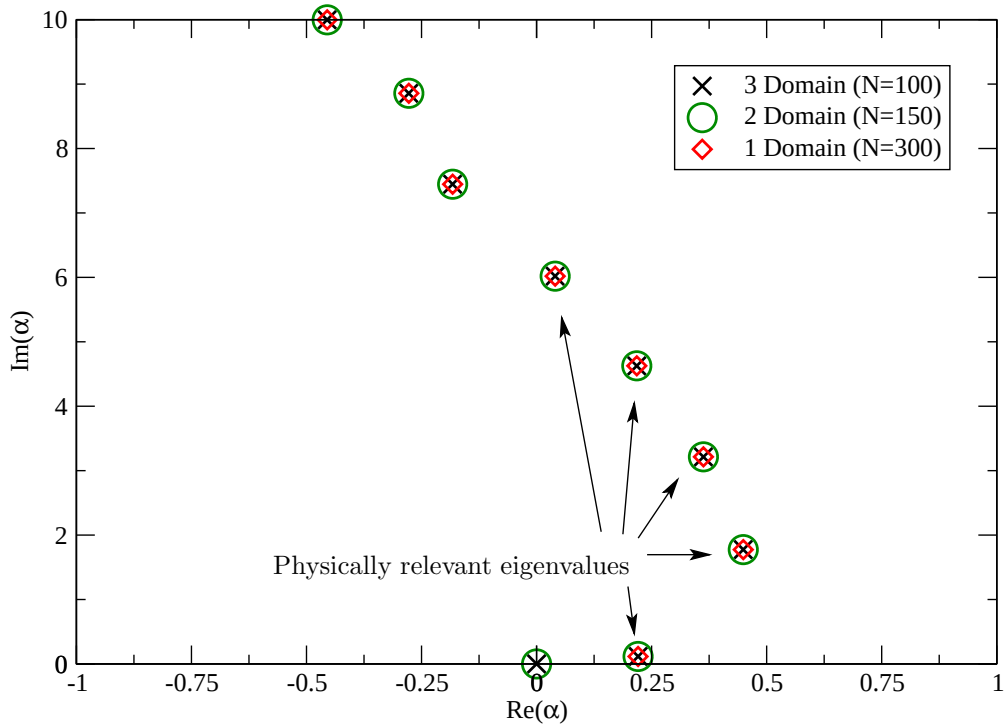

(b) Detail of the eigenvalue map for the 1, 2 and 3 domain techniques.

Figure 4.1: Eigenvalue map for the ideal gas problem with $\gamma = 1.2$, $\gamma\tilde{Q}/c_0^2 = \gamma\tilde{E}_a/c_0^2 = 50$, overdrive $f = 1.2$.

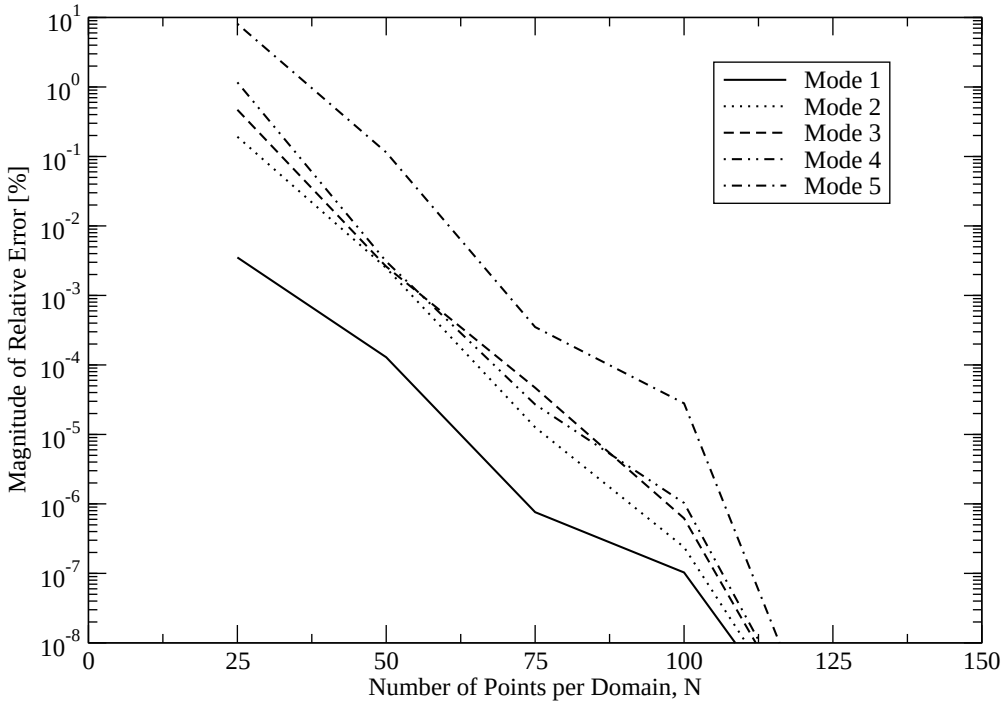

(a) Growth rate, Re(α).

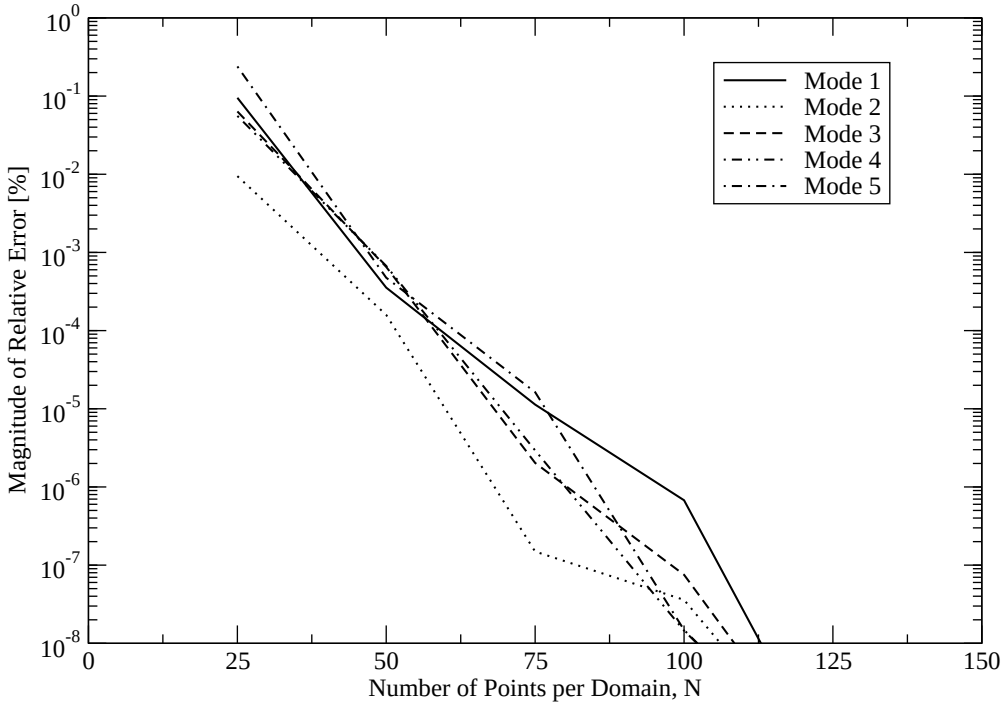

(b) Frequency, Im(α).

Figure 4.2: Error on (a) the growth rate and (a) frequency for the 3-domain method with N points per domain. The errors are computed with respect with the $N = 125$ solution.

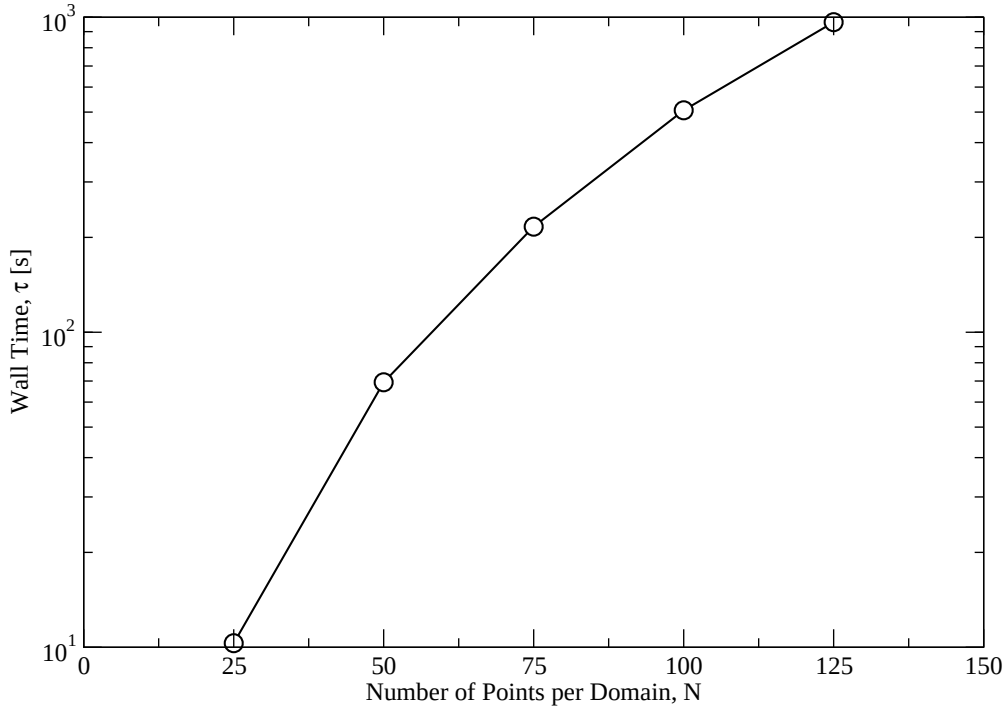

Figure 4.3: Execution wall time for the 3-domain method with N points per domain.

a shifting of the location of maximum reaction rate towards the lead shock wave. This behaviour is akin to a reduction of the induction zone length when compared to the reaction zone length, which is known to lead to a more stable wave.

4.6.2 Variation in a_s

Here, a_s is varied while keeping $a_g = 0.02$ constant. The values of $\Gamma_s = \Gamma_g = 0.2$ are held constant. The same behaviour as for the single phase SG EOS above is observed. The system is more unstable for lower values of a_s and more stable for higher values of a_s as seen from the eigenvalue map in fig 4.6. From the profiles of fig 4.7, the CJ state is seen to remain constant while the shock state corresponds to lower pressures, lower densities, higher velocities and higher shock temperatures. From fig 4.7(d), the initial reaction rate is seen to increase at the shock front and the location of the maximum reaction reaction rate again shifts closer to the lead shock for increased values of a_s. This effective reduction in induction zone length again corresponds to a more stable wave.

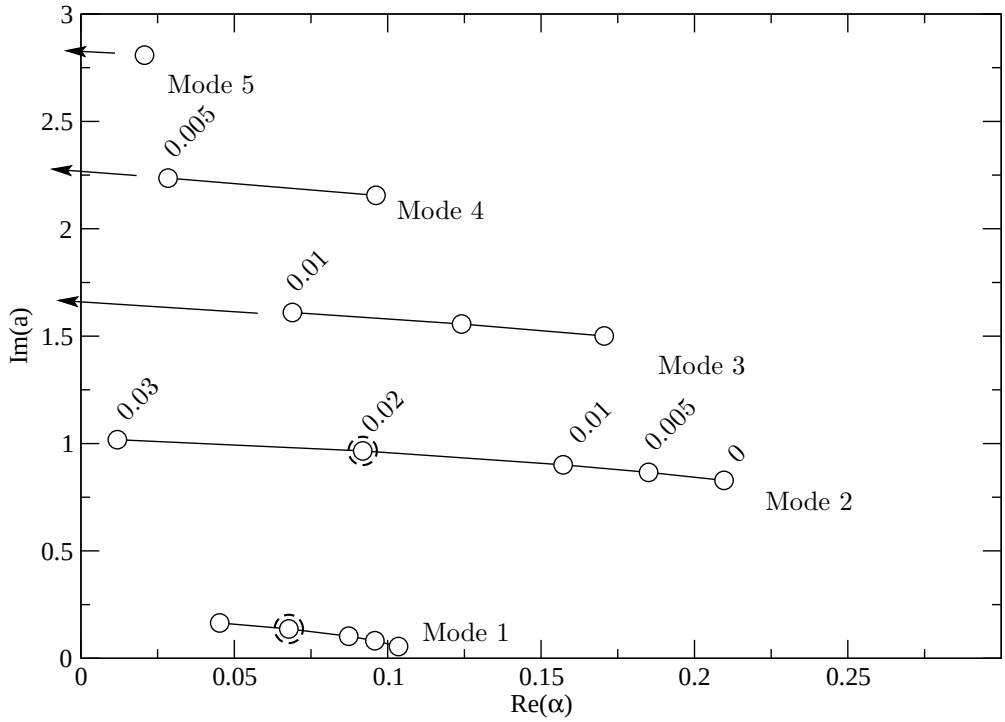

Figure 4.4: Map of eigenvalues for the case $\Gamma_s = \Gamma_g = 0.2$, $a_s = a_g = a$. The reference eigenvalues to which the following calculations are compared are indicated by the broken circles.

4.6.3 Variation in a_g

Fig 4.8 shows the variation in the growth rate and frequency of the eigenvalues for variations in a_g. Note the reduced scales on the eigenvalue maps. For variations of a_g while keeping a_s constant, no new unstable modes appear and the change in the eigenvalues is modest even for variations of a_s on the same order (0–0.03) as the variation of a_s described in the previous sections. Hence, most of the effect of changing a_s and a_g on the stability of the wave can be thought of as coming from the change in initial sound speed. The initial sound speed increase for a fixed detonation speed leads to a lower Mach number wave, which implies an effectively lower heat release. Lowering the heat release of a detonation is known to stabilize a detonation wave. The increased value of a_g results in a change in the CJ state and an essentially minor change in the VN state. The effect on the reaction rate is minimal as the influence of the Arrhenius dependence is most felt when the depletion term $(1 - y_p)^\nu$ is of order 1 at the lead shock.

4.6.4 Variation in Γ_g

When varying Γ_g in the range of 0.15–0.4 while keeping all other parameters constant, i.e. $a_s = a_g = 0.02$ and $\Gamma_s = 0.2$, the net effect is a more stable the wave with increasing Γ_g. As seen in the eigenvalue map

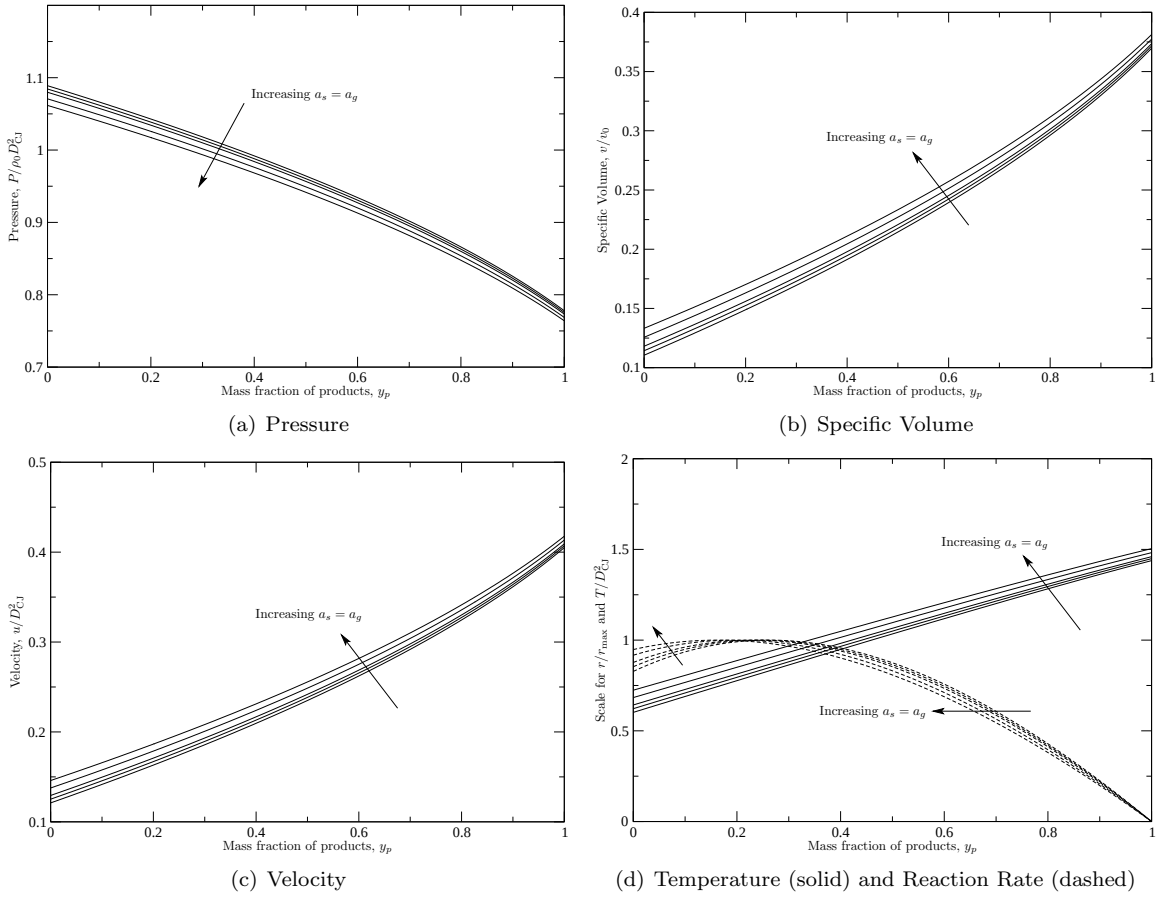

(a) Pressure

(b) Specific Volume

(c) Velocity

(d) Temperature (solid) and Reaction Rate (dashed)

Figure 4.5: Profiles of (a) pressure, (b) specific volume, (c) velocity and (d) temperature and reaction rate through the reaction zone for the case $\Gamma_s = \Gamma_g = 0.2$ and $a_s = a_g = a$. Arrows indicate the direction of increasing a. The profiles are calculated for $a = 0$, 0.005, 0.01, 0.02 and 0.03.

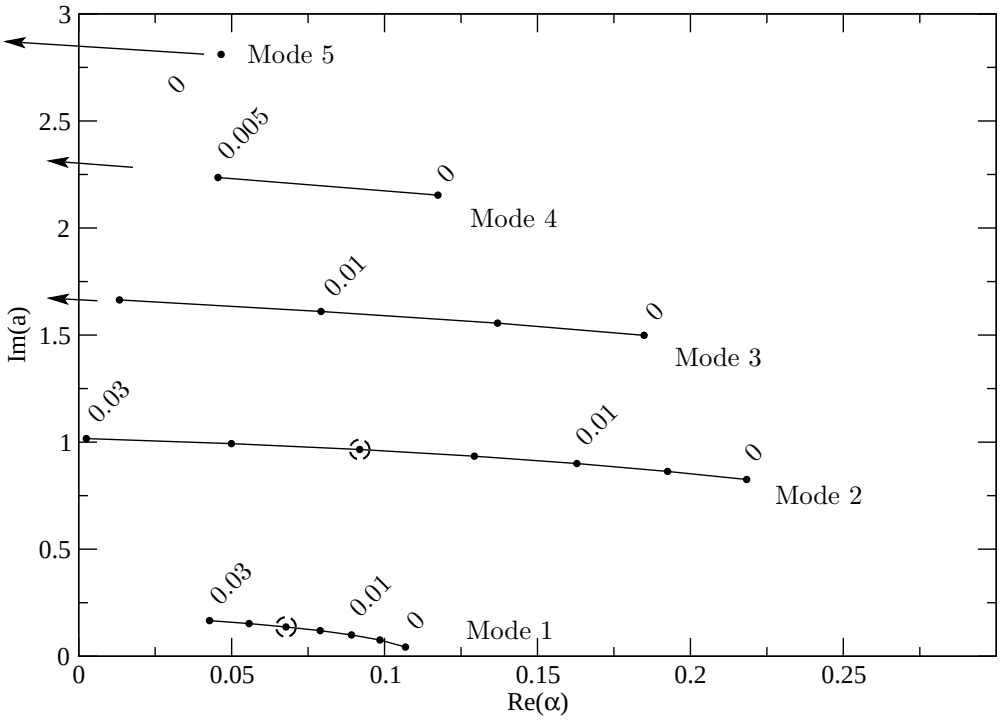

Figure 4.6: Map of eigenvalues for the case $\Gamma_s = \Gamma_g = 0.2$, $a_g = 0.02$. The reference eigenvalues of the case $a_g = a_s = 0.02$ are shown by the broken circles. Eigenvalues are computed for $a_s = 0$, 0.005, 0.01, 0.015, 0.02, 0.025 and 0.03.

shown in fig 4.10, the two higher modes quickly become stable. The lowest mode, while initially exhibiting a higher growth rate with higher Γ_g, its behaviour changes and it becomes more stable. The profiles shown in fig 4.11 and specifically the reaction rate profiles (fig 4.11(d)) show a shift of the reaction rate maximum towards the leading front until the maximum reaction rate occurs at the lead shock.

4.6.5 Variation in Γ_s

The behaviour of the eigenvalues see on the map (fig 4.12) clearly suggests a more stable wave with increasing Γ_s. The reaction rate profiles, on the other hand, show a shift in the location of the maximum reaction rate from the lead shock wave towards the back of the wave for increasing values of Γ_s (fig 4.13(d)). The retreating location of the maximum reaction rate is akin to a lengthening of the induction time, which would be expected to stabilize the wave. However, there is marked change in the behaviour of pressure, volume and most importantly velocity (figs 4.13(a)–4.13(c)) for a change in Γ_s. Comparable changes were not observed when varying a_s, a_g or Γ_g. This change in behaviour affects the thickness of the reaction zone. The thickness of the detonation wave can be obtained by integrating

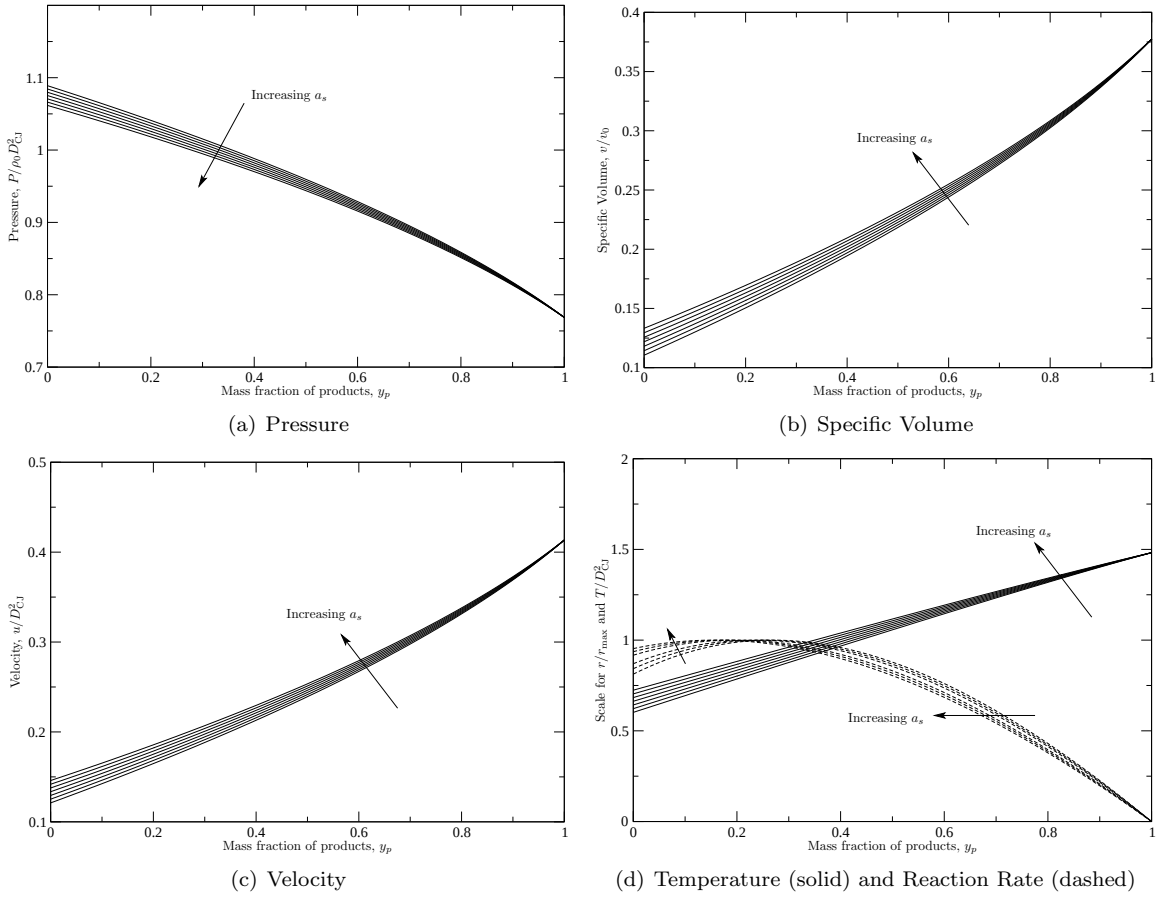

(a) Pressure

(b) Specific Volume

(c) Velocity

(d) Temperature (solid) and Reaction Rate (dashed)

Figure 4.7: Profiles of (a) pressure, (b) specific folume, (c) velocity and (d) temperature and reaction rate through the reaction zone for the case $\Gamma_s = \Gamma_g = 0.2$ and $a_g = 0.02$. Arrows indicate the direction of increasing a_s. The profiles are calculated for $a_s = 0$, 0.005, 0.01, 0.015, 0.02, 0.025 and 0.03.

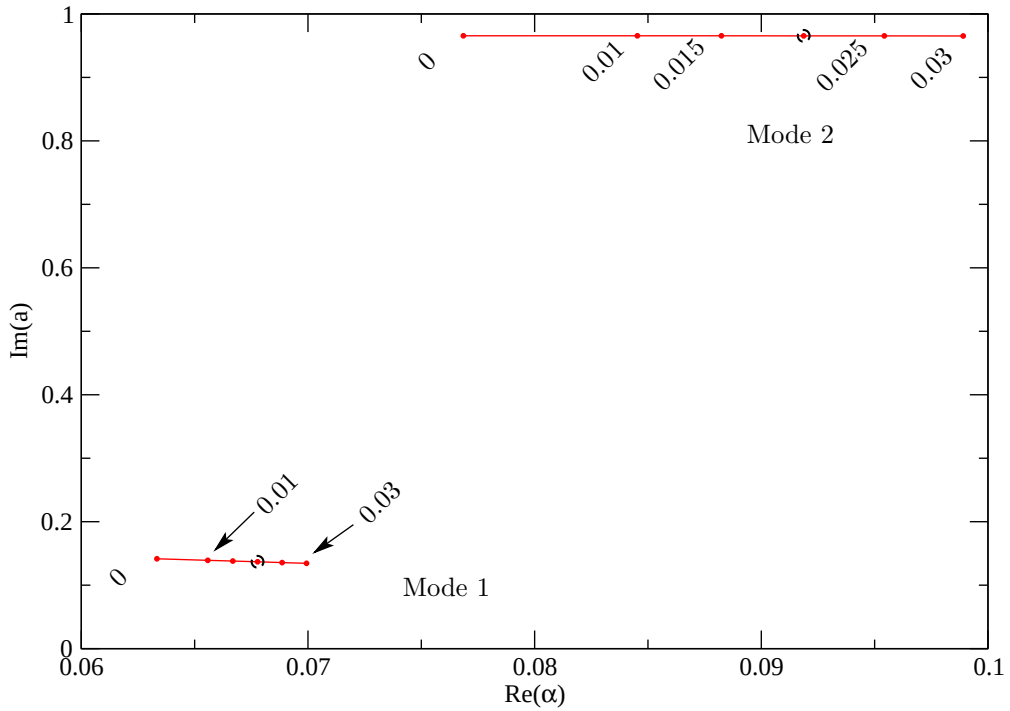

Figure 4.8: Map of eigenvalues for the case $\Gamma_s = \Gamma_g = 0.2$, $a_s = 0.02$. The reference eigenvalues of the case $a_g = a_s = 0.02$ are shown by the broken circles. Eigenvalues are computed for $a_g = 0$, 0.01, 0.015, 0.02, 0.025 and 0.03. Note the reduced scale of Re(α).

$$\frac{u}{du/dy_p} du = r dx. \tag{4.50}$$

Looking at fig 4.13(c) yields insight into the thickness of the wave. For low values of Γ_s, the slope du/dy_p increases near the back of the wave, which means the thickness there is compressed in physical space when compared to y_p space. For high values of Γ_s, the slope du/dy_p is small near $y_p = 1$, which suggests the wave thickness is expanded in physical space when compared to y_p space. Hence, while the effective induction time grows for increasing values of Γ_s, the increased wave thickness means the reaction zone also elongates, such that the effective ratio of $L_{\text{induction}}/L_{\text{reaction}}$ is still small and the wave stabilizes. The reaction rate is shown in fig 4.14 against the extent of reaction in physical space x rather than y_p space. The reaction zone for the case of $\Gamma_s = 0.35$ is indeed longer than that of $\Gamma_s = 0.15$.

4.6.6 Variation in C_{vs}/C_{vg}

The ratio of specific heats $\chi = C_{vs}/C_{vg}$ was varied between the estimated bounds of chapter 3, 0.3–3.0. Shown in fig 4.15 are the eigenvalues for 4 of the 5 cases studied. For the lowest value of $\chi = 0.3$, the wave was stable. The profiles of pressure, specific volume and velocity are independent of χ and are shown in

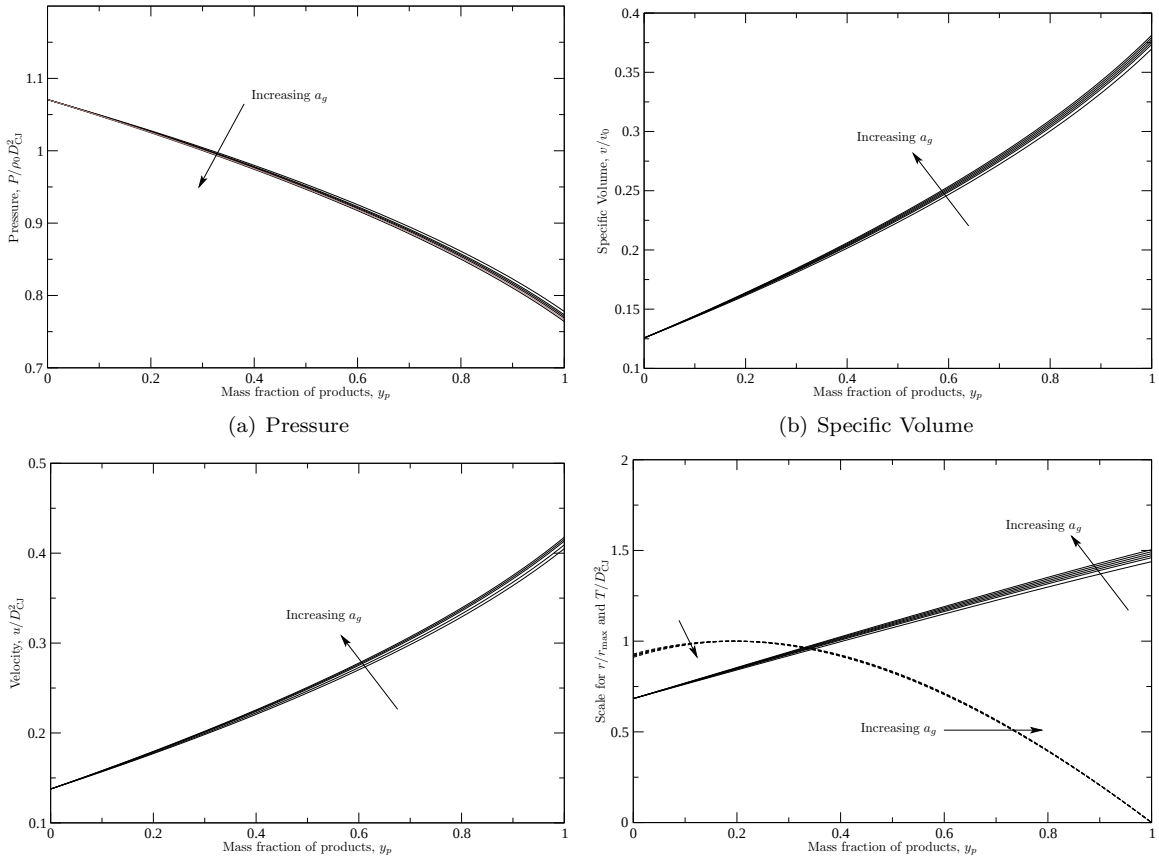

(a) Pressure

(b) Specific Volume

(c) Velocity

(d) Temperature (solid) and Reaction Rate (dashed)

Figure 4.9: Profiles of (a) pressure, (b) specific volume, (c) velocity and (d) temperature and reaction rate through the reaction zone for the case $\Gamma_s = \Gamma_g = 0.2$ and $a_s = 0.02$. Arrows indicate the direction of increasing a_g. The profiles are calculated for $a_g = 0$, 0.01, 0.015, 0.02, 0.025 and 0.03.

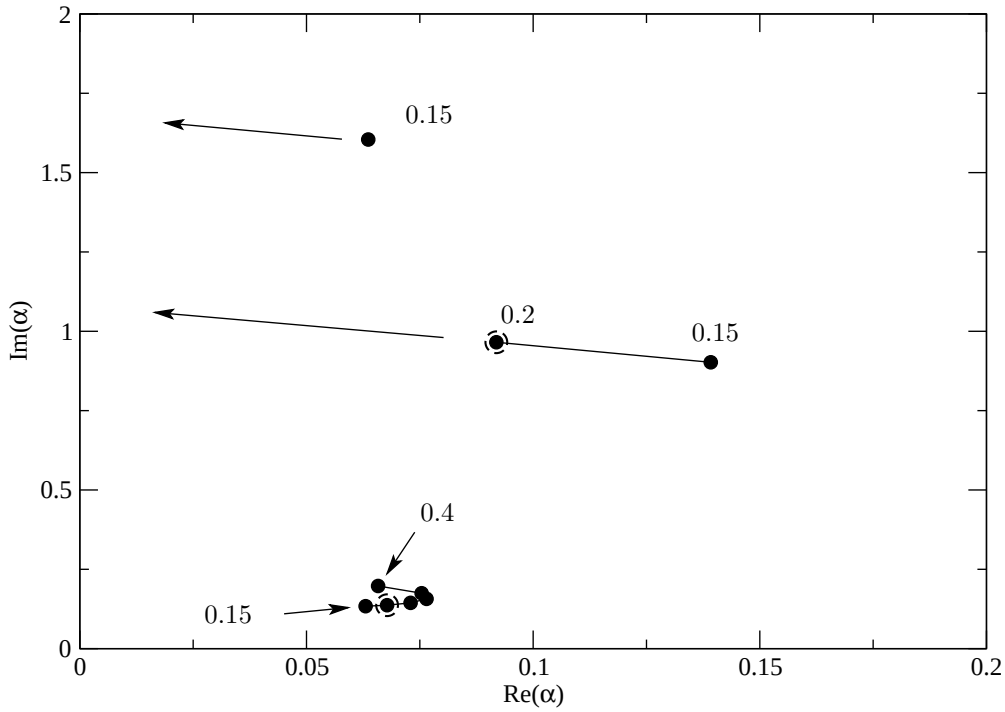

Figure 4.10: Map of eigenvalues for the case $\Gamma_s = 0.2$, $a_s = a_g = 0.02$. The reference eigenvalues of the case $\Gamma_g = \Gamma_s = 0.2$ are shown by the broken circles. Eigenvalues are computed for $\Gamma_g = 0.15$, 0.20, 0.25, 0.30, 0.35 and 0.40.

fig 4.16. The profiles of temperature along the reaction zone structure for different ratios χ are shown in fig 4.17. The temperature through the reaction zone actually drops for the case of $\chi = 0.3$, while all other values of χ exhibit increasing solid temperatures. The associated reaction rates are shown in fig 4.18. For $\chi < 0.6$, the reaction rate is maximum at the shock, while for higher values a maximum occurs within the reaction zone. Again, the receding location of the reaction rate maximum leads to a more unstable wave.

4.6.7 Variation in the Closure Condition

Perhaps the most important result in this series is the variation of the closure condition from P–T equilibrium to the $DS_s = 0$ closure condition. The stability of the base model $a_s = a_g = 0.02$, $\Gamma_s = \Gamma_g = 0.2$ with $f = 1.2$ was calculated with the $DS_s = 0$ closure closure condition and found to be 1D stable. The stability for different values of the activation energy $0.2 \leq \theta \leq 40$ were calculated. The non-dimensional activation energy of the base case is $\theta = 1.078$ in the DSD scale. The studied range thus corresponds to an increasing and decreasing change of an order of magnitude in θ. All calculations resulted in stable waves. This behaviour of the model with $DS_s = 0$ closure condition can be explained by observing the behaviour of temperature in the reaction zone. As shown in section 4.4.2, the temperature of the solid phase T_s is a function of only

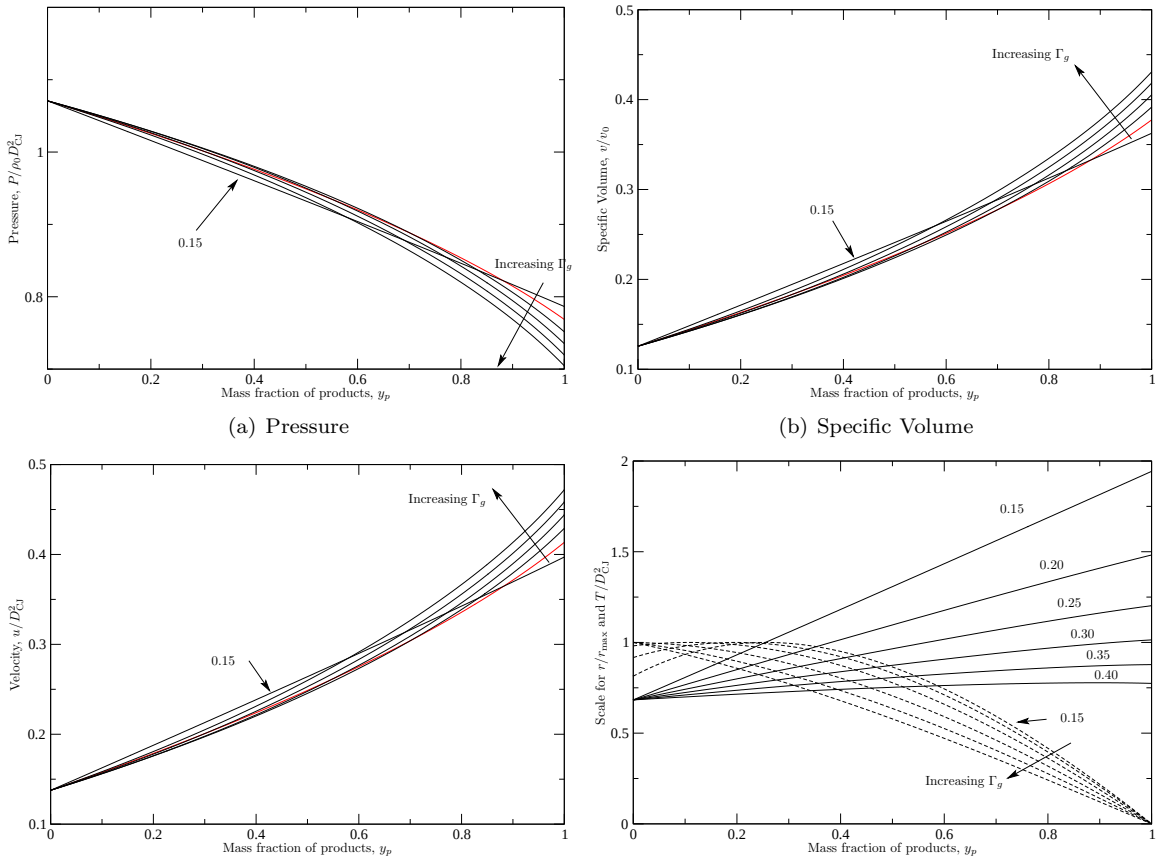

(a) Pressure

(b) Specific Volume

(c) Velocity

(d) Temperature (solid) and Reaction Rate (dashed)

Figure 4.11: Profiles of (a) pressure, (b) specific volume, (c) velocity and (d) temperature and reaction rate through the reaction zone for the case $\Gamma_s = 0.2$ and $a_g = a_s = 0.02$. Arrows indicate the direction of increasing Γ_g. The profiles are calculated for $\Gamma_g = 0.15$, 0.2, 0.25 and 0.3 and 0.35.

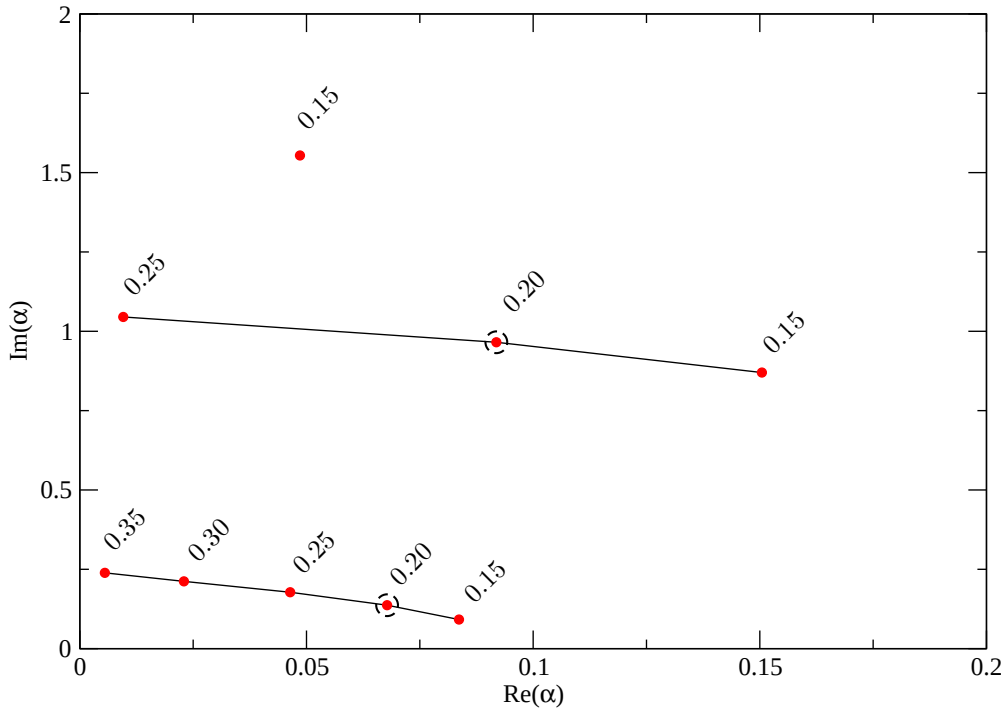

Figure 4.12: Map of eigenvalues for the case $\Gamma_g = 0.2$, $a_s = a_g = 0.02$. The reference eigenvalues of the case $\Gamma_g = \Gamma_s = 0.2$ are shown by the broken circles. Eigenvalues are computed for $\Gamma_s = 0.15$, 0.20, 0.25, 0.30 and 0.35.

the pressure P and both vary in the same direction. This result is expected as the assumption behind the $DS_s = 0$ closure condition is that the solid undergoes an isentropic process. As the pressure decreases through a ZND wave, the isentropic process is an expansion which results, for a well-behaved EOS, in a cooling of the material. The solid temperature must therefore cool through the reaction zone regardless of the reaction rate. This reaction zone profile is shown for the specific case studied here in fig 4.19(a) where the decreasing solid temperature is apparent. For the choice of $\Gamma_s = 0.2$, T_s is also a weak function of P. It can be shown that for $\Gamma_s \to \infty$, $T_s \propto P$, while for $\Gamma_s \to 0$, T_s asymptotes to a constant value throughout the reaction zone. The reaction rates associated with this reaction profile are shown in fig 4.19(b). The maximum reaction rate is always at the shock, leading to an effectively zero induction length wave regardless of activation energy. It is worth repeating that this behaviour is not a characteristic of the underlying SG EOS, but inherent to the $DS_s = 0$ closure condition. Unstable conditions would still be expected for a high enough value of θ, yet none were found here.

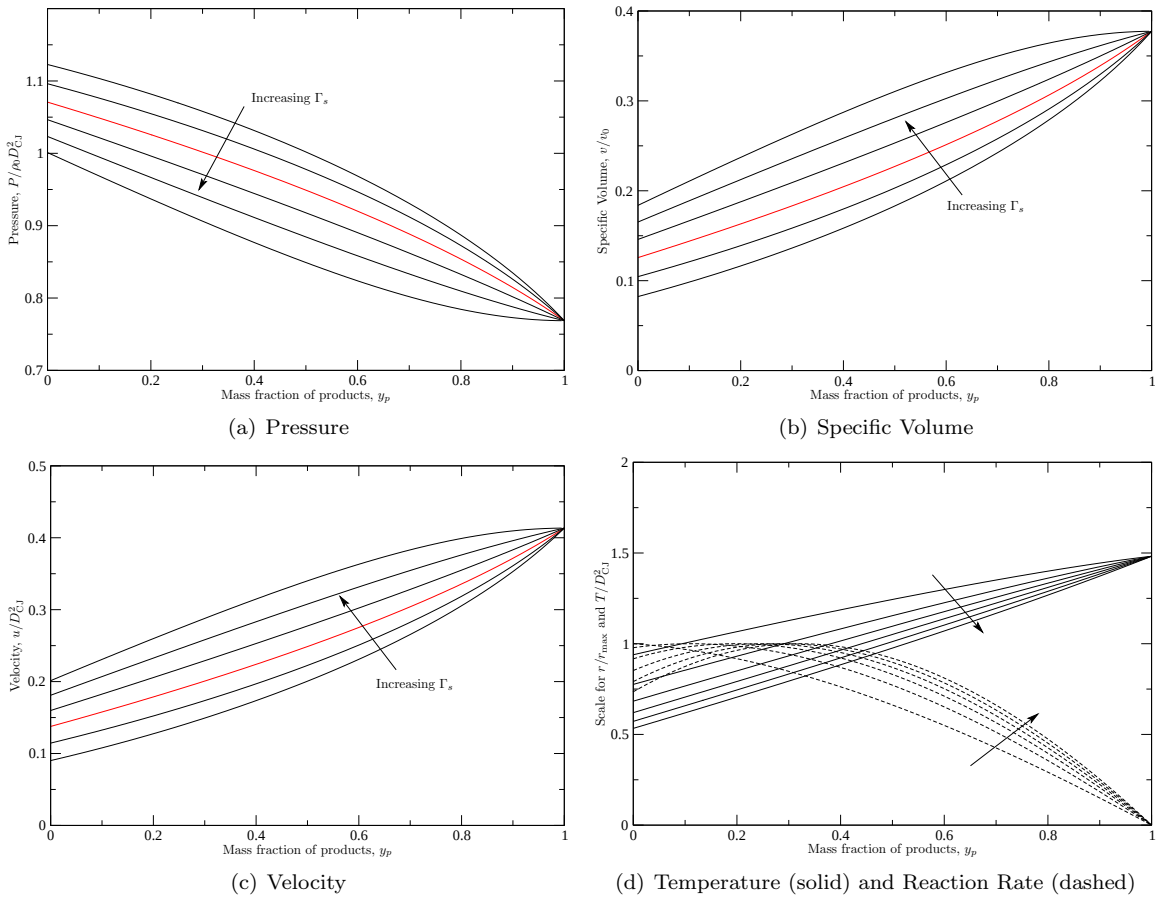

(a) Pressure

(b) Specific Volume

(c) Velocity

(d) Temperature (solid) and Reaction Rate (dashed)

Figure 4.13: Profiles of (a) pressure, (b) specific volume, (c) velocity and (d) temperature and reaction rate through the reaction zone for the case $\Gamma_g = 0.2$ and $a_g = a_s = 0.02$. Arrows indicate the direction of increasing Γ_s. The red curve is the reference case $\Gamma_s = \Gamma_g = 0.2$. The profiles are calculated for $\Gamma_s = 0.15$, 0.2, 0.25 and 0.3 and 0.35.

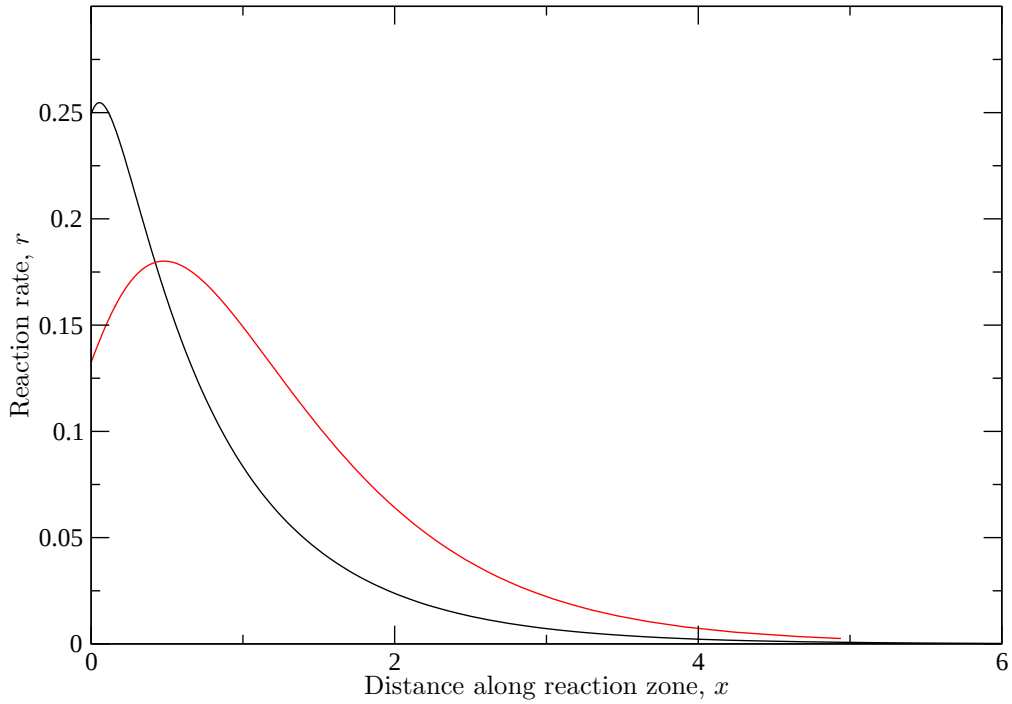

Figure 4.14: Reaction rate against reaction zone extent in physical x space for $\Gamma_s = 0.15$ (black) and $\Gamma_s = 0.35$ (red). The other parameters are $\Gamma_g = 0.2$ and $a_s = a_g = 0.02$ for both cases.

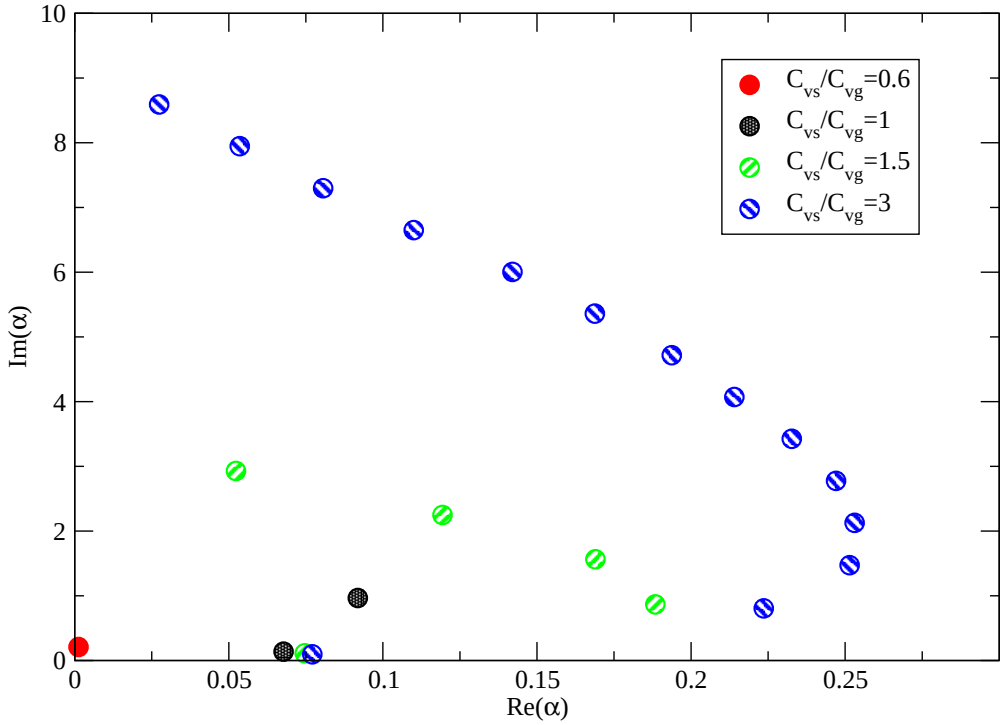

Figure 4.15: Eigenvalue map variation with the ratio C_{vs}/C_{vg} for the base case $a_s = a_g = 0.02$ and $\Gamma_s = \Gamma_g = 0.2$.

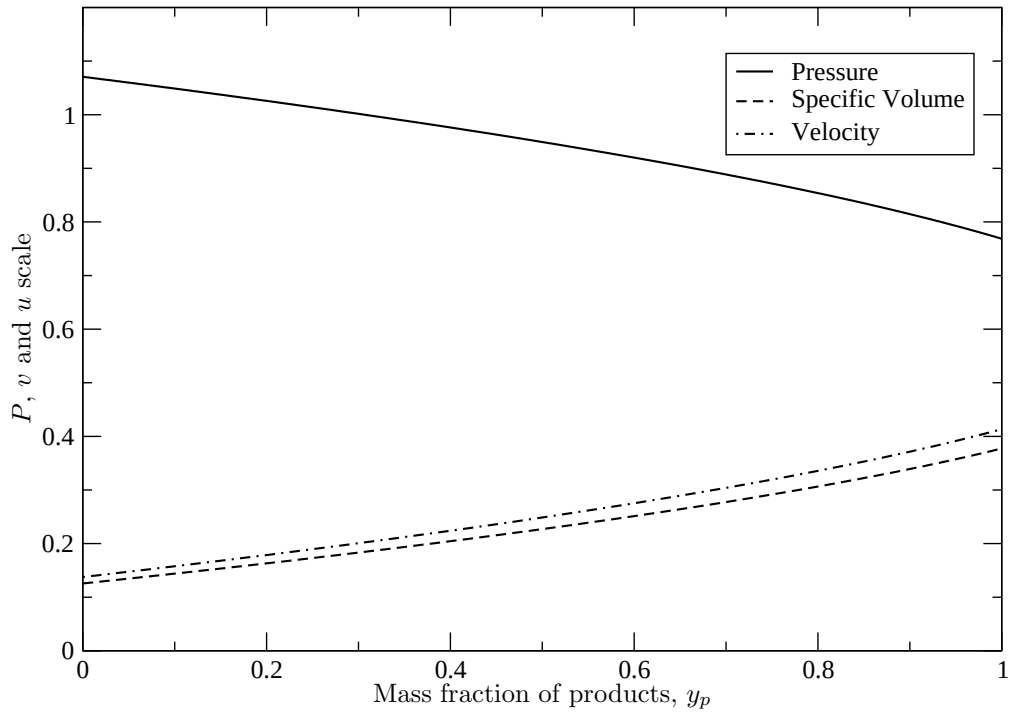

Figure 4.16: Profiles of pressure, specific volume and velocity in the ZND wave for the same base case as fig 4.15. The profiles are independent of C_{vs}/C_{vg}

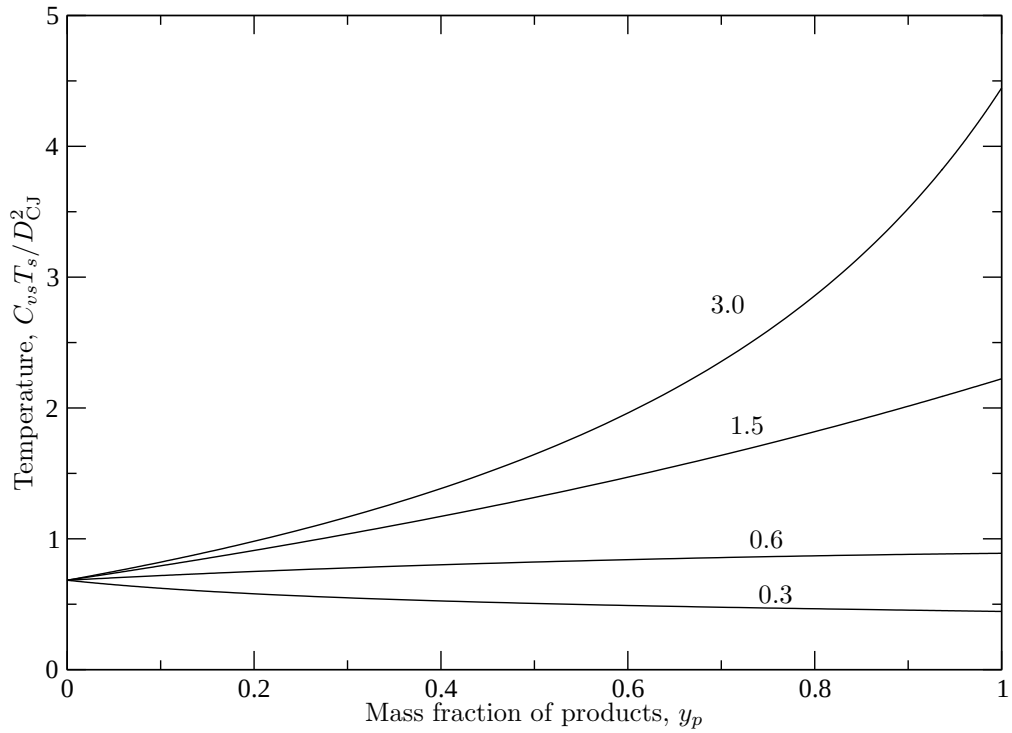

Figure 4.17: Temperature profiles for values of $C_{vs}/C_{vg} = 0.3$, 0.6, 1.5 and 3.0. The temperature profile for $C_{vs}/C_{vg} = 0.3$ is maximum at the lead shock.

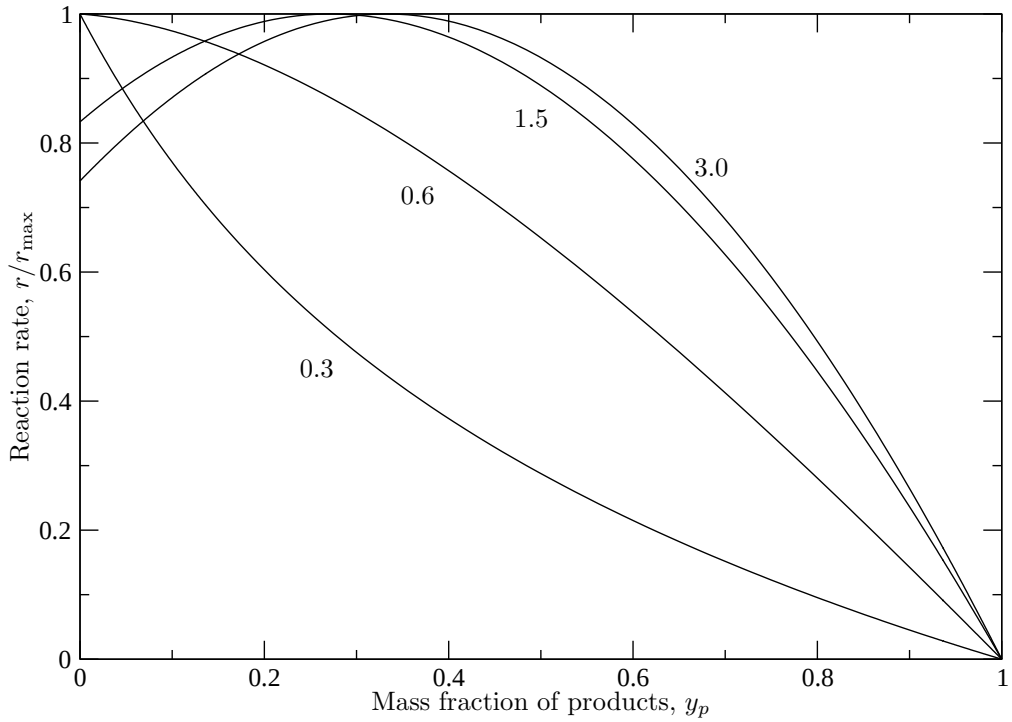

Figure 4.18: Normalized reaction rate profiles for values of $C_{vs}/C_{vg} = 0.3$, 0.6, 1.5 and 3.0. The reaction rate profiles for $C_{vs}/C_{vg} = 0.3$ and 0.6 are maximum at the lead shock.

4.6.8 Fitted Model of Chapter 3

The stability of the SSG model fitted in chapter 3 was evaluated here to determine whether the model predicts a stable or unstable wave. The chemical parameters used were those obtained after $N_g = 100$ generations of optimization. Both the P–T equilibrium and $DS_s = 0$ closure conditions were used. The resulting eigenvalue maps are shown in figs 4.20–4.21. To interpret the eigenvalue map, two approaches are used. First, the same calculation is run using two different resolutions of $N = 100$ and 200 points per domain. None of the eigenvalues with $\mathrm{Re}(\alpha) > 0$ are seen to converge, indicating that those modes present are in fact unphysical spurious modes. Also, the eigenfunctions were examined individually and all exhibited the very high frequency oscillations which are tell-tale signs of spurious modes. Thus, the SG EOS appears to predict stable waves in PBX 9502 regardless of the closure condition of the model.

4.7 Summary

The 1D stability behaviour of a multi-component model based on the SG EOS was investigated for the first time here and used the collocation solving methodology. Increasing a_s was found to have a stabilizing effect (in agreement with previous studies of the single SG EOS [74]). A decrease of the parameter a_g was found

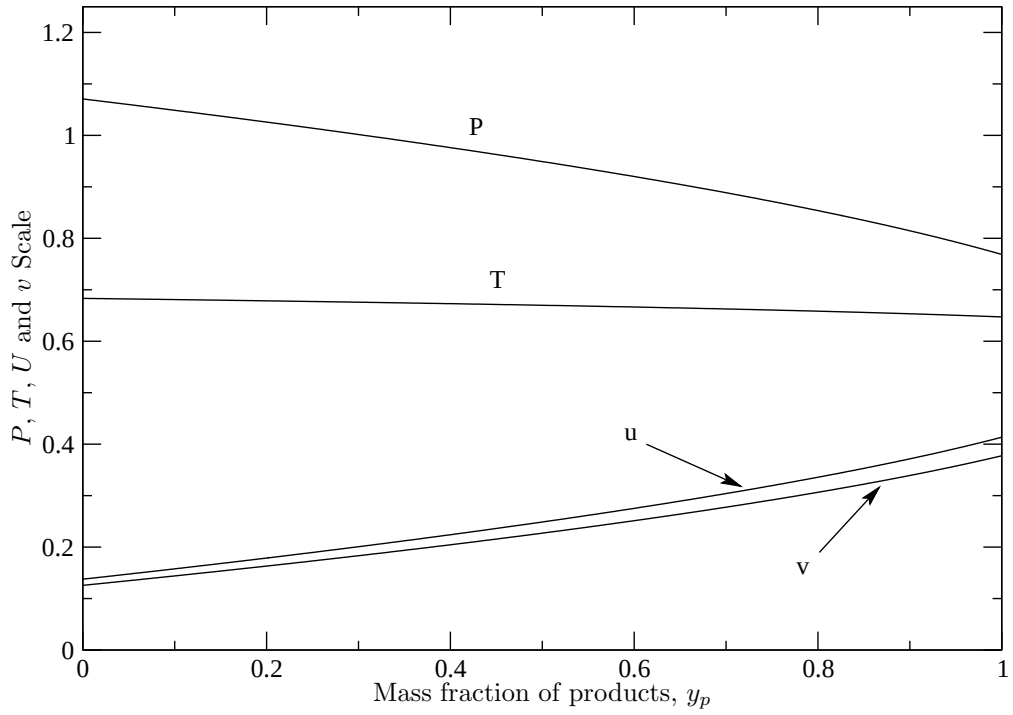

(a) Reaction Profile

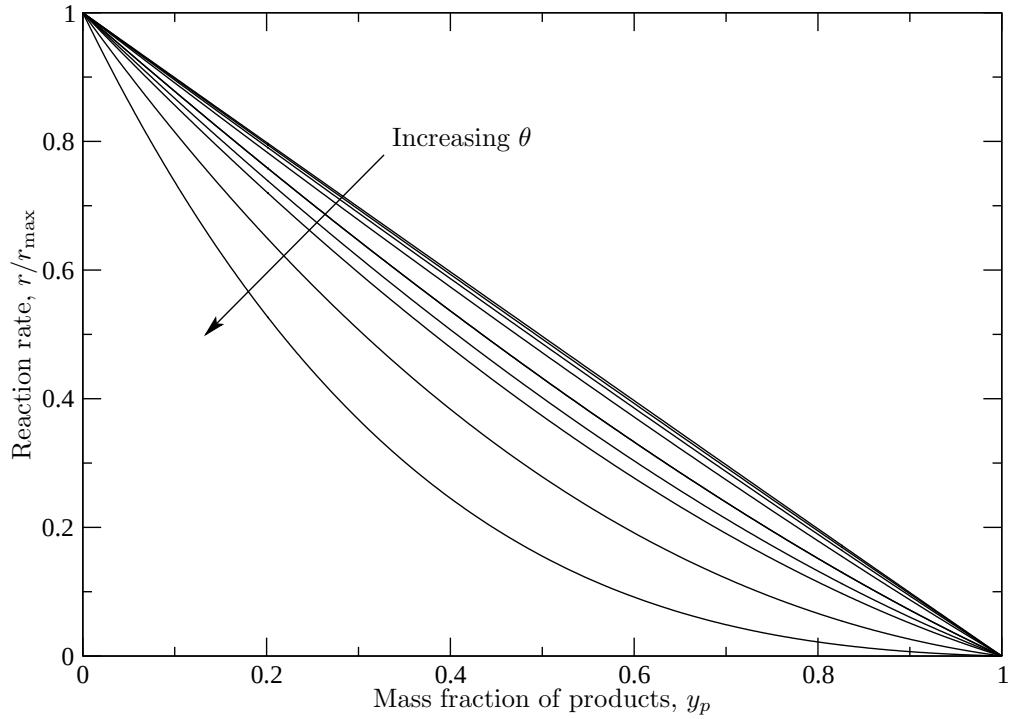

(b) Reaction Rate

Figure 4.19: Reaction profiles of pressure, specific volume, velocity and $C_{vs}T_s$ are shown in (a) for the $\Gamma_g = \Gamma_s = 0.2$, $a_s = a_g = 0.02$ model with the $DS_s = 0$ closure condition. Profiles of reaction rate are shown in (b) for activation energies $\theta = 0.2$, 0.5, 1, 2, 5, 10, 20 and 40.

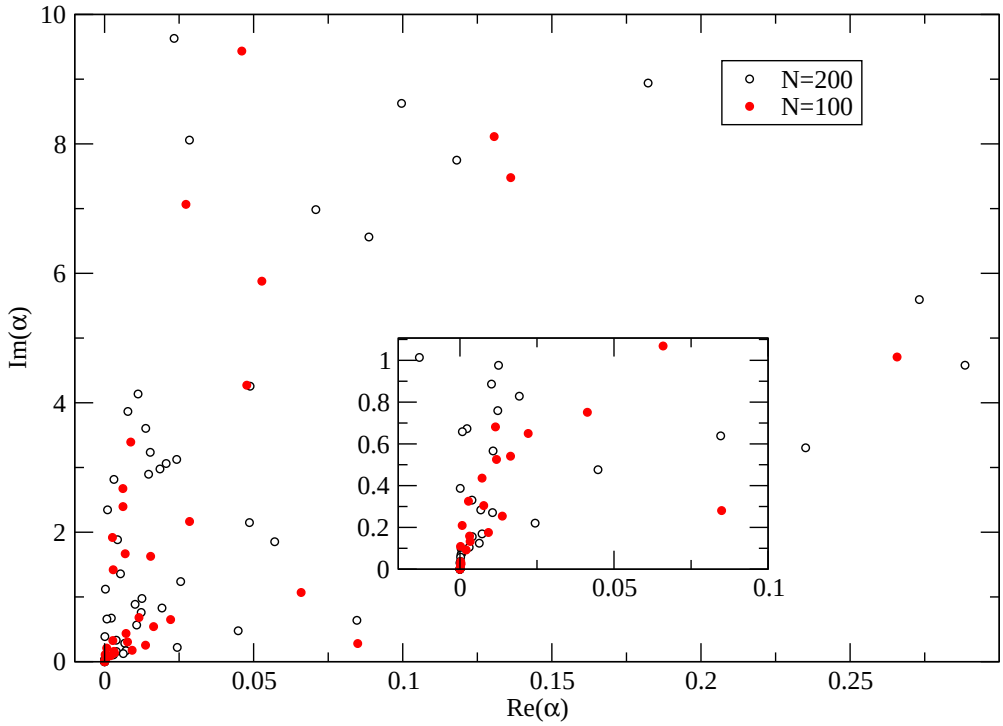

Figure 4.20: Eigenvalue map for the fitted SSG model of chapter 3. The closure condition is P–T equilibrium. The chemical parameters are those corresponding to the fit obtained after $N_g = 100$ generations.

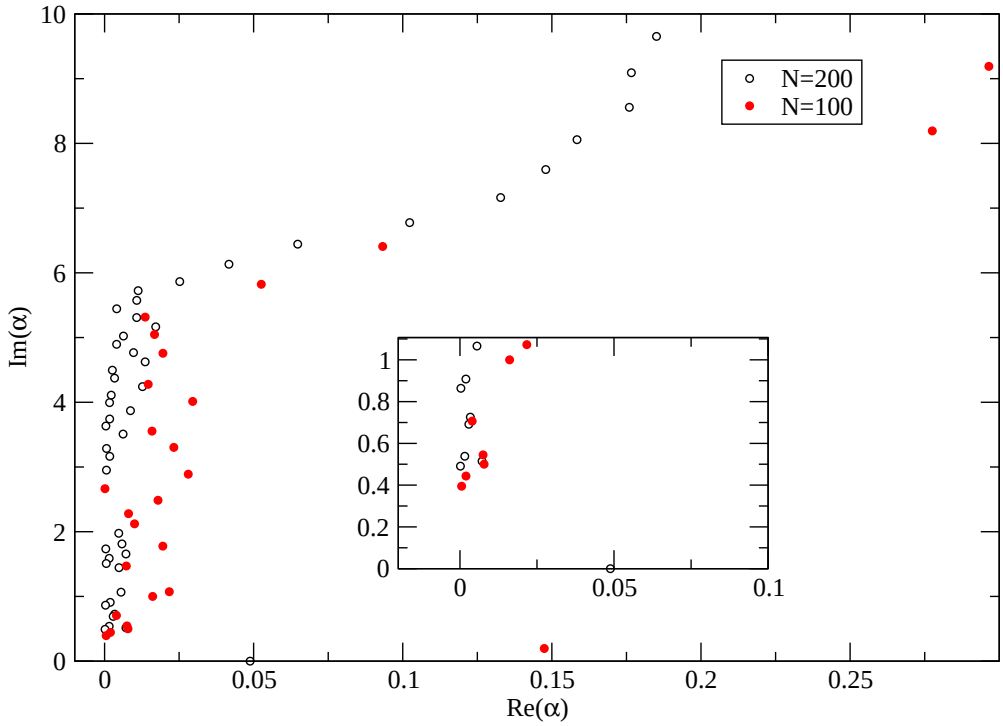

Figure 4.21: Eigenvalue map for the fitted SSG model of chapter 3. The closure condition is the $DS_s = 0$ closure condition. The chemical parameters are those corresponding to the fit obtained after $N_g = 100$ generations.

to have a stabilizing effect on the wave when all other parameters remained fixed. The influence of a_g was small when compared to the variations in the growth rate associated with variations of a_s. An increase in the value of Γ_s or Γ_g independently resulted in a more stable wave. An increase in the ratio of the specific heats C_{vs}/C_{vg} destabilized the wave. For the 2-step models fitted in chapter 3, the calculated eigenvalue maps had several spurious eigenvalues located near the origin but no unstable mode could be identified beyond the spurious modes generated by the pseudo-spectral collocation method and hence the fitted models are expected to be 1D stable.

Neutral stability boundaries would prove impractical when using the collocation method, especially when one takes into account the "sifting" of the eigenvalues that must occur and which is difficult to automate. A solving methodology which requires no initial guess and yet does not return a large number of unphysical, spurious eigenvalues would be beneficial. One proposition warrants being outlined here as a possible future numerical framework. The genetic DE algorithm used in chapter 3 to perform the chemical kinetic fitting of the SG EOS was shown to be an efficient method of solving minimization problems. The proposed method consists in solving the eigenvalue problem in much the same way as the shooting method but replaces the minimization algorithm (for example the Newton-Raphson algorithm of [67]) with the genetic DE algorithm. In its standard form, the DE algorithm stops iterating once a single solution has been found for which the residue is below a given threshold. In this case, the DE algorithm would have to be modified to observe, after every new generation is constructed, the grouping of the individuals. For multi-modal functions, the individuals in a population have been found to first migrate to the different local minima of the function before migrating to the global minimum [60, pages 45–47]. A sketch of the expected behavior for the detonation stability problem is shown in fig 4.22. The minimization termination criterion becomes the identification of all the local minima and a reasonable estimate of their location. Once the approximate location of the local minima have been found, the minimization problem can be split into individual problems, one for each of the local minima. Each minimum should correspond to one of the physically relevant eigenvalues of the stability problem.

The use of a genetic algorithm has several potential advantages. First, no guesses are required for the individual eigenvalues and only upper bounds on the maximum eigenvalue frequency and growth rate are required. Hence, only a minimum of knowledge about the system being studied is required. An eigenvalue can only be "missed" if these upper bounds are too low and overestimating the bounds is unlikely to affect the performance of the algorithm. Second, no spurious eigenvalues can be generated, unlike the spectral methods which generate mostly unphysical eigenvalues. Finally, the integration of the eigenfunction differential equations is independent of the search algorithm. Hence, adaptive refinement integration methods

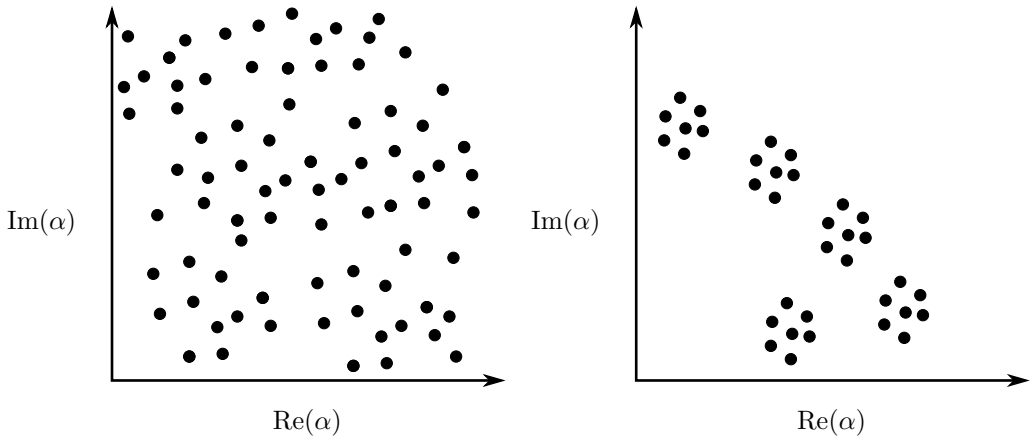

(a) Initial distribution of trial eigenvalues (b) After m iterations

Figure 4.22: Expected evolution of the trial eigenvalues when using a genetic algorithm to identify the unstable roots of the linear stability problem.

could be used to account for eigenfunctions which exhibit high oscillations. The performance of the search algorithm is also not tied to the accuracy of the eigenfunction integration. The use of genetic algorithms thus could show great promise for the implementation of the detonation stability problem to a general EOS and reaction rate.

Chapter 5

Unstable Detonation Propagation Under the Absence of Conventional Mach Reflection Structures

5.1 Introduction

Knowledge of the non-linear structure of propagating detonation waves is important to predicting certain aspects of detonation behaviour. For instance, the wave structure may influence the initiation and failure characteristics of detonation waves as is the case for gaseous detonation waves. The cellular detonation structure present in gaseous mixtures consists of a lead shock wave intersected by transverse shock waves. The points of intersection are the triple points where three shocks meet. Different regimes for cellular detonations have been identified depending on the mixture composition, the so-called regular and irregular mixtures. The behaviour of regular and irregular detonations are markedly different in the same type of experiments and correlations of different parameters with the cell size (or transverse wave spacing) are not universal. A notable example is the minimum tube diameter required for a detonation to successfully transition to an open space [83, 84].

Solid explosives are characterized by high sound speeds at room conditions. Those high initial sound speeds lead to low Mach number waves. To date, there is also no evidence of a gas-detonation like front structure in condensed explosives. The shock shapes exhibit a smooth front (see for example fig 6.13a later for the shock shape associated with the PETN based Detasheet) and measurements of velocity through the reaction zone using interferometry techniques show no clear evidence of oscillations due to wave instabilities in various materials like HMX [85], nitromethane [86] and TATB [87] . Low Mach number oblique shocks are known not to accept the conventional Mach reflection (MR) structure [21]. Despite the impossibility of the MR structure, experimental and numerical studies have observed MR-like structures in low Mach number flows, the so-called *von Neumann paradox* [88, 89, 22, 90].

Using the SG EOS, it is possible to model a detonable substance with a high enough initial sound speed to lower the detonation Mach number to a value close to unity. Shown in fig 5.1 is the initial sound speed and Mach number of a flow for a generic fluid with $\Gamma = 0.6$ and an incoming flow velocity of $u_0 = 7$ km/s. The initial sound speed of the material quickly increases to values comparable to the incoming flow velocity

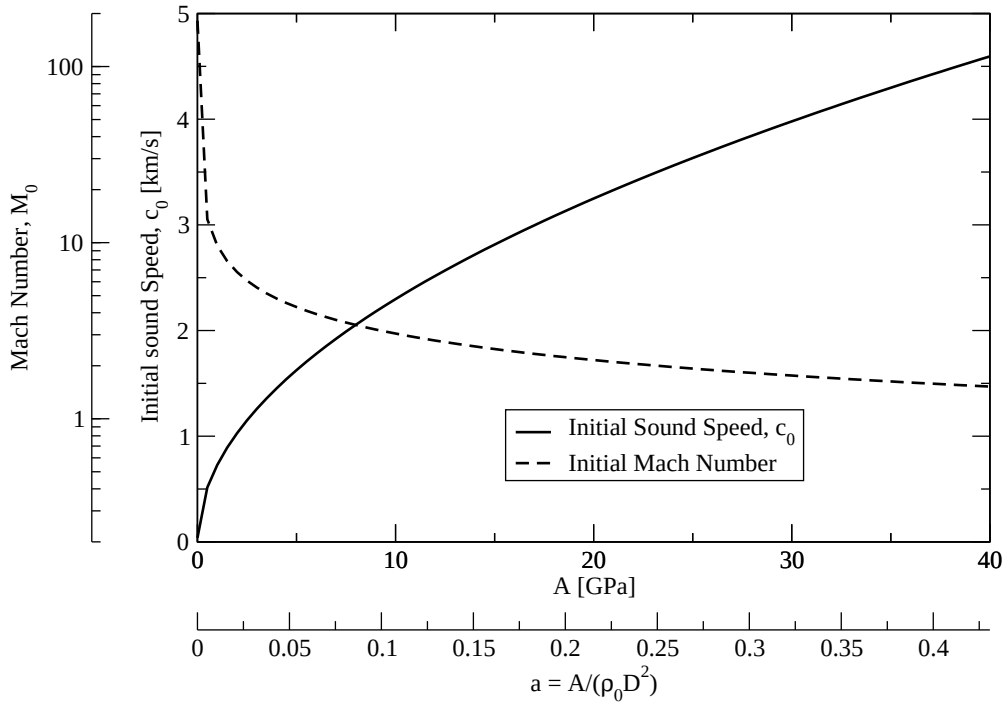

Figure 5.1: Variation of the initial sound speed, c_0, and Mach number, M_0, against A for a SG EOS with $\Gamma = 0.6$, $\rho_0 = 1.895$ g/cc and at $P_0 = 1$ atm.

causing a rapid decrease of the Mach number. With low detonation Mach numbers, conventional Mach reflections are impossible and along with them the classical cellular structure of gaseous detonation waves.

While not proposing to resolve the von Neumann paradox, the following question is asked: If waves in solid explosives are unstable and if the detonation Mach number is too low to allow the conventional MR structure, what would the resulting non-linear wave structure look like? Here, the detonation wave structure under conditions of low initial Mach number is examined for the first time in the context of a non-ideal EOS, in this case using the single-phase SG EOS described in previous chapters. Parameters representing a generic high explosives are chosen and not necessarily fitted to a particular material in order to cover a range of shock reflection regimes. The conditions under which this EOS will or will not allow different self-similar reflection patterns are examined. Finally, 2D propagating detonation waves are examined numerically.

5.2 Two-Dimensional Flow Relations

Steady, self-similar, two-dimensional, supersonic flow solutions can consist of an arrangement of oblique or normal shocks, oblique detonation waves and Prandtl-Meyer (PM) expansion fans. The particular topology of a flow pattern is found by matching pressure and flow angle across contact discontinuities. First, the 2D

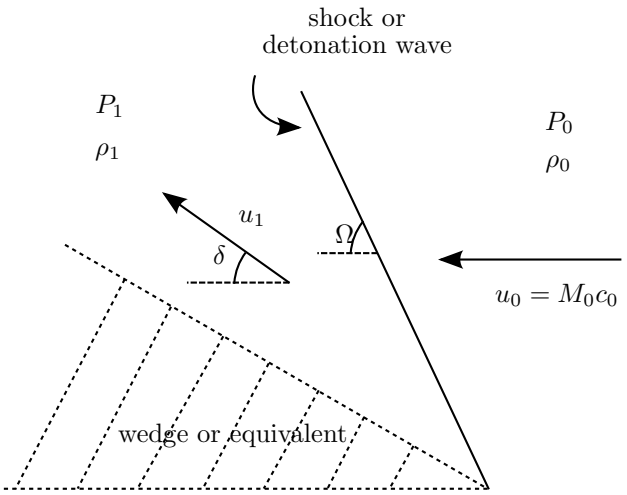

Figure 5.2: Shock polar problem setup.

steady flow relations for shocks detonation waves and PM expansions are generalized to the SG EOS. In the case of $A \to 0$, the relations reduce to those applicable to an ideal gas.

5.2.1 Oblique Shock and Oblique Detonation Relations

Oblique shock waves have been studied in depth and the shock polar relations are well understood (see for example [91]). Oblique detonation waves consist of a detonation wave stabilized in an overdriven flow $f = M_{0n}^2/M_{\mathrm{CJ}}^2 \geq 1$ [92, 84]. The polar relations of both are found in a similar fashion. The conservation laws across a control volume encompassing the shock or detonation wave yield

$$\rho_0 u_{0n} = \rho_1 u_{1n}, \tag{5.1}$$

$$P_0 + \rho_0 u_{0n}^2 = P_1 + \rho_1 u_{1n}^2, \tag{5.2}$$

$$u_{0t} = u_{1t}, \tag{5.3}$$

$$h_0 + \frac{u_{0n}^2}{2} = h_1 + \frac{u_{1n}^2}{2}, \tag{5.4}$$

where u_{in} is the wave-normal velocity and u_{it} is the velocity tangential to the wave. The different parameters relevant to the problem of oblique shocks and detonations are sketched in fig 5.2. The velocities are related

by

$$u_{0n} = u_0 \sin(\Omega), \tag{5.5}$$

$$u_{0t} = u_0 \cos(\Omega), \tag{5.6}$$

$$u_{1n} = u_1 \sin(\Omega - \delta), \tag{5.7}$$

$$u_{1t} = u_1 \cos(\Omega - \delta). \tag{5.8}$$

The enthalpy for a single phase SG EOS is given by

$$h = \frac{(\Gamma + 1)\, P + A}{\rho \Gamma} - \lambda Q, \tag{5.9}$$

where $\lambda_0 = 0$ for both the shock and detonation wave and $\lambda_1 = 0$ for an oblique shock and 1 for an oblique detonation wave. The two parameters which control the flow conditions are the incoming velocity u_0 (or equivalently M_0) and the wave angle Ω. The flow deflection angle δ could also be used instead of either of the previous 2 variables. Upon solving for the density ratio, $\rho_1/\rho_0 = x$, the pressure ratio, $P_1/P_0 = y$, the deflection angle δ and the post-shock Mach number, M_1, the oblique shock relations are found to be

$$x = \frac{\rho_1}{\rho_0} = \frac{(2 + \Gamma)\, M_0^2 \sin^2 \Omega}{2 + \Gamma M_0^2 \sin^2 \Omega} \tag{5.10}$$

$$y = \frac{P_1}{P_0} = 1 + \frac{2}{\Gamma + 2} \left(\Gamma + 1 + \frac{A}{P_0} \right) \left(M_0^2 \sin^2 \Omega - 1 \right) \tag{5.11}$$

$$\tan \delta = \frac{(M_0^2 \sin^2 \Omega - 1) \cot \Omega}{\frac{\Gamma+2}{2} M_0^2 - M_0^2 \sin^2 \Omega + 1} \tag{5.12}$$

$$M_{1N}^2 = M_1^2 \sin^2(\Omega - \delta) = \frac{\Gamma M_0^2 \sin^2 \Omega + 2}{2(\Gamma + 1) M_0^2 \sin^2 \Omega - \Gamma}. \tag{5.13}$$

The only relation which explicitly contains the pressure offset, A, is the pressure ratio. All other relations are identical to those of a perfect gas, and depend on the parameter A only through M_0. In other words, the main effect of an increasing value of A is to increase the initial sound speed and therefore decrease the Mach number for a constant incoming velocity u_0. The oblique detonation relations are found in a similar

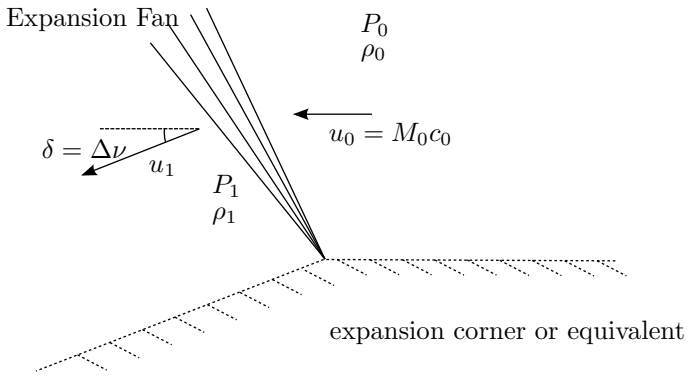

Figure 5.3: Expansion fan problem setup.

fashion

$$x = \frac{1 + (\Gamma+1)\, M_0^2 \sin^2\Omega + \sqrt{\Delta(q)}}{2\,(1+q) + \Gamma M_0^2 \sin^2\Omega}, \tag{5.14}$$

$$y = 1 + (\Gamma + 1 + A/P_0)\, M_0^2 \sin^2\Omega \left(\frac{x-1}{x}\right), \tag{5.15}$$

$$\Delta(q) = 1 - 2\,[1 + (\Gamma+2)\, q]\, M_0^2 \sin^2\Omega + M_0^4 \sin^4\Omega, \tag{5.16}$$

$$q = \frac{\Gamma Q}{c_0^2} = \frac{\left(M_{\mathrm{CJ}}^2 - 1\right)^2}{2\,(\Gamma+2)\, M_{\mathrm{CJ}}^2}. \tag{5.17}$$

While the minimum velocity for which an oblique shock wave can exist is $M_0 = 1$, oblique detonation waves can only exist when the incoming flow velocities are above the CJ velocity $M_0 \geq M_{\mathrm{CJ}}$. From the conservation of mass and the definitions of u_{iN} and u_{it}, a relation can be obtained for the deflection angle δ

$$\tan\delta = \frac{(x-1)\tan\Omega}{x + \tan^2\Omega}, \tag{5.18}$$

whereas the conservation of momentum and the identity $u_i^2 = u_{in}^2 + u_{it}^2$ yield a relation involving the post detonation Mach number M_1

$$M_{1n}^2 = M_1^2 \sin^2(\Omega - \delta) = \frac{1 + (\Gamma + 1 + A/P_0) M_0^2 \sin^2\Omega - y}{(\Gamma+1)y + A/P_0}. \tag{5.19}$$

5.2.2 Prandtl-Meyer Flow

The Prandtl-Meyer flow pattern is a 2D isentropic expansion or compression wave. While the same relations hold for both expansions and compression waves, the latter always result in a non self-similar flow pattern. In the rest of this chapter, the terms *PM fan*, *expansion fan*, *PM expansion* and *PM flow* are used interchangeably and it is understood that the possible isentropic flow patterns are restricted to centered

expansion fans. To describe a particular expansion fan, one must specify either u_0 or M_0 (or equivalently the initial Prandtl-Meyer function, $\nu_0(M_0)$) and either the flow deflection angle through the expansion fan or the pressure change across the fan. The exiting flow Mach number could also be specified instead of the flow deflection although in the cases investigated here, the final Mach number is unknown. The typical parameters of the PM expansion fan are sketched in figure 5.3. The change of state through an expansion fan is given by the Prandtl-Meyer function, ν, and an isentropic relation between pressure and Mach number. Other thermodynamic variables can be obtained by using the isentropic flow relations 2.17-2.19. The PM function ν of the SG EOS is identical to that of an ideal gas if the substitution $\gamma \rightarrow \Gamma + 1$ is made.

$$\mu_1 = \sqrt{\frac{\Gamma+2}{\Gamma}}, \tag{5.20}$$

$$\mu_2 = \sqrt{M^2-1}, \tag{5.21}$$

$$\nu = \mu_1 \tan^{-1}\left(\mu_1\mu_2\right) - \tan^{-1}\left(\mu_2\right), \tag{5.22}$$

$$\left[\left(\Gamma+1\right)P_0 + A\right]\left(1+\frac{\Gamma}{2}M_0^2\right)^{\frac{\Gamma+1}{\Gamma}} = \left[\left(\Gamma+1\right)P_1 + A\right]\left(1+\frac{\Gamma}{2}M_1^2\right)^{\frac{\Gamma+1}{\Gamma}}. \tag{5.23}$$

The presence of the pressure offset A has a direct influence on those relations involving pressure where it appears as an additive term. A second, indirect effect of A is to raise the initial sound speed and lower the flow Mach numbers.

5.2.3 Shock Reflection Matching Conditions

The analytical solutions of the self-similar shock reflection problem are found by imposing that the flow deflection match the shape of the wall in the case of a regular reflection (RR) or that the local pressure and flow deflection be equal across a contact surface in the case of irregular reflections (IR). To emphasize this fact, some features in figures 5.2 and 5.3, are represented with dashed lines. These dashed features can either be real obstacle (ex.: solid wedges in a wind tunnel) or equivalent flow features (i.e. a contact surface).

5.3 Non-Reactive Reflections

The set of possible reflection patterns is divided into two broad categories: the reactive reflection patterns (discussed in section 5.6) with one wave being an oblique detonation wave, and the non-reactive reflection patterns in which all the waves are non-reactive shocks and PM expansions. The goal here is not to predict exact transition boundaries, but to formulate an EOS for a "typical" explosive which would not allow the

expected irregular reflection patterns, i.e. the standard Mach reflection pattern. The problem is hence analyzed *away from the boundaries*. The model parameters are fixed at reasonable values for a solid HE. Namely, $\rho_0 = 1.895$ g/cc, $P_0 = 1$ atm, $u_0 = 7$ km/s. The pressure offset A is varied and, unless specified otherwise, $\Gamma = 0.6$.

5.3.1 Topologies

There are two classes of reflections that can exist in which only one confluence point occurs. First, there is the case of regular reflections (RR), in which two oblique shock waves meet at a point located along a solid surface. The incident shock deflects the flow towards the wall and the reflected shock is able to rectify the flow angle so that it is parallel with the wall again. The other class comprises several topologies designated collectively as irregular reflections. The defining characteristic of irregular reflections is that the confluence point is located off the wall surface and is the convergence point of 3 (or possibly 4) waves. Four distinct possible types of irregular self-similar reflection topologies have been identified and are detailed in table 5.2. The boundaries between the different IR topologies are described in table 5.1.

Boundary	Description
MRf↔MRb	The Mach stem is perpendicular to the incoming flow. This boundary corresponds to the von Neumann point and also describes the transition point beyond which regular reflection solutions exhibit a higher final pressure than Mach reflection solutions for a given geometry.
MR↔vNR	Reflected wave (R) is perpendicular to the flow behind the incident shock (I).
vNR↔GR	Reflected polar sonic point lies on the subsonic branch of the incident polar. In other words, the flow Mach number behind the reflected shock (R) is unity.
GR↔NR	Expansion wave connecting the sonic point of the reflected polar to the incident polar intersects the incident polar at its sonic point. In other words, the flow behind the Mach stem is sonic.

Table 5.1: Descriptions of the boundaries differentiating the irregular reflection patterns

5.3.2 Inaccessible Solutions

The first task is to identify the boundaries at which different reflection types become unaccessible. For a given parameter pair (Γ, A), there is a critical incident shock deflection angle beyond which no regular

type	Number of waves	sketch
Mach Reflection with forward sweep (MRf)	3	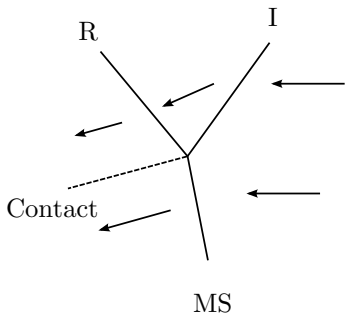
Mach Reflection with backward sweep (MRb)	3	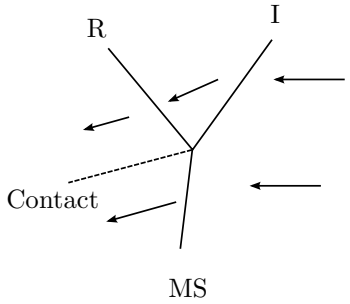
von Neumann Reflection (vNR)	3	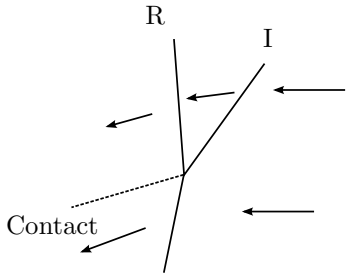
Guderley Reflection (GR)	4	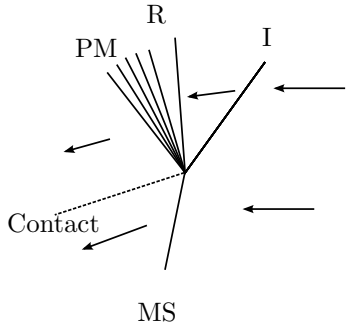
No possible shock polar match (NR)	?	unknown (unsteady?)

Table 5.2: Description of the different irregular reflection topologies identified.

reflection can occur. Two different criteria can be used. One is the detachment criterion, which is reached when the maximum turning angle of the reflected shock polar is equal to the incident shock deflection angle. Beyond this point, there is no intersection between the reflected shock polar and the zero deflection axis. The second criterion is the sonic criterion, which is attained when the deflection angle at the sonic point of the reflected polar is equal to the incident shock deflection angle. Beyond this point, the flow behind the reflected wave becomes subsonic and the RR pattern becomes susceptible to downstream influences. The existence of two different criteria for the transition point between regular and irregular reflection is evidence of the hysteresis inherent to the problem of shock reflection. To steer clear of the hysteresis problem, both criteria are examined and the model parameters are selected only in regions where both criteria yield the same outcome.

Figures 5.4-5.6 show the boundaries, for $\Gamma = 0.6$, at which the available IR, when RR is no longer possible, is in the vNR, GR and NR regions respectively. This does not mean that there is only one type of IR possible. Rather, it means that, for the particular values of A shown and as the incident deflection angle, δ, is increased, the reflection pattern will first transition from the RR to the IR type identified. The result using the detachment criterion is shown; the sonic criterion yields a similar result. For example, in fig 5.5, the system will transition from a RR to a GR. If the incident deflection angle is increased further, the system will enter the NR region. One can therefore think of the different IR types to be following a sequence, MRf, MRb, vNR, GR and finally NR. The sequence loses its first elements as the parameter A is increased.

The different boundaries are summarized in figure 5.7. Here, every point on the graph corresponds to a different value of the parameter pair (Γ, A) and the label identifies the first IR type accessible by the system. Ultimately, this information is used to select parameter pairs in the GR and NR regions for which the dynamic structure of propagating detonations is to be examined.

5.4 Numerical Simulations of the Non-Reactive Reflections

Knowledge of the non-reactive structure that may occur at the detonation front will be useful when analyzing the structure present in the detonation simulations. For all the simulations, the AMRITA framework of J.J. Quirk was used, with the 5^{th} order WENO scheme of Aslam et al. [93, 94]. The AMRITA framework, among other characteristics, makes it easy to turn on and off grid refinement, which was set at 4 levels of refinement with a refinement ratio of 4 between each grid level. All simulations were computed on a dual quad-core machine with 16GB or RAM. Because the non-reactive problems do not have an intrinsic scale,

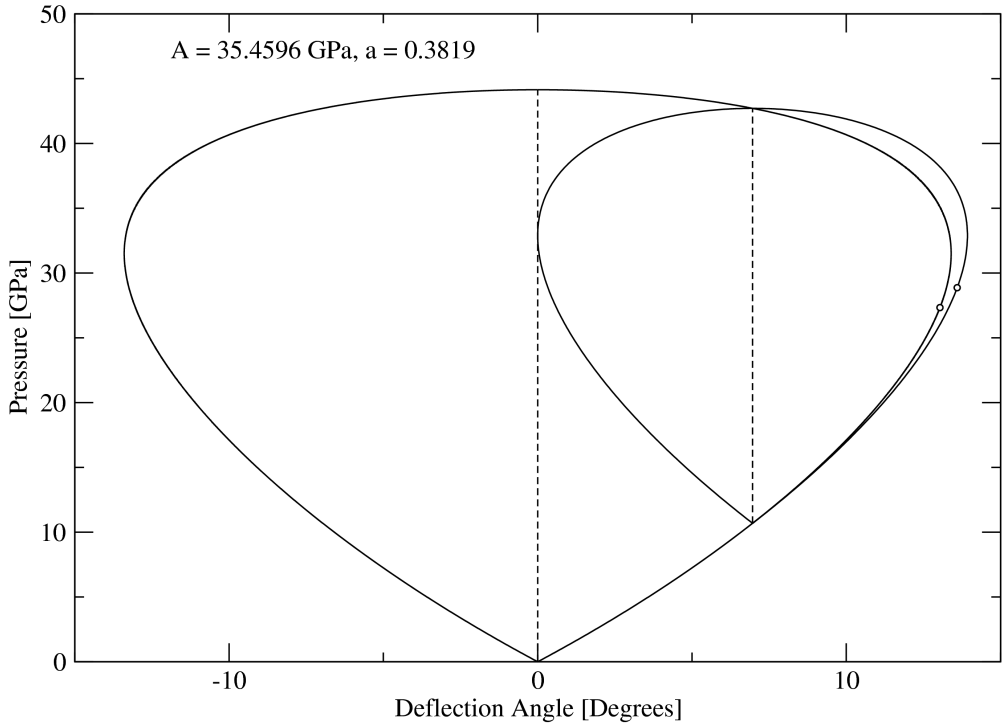

Figure 5.4: Reflected polar pattern for $\Gamma = 0.6$ at the normal reflected wave critical point. The first accessible IR for $A > 35.4596$ GPa is the vNR reflection. The small circles denote the sonic points.

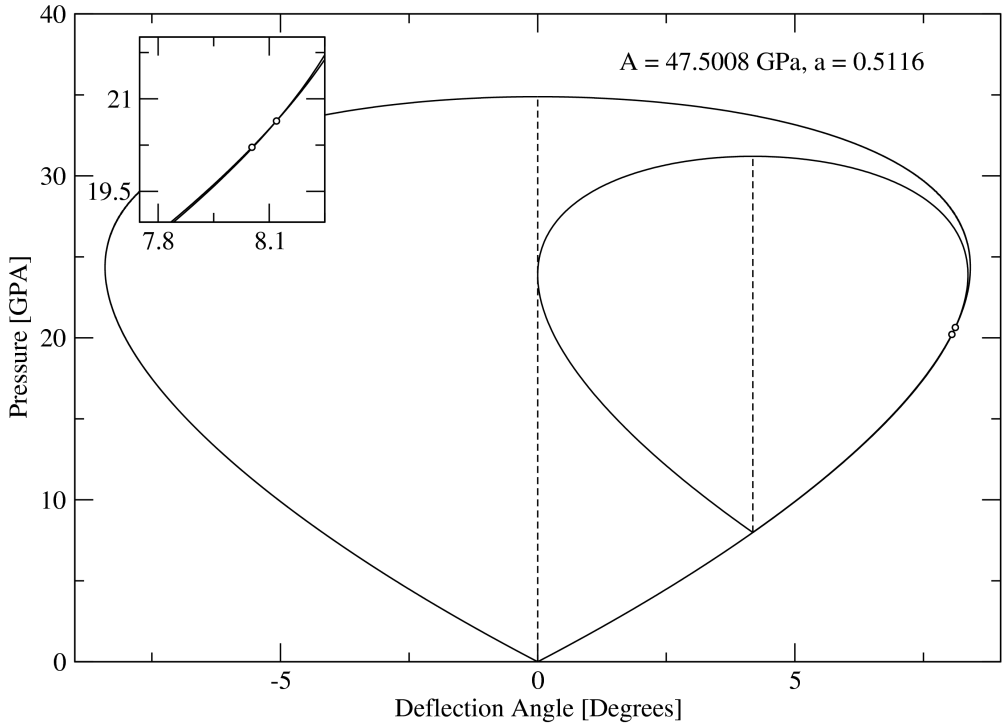

Figure 5.5: Reflected polar pattern for $\Gamma = 0.6$ at the sonic intersection critical point. The first accessible IR for $A > 47.5008$ GPa is the GR reflection. The small circles denote the sonic points.

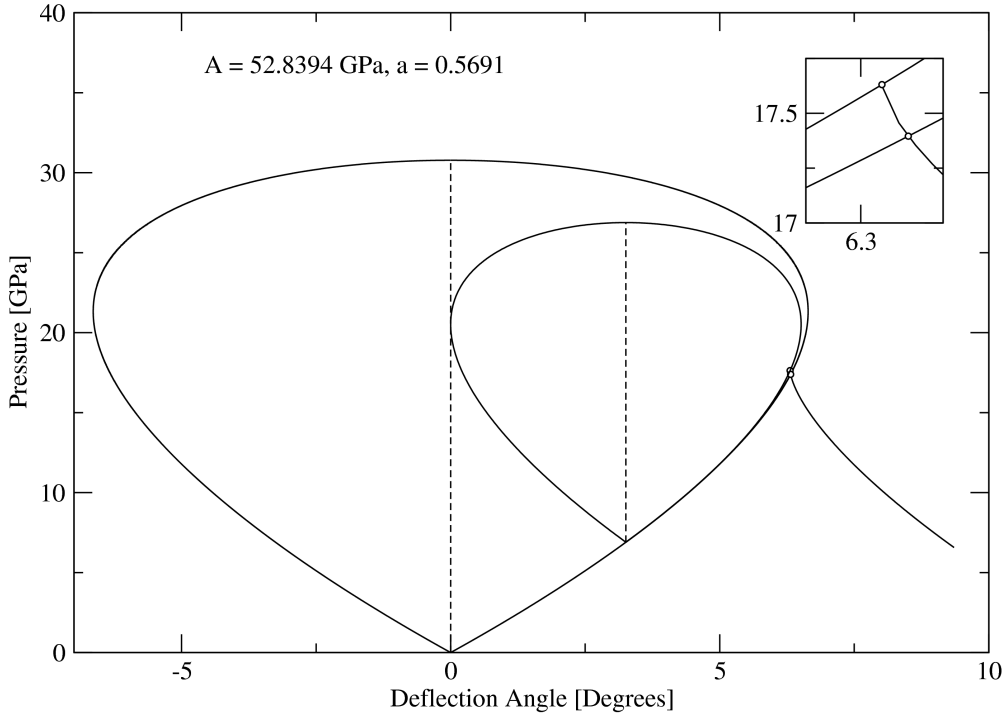

Figure 5.6: Reflected polar pattern for $\Gamma = 0.6$ at sonic expansion critical point. The first accessible IR for $A > 52.8394$ GPa is the NR reflection. The small circles denote the sonic points.

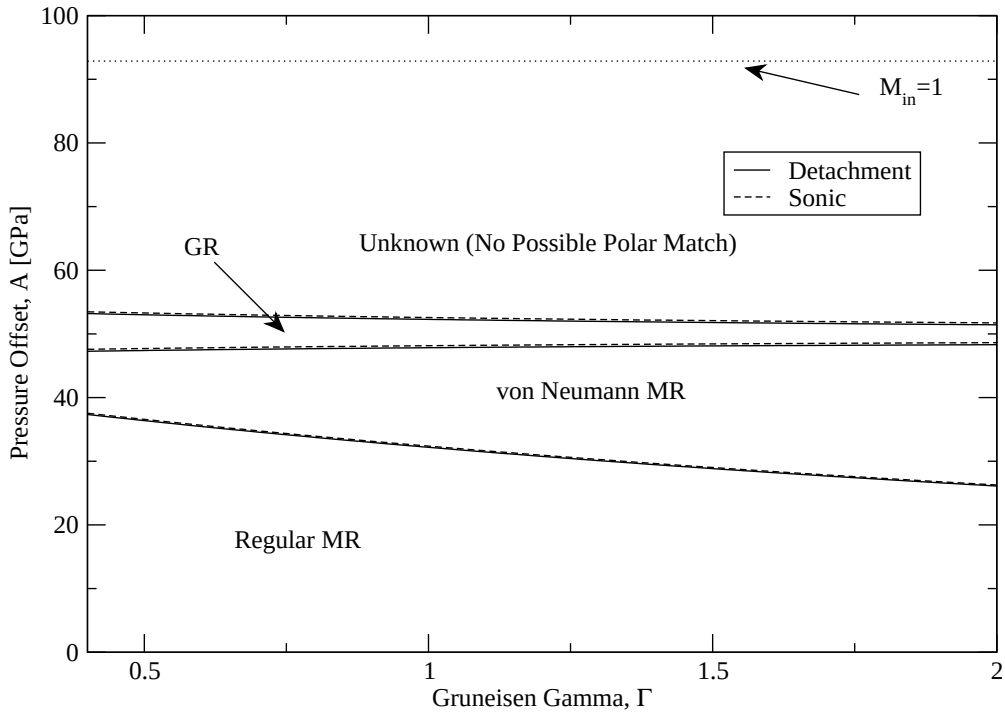

Figure 5.7: Boundary plot of possible non-reactive, steady, 3 and 4 wave flow fields.

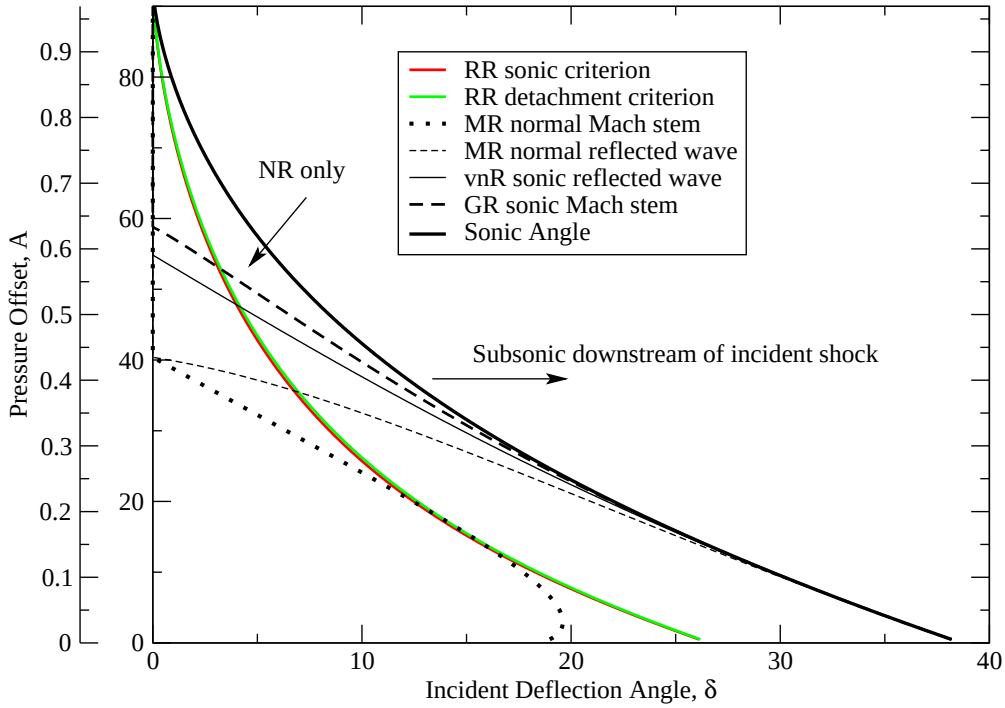

Figure 5.8: Map of A against incident shock deflection angle for different critical features of reflection solutions in the case of $\Gamma = 0.6$ and $u_0 = 7$ km/s. Left of the red/green lines, RR is possible; right of the solid black line, the post-incident shock state is subsonic and no reflection occurs.

the channels were rescaled to have the (initial state) inlet height be unity. The resolution of the simulations was varied between 300 and 2000 fine cells per unit height. The solutions reported were simulated with 1200 fine points per unit height.

5.4.1 Selection of Test Cases

EOS parameter sets and geometries were selected for the non-reactive case. The test matrix was chosen so as to study the topology of the different shock reflection solutions identified. To select those test cases, the information in fig 5.7 can be represented for one particular value of the Grüneisen Gamma, such that the critical incident deflection angles for different features to appear in the flow can be analyzed. These critical angles are plotted along with the value of the pressure offset $a = A/\rho_0 u_0^2$ in fig 5.8. For a given value of a, the different possible flow fields are delimited by the different boundary lines. The boundaries of fig 5.7 correspond to the values of a for which the critical angle of a flow feature reaches the critical angle for the sonic and detachment criteria (green and red lines). These different boundaries in fig 5.8 correspond to a vertical slice in fig 5.7, i.e. are only for a single value of Γ. The chosen test matrix of non-reactive cases is shown in table 5.3.

A	$a = A/\rho_0 D^2$	δ	Ω	Reflection type	Simulation setups used	Outcome
20	0.21539	3	30.261471	RR	Pseudo-Steady	Match
51	0.54924	3	52.7103	RR	Pseudo-Steady	Match
20	0.21539	18	48.94021	MR	Pseudo-Steady Rotated Pseudo -Steady Steady	Fail Fail Match
35	0.37693	10	51.534096	vNR	Pseudo-Steady Steady Dumptank	Fail Unstart Unstart
46	0.49540	6	54.461275	GR	Pseudo-Steady Steady	Fail Unstart
46	0.49540	7.6	58.605358	NR	Pseudo-Steady Steady	Fail Unstart

Table 5.3: Test matrix of non-reactive cases which were simulated numerically. The "outcome" is the overall result of the simulations. "Match" means the simulation reproduced the theoretical solution. "Fail" applies to the pseudo-steady and rotated pseudo-steady setups. In this case, the wave propagated but the pressure behind the reflected shock and Mach stem was higher than the possible maximums. "Unstart" applies to the two steady cases. In this instance, the wave pattern was disgorged in front of the wedge.

5.4.2 Description of the Numerical Setups

Four numerical setups were used to observe the non-reactive reflection patterns. Two pseudo-steady setups were used. The first non-steady setup involved a normal shock traveling over a ramp (fig 5.9(a)). The second non-steady setup consisted of a rotated setup of the first one. An oblique, non-steady shock was initialized and allowed to travel over a flat plate located on the bottom boundary of the domain (fig 5.9(b)). Finally, two steady setups with one or more incoming flows on the left of the domain and transmission boundary condition(s) at the right side of the domain were used (fig 5.9(c) and 5.9(d)). One steady setup involved a rectangular domain with one inlet at the left, one outlet at the right and a half diamond-shaped obstacle to which the incident shock is attached (fig 5.9(c)). A more complex domain was used in conjunction with the vNR reflections (fig 5.9(d)). In these simulations, the leftmost part of the domain consisted of an inlet at the initial state conditions. The top part of the left boundary was an inlet at the post-Mach-stem conditions. The right and top boundaries consisted of outlet boundary conditions. A wedge shaped obstacle was defined along the bottom boundary. The complete flow field corresponding to the theoretical solution was initialized at the start of the simulation. Note that although the third problem setup used is called "steady", the calculation performed is still time-dependent; only the incident shock, spanning the whole channel width, was initialized at the start of the simulation. The name refers to the fact that the problem is expected to asymptote, for long run times, to a steady configuration.

Several diagnostics are used to characterize the result of the simulations: a steady-frame Mach number map, a gray-scale pressure map where white is the maximum pressure in the flow field and a pressure

gradient map. In the latter, brightness is correlated to the magnitude of the pressure gradient $\bigtriangledown P$ and the color information is related to the direction of the pressure gradient. Actual correspondence scales are not reported for the three field maps; these diagnostics are used to qualitatively assess the reflection topology. In addition to the field maps, a quantitative diagnostic is used to match the numerical solutions to the theoretical ones. For each solution, the confluence or triple point is identified. Pressure and density are plotted as a function of angle along a circle of a small radius (0.005 to 0.015 unit height) around the triple point. The circular path associated with the MR simulation in the rotated pseudo-steady setup is shown in fig 5.18. The reference zero angle is always either straight to the left or the right of the triple point, whichever side corresponds to the initial state of the material. The same diagnostics are used for all four non-reactive numerical setups.

The numerical setups used for each test case is shown in table 5.3 along with the general outcome. Test case/simulation setup combinations marked "Match" means the theoretical results were recovered. Those marked "Fail" means the detonation propagated with the characteristic profile described below. "Unstart" refers to the condition by which the wave pattern moved ahead of the wedge towards the inlet of the domain.

5.4.3 Pseudo-Steady Simulations

The initial conditions are those of fig 5.9(a) and consist of a plane, normal shock wave traveling from left to right over a solid ramp. The angle of the ramp sets the shock angle of the incident wave, Ω. The post-shock state specifies the left inflow boundary conditions. All other boundaries are reflection boundaries.

In the pseudo-steady case, both RR test cases recovered the theoretical pressures calculated using the steady analysis. The results are shown in figs 5.10–5.13. All other test cases failed. The pressure behind the incident shock was always recovered, which is not surprising as this state is set at the beginning of the simulation. The pressure behind the reflected wave and the Mach stem were too high in all cases, even exceeding the maximum pressures allowed by the reflected and incident polars. The MR case, shown in figs 5.14–5.15 exhibited this anomalous behaviour. The comparison with the theoretical pressures in fig 5.16(b) shows the pressure is uniform behind the Mach stem and reflected wave but above even the maximum pressure allowable by the incident polar. The MR case was simulated using up to 2000 points per unit height and the solution was determined to have converged and the high pressure was not a result of a poorly resolved calculations.

The vNR, GR and NR cases all exhibit the same anomalous behaviour. The vNR results are shown as an example in figs 5.16–5.17. Marching along the circular arc around the triple point, three shock waves and one contact discontinuity can be identified. There also appears to be an expansion going from a high pressure

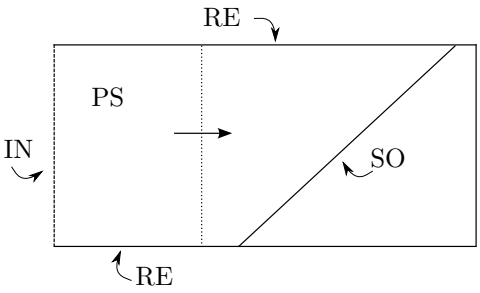

(a) Pseudo-steady problem

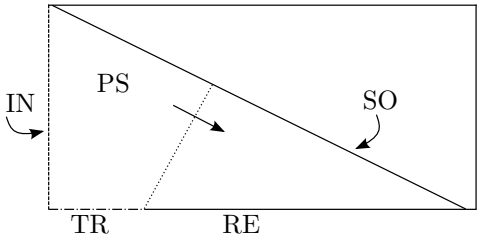

(b) Rotated pseudo-Steady problem

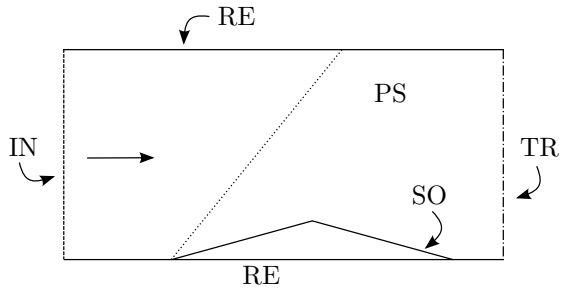

(c) Steady problem

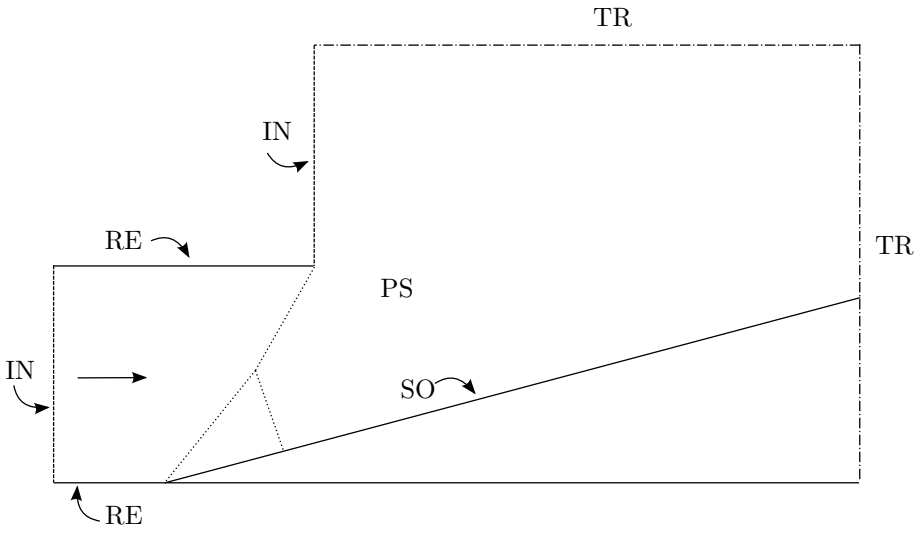

(d) Steady problem with a dump tank

Figure 5.9: Sketch of the different numerical problems solved for the non-reactive case. The different labels are “IN”, an inflow boundary condition, “RE”, a reflection boundary condition, “TR”, a transmission boundary condition, “SO”, a solid obstacle, “PS”, the post-shock state. Dotted lines correspond to shock waves as they are initialized at the start of the computation.

behind the Mach stem to a lower pressure behind the reflected shock. This expansion fan is inconsistent with the PM expansion of the GR structure. In the GR structure, the pressure behind the reflected wave should be higher than that behind the Mach stem. The pressure behind the incident shock wave always corresponds to that calculated theoretically, but significant over-pressures are present behind the reflected shock and Mach stem; those pressures are still higher than the maximum pressures allowable by the incident and reflected polars.

The trajectory of the triple point was taken into account. Because the triple point trajectory is a priori unknown, the theoretical solutions were adjusted using the measured triple point track. The triple point track was below 3.3° for all cases, and the discrepancy introduced by the track angle was small and could not account for the mismatch between the theoretical and numerical pressures calculated.

5.4.4 Rotated Pseudo-Steady Simulations

One of the possibilities investigated to explain the difficulty of the pseudo-steady simulations to reproduce the theoretically calculated flow patterns is linked to the representation of the solid ramp. Owing to the design of internal boundaries (such as solid obstacles) in the AMRITA framework, sharp concave corners cannot be matched exactly and some leakage can occur at the corner point [95] . To rule out this possibility, the rotated pseudo-steady simulation setup was crafted, in which the incoming shock is oblique and the solid ramp is coincident with the bottom boundary of the domain (fig 5.9(b)). A solid ramp internal boundary is imposed from the top left of the domain down to the bottom boundary of the domain so as to avoid the time-dependent inflow boundary which would result from the incoming shock extending across the entire height of the domain. The rotated pseudo-steady simulation was computed for the MR case and the same problematic flow-field was obtained, thereby ruling out the internal boundary as a source of the discrepancy. The Mach number map as well as pressure and density around the triple point are shown in figs 5.18, 5.19 and 5.20 respectively.

5.4.5 Steady Simulations

While the steady case, for long simulation times, should exactly reproduce the steady theoretical analysis, it suffers from certain drawbacks as well. For one, much of the flow downstream of the triple point is subsonic and influenced by the particular details of the domain shape. For the current simulations, this meant that in the case of a ramp extending to the exit (right) face of the domain, the flow would either choke after the reflected shock interacted with the ramp and the top side of the domain or the transmission boundary currently implemented in the AMRITA framework (linear extrapolation) would fail due to a shock

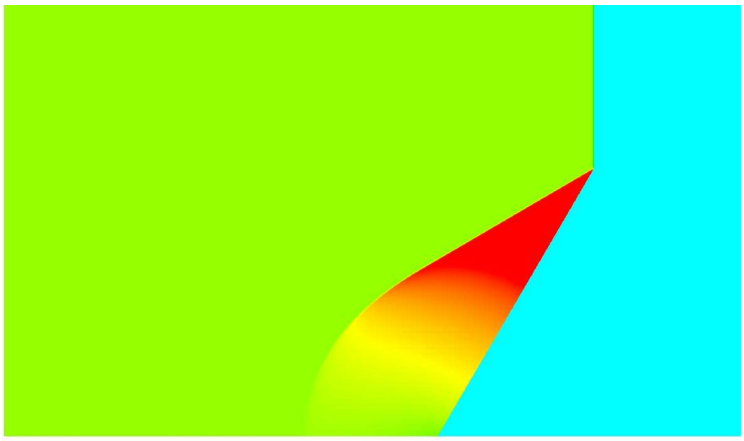

(a) Mach Number

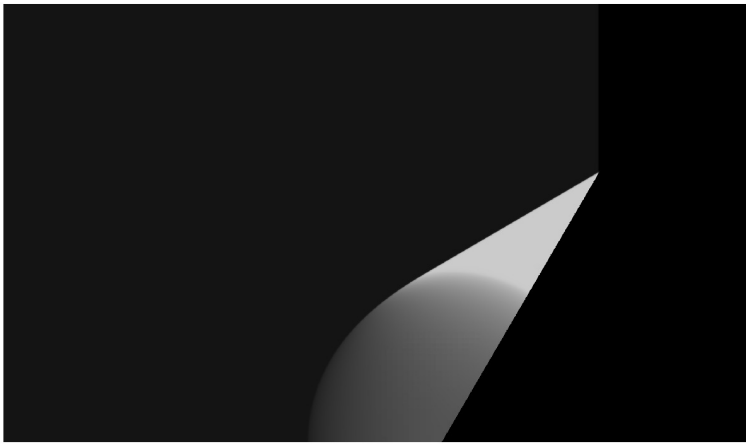

(b) Pressure

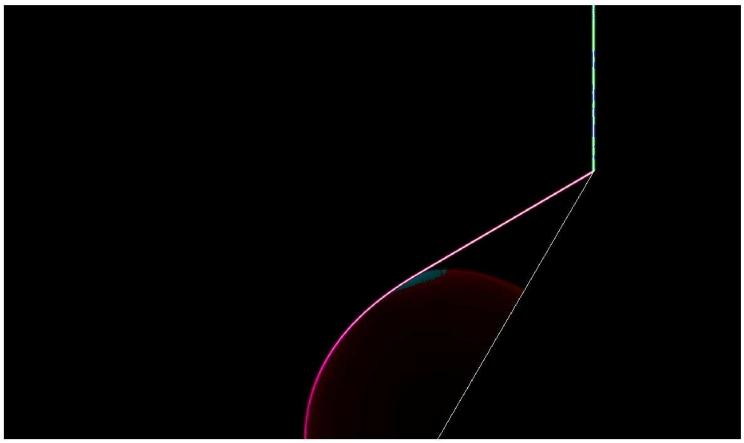

(c) Pressure Gradient

Figure 5.10: Maps of Mach number, pressure and pressure gradient for a RR with $A = 20$ GPa.

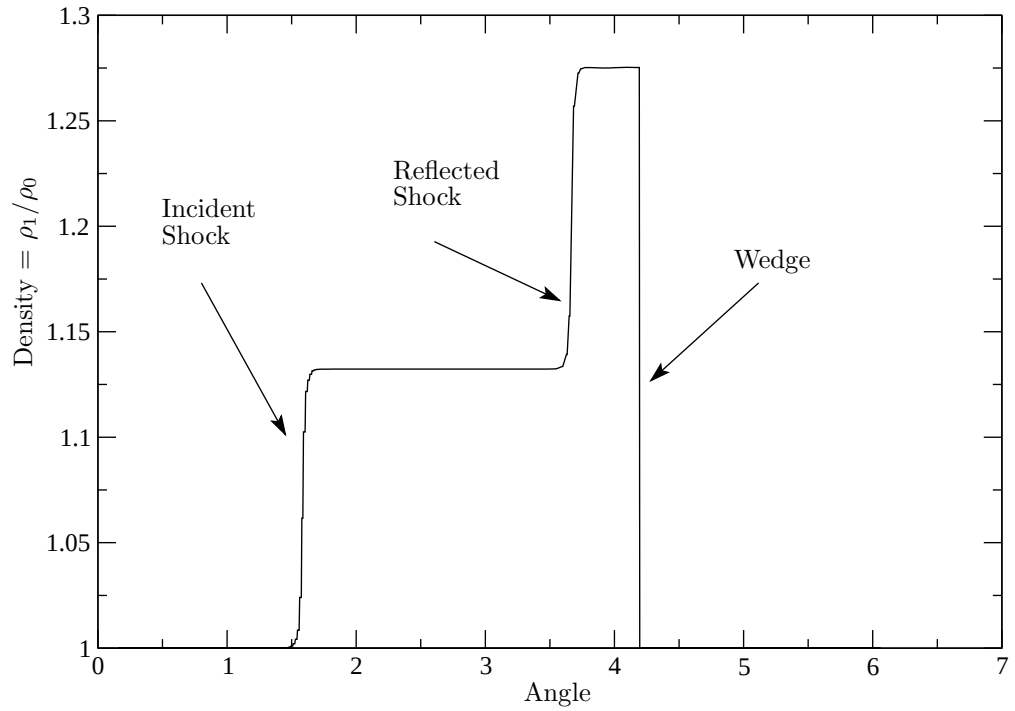

(a) Density

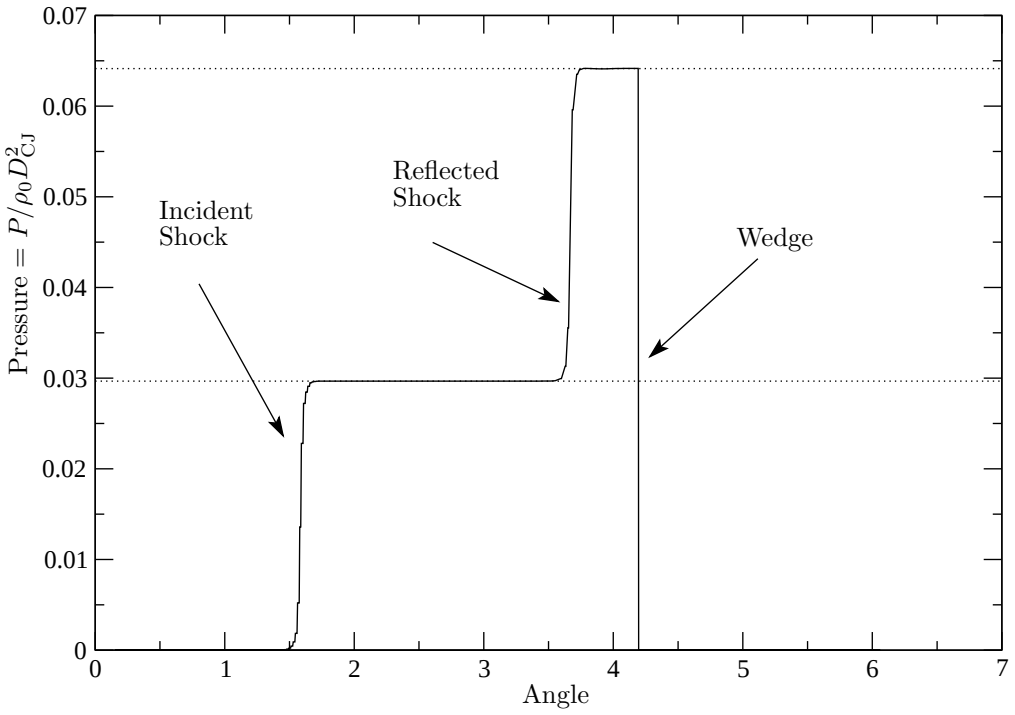

(b) Pressure

Figure 5.11: Density and pressure around the reflection point for the RR case of fig 5.10. The radius of the circle along which the state was sampled was varied between 0.005 and 0.015. The dashed lines correspond to the analytical solution from the shock polar.

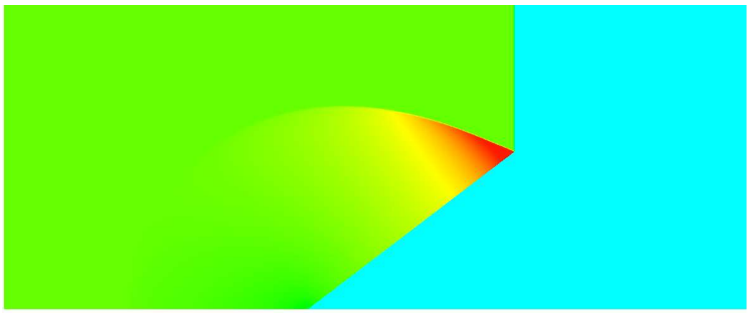

(a) Mach Number

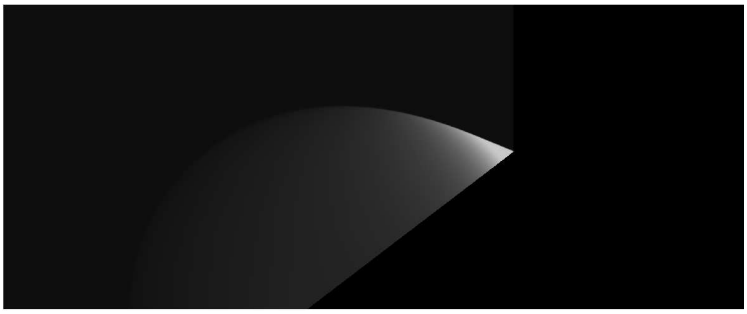

(b) Pressure

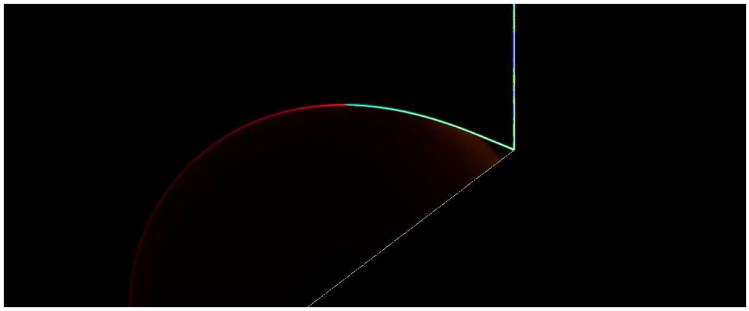

(c) Pressure Gradient

Figure 5.12: Maps of Mach number, pressure and pressure gradient for a RR with $A = 51$ GPa.

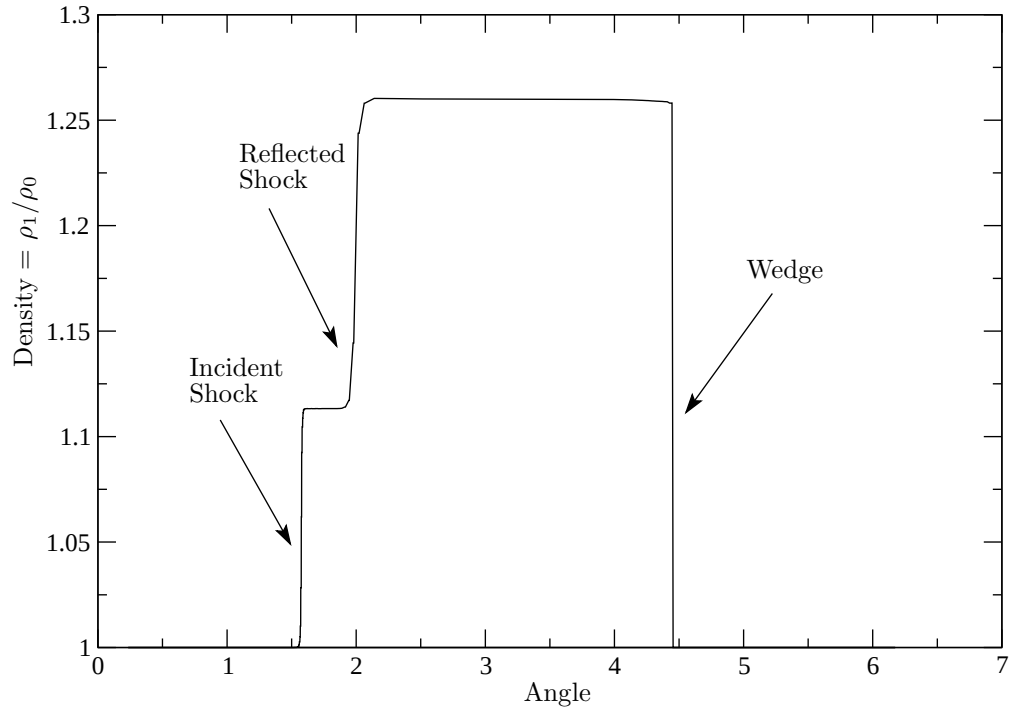

(a) Density

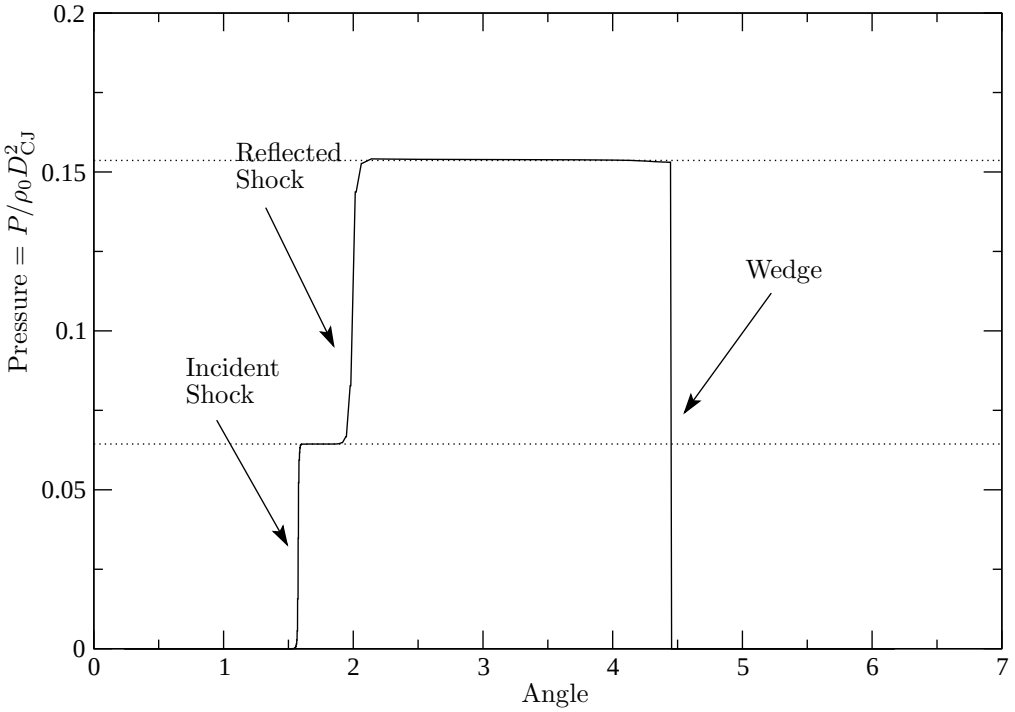

(b) Pressure

Figure 5.13: Density and pressure around the reflection point for the RR case of fig 5.12. The radius of the circle along which the state was sampled was 0.01.

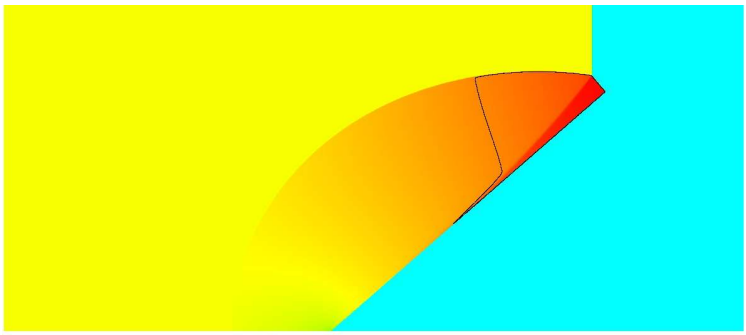

(a) Mach Number

(b) Pressure

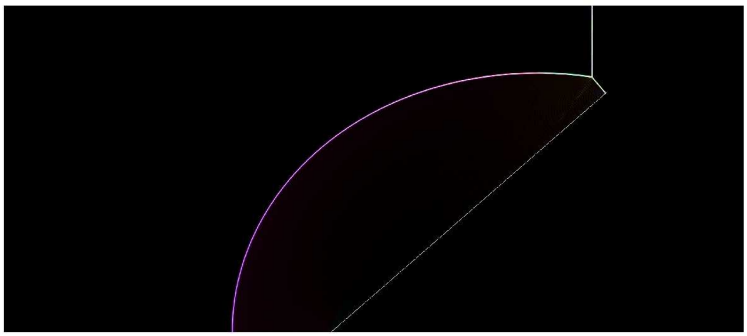

(c) Pressure Gradient

Figure 5.14: Maps of Mach number, pressure and pressure gradient for a MR with $A = 20$ GPa. The black line in the Mach number map corresponds to the sonic locus $M = 1$.

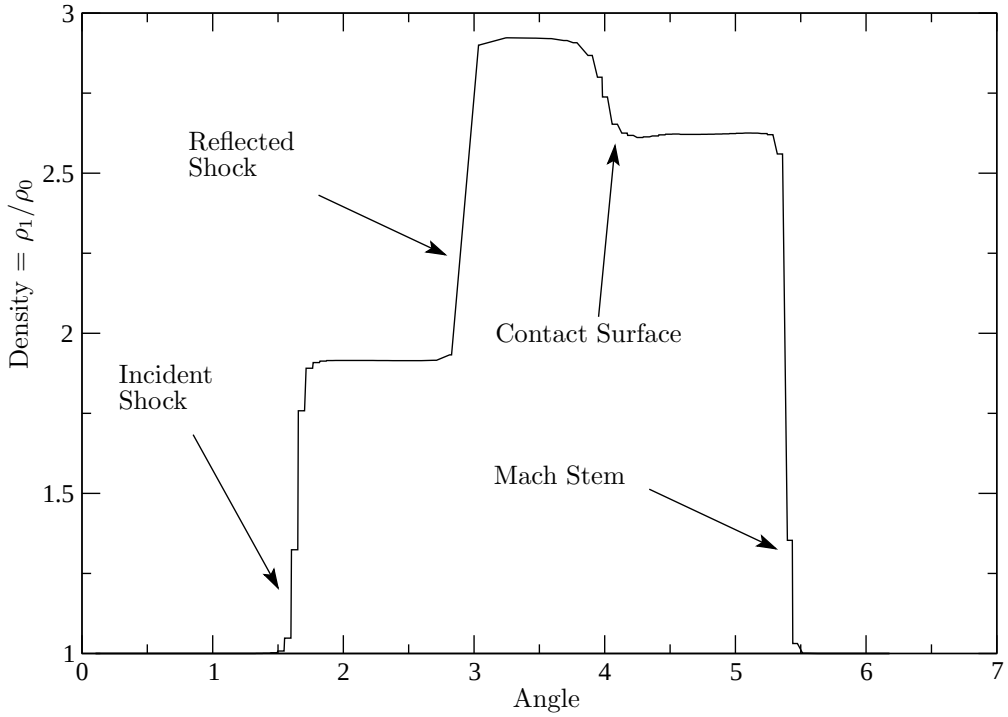

(a) Density

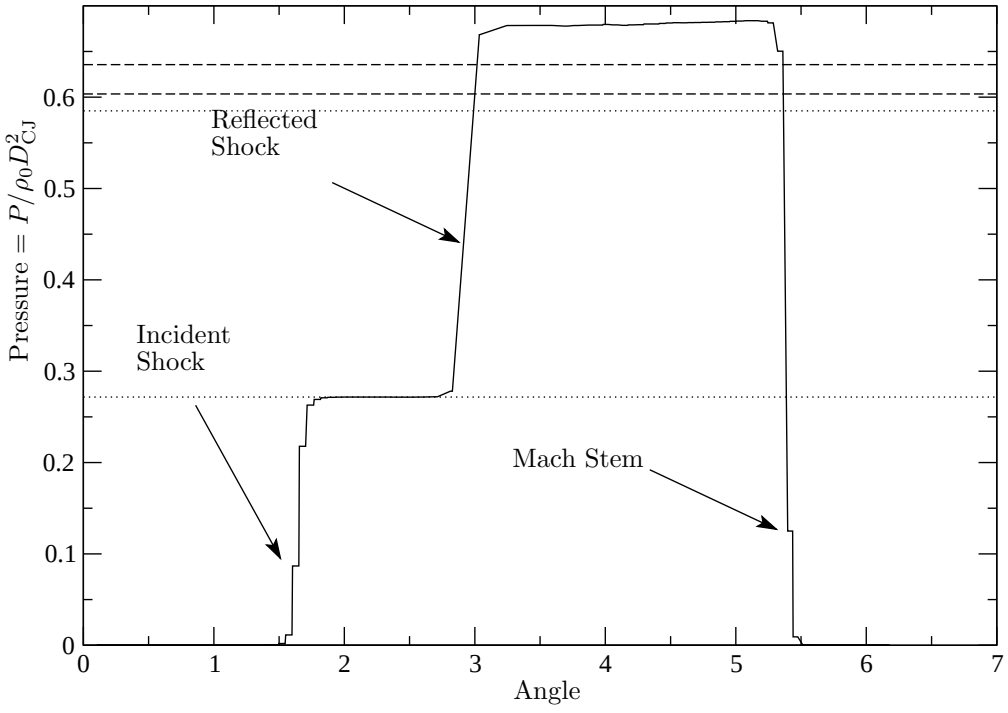

(b) Pressure

Figure 5.15: Density and pressure around the reflection point for the MR case of fig 5.14. The dotted lines are the theoretical solution. The top two dashed lines are, from the top, the maximum pressure allowed by the incident polar and by the reflected polar, respectively.

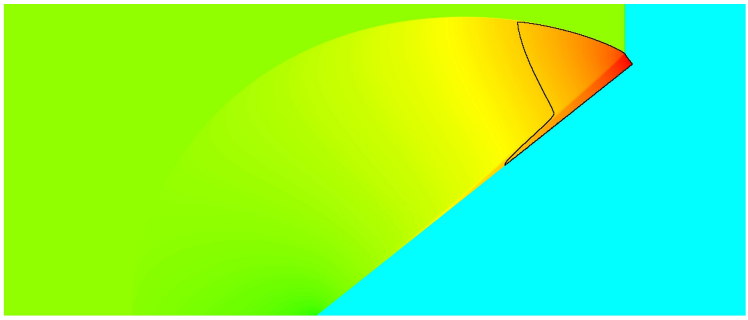

(a) Mach Number

(b) Pressure

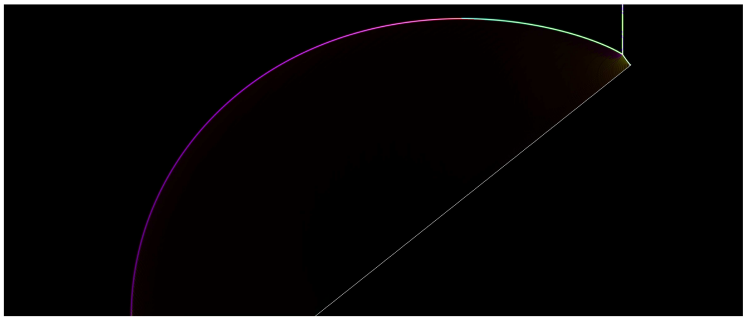

(c) Pressure Gradient

Figure 5.16: Maps of Mach number, pressure and pressure gradient for a vNR with $A = 35$ GPa. The black line in the Mach number map corresponds to the sonic locus $M = 1$.

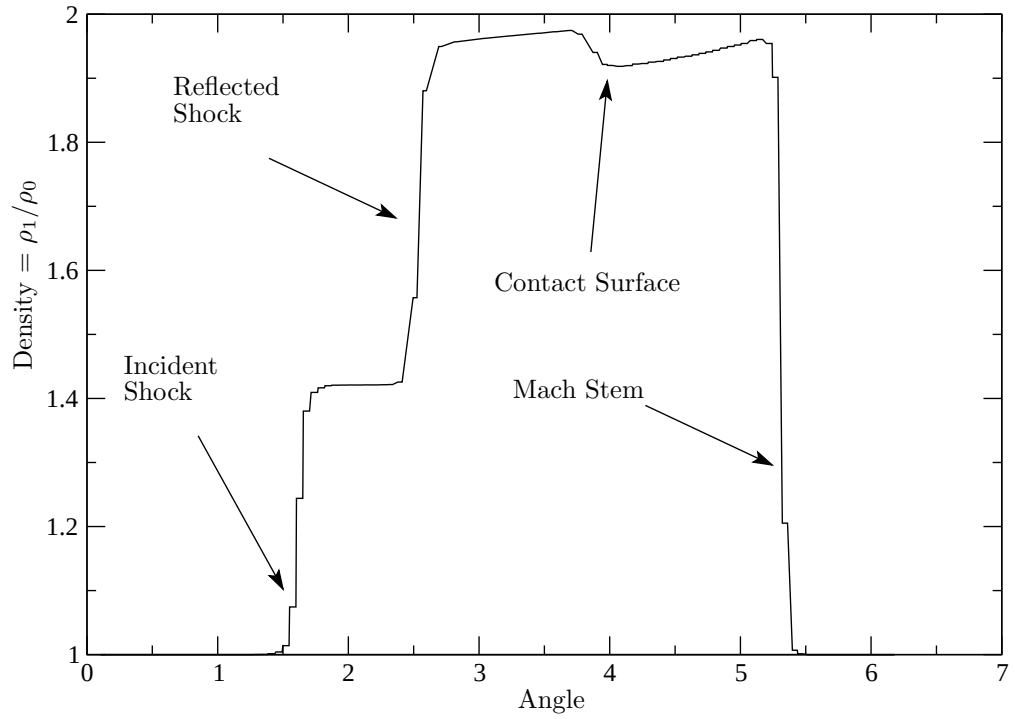

(a) Density

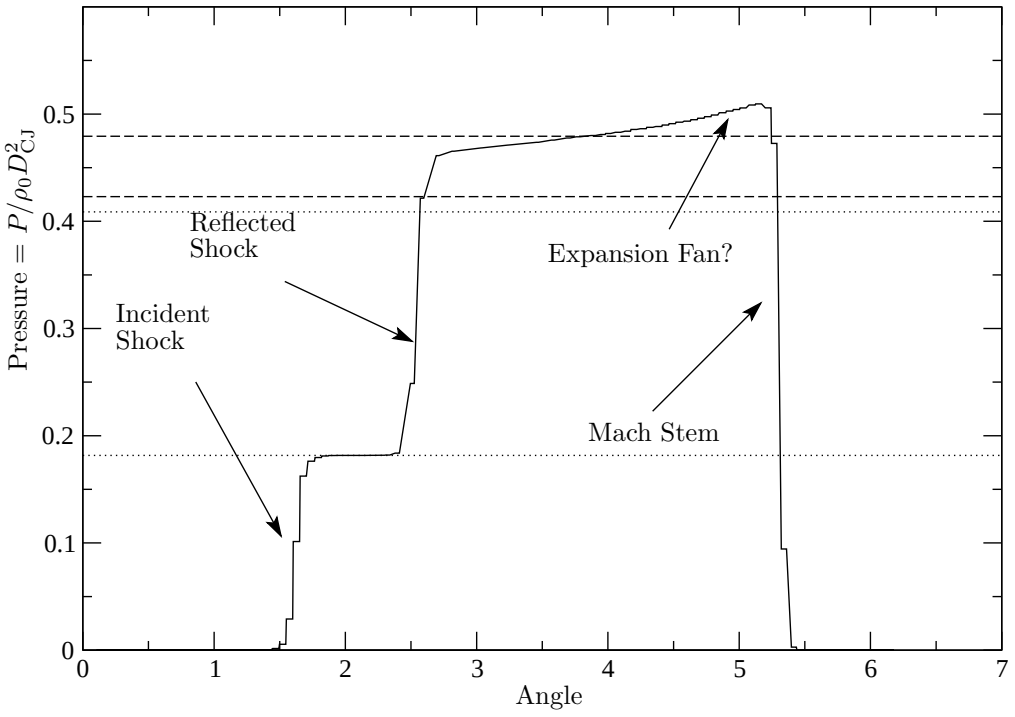

(b) Pressure

Figure 5.17: Density and pressure around the reflection point for the vNR case of fig 5.16. The dotted lines are the theoretical match and the dashed lines are the maximum pressures allowed by the incident and reflected polars, respectively from the top.

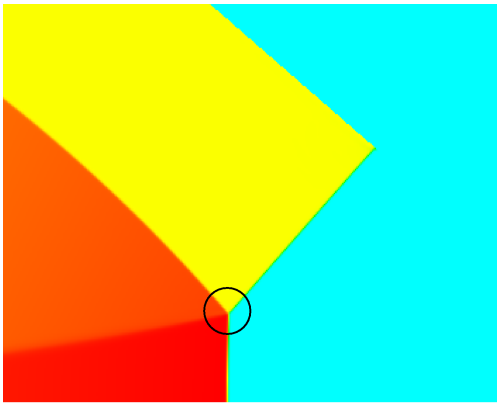

Figure 5.18: Colour map of the steady-frame Mach number. Circular marker shows the path along which pressure and density are sampled. In this case, the path radius is 0.01. The theoretical solution is a MR and the numerical setup corresponds to the rotated pseudo-steady case (fig 5.9(b)).

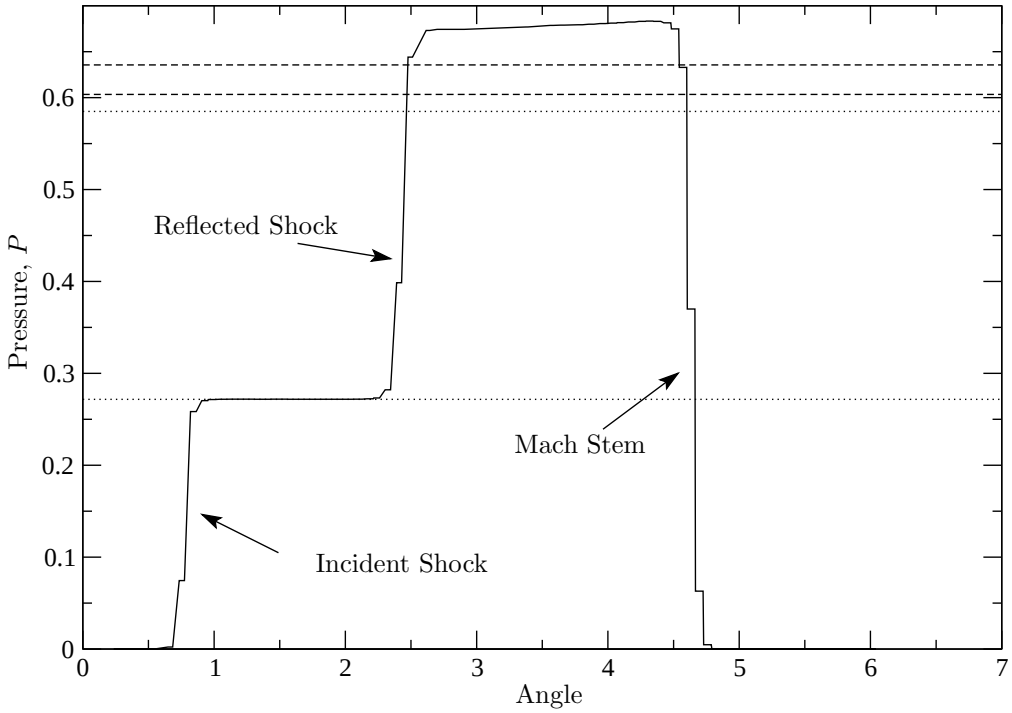

Figure 5.19: Pressure around the triple point corresponding to the Mach number map of fig 5.18. The dotted lines are the theoretical match; the dashed lines are the maximum pressures allowed by the shock polars.

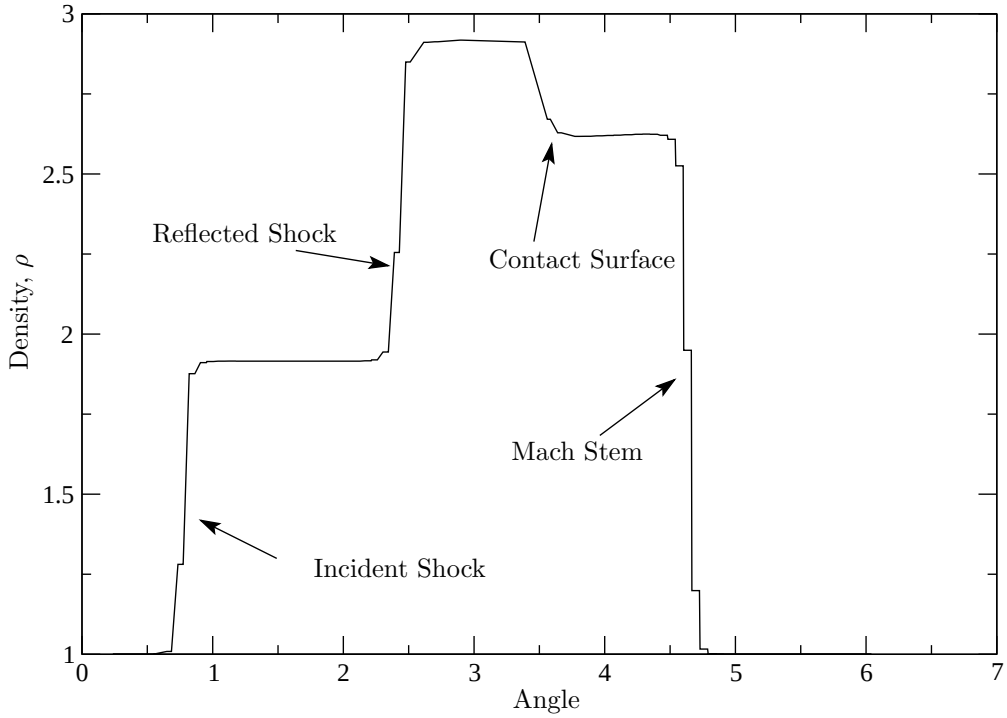

Figure 5.20: Density around the triple point corresponding to the Mach number map of fig 5.18.

wave intersecting the domain boundary. Disturbances would propagate from the exit upstream, pushing the incident shock and Mach stems ahead of the wedge and eventually to the inflow boundary of the domain. One workaround for this problem was to replace the straight wedge with a symmetric half-diamond. The expansion fan originating at the apex of the obstacle would serve to re-accelerate the flow, so that most of the backplane would be supersonic again. This was sufficient for the present purposes and no information would travel upstream from the right side of the computational domain. A second drawback of the steady simulation setup is the difficulty to devise a set of initial conditions that are physically realizable. As a result, there is always the chance that the computation, starting from an unphysical initial condition, will not evolve to the steady, physically meaningful solution, but to a different, physically incorrect, solution.

The MRb case was first run and it was found that the steady configuration could reproduce the theoretical calculation. Pressure and density are shown in figs 5.21 and 5.22 respectively. For the vNR and GR cases, the steady calculations in the same domain resulted in a disgorged shock or unstart.

The boundary case between MR and vNR was investigated using the more complex setup shown in fig 5.9(d). In this case, the theoretical flow field was initialized in the computational domain with appropriate boundary conditions. If the flow field were steady, then no change in the flow structure should be observed. The reflected shock (normal to the front wedge surface) was observed to slowly creep towards the leading apex until the shock detached from the wedge and reached the inlet of the domain. No discernible disturbances

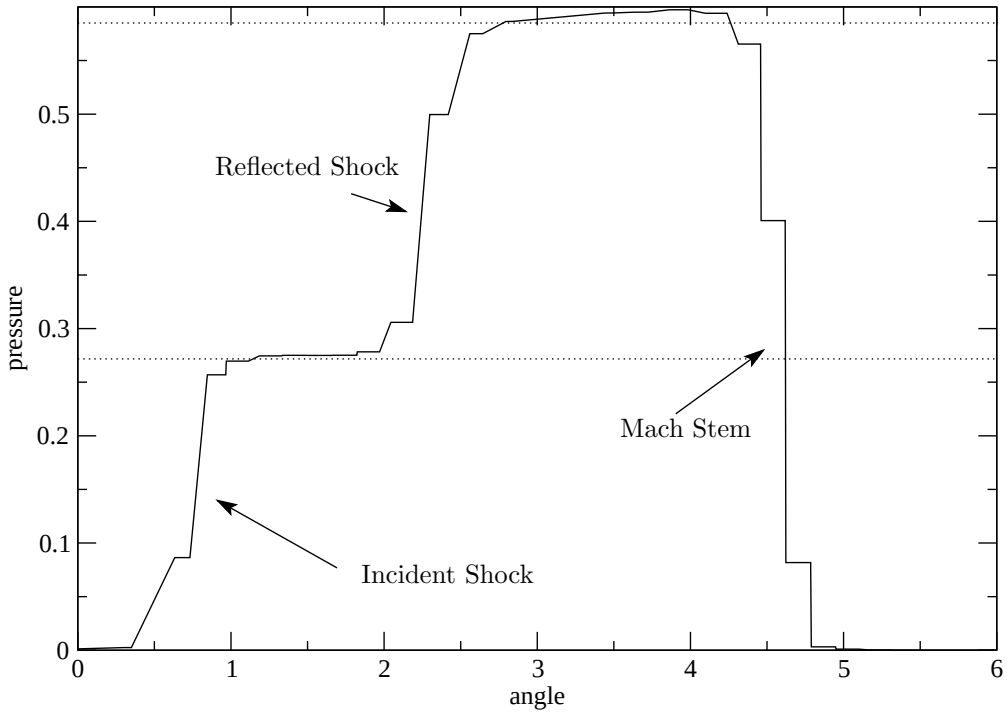

Figure 5.21: Pressure around the triple point for the MR (backwards sweep) simulation in the steady (5.9(c)) configuration.

propagating from the boundaries were observed, suggesting the structure is inherently unstable.

5.5 Existence of the vNR and GR Flow Patterns

The apparent difficulty in finding a non-reactive numerical solution involving the vNR and GR reflection patterns raises a question about the stability of such solutions. The stability of the vNR and GR solutions is examined here as well as past attempts to capture the nature of such solutions.

5.5.1 Instability of the MR↔vNR, vNR and GR Solutions

A physical argument was used by Hornung [96] to assess the stability of RR and MR patterns. The development of that argument was motivated by several unsuccessful attempts at observing hysteresis predicted around a transition point [96]. A similar physical argument is used here to assess the stability of the vNR and GR patterns. The vNR pattern appears to be unstable and the GR pattern may also be unstable, although a definitive conclusion was not reached.

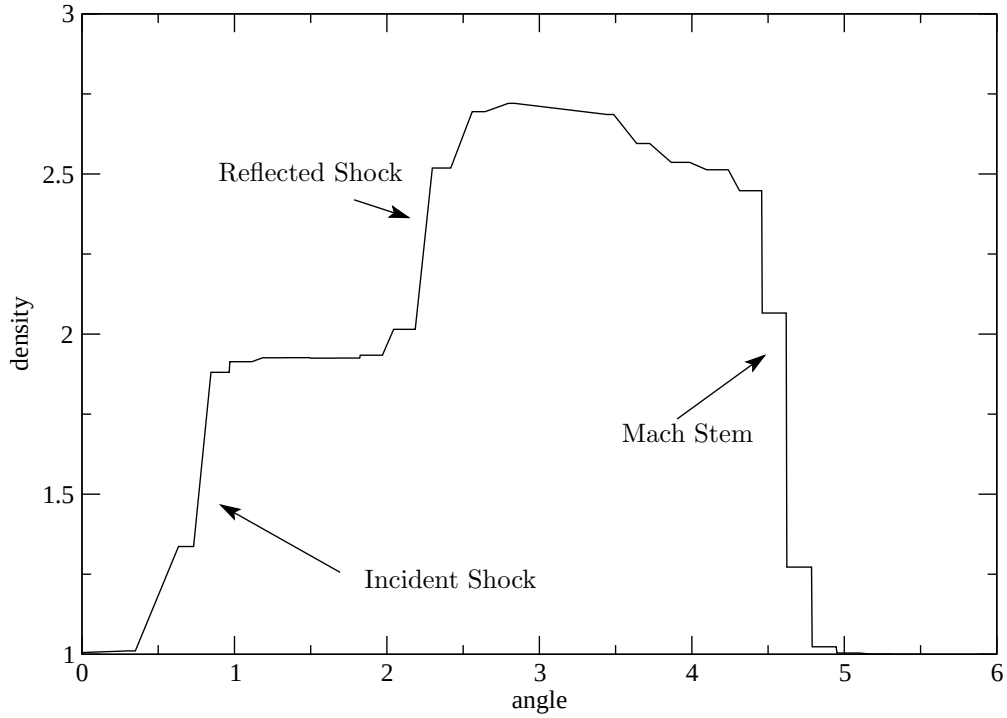

Figure 5.22: Density around the triple point for the MR simulation in the steady (5.9(c)) configuration. The dotted lines are the theoretical match. The jagged appearance is due to the small radius (in this case 0.005) of the circle along which the state is sampled.

Transition solution: MR↔vNR

At the transition point between MR and vNR, the reflected shock is a normal wave. The shock polar would be similar to the one shown in fig 5.4. Let's assume a slight downstream disturbance causes the pressure behind the Mach stem and reflected waves to increase. This disturbance would cause the Mach stem shock to rotate towards the incoming flow by a small amount (i.e. the Mach stem becomes "more normal" to the incoming flow) resulting in the contact surface bending towards the wedge surface. Because the reflected shock is already a normal shock, there is no way for the reflected shock to rotate by a small amount to respond to a small increase in pressure. As a result, the only possible outcome is that the reflected wave will move forward toward the leading apex of the wedge. The influence of the disturbance on the reflected wave (the wave moving forward) and the effect of the disturbance on the Mach stem (a more normal wave resulting in a contact surface deflection towards the wall) complement each other rather than having opposite effects. The result is a wave unstable to positive pressure perturbations. The effect of positive disturbances is shown in fig 5.23(a). In the opposite situation, a small disturbance behind the Mach stem causes the pressure to decrease, resulting in a rotation of the Mach stem away from the incoming flow by a small amount (i.e. a "more oblique" Mach stem) and a deviation of the contact surface away from the wall. The reflected wave

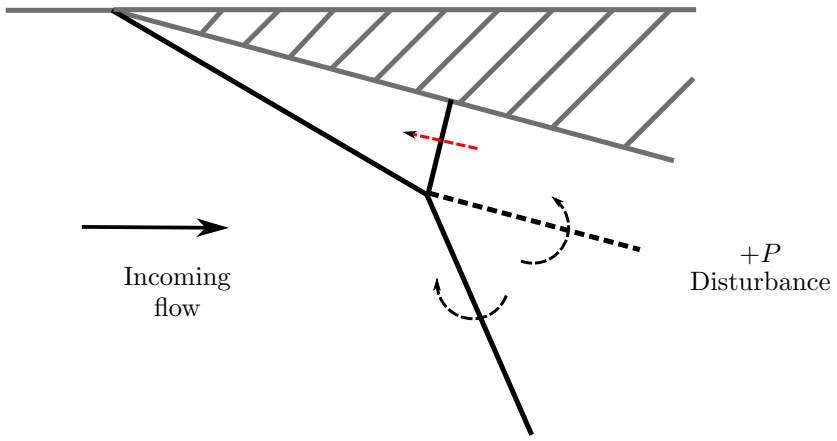

(a) MR↔vNR Transition

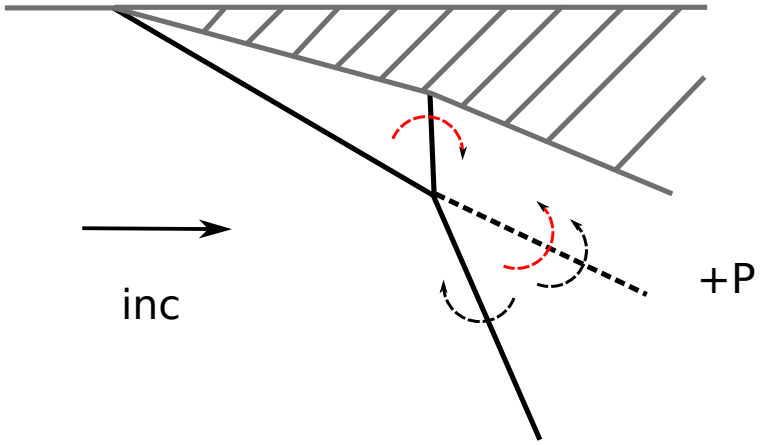

(b) vNR

Figure 5.23: Effect of a positive pressure disturbance on the flow patterns for the (a) MR↔vNR transition pattern and the (b) vNR reflection. Black arrows represent the effect of the Mach stem on the contact surface, red arrows represent the effect of the reflected shock on the contact surface.

can now respond by small rotation. The consequence of the reflected shock rotation is an adjustment to the decrease in pressure, but also a deviation of the contact surface towards the wedge surface. This deviation of the streamline therefore tends to pull the contact surface back and stabilize the flow. The net effect is that the reflected wave can adjust to a negative pressure disturbance, but not a positive pressure disturbance, leading to its slow creep towards the leading apex.

vNR Solution

The vNR solution has a similar behaviour, except this time the "reflected" wave must be supported by the downstream geometry. The effect of a positive pressure disturbance on the vNR solution is shown in fig 5.23(b). To adapt to a downstream, positive pressure disturbance, the Mach stem would need to rotate towards the incoming flow, resulting in the contact surface bending towards the wall (black arrows). The

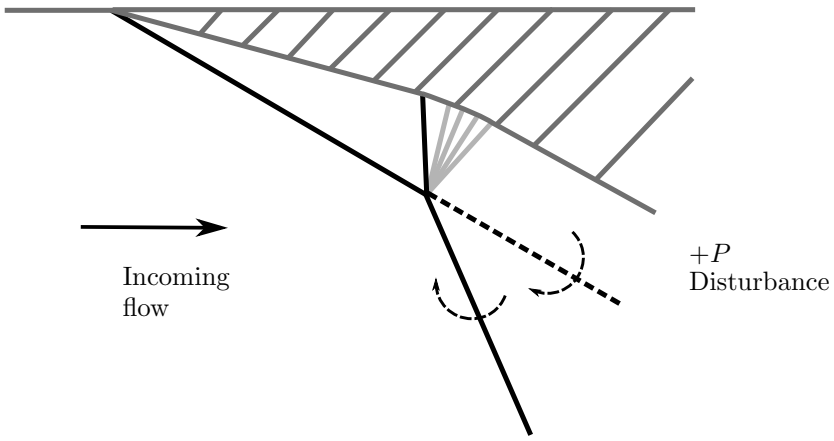

Figure 5.24: Effect of a positive pressure disturbance on the flow patterns for the GR pattern.

positive disturbance also implies a rotation of the reflected wave towards a normal shock configuration and a turning of the contact surface towards the wedge surface (red arrows). Both the Mach stem and the reflected wave are "working together" instead of having opposite effects. There is no opposing effect on the contact surface for a negative pressure disturbance either and hence the vNR solution is expected to be unstable.

GR Solution

A positive pressure disturbance turns the Mach stem clockwise, which would imply a movement of the contact surface away from the wall (fig 5.24). In the GR reflection, the flow is always locally supersonic behind the incident shock, reflected shock and PM expansion. As a result, information cannot be communicated to the PM expansion. One interpretation of the argument is that the movement of the contact surface away from the wall to comply with the changes in the Mach stem creates a diverging channel behind the PM expansion. Supersonic flow in a divergent channel results in a pressure increase, which would amplify the effect of the disturbance. The stability of this wave pattern is not easily investigated using this argument, although its similar behaviour in simulations when compared to the vNR case may indicate the structure is unstable as well.

5.5.2 Experimental and Numerical Studies

The von Neumann reflection regime has been studied numerically by Tesdall, Hunter, Sanders and other researchers [97, 98, 99, 21] using 3 different approaches. Tesdall and Hunter [97] first studied the regime of the von Neumann reflection regime using the unsteady transonic small disturbance equations (UTSDE), which is an asymptotic expansion of the shock reflection problem off thin wedges. Tesdall, Sanders and Keyfitz [98] reported highly resolved numerical solutions of a non-linear wave system similar to the Euler equations.

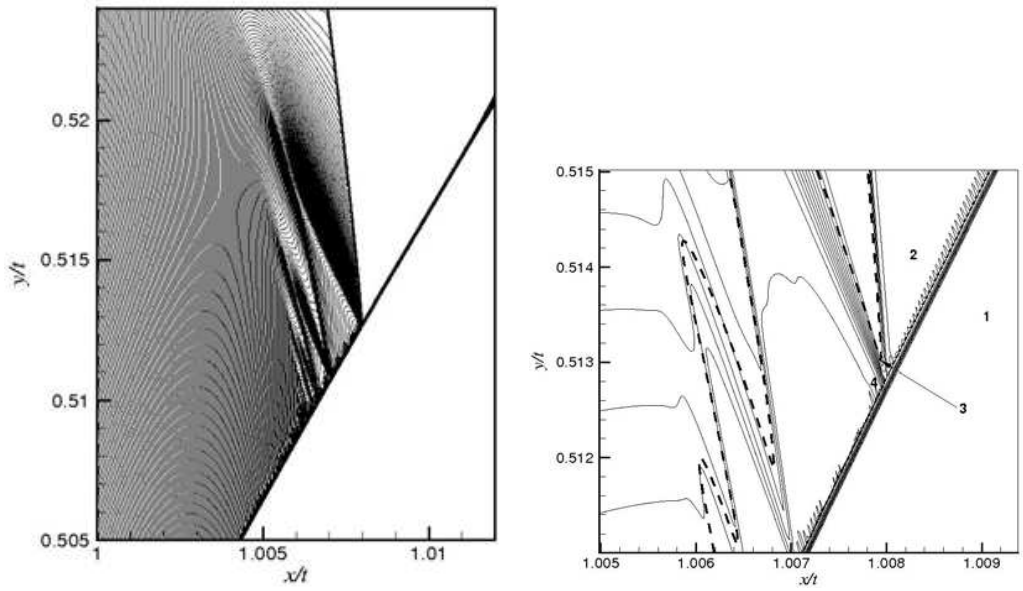

(a) Contour lines of horizontal velocity

(b) Contour lines of vertical velocity

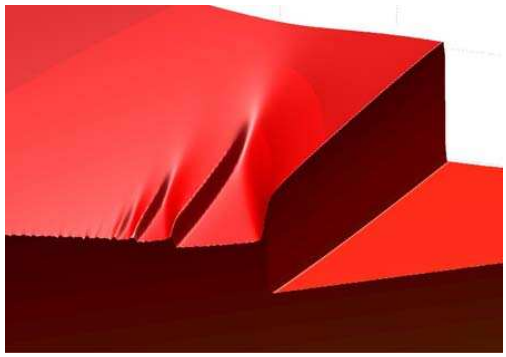

(c) Surface plot

Figure 5.25: Results from [21] showing the structure the authors refer to as Guderley Mach reflection. The dotted line in (b) is the locus of $M = 1$.

This non-linear wave system has no physical equivalent, but shows a structure similar to that of the Euler equations and was proposed as an easier system on which to investigate the von Neumann reflection. Finally, the same authors reported highly resolved calculations of the Euler equations in self-similar variables [99] for weak shocks propagating over a thin wedge. The key findings are also discussed in [21]. Using all three methods, the structure which is exhibited consists of a series of triple points along the Mach stem. Each triple point is the meeting point of three shock waves and an expansion fan. The solutions presented suggest an infinite number of supersonic patches enclosed between the triple points are generated. Fig 5.25 shows the solution the authors predict using the UTSDE method.

Vasilev et al. [22] have attempted to resolve the von Neumann paradox theoretically by analyzing shock polars. The solutions they propose are reproduced in fig 5.26. The existence of supersonic patches located

behind the reflected wave in the case they label ?R and behind both the reflected shock and Mach stem in the case they label GR terminate at the contact surface. These solutions are problematic. The transition line between sonic and supersonic (delimiting the white supersonic patches in fig 5.26) supposes the existence of a weak shock wave. In accordance with their solution, this weak shock would have to terminate at the contact surface without the presence of other features (shocks, expansion fans, etc) at this same point. It is impossible for a shock wave to terminate at a contact surface without other flow features present. This occurrence would imply the uniform flow on the bottom of the contact surface (in fig 5.26, items labeled b and c) can match both the pre- and post-shock states.

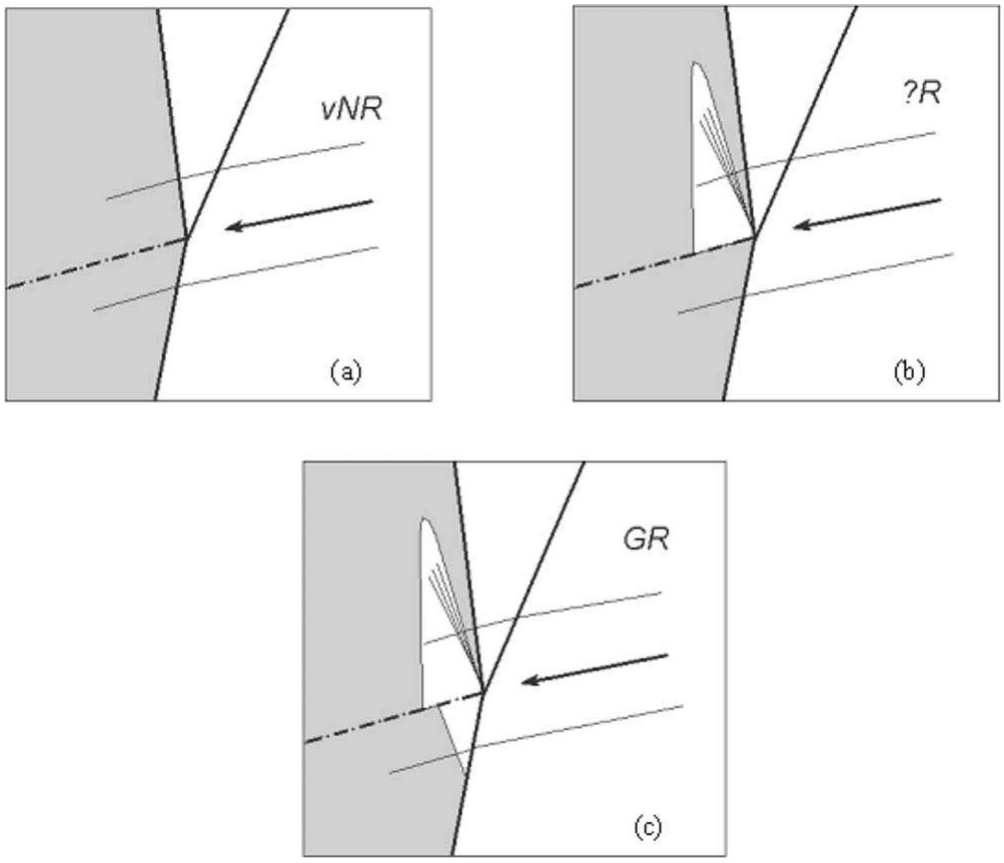

Figure 5.26: Figure 3 from [22] showing what they refer to as supersonic patches behind the triple point observed in numerical simulations.

An early experimental and numerical study by Colella and Henderson [88] attempted to identify the structure of a weak shock reflection over a wedge. The experiments and the numerical solution did not exhibit the same structures which Tesdall and others have later predicted. Colella and Henderson conclude to the existence of a new structure (which they also call von Neumann reflection) consisting of a continuous, curved Mach stem-Incident shock followed by a continuous compression region which steepens into a shock

later downstream. Recent experimental studies by Skews and Ashworth [100] and Skews et al. [101] studying the reflection of weak shock waves using highly resolved optical diagnostics have come to the conclusion that in the absence of a possible Mach reflection, the structure identified by Tesdall and others is the correct flow solution.

5.6 Reactive Reflections

Cellular detonation structures in which the Mach stem is an oblique detonation wave have been calculated for gaseous explosives [84] and were found not to occur in those mixtures. The existence of solutions involving oblique detonations is now dependent on both the incoming flow Mach number M_0 and the CJ detonation Mach number M_{CJ}. The overdrive of the triple point $f = M_0/M_{\mathrm{CJ}}$ depends on the 2D non-linear structure of the detonation wave. Assuming the 2D detonation wave travels longitudinally at the CJ velocity, the overdrive becomes a measure of the triple point track angle $f = 1/\cos^2 \Omega_{\mathrm{TP}}$. This relationship is shown in fig 5.27. Track angles of more than 45° are not expected and overdrives in the range of $1 < f < 2$ are expected. In figure 5.28, shock polars for $A = 20$ and 40 GPa are shown. The three detonation polars correspond to $f = 1.01$, 1.3 and 1.5. Five reflected polars are shown for each value of A. Several matches are possible, depending on the geometry of the wave. There are also regions where no match is possible between an oblique detonation wave and a reflected sock. More information would be needed to determine whether matches with the detonation polar are possible.

5.7 Detonation Simulations

The chemical kinetic model considered for the detonation simulations consisted of a single step reaction with both pressure dependence and temperature dependence (eqn 5.25). The chemical kinetic parameters $n = \theta = 5$ and $\nu = 1$ were selected

$$e(P, V) = \frac{(P + A)V}{\Gamma} - \lambda Q, \tag{5.24}$$

$$\frac{d\lambda}{dt} = k\,(1 - \lambda)^{\nu}\, P^{n} e^{-\theta(\Gamma+1)/[(P(\Gamma+1)+A)V]}. \tag{5.25}$$

The AMRITA framework was used on the same machine used previously with 4 refinement levels and a ratio of 4 between each level. The grid resolution was 128 fine points per half reaction zone length $\Delta_{1/2}$ on the finest grid. The channel dimensions were $100\Delta_{1/2}$ and $20\Delta_{1/2}$ wide. The initial conditions consisted of the 1D ZND solution structure. Four density perturbations were placed ahead of the wave to generate transverse

motion. The adaptive mesh refinement (AMR) was aggressively configured in order to run each simulation in less than a week. The chosen refinement criteria resulted in the AMR dropping at least the finest level as soon as reaction was close to completion. Any transverse shock activity taking place behind the reaction layer was thus most likely under resolved. The AMR behaviour is noticeable, as shown in fig 5.33(a) where shock waves are well defined close to the wave structure, but appear "fuzzy" a short distance downstream.

Four different values of non-dimensional pressure offset were selected, namely $a = A/\rho D_{\mathrm{CJ}}^2 = 0.1$, 0.2154, 0.4954 and 0.6462. These choices correspond to regions where the first possible IR is a MR, vNR, GR or NR respectively. A pseudo-schlieren image and a vorticity map (pseudo soot foil image) were generated at different times for each run and are presented in figs 5.29–5.32. For each value of a, 2 pseudo-schlieren snapshots and 2 pseudo-soot foils are shown. One pseudo-schlieren and pseudo-soot foil show the early stages of development, while the other show the wave structure near the end of the computational domain. A red line denotes the location of 1/2 depletion. For all 4 cases of a, the wave successfully propagated for $100\Delta_{1/2}$ as evidenced by the pseudo-soot foil records. For case $a = 0.1$ and 0.2154, a sharp transition occurs at about $10\Delta_{1/2}$ downstream of the perturbations and several small cell-like structures are created. The detonation wave then relaxes to larger structures.

The detonation structure near the end of the computational domain is shown for all 4 cases in fig 5.33. The case of $a = 0.1$ for which the first IR is a MR (fig 5.33(a)) exhibits a structure reminiscent of the single head spin mode in a gaseous detonation wave. A single triple point is present and in this case, reaction is attached to the transverse wave. There is evidence of instabilities at the front, suggesting further smaller cells may be created. The cases of $a = 0.2154$ and 0.4954 shown in figs 5.33(b)–5.33(c) (the vNR and GR cases respectively) exhibit similar structures. Most noticeable is a triangular structure which occurs at varying scales along the front. Finally, the case of $a = 0.6462$ for which there is no predicted steady reflection pattern is shown in fig 5.33(d). In this case, the structure appears to be detached from the front along most of the wave except near points where two transverse waves recently collided (located symmetrically near the center of the wave). Despite the impossibility of triple point structures, unsteady transverse shocks are propagating along the wave structure. Comparing the overall aspect of each waves in figs 5.33(a)–5.33(d), the waves appear to become globally flatter as a is increased.

An example of the triangular structure observed in the cases of $a = 0.2154$ and 0.4954 is shown in more detail in fig 5.34. This triangular structure is characterized by decaying Mach stems, i.e. that the reaction stays attached to the Mach stem near the triple point, but lags behind the front in other regions. This lagging reaction zone is labeled "back of reaction", while the decayed part of the Mach stem is labeled "incident shock". The "Mach stem" length can appear negligible and varies from structure to structure.

The transverse wave with attached reaction overtakes the lagging reaction front. Most surprising is the varying number of scales at which these structures appear and the fact they seem to propagate in a sequence with the transverse waves all traveling in the same direction.

The 2D simulations presented here must be considered in context. Given the current computational capabilities, the maximum resolution had to be restricted. The length of the domain also had to be restricted to reduce the computational time. Using the collocation algorithm of chapter 4, the wave was found to be stable for the 1D case. A previous study on the single phase SG EOS with a pressure dependent reaction [74] calculated 2D neutral stability curves for $a = 0$–0.2. Two-dimensional instabilities were shown to require a much lower pressure exponent (roughly 2 instead of 7) to become unstable. Given that the Arrhenius dependence of the current model would serve to destabilize the wave further, it is most likely the cases of $a = 0.1$ and 0.2154 are indeed 2D linearly unstable. For the case of $a = 0.4954$, the sudden generation of triple points evidenced by the increased brightness (corresponding to vorticity) on the pseudo-soot foil of fig 5.31(d) points to an unstable wave as well. The case of $a = 0.6462$ is more problematic as the transverse activity is very regular over the length of the domain and there is no sudden generation of transverse activity. This last case may be near a stability boundary.

5.8 Summary

Irregular shock reflection patterns were studied in the context of a SG EOS and for parameters reasonable for an HE. Different reflection patterns were found to be impossible for certain values of the pressure offset, A. The boundaries involve high values of the pressure offset. Taking the solid phase fit of chapter 3 implies the explosive PBX 9502 is in the regular MR region on the boundary between the MR and vNR regions. In other words, the final structure of an unstable wave in PBX 9502 can definitely involve vNR structures and possibly also conventional MR structures. Interestingly, the vNR structure was determined here to be unstable using a combination of non-reactive numerical simulations and a variation of the theoretical argument proposed by Hornung [96]. An attempt was made at simulating the non-linear detonation structure in two dimensions. For PBX 9502, the most relevant simulation case would be that of $a = 0.2154$, which exhibits a peculiar triangular structure composed of a partially decayed lead shock and a transverse wave. Simulations on a larger domain (involving larger computational resources) would be required to ascertain that this structure is indeed the fully-developed detonation structure.

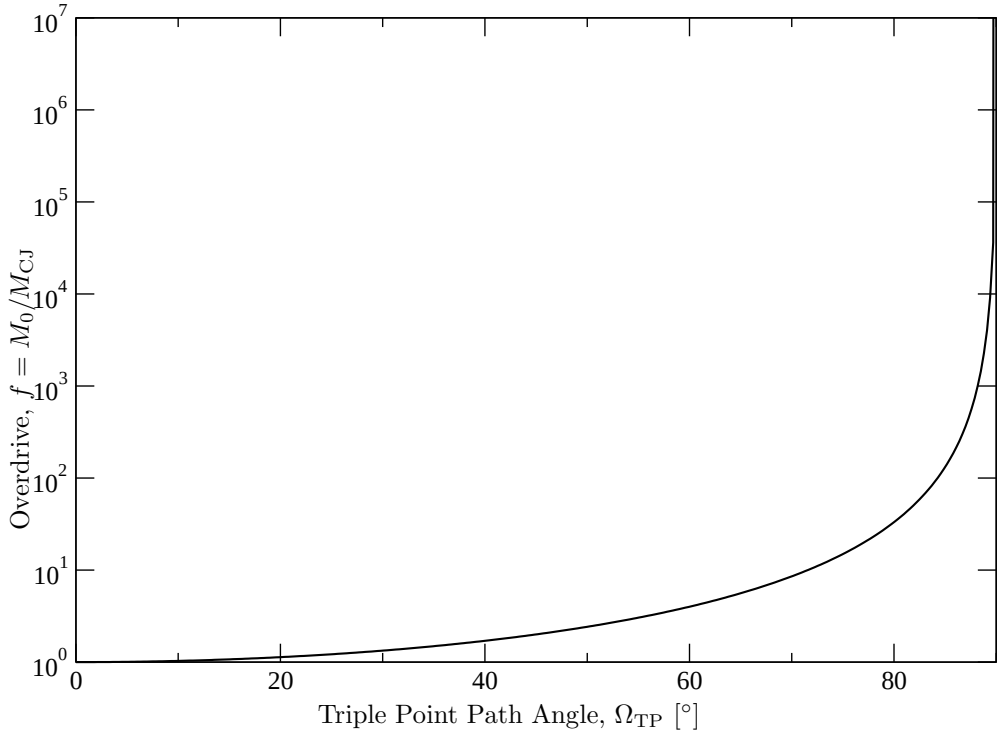

Figure 5.27: Overdrive of the incoming velocity $f = M_0/M_{\mathrm{CJ}}$ used for the construction of the reactive reflection patterns.

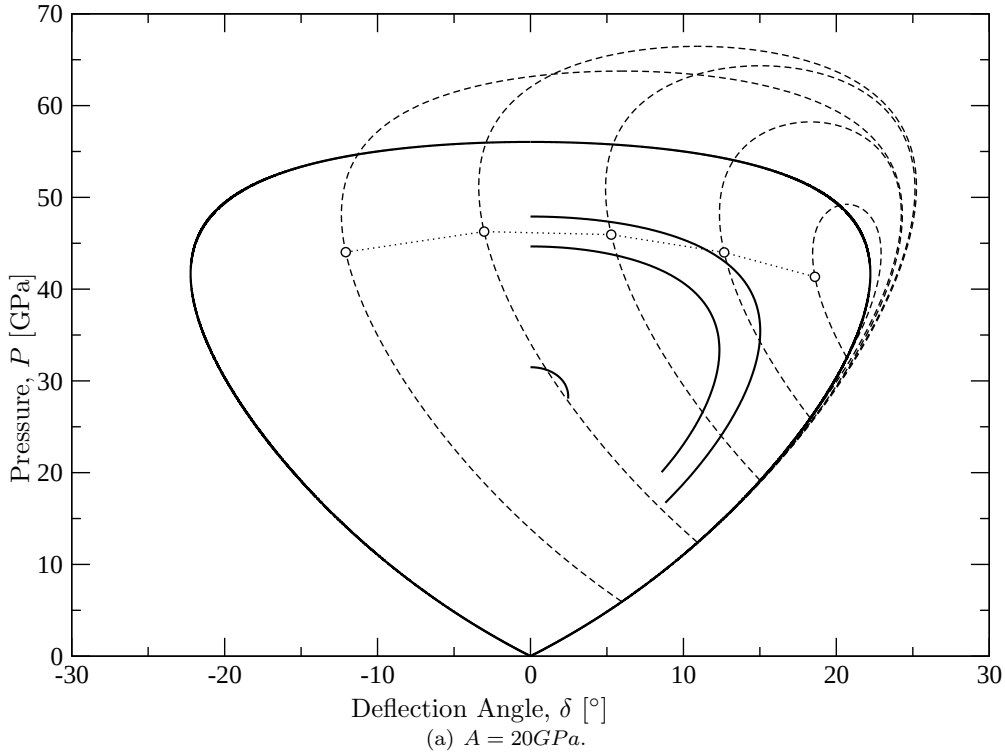

(a) $A = 20GPa$.

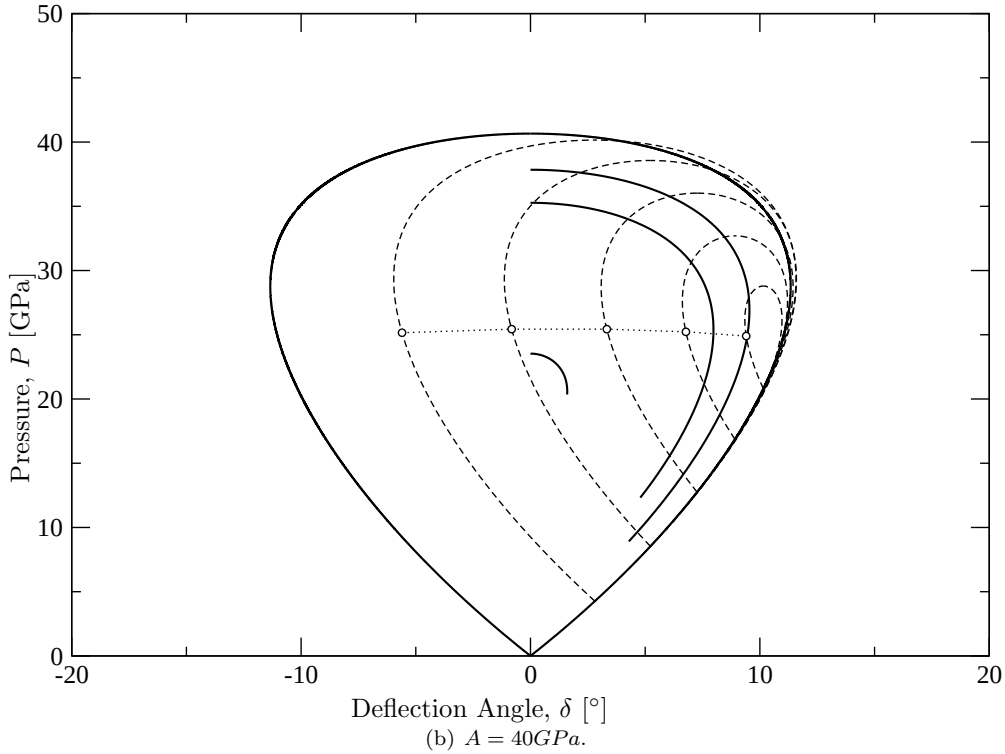

(b) $A = 40GPa$.

Figure 5.28: Polar diagrams for the cases $A = 20$ and 40 GPa. The dotted lines are reflected polars. The thick closed lines are the incident polars while the thick open lines are the detonation polars for overdrive factors $f = 1.01, 1.3$ and 1.5. Higher overdrives result in higher pressures.

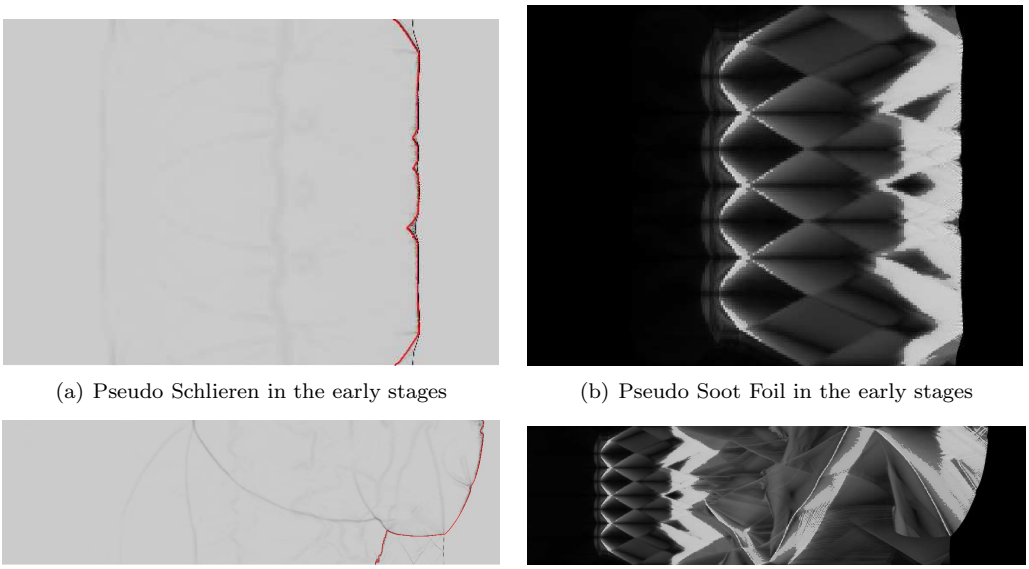

(a) Pseudo Schlieren in the early stages

(b) Pseudo Soot Foil in the early stages

(c) Pseudo Schlieren in the late stages

(d) Pseudo Soot Foil in the late stages

Figure 5.29: Schlieren and vorticity for $a = 0.1$.

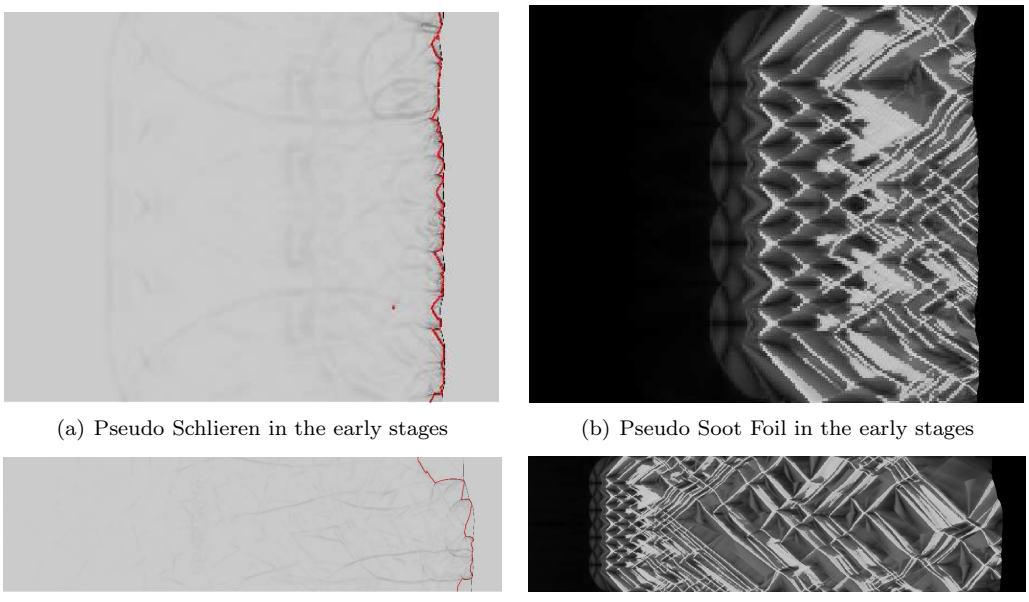

(a) Pseudo Schlieren in the early stages

(b) Pseudo Soot Foil in the early stages

(c) Pseudo Schlieren in the late stages

(d) Pseudo Soot Foil in the late stages

Figure 5.30: Schlieren and vorticity for $a = 0.2154$.

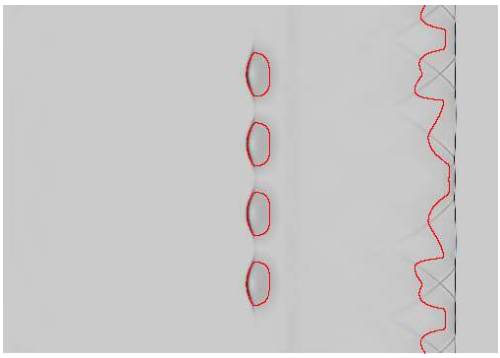

(a) Pseudo Schlieren in the early stages

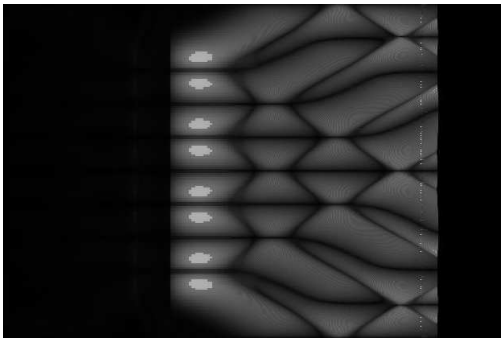

(b) Pseudo Soot Foil in the early stages

(c) Pseudo Schlieren in the late stages

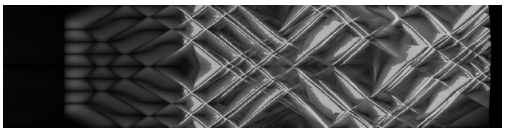

(d) Pseudo Soot Foil in the late stages

Figure 5.31: Schlieren and vorticity for $a = 0.4954$.

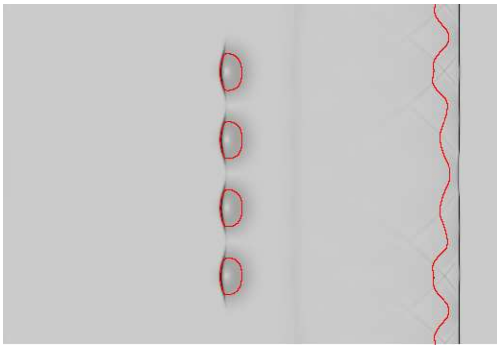

(a) Pseudo Schlieren in the early stages

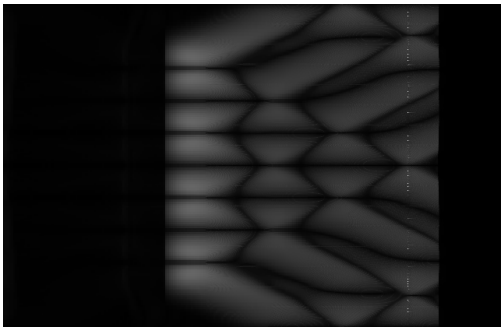

(b) Pseudo Soot Foil in the early stages

(c) Pseudo Schlieren in the late stages

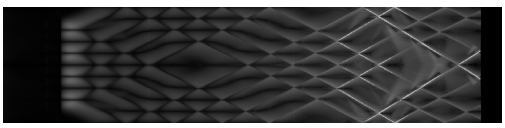

(d) Pseudo Soot Foil in the late stages

Figure 5.32: Schlieren and vorticity for $a = 0.6462$.

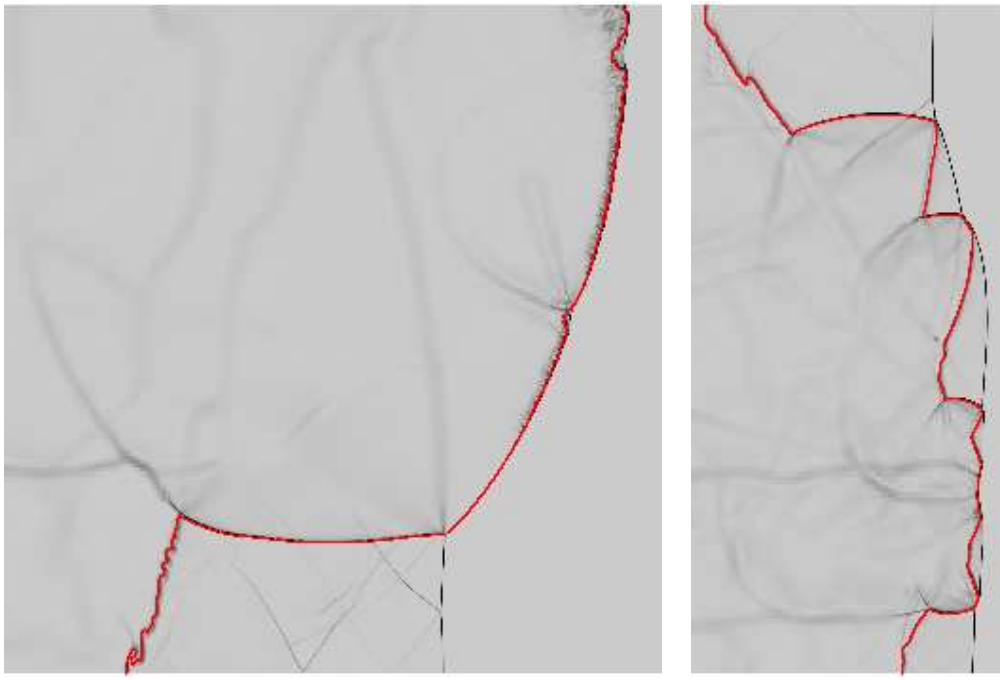

(a) a=0.1 (b) a=0.2154

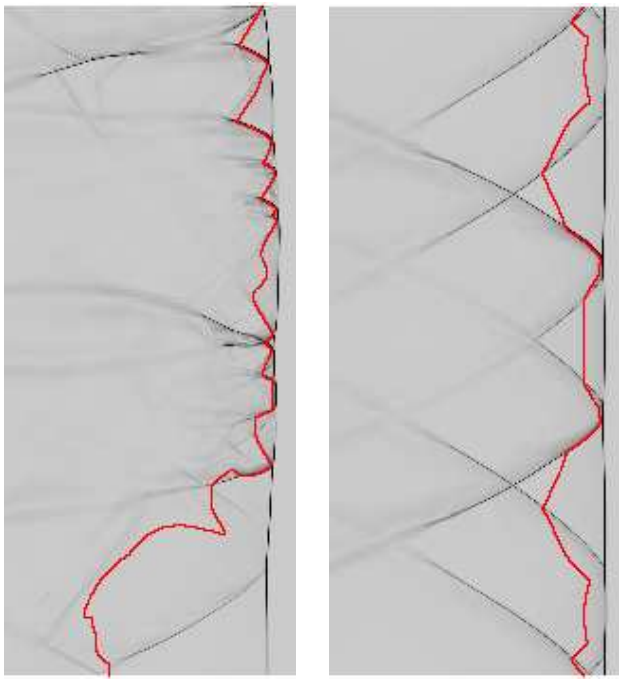

(c) a=0.4954 (d) a=0.6462

Figure 5.33: Schlieren snapshots of the 2D wave structure near the end of the domain for all 4 values of a. The detonations are propagating from left to right and the height of all 4 images is $20\Delta_{1/2}$.

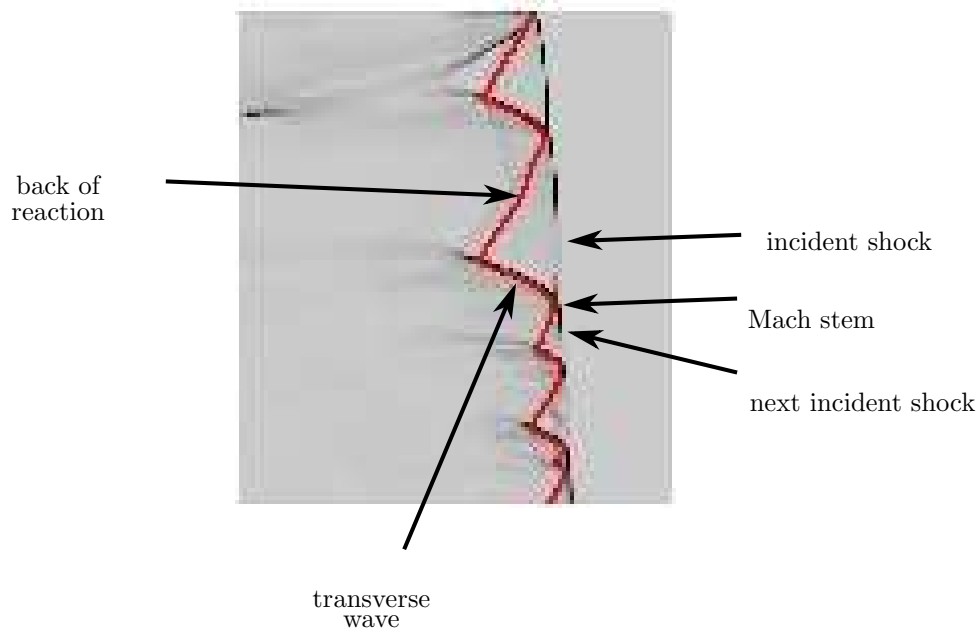

Figure 5.34: Detail of the detonation structure near the end of the computational domain for the case of $a = 0.4954$. Note the triangular structure which appears to consist of an incident non-reactive shock, a reactive transverse wave and a very short mach stem, which quickly decays to the next incident shock.

Chapter 6

Rate-Stick Experiments and DSD Modelling of Highly Non-Ideal Explosives (ANFO)

The non-ideal HE ammonium nitrate fuel oil (known as ANFO) is easy to manufacture from widely accessible individual components. It consists of ammonium nitrate (AN), typically in a porous spherical prill form, blended with fuel oil (FO, no. 2 diesel fuel). It is the most widely used HE in the world, being a common explosive used in mining applications. Its accessibility and ease of manufacture make it of prime interest for preventive purposes. ANFO is an interesting and challenging energetic material to study. First, it is a highly heterogeneous material with both solid and liquid reactants which can react both independently and combined through various kinetic pathways. Second, the ANFO mixture itself is porous as it is essentially a packed bed of roughly spherical particles. Third, it has a relatively low density (only half that of PBX 9502) and can exhibit low detonation velocities especially in smaller charges (on the order of 4 km/s or lower).

As an example of the multiple reaction pathways, one can consider first the decomposition of AN with FO

$$71NH_4NO_3 + 2C_{12}H_{23} \rightarrow 71N_2 + 24CO_2 + 165H_2O. \tag{6.1}$$

Because AN contains both nitrogen and oxygen in a single molecule, another possible pathway is the decomposition of pure AN into nitrogen, water and oxygen

$$NH_4NO3 \rightarrow N_2 + 2H_2O + \frac{1}{2}O_2. \tag{6.2}$$

Since the decomposition of AN yields oxygen, it is technically possible to observe the decomposition of FO with oxygen directly. Also, because the reaction zone of NIHEs is so thick (cms-inches), for unconfined material, entrainment can lead to burning of some hot reactants or intermediate species with surrounding air.

In light of the need for more accurate modelling tools, data is needed to accurately calibrate ANFO detonation models. Rate-sticks experiments, such as those performed here, consist of a cylindrical charge of explosive which is initiated at one end. The axial detonation velocity is recorded along the length of the charge as well as the time of the breakout of the wave along one diameter line at the bottom of the charge.

Assuming the detonation shape is steady and axisymmetric and that the detonation propagation speed is constant by the end of the charge, the breakout measurement yields the detonation shock shape. Ultimately, this measurement allows the calculation of the relationship between the local normal detonation velocity, D_n, and the wave curvature, κ. This information can then be used in the calibration of models, as seen in chapter 3 for PBX 9502.

One characteristic of interest in rate-stick experiments is the material used as a confiner material, i.e. the cylindrical tube which holds the material. In the present experiment, cardboard tubes are used. A shock polar analysis of the interaction between a detonation in ANFO and a cardboard confinement was performed by Sharpe and Bdzil [102] and shows cardboard does not confine the detonation. Other confinement materials, with varying densities and sound speeds, will result in different interactions between the detonation wave and the confining materials. When the axial detonation velocity is greater than the sound speed in the confining material (which is most often the case for conventional high explosives or IHEs), the interaction between the detonation wave and the confining material is local and can be solved by a shock polar analysis. The solution of this polar analysis yields at least one important characteristic associated with an explosive-confiner pair, the edge angle. This edge angle is the angle defined by the normal to the shock surface and the vertical at the edge of the charge, where the explosive meets the confining material. A summary of possible explosive-confiner interactions is given in [103] and appendix C of [25]. In the case of an unconfined material, as is essentially the case here, the edge angle the detonation forms is the sonic angle (the sonic angle on the HE shock polar). The flow at the edge of the HE and the confiner are then connected by a Prandtl-Meyer fan.

The information obtained from rate-sticks can be used in calibrating the DSD model, as is done here. The DSD model in essence replaces the detonation structure by a surface with a given propagation law which expresses the surface velocity as a function of its curvature. This model can be calibrated using the $D_n - \kappa$ information and edge angle observation obtained from rate-stick experiments. In the case of NIHEs, an additional complication arises when the ANFO is surrounded by a high-sound-speed (metal) confiner, due to the low detonation propagation speed. When the speed of the detonation is less than the sound speed in the confining material, information in the confiner can run ahead of the detonation. This can result in energy transfer to the unreacted material from the detonation wave and the products via the confining material. Such cases will be the subject of further investigation of the NIHE ANFO.

The present rate-stick experiments are motivated in part by previously obtained results which showed anomalous $D_n - \kappa$ behaviour for a lot of ANFO explosive which had been stored in a bunker for over a year [23]. Four different mixtures are used in the present series of experiments to try and establish the effect of

prill size, prill density, prill porosity and FO content on the properties of detonations in ANFO, and the resulting DSD calibration.

6.1 Experimental Setup

6.1.1 Confiner Material

In the present set of experiments, cardboard tubes (rainguard sonotube) were chosen to confine the ANFO in a cylindrical geometry. The cardboard was sufficiently rigid to support several hundred kilograms of HE, but provided no influence on the dynamics of detonation propagation. Two different diameters were used: 203.2 mm (8 in.) with a thickness of approximately 2.6 mm and 304.8 mm (12 in.) with a thickness of approximately 3.1 mm.

6.1.2 Axial Detonation Velocity Diagnostic

The velocity of the detonation was measured along the length of the charge using 10 Dynasen shorting shock pins located every diameter from the end of the charge with the first pin located 1 diameter away from the end of the charge. The shock pins are composed of a metal electrode housed in a grounded metallic casing. The electrode and the grounded casing are separated by a short distance. When a shock wave passes by the shock pin, the casing is deformed and contacts the electrode. A voltage differential of 100 V is imposed between the electrode and the casing using a charged capacitor. Once contact is made, the capacitor discharge is recorded on an oscilloscope. The shock pins were mounted on the side of the tube such that each shock pin protruded inside the tube by about 1.04 mm. A picture of a typical shock pin mounted to the tube is shown in fig 6.1. The foam component is there to hold the pin perpendicular to the tube surface.

6.1.3 Shock Shape Diagnostic

A pentaerythritol tetranitrate (PETN) paint strip was used to record the breakout time of the detonation wave at the end of the charge. In this method, the detonation wave strikes a Plexiglas plate, glued to the end of the charge, on which a thin strip of PETN powder was deposited along the diameter of the charge. PETN is, by definition, the most sensitive secondary explosive and the impact of the detonation wave promptly initiates the PETN. The light generated by the initiated PETN is recorded by a camera located in a nearby bunker. The PETN strip thickness is 0.1-0.3 mm. Because of this very small thickness, the local initiation of the PETN via the ANFO detonation does not transition to a detonation. Detailed views of the PETN strip and Plexiglas plate are shown in fig 6.2. In fig 6.2(b), the PETN powder is covered by a strip of copper

tape. This strip of tape serves two goals. First, it holds in place the PETN powder, which would otherwise slide off the plate. Second, it blocks light generated by ANFO mixture. The light initially recorded by the camera is thus only light from the PETN powder. A plate already assembled to the tube at the firing site is shown in fig 6.3(a).

The camera used to record the light emitted by the PETN was a Cording model 136 streak camera. A streak camera has a thin, slender field of view, which was here aligned with the PETN strip. The light emitted by the PETN on this field of view enters the camera and is projected onto a rotating mirror. The rotation of the mirror causes the image to "sweep" along a film track, such that luminous events on the field of view moving horizontally will appear as straight or curved lines on the film track. The film record is thus an actual $x - t$ diagram of the detonation time of arrival along the bottom diameter of the charge. On this record, a straight line implies an event moving at a constant speed. A positive curvature line implies a feature slowing down, and a negative curvature line implies an accelerating phenomenon. The particular camera model used in the present series of tests provides continuous access, i.e. that when the streak image reaches the end of the film record length, it "wraps" back around to the beginning, and any timing error does not result in the loss of data. The streak camera was located in a small bunker only a few meters from the charge and was therefore protected via large plywood forms filled with sand. These sandboxes being quite heavy, they were also used to stabilize the charge itself. The front of the camera bunker as well as the sandboxes are visible in fig 6.3(b). The record of the time of arrival can be related to the wave shape. Assuming the axial propagation velocity of the wave is steady, the film record is related to the wave shape via two scales. One scale is derived using the rotational speed of the streak camera mirror. This scale relates the distance of objects along the film track with the time of arrival of these objects at the bottom of the charge. There is a nonlinearity in the conversion factor between the rotational speed of the mirror and the time scale along the film track which was taken into account in the analysis. The second scale is measured using still photographs of the bottom of the charge made with the same streak camera. On these still photographs, a scale is visible (fig 6.4). This scale relates the position along the width of the film track with the position along the diameter of the charge. Using these two scales, the film record is transformed into an $x - t$ diagram of the time of arrival of the detonation at the bottom of the charge vs. the position along the diameter of the charge. This record is transformed into a wave shape by assuming the axial wave propagation velocity is steady, such that $\Delta z = D_0 \Delta t$. Here, D_0 is the measured steady detonation velocity along the charge, Δt is the relative time of arrival of the wave and Δz is the relative height coordinate of the detonation wave shape. The complete transformation procedure is given in appendix D. A sample still frame and streak record are shown in fig 6.4.

6.1.4 Complete Tube Assembly

A sketch of the experimental setup is shown in fig 6.5. The tube is mounted vertically on a wooden stand. The light emitted by the PETN light strip, located at the bottom of the tube, is reflected in a first surface angled mirror below the shot assembly. The streak camera is located in a concrete bunker and a glass port in the bunker wall allows visual access to the charge. The charge is initiated at the top using an explosive train composed of an RP-83 detonator and a booster. The detonator initiates one or more layers of rubberized PETN explosive (in this case layers of C-6 or 6 g/in^2) which in turns initiates the ANFO charge. A single layer of C-6 was used for all charges except the Fragmax ammonium nitrate charges which required 2 layers of C-6 explosive. A fully assembled 304.8 mm charge is shown being loaded in fig 6.3(b). Part of the bunker which houses the streak camera is visible on the far right with a sand filled box in the center acting as a protective barrier. Each explosive charge was assembled on the firing pad following the steps:

1. Construct the protective sand filled barrier for the camera bunker.
2. Assemble the wooden shot stand and install the angled first-surface mirror to direct the light from the PETN strip.
3. Roughly align the PETN strip and secure the Plexiglas plate to the shot stand.
4. Mount the cardboard tube (confiner) vertically over the Plexiglas plate and glue the bottom of the tube to the plate to ensure no ANFO leaks at the bottom of the charge.
5. Fill the charge with ANFO. Each charge was filled in increments of 2-3 in and tamped with a metal plate at the end of a long rod. The tamping ensured no air pockets were present and the packing density was as uniform as possible.
6. As the tube is being filled, install the shorting pins on the side of the charge.
7. Place the booster and detonator on top of the ANFO charge, inside the cardboard tube.
8. Finalize the alignment of the camera with the PETN strip.

The ANFO mixture used in a particular shot was mixed in batches of 40 lbs in a load shed. The ammonium nitrate and the fuel oil were carefully weighed to ensure the FO% was within 0.014 percentage points of the desired value. The 40 lbs batches were then mixed together in a large tumbler to ensure consistency of the charge over the entire length of the charge. The ANFO mixture was always mixed within 6 days of the firing of the charge. In addition to the above steps, the sides of the first 4 shots were covered

with a tarp, leaving a roughly 12 in. gap between the tarp and the outside charge surface. Two 1.5 kW electric heaters were placed between the tarp and the charge in an attempt to heat the charge to a uniform temperature. (See section 6.2.)

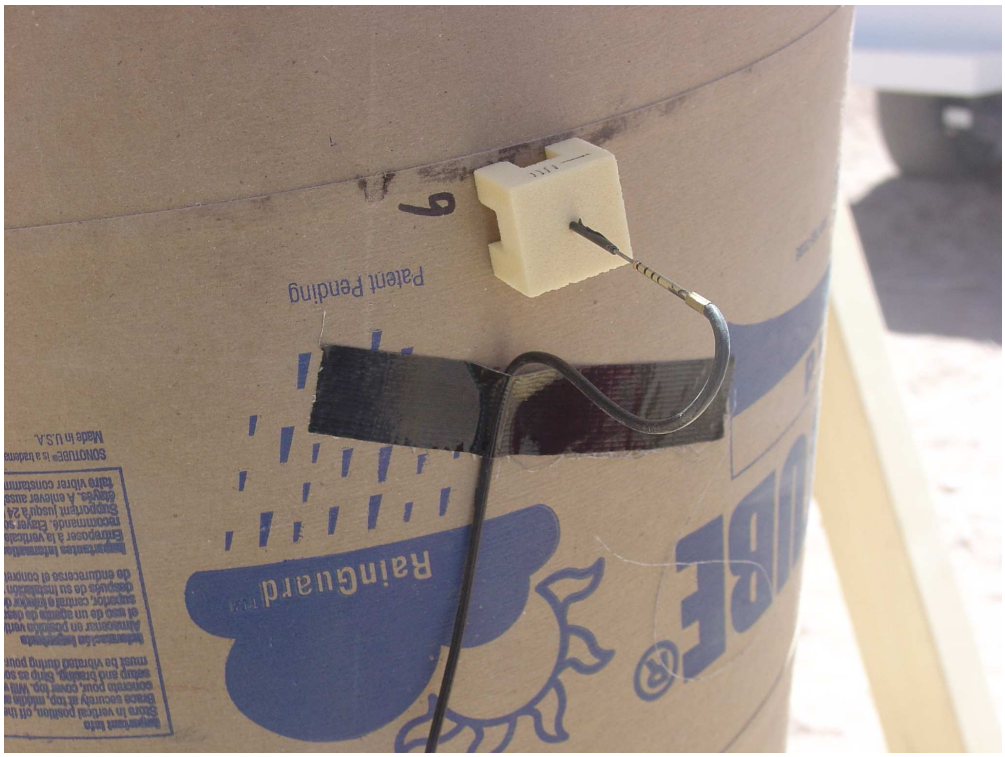

Figure 6.1: Shorting pin mounted in an assembled charge to record the detonation velocity.

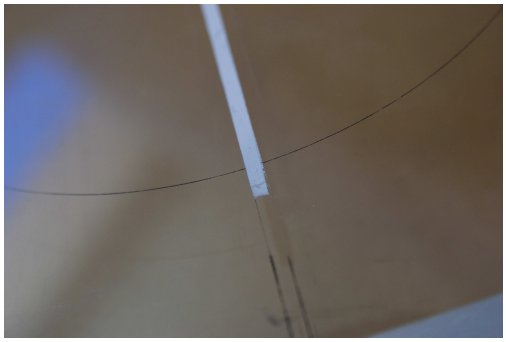

(a) Detail of the painted PETN strip.

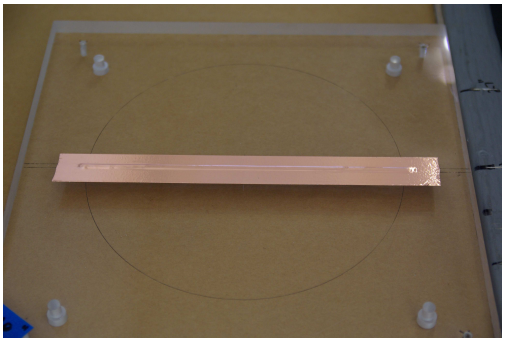

(b) Plexiglas plate with covered PETN strip.

Figure 6.2: Details of the finalized PETN paint strip on the bottom plate of the charge.

(a) Plexiglas plate mounted to the bottom of the cardboard confiner of a charge.

(b) An assembled 304.8 mm charge during the filling operation.

Figure 6.3: A 304.8 mm charge as an example of the design of the charge showing in (b) the complete charge during the fill operation. The sandboxes protecting the bunker of the streak camera are visible on the right. Shown in (a), the assembly of the clear acrylic plates and the supporting legs. The plate is glued to the bottom of the charge.

Shot #	T_b (°C)	T_m (°C)	T_o (°C)
4	21.5	21.5	19
5	19.5	20.5	10.5
6	24.5	16.5	10-15
7	19.5	24.5	6-9
8	23.5	22.5	19-22
9	25.0	25.5	24.5
10	24.5	25.5	26-27
11	29.5	28.0	27-32

Table 6.1: Temperatures recorded for the ANFO shots. T_b and T_m are the value of the temperature at the bottom and the middle of the charge respectively before the shot was fired. T_o is the ambient temperature.

6.2 Uniformity of Charge Temperature

An attempt was made at controlling the temperature of the different shots. On cold days, two electric heaters and a tarp were used as described above. On hot days, the filling process was completed as quickly as possible to avoid letting the material heat in the sun. On most tests, the ANFO mixture was allowed to reach a uniform temperature in a temperature controlled storage room before it was brought to the test pad. Three thermocouples were used; one measured the ambient air temperature while the other measured the temperature of the ANFO at the bottom of the charge and around the middle of the charge length. The target charge temperature was 25°C and the actual temperatures recorded before the shot was fired are shown in table 6.1. The time records of the different temperatures are shown in appendix C in figures C.2-C.2.

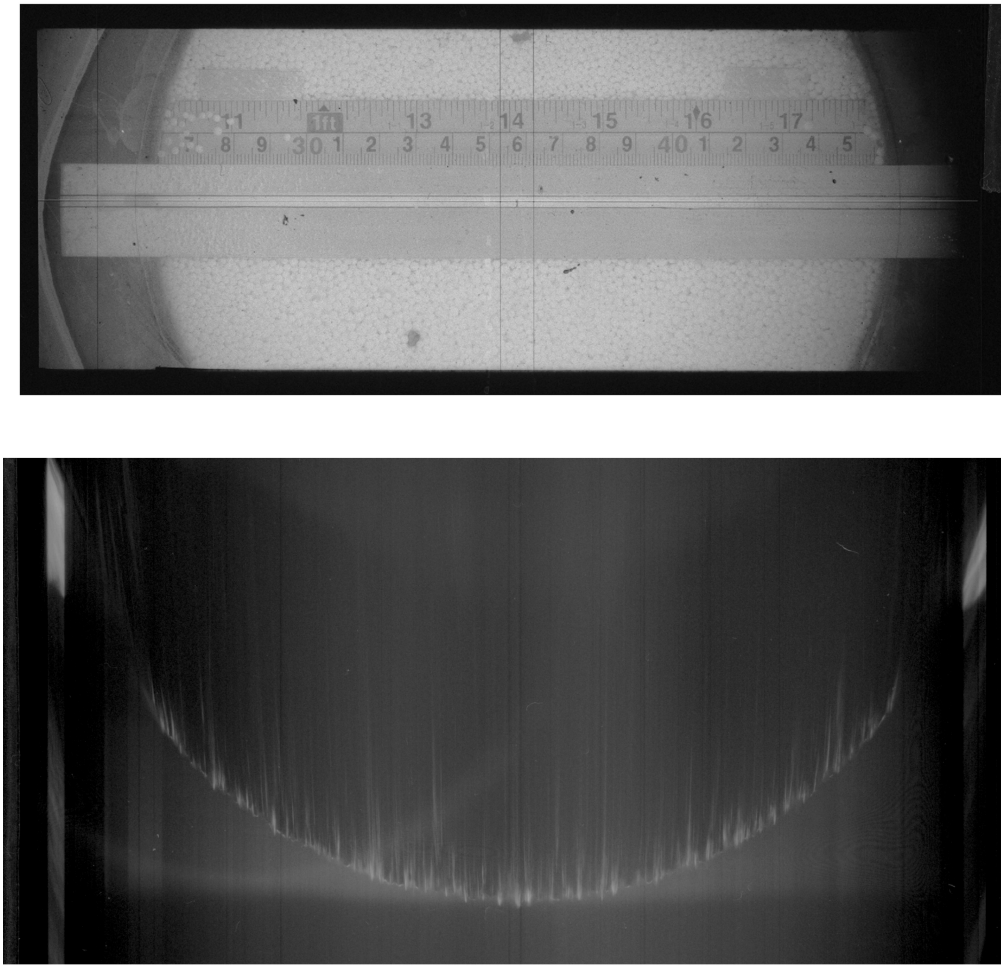

Figure 6.4: Sample still frame (top) and streak record (bottom). The scale from which the horizontal length scale is derived is visible on the still frame. The vertical length scale is derived from the axial detonation propagation velocity and the mirror rotational speed.

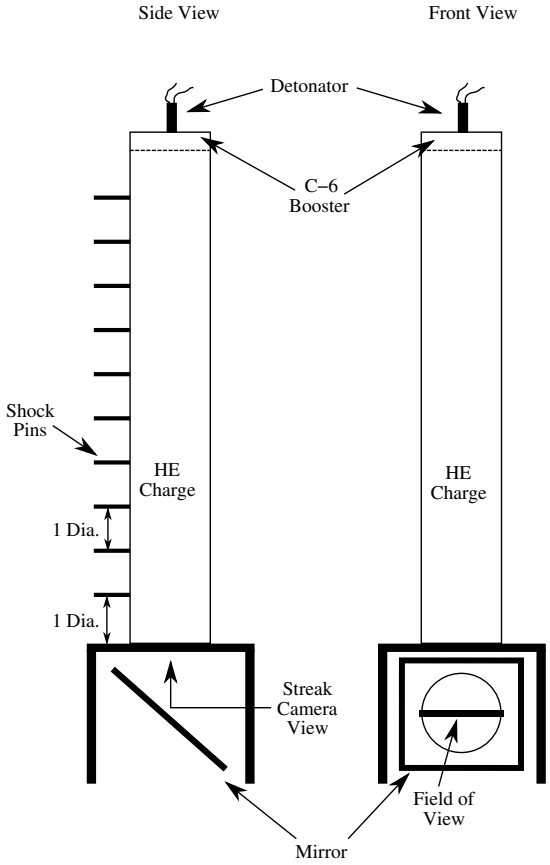

Figure 6.5: Setup of the large-scale rate-stick experiments.

6.3 Different Materials Tested

In order to vary the characteristic of the mixture, three different types of AN prills and two different mixture compositions were tested. The three different types of AN prills are the *regular HE grade* prills and two types of specialty prills sold under the trademarks *Fragmax* and *expan*. The Fragmax AN prills consist of smaller, less porous prills, which results in higher density charges. The expan prills are of roughly the same size as the regular HE grade but contain 0.03% by mass of plastic microballoons inserted during the manufacturing process. The presence of the microballoons blocks some of the voids naturally present in the prills. The regular HE grade prills were tested in mixture of 6% and 5% FO by weight, in order to verify the anomalous behaviour observed by Catanach and Hill [23]. The specialty prills were tested in a mixture of 6% FO by weight, which is the standard, stoichiometric FO ratio used for ANFO. By using the Fragmax prills, the prill diameter and charge density is varied. By using the expan prills, the amount of porosity in the prills is varied.

A summary of the physical characteristics of the different AN materials and the final mixed products is

presented in table 6.2.

The three different types of AN prills were photographed and are shown at the same photographic scale in figure 6.6. These photographs were used to measure the average diameter of the different prill types using the NIH software ImageJ. These measurements should only be considered to be a rough estimate of the size distribution and as such, only the average diameter as well as the maximum and minimum diameters measured are reported and no standard deviations were calculated or binning analysis performed. At least 200 measurements were taken for each image. The regular HE grade prills and the expan prills were easily measurable, but the Fragmax prills (which had been mixed with FO by the time the picture was taken) proved harder to measure. A lot of very fine particles are visible on the Fragmax images, which aren't visible for the regular HE grade and expan prills. These fine particles are also seen to stick to the outside of larger prills in the Fragmax picture making them hard to discern and measure. It is possible that the very fine material was also present in the HE grade and expan AN bags, but was not collected when the samples were taken for the pictures. Such fine material, in dry samples, may adhere to surfaces due to static electricity.

The expan prills are nominally of the same size as the regular HE grade prills and have a similar diameter distribution. The Fragmax prills are of a noticeably smaller diameter than the other two types of prills, but with a wide diameter variation. The main characteristics of the different prills and the resulting charge densities (averaged between the 203.2 mm and 304.8 mm charges for each type of experiment) are also shown in table 6.2.

Prill		Mixed Explosive
Type	Average Diameter (Min–Max) [mm]	Density [g/cc]
Regular HE grade	2.2 (1.6–3.9)	0.883–0.903
Fragmax	0.6 (0.1–1.3)	1.168–1.169
expan	2.0 (1.0–3.5)	0.793–0.807

Table 6.2: Physical characteristics of the different AN prills and the finished mixed explosives.

6.4 Previous Data on ANFO

Rate-stick data on ANFO was obtained by Catanach and Hill [23] as well as Bdzil et al. [24]. Nominally standard ANFO (i.e. regular prills with a 6% FO ratio) was tested in cardboard tube over a range of charge diameters, from 77 mm to 205 mm. In Hill [23], the shock shapes were fitted to obtain the $D_n - \kappa$ data experimentally, which exhibited a non-standard behaviour, where the curvature-velocity data:

1. shows little or no overlap between sticks of different sizes and smaller sticks lie to the right of larger ones,

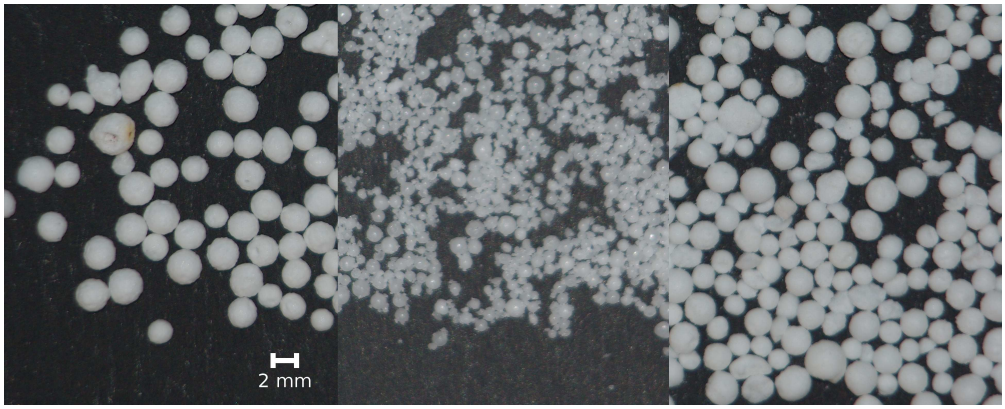

Figure 6.6: The three different types of AN prills tested in this series of experiments. On the left are regular HE grade prills. In the center are the Fragmax AN prills and on the right are the expan AN prills. All three images were taken at the same magnification.

2. exhibits a large velocity deficit with little κ variation, and

3. reaches a maximum κ an an intermediate R,

as shown in fig 6.7 taken from [23].

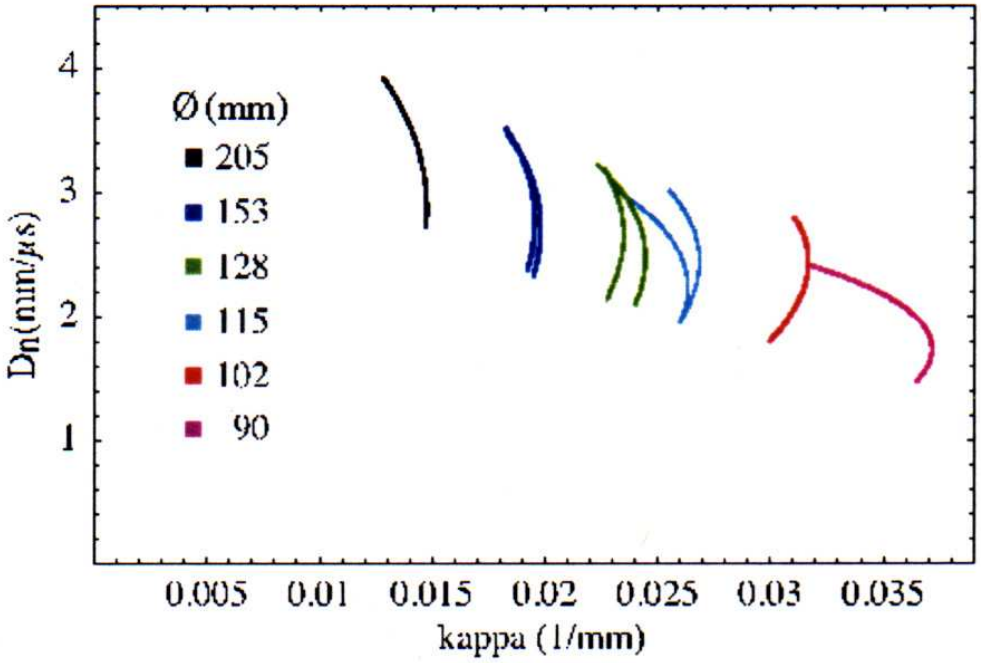

Figure 6.7: Local normal propagation velocity vs. local curvature. Fig 4 from [23].

This anomalous behaviour has been attributed to the storage history of the particular material lots used for these experiments. The ammonium nitrate and fuel oil mixtures had already been mixed when a forest fire started burning in the area. This fire forced the tested material to be stored for very long periods of

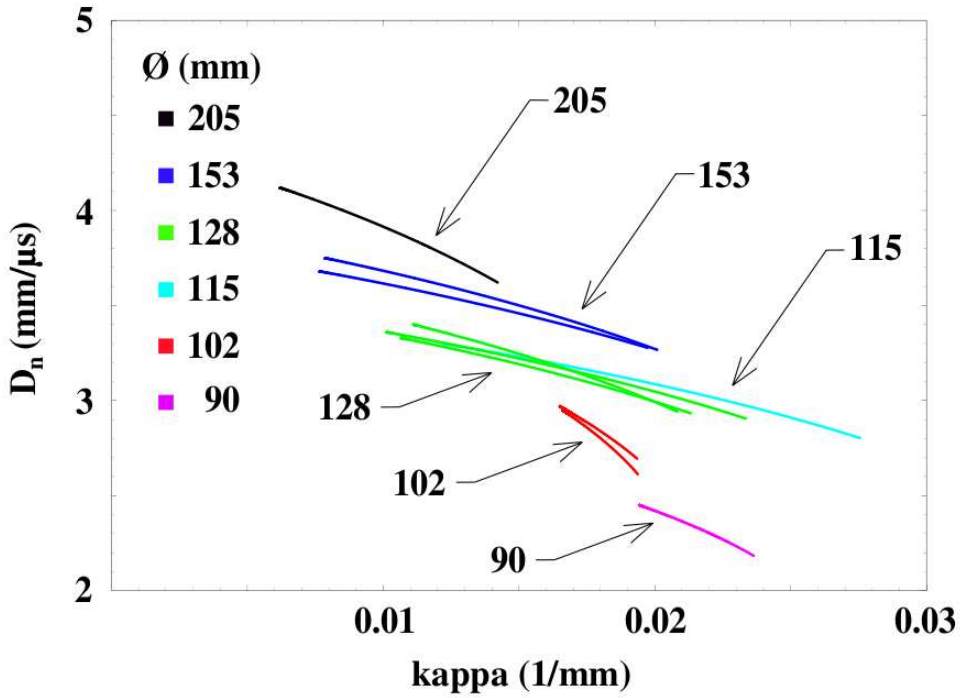

Figure 6.8: Normal velocity vs. curvature relationship for unconfined ANFO. Fig 2 from [24].

time in a hot climate and possibly heated by the fire. The long storage time allowed some of the fuel oil to seep out of the mixture, leaving a final mixture with about 5% FO [24]. In addition, the crystal structure of AN is known to change when it's cyclically heated and cooled. This long storage time and the possibly large temperature variations of the storage area are suggested as potential causes for material changes that would have influenced the behaviour of the material.

A second set of paper tube confined ANFO rate-sticks is presented along with a DSD calibration in [23]. In this case, the experimentally measured relationship between the local normal velocity, D_n, and the local total curvature, κ, are closer to an expected behaviour. For each charge diameter, the $D_n - \kappa$ relationship is "flatter" than that of [23]. There is still no overlap between the $D_n - \kappa$ relationships measured at different charge diameters. (See fig 6.8.)

Older data about the detonation properties of ANFO can be found in the Ph.D. thesis of Yancik [104]. A lot of the work in this thesis characterizes the detonation phase velocity and the sensitivity of ANFO mixtures when one alters the

1. prill density,
2. prill porosity,
3. FO weight %

4. confinement.

The detonation velocities were measured via time of arrival gauges and sensitivity of the different mixtures was measured in the required minimum number of blasting caps, amount of a particular booster explosive, etc. Hence, a higher sensitivity means that a smaller booster is required or a lower number of blasting caps. Some of the conclusions, with the most interesting ones highlighted are

1. positive mixing of the AN and FO results in higher detonation velocities,
2. protecting the material from moisture results in higher detonation velocities and higher sensitivity,
3. *the stoichiometric ratio of regular HE grade prills with no. 2 FO is around 5.5%,*
4. critical (minimum) diameters for HE propagation are 1.5 inches in iron pipes and 4 inches unconfined,
5. *an increasing diameter for an iron confined charge requires a larger amount of booster material,*
6. *an increasing diameter for an unconfined charge requires a smaller amount of booster material,*
7. *while the detonation velocity increases roughly linearly with charge density, a charge with a 15% higher density requires 4 times more booster material,*
8. *smaller diameter prills (obtained here through grinding) yield a higher detonation velocity and a more sensitive mixture, even a cap sensitive mixture for fine enough material,*
9. water content does not change the sensitivity dramatically, but reduces the detonation velocity with a failure observed for 10% moisture,
10. *cycling through the 89.9F (*$23.2^\circ C$*) transition point and hence altering the prill structure yields a more sensitive mixture.*

While DSD modeling requires only information on the explosive mixture as a whole, some data on the ammonium nitrate component is worth mentioning. This research comprises a series of reports from Queen's University, Kingston, Canada, mainly driven by research into industrial accidents [105, 106]. These reports span both the properties of molten [107, 108, 109, 110, 111, 112] and prilled [113, 114, 115, 116] ammonium nitrate. The topics range from shock initiation studies [107, 109, 113, 115, 116] to thermal decomposition [108], to projectile initiation [110] and to detonation and deflagration-to-detonation transition [111, 112, 114].

In [109], the Hugoniot curve of ammonium nitrate is experimentally determined, but only in its molten form and not as solid prills.

Shot Number	AN Type	FO Ratio	Charge Diameter (mm)	Designation
4	Regular HE Grade	5%	203.2	RHE5
6	Regular HE Grade	5%	304.8	RHE5
5	Regular HE Grade	6%	203.2	RHE6
7	Regular HE Grade	6%	304.8	RHE6
8	expan	6%	203.2	EXN6
11	expan	6%	304.8	EXN6
9	Fragmax	6%	203.2	FGM6
10	Fragmax	6%	304.8	FGM6

Table 6.3: Summary of the 8 experiments performed.

In [108], the authors point out that multiple kinetic pathways exist for ammonium nitrate and that the equilibrium products are dependent on the temperature at which the decomposition occurs. This fact further reinforces the idea that ANFO kinetics would be difficult to determine as the CJ state and the thermodynamic path through the reaction zone are heavily dependent on the confinement of the charge. As a result, different confinement situations could drive ANFO to react along different kinetic pathways. Also, even if the Hugoniot characteristics of the different components (AN and FO) could be determined independently, there is no simple mixture rule for shock response.

6.5 Experimental Results

The resulting data from the rate-stick experiments consists of detonation velocity measurements along the axis of the charge by the shorting pins and records of the wave breakout from the streak camera. Eight experiments were performed using four different mixtures of AN at two diameter charges. Table 6.3 shows the conditions of the 8 experiments.

6.5.1 Axial Detonation Velocity Measurements

The analysis of the rate-stick data to obtain the $D_n - \kappa$ data, both the fitting method presented in section 6.5.3 and the DSD method presented in section 6.6, assume that the wave is steady. This assumption implies two different concepts:

1. the axial detonation propagation velocity is constant,

2. the detonation front shape does not vary with time.

In the present section, the variations in the axial propagation velocity are quantified. The detonation shock shape, for a granular material, is not invariant. The relationship between curvature and propagation

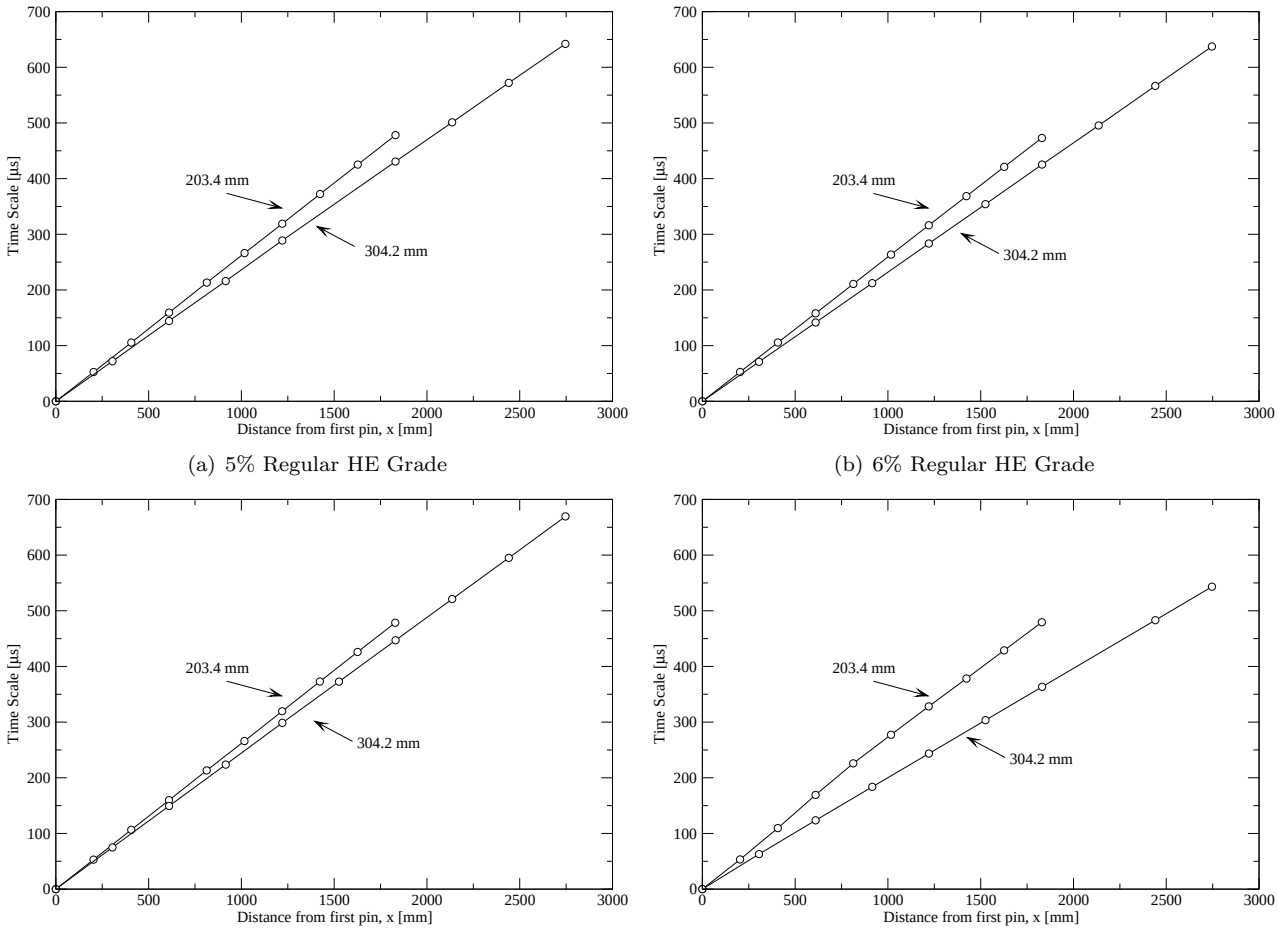

(a) 5% Regular HE Grade

(b) 6% Regular HE Grade

(c) 6% expan

(d) 6% Fragmax

Figure 6.9: x–t diagrams for the 4 different mixtures tested and both diameters.

velocity is based on an "average wave curvature". In other words, the small scale structure of the front are overlooked and the "global" wave curvature is the one considered here.

Two different measurements of velocity are reported in this section. First, the axial detonation velocity measurements along the length of the charge are calculated by assuming a constant velocity between each pair of shorting pins. Knowing the distance between the pins, the average velocity at the midpoint is the difference in time of arrival divided by the separating distance. The original $x-t$ diagrams constructed from the time of arrival at the different pins are shown in fig 6.9. The distances are reported in fig 6.9 in actual length of mm.

Figs 6.10(a) and 6.10(b) show the variation of axial velocity for the 203.2 mm and 304.8 mm charges respectively. The location of the axial velocity measurement is reported as distance from the end of the charge in length over diameters, L/D. The wave breakout time is measured at $L/D = 0$.

The second reported detonation velocity measurement is the final wave velocity at the breakout point, $L/D = 0$. The terminal velocities reported in table 6.4 are calculated by fitting the $x - t$ diagram of the time of arrival of the detonation lead shock at the different pins. The terminal velocity has also been calculated by averaging the axial velocity measurements from the 2-point finite differences over the "steady" portion of the wave. This "steady" portion is estimated visually. Both methods were found to be in close agreement. See appendix C for a comparison between this method and the average of the 2-point finite difference velocity measurements. The standard deviation of the last four axial velocity measurements is also reported in table 6.4 and gives an estimate of the "steadiness" of the wave.

All 203.2 mm charges, except the Fragmax based charge, show no apparent trend in the axial velocity measurement. For the 304.8 mm charges, the 6% regular HE grade and expan based charges show no apparent trend. The 5% regular HE grade based charge presents a slightly accelerating trend as the wave approaches the end of the charge. The standard deviation is similar for all those experiments, in the range 0.0255-0.0576 mm/μs. The Fragmax based charges exhibit more interesting dynamics over the measurement range. In the case of the 203.4 mm charge, the wave initially decelerates and subsequently re-accelerates to finally plateau. The standard deviation for the last 4 measurements is within the same range as for the other mixture compositions, indicating that this wave is "as steady" as those of other compositions. The 304.8 mm diameter charge of Fragmax based ANFO exhibits only an initial acceleration followed by a "very steady" plateau (see fig 6.10(b)), as indicated by the substantially lower value of the standard deviation. For this charge, a booster comprised of two layers of C-6 Detasheet explosives instead of a single layer was used. All other experiments used a single layer of the same explosive as a booster. This indicates that the Fragmax based ANFO is "harder" to initiate, i.e. it requires a larger amount of booster explosive to achieve a steady wave in the same distance. Plots of the velocity variation along the charge length for the individual charges tested are shown in appendix C.

The terminal axial velocity, D_0, is shown in fig 6.11 along with the data of [23]. The velocity difference between the 5% and 6% regular HE grade based charges is at most 1% for both the charge diameters. The values of D_0 for the expan mixture are also very close to those of the regular HE grade mixtures. The value of D_0 for the Fragmax based mixture is larger than that of other mixtures for the 304.2 mm charge, but not for the 203.2 mm charge, resulting in a significantly steeper diameter effect curve. This indicates that the detonation velocity for an infinite diameter charge is higher for Fragmax, but that its failure diameter is also much larger than that of the 3 other mixtures tested.

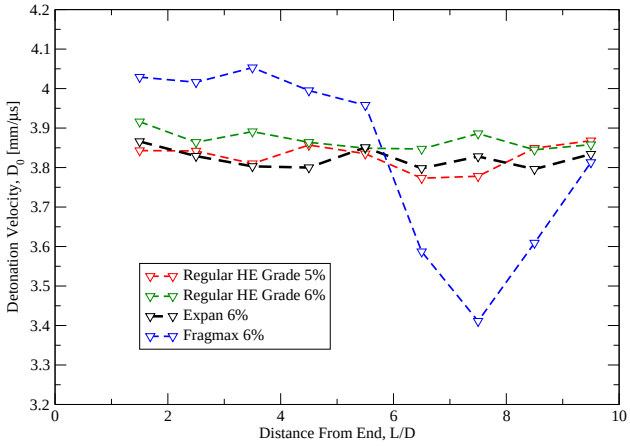

(a) 203.2 mm charges.

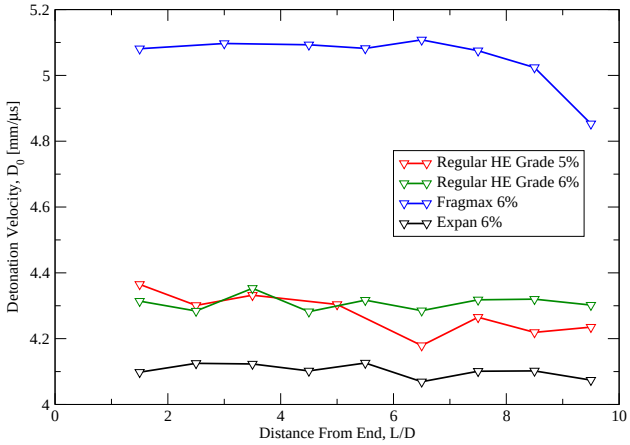

(b) 304.8 mm charges.

Figure 6.10: Variation of the axial detonation velocity, D_0, for the all 8 experiments.

6.5.2 Streak Photography of the Wave Breakout

In this diagnostic, the wave breakout was observed via the flashing of the PETN paint. One has to assume that there is either no noticeable lag or a consistent lag (independent of shock strength) between the transmission of the lead shock wave into the PETN strip and the emission of light by this same PETN strip. While this assumption was not directly tested, there is still value in observing the qualitative differences between the streak records of the different types of explosives. In figure 6.13 five digitized streak records are shown, namely the records of the breakout of a detonation wave in:

(a) a point initiated wedge of C-6 (see fig 6.12);

(b) a 203.4 mm charge of the 6% regular HE grade based ANFO;

(c) a 203.4 mm charge of the 5% regular HE grade based ANFO;

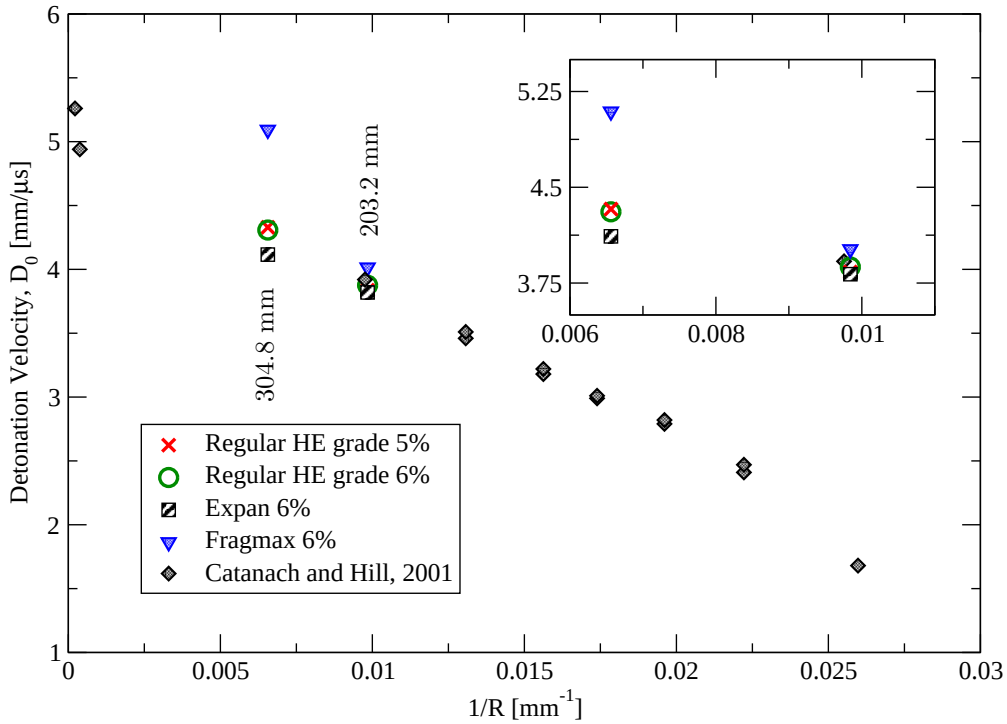

Figure 6.11: Variation of the steady detonation velocity for the 4 different charge types in the current study. Reproduced is the data from [23].

Explosive Type	FO %	203.4 mm		304.8 mm	
		Velocity (km/s)	Std. Deviation	Velocity (km/s)	Std. Deviation
Regular HE Grade	6%	3.876	0.0460	4.308	0.0576
Regular HE Grade	5%	3.836	0.0347	4.329	0.0521
Fragmax	6%	4.014	0.0459	5.093	0.0167
expan	6%	3.819	0.0541	4.116	0.0255

Table 6.4: Terminal detonation velocity and standard deviation of the last 4 velocity measurements for the different charge types and both charge diameters.

(d) a 203.4 mm charge of the 6% expan based ANFO;

(e) a 203.4 mm charge of the 6% Fragmax based ANFO;

The record from the point initiated wedge of C-6 provides a baseline for the behaviour of the PETN strip. The detonation wave shape in this material is known to be smooth and the streak record reflects this fact readily. By comparison, the streak records for the 5% and 6% regular HE grade based ANFO as well as the expan based ANFO show a "spotty" breakout wave, suggesting that the detonation wave shape consists of a shock that is transmitted in the air gaps with the AN prills possibly acting as distinct initiation points. By comparison, the streak record from the Fragmax based ANFO more closely resembles that of the C-6 baseline. The streak record is much smoother than that of the other 3 types of AN. Even under high

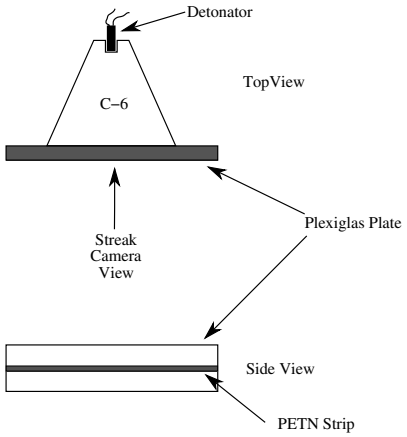

Figure 6.12: Schematic of the C-6 wedge setup to test the response of the PETN strip diagnostic.

	Test 7	Test 11
AN-type	Regular HE grade	expan
Average (mm)	2.38	2.21
Std. dev. (mm)	1.19	0.96
Minimum (mm)	0.76	0.73
Maximum (mm)	6.09	5.96

Table 6.5: Measurements of the distance between subsequent "spots" on streak images for tests 7 and 11.

magnification, no "prill structure" is discernible.

The distance between the subsequent "spots" was measured for two streak records, shots 7 and 11, respectively regular HE grade and expan prills. The average spacing (2.38 mm and 2.21 mm respectively) is in relatively good agreement with the prill sizes measured from photographs of the material. The minimum spacing was smaller than the minimum prill size measured in the photographs and the maximum spacing was much larger than the maximum prill diameter measured from photographs. The distance measurement was challenging and it is likely that some regions were mistaken and counted as two separate "spots" when only one large one was present. Also, some prills may have not been visible on the streak records or did not react promptly, leaving larger gaps than expected. The measurements taken on the two tests are shown in table 6.5. The range defined by the mean $\pm$ 1 standard deviation is in fairly good agreement with the range of diameters measured from photographs.

6.5.3 Experimental $D_n - \kappa$

The streak record, after the geometric transformation outlined above and in appendix D, yields the detonation shock shape. The goal here is to determine, from the experimental shock shape, the relationship between the wave curvature, κ, and the normal detonation velocity, D_n. The wave shape is fitted using the

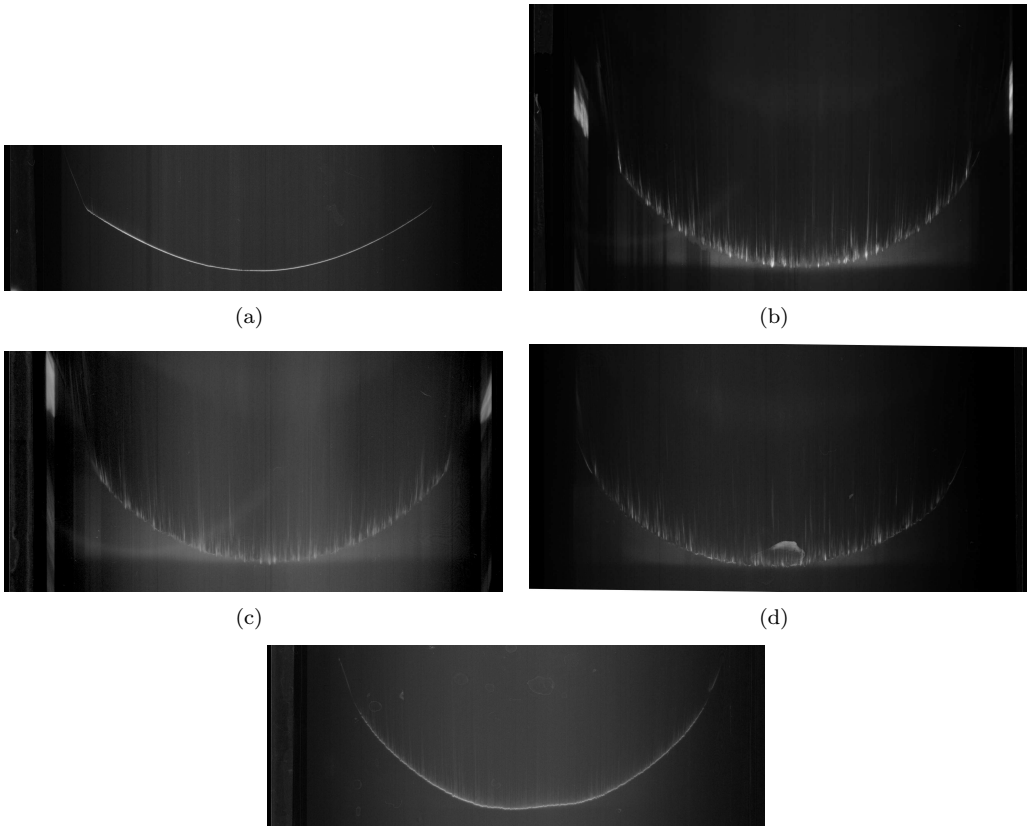

(a) (b) (c) (d) (e)

Figure 6.13: The different streak types corresponding to the different types of prills.

series

$$z(\hat{r}) = -\sum_i \overline{a}_i \left(\ln \left[\cos \left[\overline{b}_i \frac{\pi}{2} \frac{\hat{r}}{R} \right] \right] \right)^i, \tag{6.3}$$

using a least squares minimization. A one term expansion is found to be adequate, given the irregular (granular) nature of the breakout, which agrees with previous work [23]. The shock shape fit is differentiated twice to obtain the curvature as a function of the charge axis position, $\kappa(\hat{r})$. The slope of the shock shape at a particular position is

$$s(\hat{r}) = \frac{dz(\hat{r})}{d\hat{r}} = \frac{\overline{a}_1 \eta \pi}{2R} \tan \left(\overline{b}_1 \frac{\pi \hat{r}}{2R} \right) = \tan(\theta(\hat{r})) \tag{6.4}$$

The normal velocity, $D_n(\hat{r})$, can be obtained from the fitted front shape and the measured velocity, D_0

$$D_n(\hat{r}) = \frac{D_0}{\sqrt{1 + s(\hat{r})^2}}, \tag{6.5}$$

where D_0 is the axial propagation velocity of the detonation wave at the end of the charge. The curvature of the wave is related to the local slope of the wave and its derivative. The curvature, κ, can be written in polar coordinates:

$$\kappa = \bigtriangledown \cdot \hat{n} = \frac{1}{\hat{r}} \frac{d}{d\hat{r}} \left(\hat{r} n_{\hat{r}}(\hat{r}, \phi) \right) + \frac{1}{\hat{r}} \frac{d}{d\phi} \left(n_{\phi}(\hat{r}, \phi) \right), \tag{6.6}$$

where $\hat{n}(\hat{r}, \phi) = n_{\hat{r}} \hat{e}_{\hat{r}} + n_{\phi} \hat{e}_{\phi}$ is the normal of the corresponding detonation wave shape, $z(\hat{r}, \phi)$. In this case, the wave shape is assumed to be axisymmetric and our fitting function is only dependent on the radius, $z(\hat{r})$. The normal of the wave shape in the radial direction is given by $n_{\hat{r}} = |\hat{n}| \sin(\theta) = \sin(\theta)$, where the angle θ is the local slope of the wave shape $z(\hat{r})$. The curvature can be expressed as

$$\kappa = \frac{\sin(\theta)}{\hat{r}} + \cos(\theta) \frac{d\theta}{d\hat{r}}. \tag{6.7}$$

From the identity $\cos^2\theta + \sin^2\theta = 1$ and the definition of the slope, $s(\hat{r}) = \tan(\theta)$, the following identities can be obtained

$$\sin(\theta) = \frac{s(\hat{r})}{\sqrt{1 + [s(\hat{r})]^2}}, \tag{6.8}$$

$$\cos(\theta) = \frac{1}{\sqrt{1 + [s(\hat{r})]^2}}, \tag{6.9}$$

$$\frac{d\theta}{d\hat{r}} = \frac{ds/d\hat{r}}{1 + [s(\hat{r})]^2}. \tag{6.10}$$

A simple substitution gives the same result as [23] for the curvature of the wave as a function of the radius

$$\kappa(\hat{r}) = \frac{ds/d\hat{r}}{(1 + s(\hat{r})^2)^{3/2}} + \frac{s(\hat{r})}{\hat{r}\sqrt{1 + s(\hat{r})^2}}. \tag{6.11}$$

$D_n(\hat{r})$ and $\kappa(\hat{r})$ can be viewed as parametric curves of $D_n(\kappa)$. The angle of the wave normal with the vertical at the edge of the charge, the edge angle ϕ_e, can also be calculated from the fitted shock shapes and those are given in table 6.6. As stated before, because cardboard provides no confinement, these edge angles correspond to sonic edge angle [25]. Figure 6.14 shows the result of the fitting analysis for the different charges. As in [23], there is little to no overlap of the $D_n - \kappa$ curves of two different diameters for the same explosive. Only the expan based ANFO shows a close although not perfect agreement between the two different diameter rate-sticks. All other formulations show large departures between the two rate-sticks. Figure 6.15 shows the

corresponding $D_n - \kappa$ curves for the 203.2 mm 6% regular HE grade mixture. Unlike the nearly vertical $D_n - \kappa$ data of [23], this data set shows a much flatter $D_n - \kappa$ relationship for all formulations. The long storage time of the material used in [23] (several months) may have allowed some of the fuel oil to seep out or evaporate, such that the final FO % was lower than 6%. Since the data of [23] corresponds to neither the 5% nor 6%, it is possible that, in addition to the reduced fuel oil ratio, the exposure to the heat of the Cerro Grande fire caused structural changes in the prill material which have influenced its behaviour substantially.

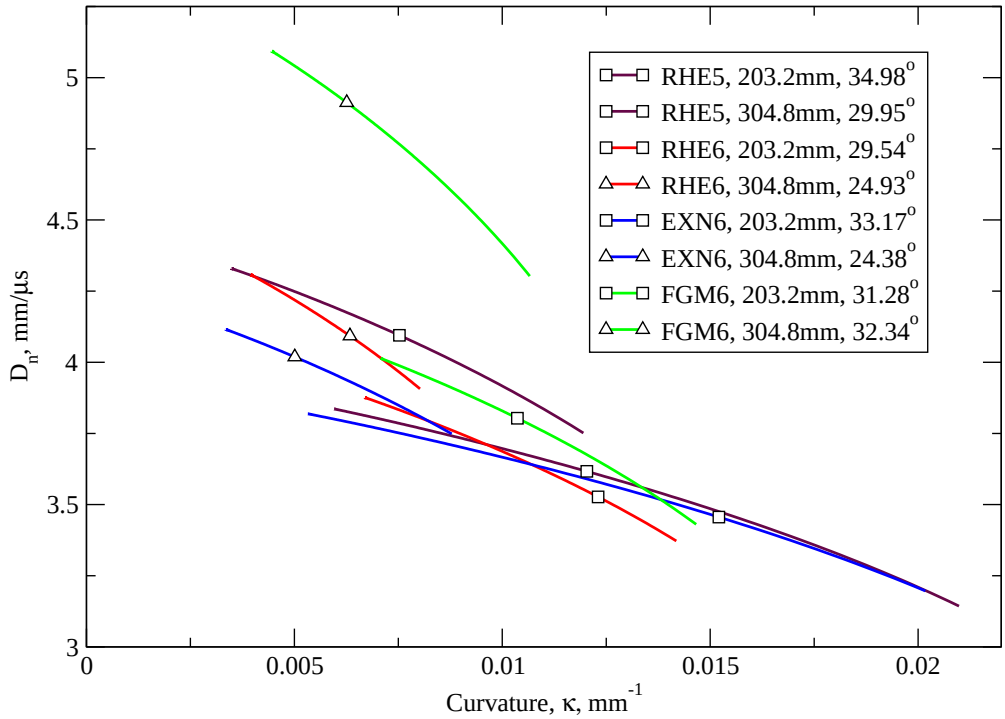

Figure 6.14: Curvature-velocity relations obtained from fitting the experimental shock shapes and differentiation. RHE5 and RHE6 correspond to the regular HE grade mixtures with 5% and 6% FO respectively. EXN6 corresponds to the expan based mixture and FGM6 corresponds to the Fragmax based mixture.

Type	Diameter	Edge angle
Regular HE Grade 5%	203.2 mm	34.98°
Regular HE Grade 5%	304.8 mm	29.95°
Regular HE Grade 6%	203.2 mm	29.54°
Regular HE Grade 6%	304.8 mm	24.93°
expan 6%	203.2 mm	33.17°
expan 6%	304.8 mm	24.38°
Fragmax 6%	203.2 mm	31.28°
Fragmax 6%	304.8 mm	32.34°

Table 6.6: Edge angles of the 8 different tests.

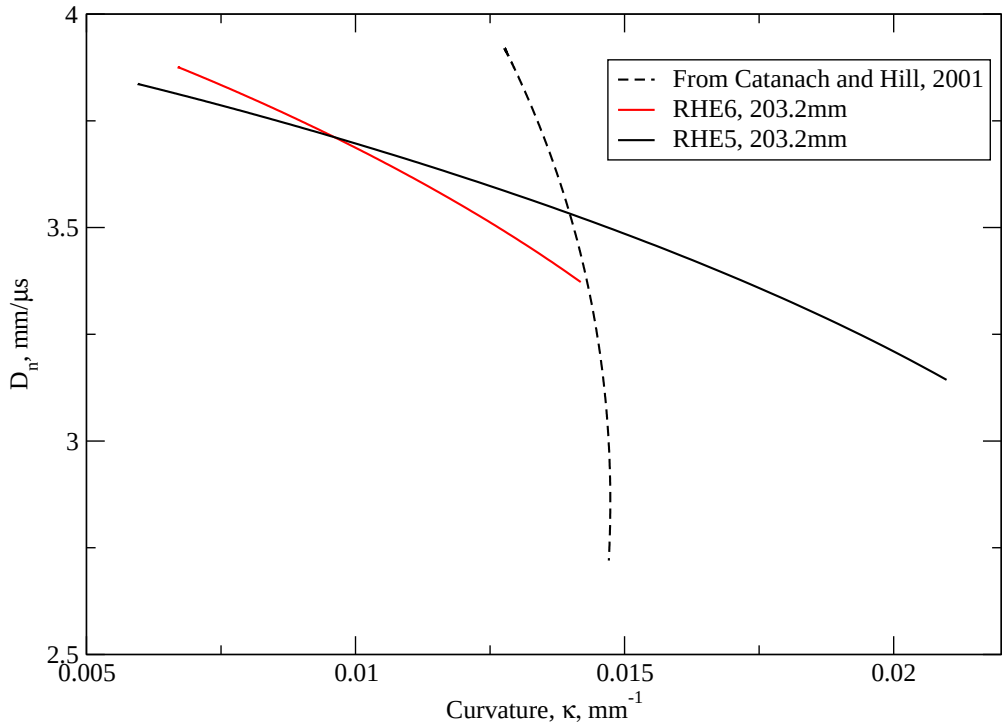

Figure 6.15: Comparison of the curvature-velocity relations from this work and that of [23] for the 6% and 5% FO mixture with regular HE grade prills in a 203.2 mm charge. The experiments from [23] were initially mixed at 6% FO ratio and the FO ratio was likely reduced due to the storage conditions.

6.6 DSD Modelling

The rate-stick experiments described in this chapter have been used to calibrate a DSD model. The actual calibration code used for this case was written by Dr. Tariq Aslam using the techniques of previous calibrations [24]. This section contains a short review of the DSD model and calibration procedure, and the results of the fitting procedure.

6.6.1 Description of the DSD Model

The DSD model replaces the detonation shock and reaction zone with a surface which propagates according to an intrinsic surface propagation law. This assumes that the detonation wave radius of curvature is much larger than the detonation wave reaction thickness,

$$R_c \gg \Delta. \tag{6.12}$$

A generalized evolution equation for HE can be derived for the propagation of the detonation wave as a function of its curvature, acceleration, and transverse flow, [24],

$$\kappa_s + \frac{\sin\phi}{\hat{r}} = F(l) - A(l)\frac{Dl}{Dt} + B(l)\frac{\partial^2 l}{\partial \xi}, \tag{6.13}$$

where $l = D/D_{\mathrm{CJ}} - 1$, κ_s is the curvature measured in the streak camera window, and $(\sin\phi)/\hat{r}$ the cylindrically axisymmetric component of the curvature. When specialized to the steady-state rate-stick problem, the DSD analysis yields a set of 3 ODE's which can be integrated to obtain the shock shape

$$\kappa_s \frac{D_0}{D_{\mathrm{CJ}}}\sin\phi\frac{d\kappa_s}{d\phi} = -\frac{D_0}{D_{\mathrm{CJ}}}\cos(\phi)\,\kappa_s^2 - \frac{1}{B(l)}\left\{\kappa_s + \frac{\sin\phi}{\hat{r}} - F(l) - \left(\frac{D_0}{D_{\mathrm{CJ}}}\sin\phi\right)^2 A(l)\kappa_s\right\}, \tag{6.14}$$

$$\frac{d\hat{r}}{d\phi} = \frac{\cos\phi}{\kappa_s}, \tag{6.15}$$

$$\frac{dz}{d\phi} = -\frac{\sin\phi}{\kappa_s}, \tag{6.16}$$

where D_0 is the phase speed of the detonation, $\hat{r}$ and z are the radial and shock displacement coordinates and ϕ is the local normal wave angle. This set of ODEs is subject to the boundary conditions

$$\kappa(0) = \kappa_{\mathrm{CL}} + G\phi^2 + \ldots, \tag{6.17}$$

$$\hat{r}(0) = 0, \tag{6.18}$$

$$z(0) = 0, \tag{6.19}$$

at the centerline $\phi = 0$. The local solution, eqn 6.17, is used near the centerline for $0 \le \phi \le \delta \ll 1$ and the solution is further integrated using a standard numerical ODE solver. Integration is carried out to a prescribed value of ϕ at the charge edge. The functions, $A(l), B(l), F(l)$ are functions of the local propagation velocity and can be specified in one of two ways. These functions can either be derived from a knowledge of the EOS and chemical kinetic rate law(s) which describe a particular material (see, for example, [25]). In the case of a material for which little information is known about the EOS and rate law(s), these functions can be prescribed arbitrarily, subject to the basic restriction that $A(l), B(l), F(l) \ge 0$. In our case, for the various ANFO compositions, the shock acceleration and transverse flow terms are omitted, i.e. $A(l) = B(l) = 0$. The basis for this is that the terms corresponding to $A(l)$ and $B(l)$ are higher-order corrections to the leading order velocity-curvature DSD form; the inclusion of such are likely not justified for detonations in

NIHE due to the structural complexity of the detonation propagation in the granular HE [24]. A linear curvature-velocity relationship is selected for calibration,

$$D_n = D_{\mathrm{CJ}}\left(1 - \beta\kappa\right) \tag{6.20}$$

The above set of ODEs is integrated to obtain the DSD shock shapes and the theoretical diameter effect curve. In this case the (sonic) edge angle is fixed at $\phi = 28°$, a value based on the results in table 6.6 and [24]. The parameters D_{CJ} and β are fitting parameters and the error in the shock shapes (here at 2 different diameters per ANFO formulation) and diameter effect curve (2 data points per ANFO formulation) between the DSD calibration and the experiments is minimized using a downhill-simplex method. The minimized cost function is

$$\mathrm{COST} = \sum_i E_i^2,\ i = 1, \ldots, m. \tag{6.21}$$

Because the shock shapes and diameter effect curves contain very different number of points, weighting functions determine the importance of each measurement and the E_i for the shock shapes and diameter effect curve are respectively

$$(E_i)_{\mathrm{shape}} = W_s \frac{Z_{ij,\mathrm{calc}} - Z_{ij,\mathrm{exp}}}{R_{j,\mathrm{exp}}}, \tag{6.22}$$

$$(E_i)_{\mathrm{diameter}} = W_R \frac{R_{i,\mathrm{calc}} - R_{i,\mathrm{exp}}}{R_{i,\mathrm{exp}}}. \tag{6.23}$$

Typically, $W_R < W_s$. Z_{ij} is the i-th point shock shape displacement of the j-th shock shape and R_j is the radius of the j-th shock shape.

Previous Calibrations of Other Explosives

The original description of the DSD model was presented in [25]. In this paper, the solid explosive PBX-9404 and the liquid explosive nitromethane are modeled. The diameter effect curve of PBX-9404 is well reproduced and that of nitromethane is also well reproduced although somewhat less accurately. The diameter effect curves are reproduced in fig 6.16.

Also extensively calibrated and validated are the IHE PBX 9502 [19, 117, 118] and the CHE PBX-9501 [119]. A recent review article covers the recent history of the application of the DSD model [3].

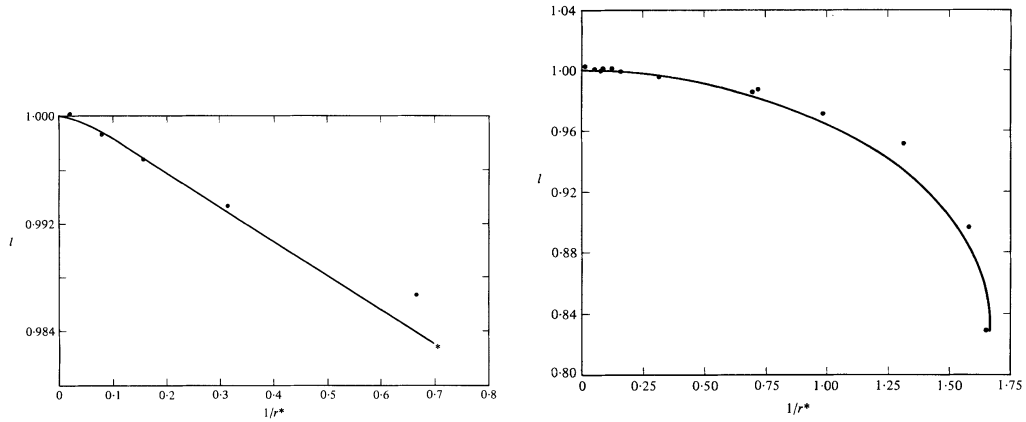

(a) Nitromethane (b) PBX9404.

Figure 6.16: Diameter effect curves of the nitromethane and PBX-9404 fits from [25].

6.6.2 Calibrated linear $D_n - \kappa$ ANFO DSD Model

The data from both the 203.2 mm and 304.8 mm charges are used in each fit and one DSD fit is obtained for each material tested. The shock shapes are split about the centerline of the charge and data from both sides of the explosive are superimposed and fitted simultaneously. For every calibration, there are therefore 4 half shock shapes used as data; two from the 203.2 mm charge and two from the 304.8 mm one. The two data points of the diameter effect curve are also fitted.

The fitted parameters are shown in table 6.7. The shock shapes, for all four materials, are shown in fig 6.17 and the fitted $D_n(\kappa)$ relationships for all materials are shown in fig 6.18. Fragmax (FGM6) has the steepest slope with the highest predicted D_{CJ}. The different materials can be ordered by decreasing D_{CJ} value from Fragmax (FGM6), 5% regular HE grade (RHE5), 6% regular HE grade (RHE6) and expan (EXN6). The different mixtures follow the same order when ordering the gradient of the $D_n(\kappa)$ curve in decreasing order. As a result, the curves of $D_n(\kappa)$ for the different explosives all cross for large enough values of κ. The diameter effect curves, shown in fig 6.19, also exhibit a crossing point for $0.075 \lesssim 1/R \lesssim 0.012$. The ordering of the diameter effect curve gradients yields the same sequence with FGM6 having the steepest diameter effect curve, followed by RHE5, RHE6 and EXN6. Consequently, FGM6 is expected to have the largest failure diameter followed in decreasing order by RHE5, RHE6 and finally EXN6 which would be able to propagate in the smallest geometries.

The infinite diameter detonation velocity, D_{CJ} is highest for the Fragmax based ANFO and lowest for the expan based ANFO. Both regular HE grade based ANFO mixtures have similar D_{CJ} speeds, with the 5% FO mixture having a slightly higher D_{CJ} than the 6% FO mixture. One would expect a stoichiometric mixture to have a higher D_{CJ} and the behaviour of the 5% and 6% FO regular HE grade mixtures is surprising. The

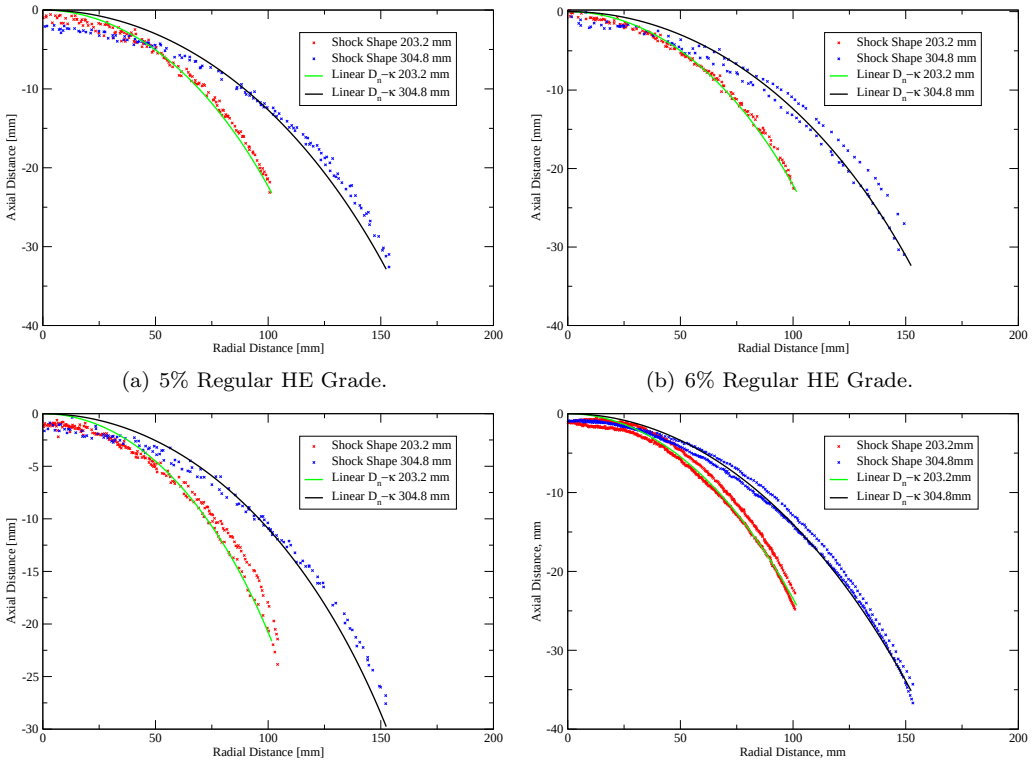

(a) 5% Regular HE Grade.

(b) 6% Regular HE Grade.

(c) 6% expan.

(d) 6% Fragmax.

Figure 6.17: DSD fits of the shock shapes for the 4 different ANFO mixtures tested and the fitting parameters of table 6.7.

largest influence of FO ratio is also expected to be for FO-lean mixtures (FO ratio $< 6\%$) rather than for FO-rich mixtures [104]. Because the value of D_{CJ} is an extrapolation of only 2 data points, this variation might be explained by experimental variability. The variation of D_{CJ} between the different mixtures is consistent with the density of the different material. This variation is shown in fig 6.20. Aside from the surprising behaviour of the regular HE grade mixtures, the variation of D_{CJ} with density appears to be linear.

Formulation	D_{CJ}(km/s)	β(mm)
Regular HE 5%	5.003	29.06
Regular HE 6%	4.902	26.67
Fragmax 6%	6.795	47.50
expan 6%	4.404	18.00

Table 6.7: DSD fitted parameters for the four ANFO formulations tested.

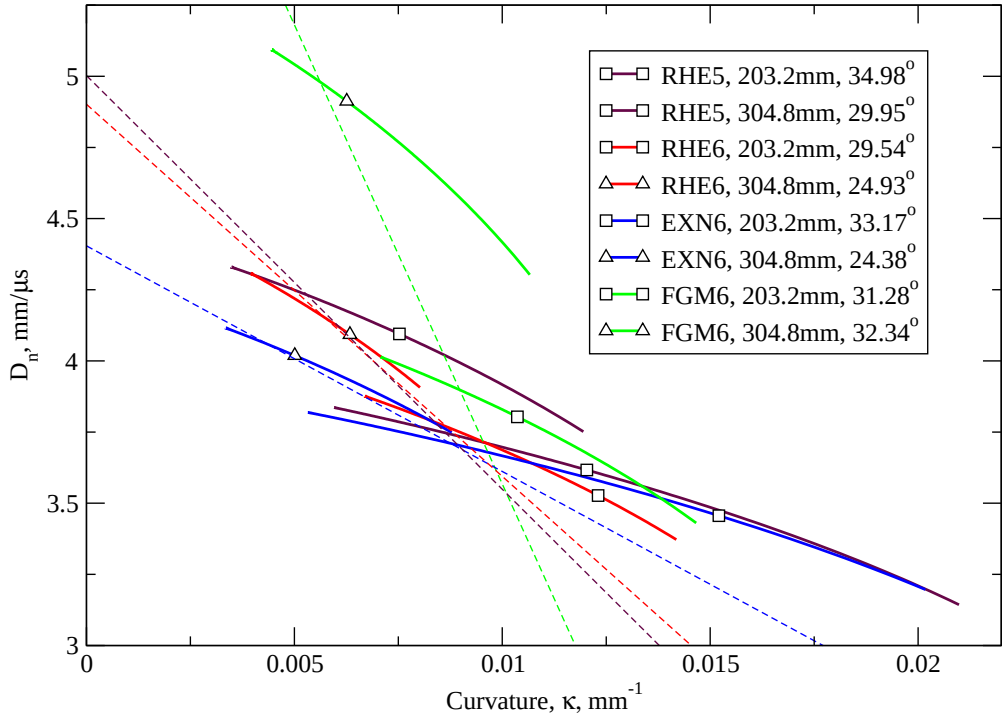

Figure 6.18: DSD $D_n - \kappa$ curves with experimental data for all 4 mixtures of ANFO tested. RHE5 and RHE6 correspond to the regular HE grade mixtures with 5% and 6% FO respectively. EXN6 corresponds to the expan based mixture and FGM6 corresponds to the Fragmax based mixture.

6.7 Summary

Rate-stick experiments were performed for 4 different formulations of ANFO, namely three 94%AN 6%FO mixes with regular HE grade AN prills, Fragmax prills and expan prills and one 95%AN 5%FO mix with regular HE grade AN prills. The non-ideal behaviour of the 4 different formulations was apparent from the experimentally determined $D_n - \kappa$ curves which do not overlay for different diameters. Both formulations of regular HE grade prills showed very similar behaviour with the 5% regular HE grade ANFO having a higher predicted D_{CJ} velocity than the 6% regular HE grade mix. This behaviour is surprising and possibly explained by experimental variability. The Fragmax based AN exhibited a much larger detonation velocity for larger charges and is predicted to also have the highest D_{CJ} of all tested materials. The expan based ANFO had the lowest detonation velocity for the larger charge and also the lowest predicted D_{CJ} velocity. This behaviour is predicted to reverse for smaller charges, indicating that the failure diameter is smallest (smaller tubes can propagate) for the expan based ANFO and largest for the Fragmax based ANFO (requires large tube diameters to propagate). The failure diameter of the regular HE grade ANFO is expected to fall between those bounds.

More experimental data is obviously needed to better model the behaviour of ANFO. In addition to more

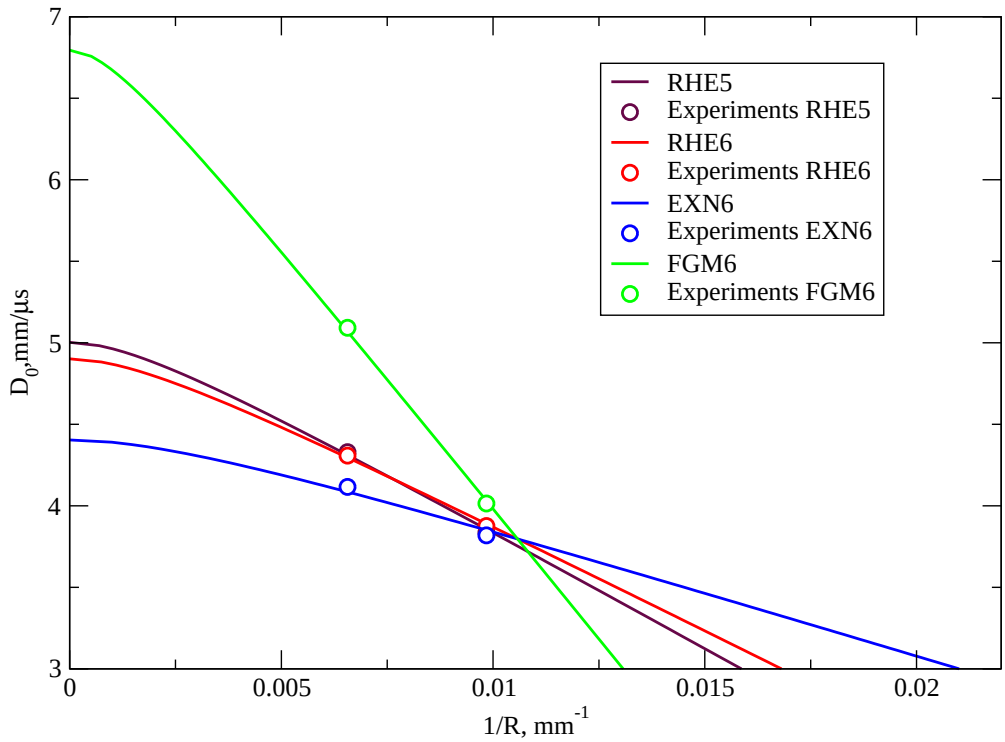

Figure 6.19: DSD diameter effect curves with experimental data points for all 4 mixtures of ANFO tested. RHE5 and RHE6 correspond to the regular HE grade mixtures with 5% and 6% FO respectively. EXN6 corresponds to the expan based mixture and FGM6 corresponds to the Fragmax based mixture.

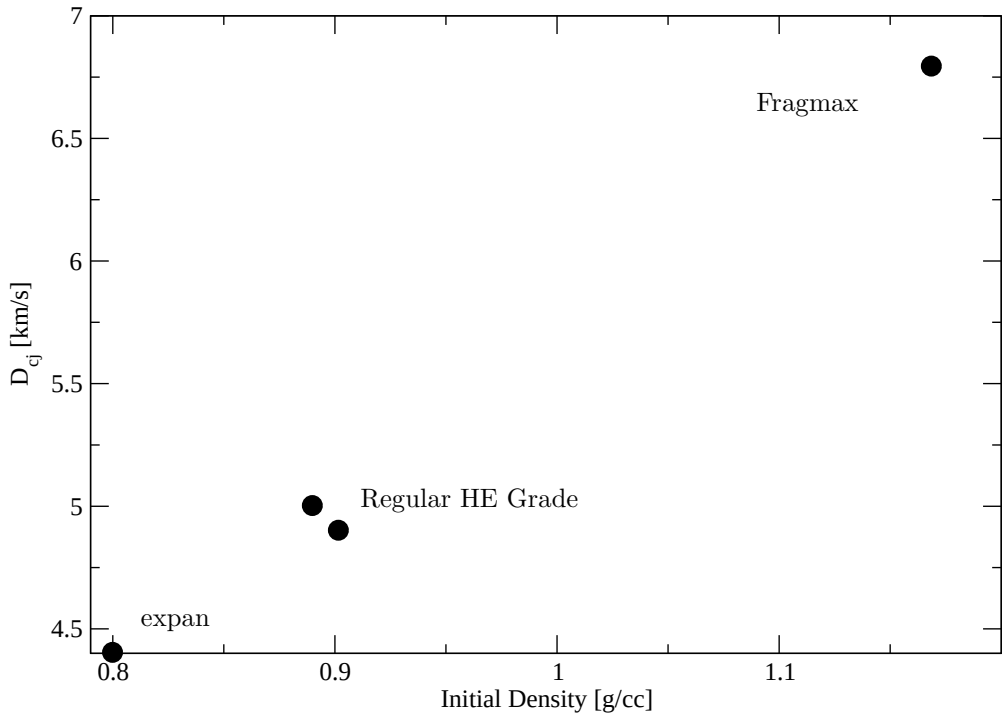

Figure 6.20: Variation of the value of D_{CJ} from the DSD fit with initial mixture density for the 4 different mixtures tested. The value of density reported is the average of the two charges fired. Except for the variation of D_{CJ} for the 5% and 6% regular HE grade charges, the variation of density appears linear.

data in essentially unconfined geometries (as in the present experiments), experiments have been scheduled in which the confiner material has a higher density and higher sound speed. Certain confiner materials have sound speeds higher than the ANFO propagation velocity and that data, combined with highly resolved numerical simulations, will be used to better calibrate and possibly modify the current DSD framework. Modifications to the current DSD approach are likely necessary to accurately model NIHEs such as ANFO.

Chapter 7

Conclusion

The two main goals pursued in this work:

- the development of a detonation propagation model for an IHE using a simplified EOS,
- studying the impact of variations in model parameters and model construction on the resulting model behaviour,

were achieved using a SG EOS. The use of a single SG EOS in a 3 species, 2 step reactive burn model was shown to retain enough flexibility to capture the dynamics of propagation detonations despite the limited ability of the SG EOS to fit reactant shock Hugoniot data. Multiple calibrations were found to be possible for the $D_n - \kappa_0$ data, suggesting there is enough flexibility in this simplified model to capture behaviours in other regimes, such as detonation initiation. The use of a slightly less restrictive solid EOS (such as a Birch-Murnaghan EOS for example) might be advised in such a case. The analytical tractability of the current models permitted the examination of their linear stability and non-linear structure. Most importantly, the impact of different changes in the model could be investigated independently. Linear stability calculations showed that an increase in the initial sound speed (controlled by a_s) resulted in a stabilizing effect. Increasing the product pressure offset a_g resulted in a destabilizing effect. The stability of the wave was dominated by the variation of a_s with equivalent variations in a_g resulting in smaller changes in the eigenvalues growth rate. Changing the closure condition from P–T equilibrium to the $DS_s = 0$ closure had a dramatic stabilizing effect.

The non-linear structure of detonation waves was investigated using a single phase SG EOS model with 1 step kinetics. Here, the initial sound speed of the material was increased via a_g for a fixed detonation speed, leading to the impossibility of different flow patterns, namely the classical Mach reflection pattern. The different possible shock reflection patterns were investigated theoretically and the conditions under which this choice of EOS would not allow the classical Mach reflection pattern were determined. Different reflection patterns were investigated numerically and it was found that several theoretically possible solutions are unstable configurations. A single step chemical kinetic scheme with both P^n and Arrhenius dependences was

used and parameters were chosen to yield an unstable wave. Propagating detonation waves were simulated and markedly different behaviour was observed for varying values of the pressure offset a. For the higher values of a, no triple-point structure was discernible.

Finally, the last chapter presents a departure from the theoretical and numerical work presented previously. The results of rate-stick experiments using the highly non-ideal HE ANFO were presented. An attempt was made at modelling the explosive behaviour using DSD. Four different ANFO mixtures were tested, including three different types of AN. The DSD modelling was only partially successful, outlining the need for a modified DSD framework which can handle such non-ideal HEs.

7.1 Future Work

A first, straightforward extension of the current work consists in using more complex EOS models to represent the behaviour of the solid reactants. A Mie-Grüneisen EOS based on a Birch or Birch-Murnaghan EOS yields an unreacted shock Hugoniot with the correct overall curvature. The wrong curvature of the SG EOS was the most severe limitation in the applicability of the models considered in this work. Given an EOS with the right curvature and the fact that multiple solutions were found to be possible when calibrating the current models to axis curvature data suggests a truly predictive IHE model based on an analytically tractable EOS could be developed to capture both propagation and initiation characteristics of PBX 9502.

A challenging, long-term goal in the modelling of insensitive and non-ideal high explosives is to incorporate the effect of porosity and pore collapse in reactive burn models. The porous nature of these explosives manifests itself in both the mechanical response as well as the chemical response of the material. Porous material will have a different shock response depending on the strength of the shock as pores collapse and the compressibility of the material asymptotes to the bulk material compressibility. Also, voids, cracks and defects initially present in a material can lead, through jetting, shock focusing, etc, to localized, highly non-uniform regions with high temperatures. These hot-spots can act as local ignition points, but their length and time scales are too small compared to the engineering scale of typical devices to make detailed numerical simulations a viable option. The development of chemical kinetic models which can adequately capture the effect of hot-spot formation on the dynamics of an explosive is needed for the next generation of homogeneous reactive burn models to be applicable to a wider range of insensitive and non-ideal high explosives.

Appendix A

Derivations Referred to in Chapter 2

A.1 Alternate Derivation of the $P - v - T$ EOS

Starting from the following 2 thermodynamic relations

$$\gamma = \frac{C_P}{C_v}\frac{1}{PK_T}, \tag{A.1}$$

$$PK_T = \frac{g}{\gamma g - \Gamma^2}, \tag{A.2}$$

where g is a non-dimensional heat coefficient, $g = PV/C_vT$, yields

$$\Gamma^2 = \gamma\frac{Pv}{T}\left(1/C_v - 1/C_P\right). \tag{A.3}$$

Substituting the assumed function for the adiabatic index and imposing $\overline{\gamma} - \Gamma = 1$ yields

$$P + \frac{A}{\overline{\gamma}} = \frac{\left(\overline{\gamma} - 1\right)^2}{\overline{\gamma}\left(\frac{1}{C_v} - \frac{1}{C_P}\right)}\frac{T}{V}. \tag{A.4}$$

This is analogous to the equation of state, $PV = RT$ of ideal gases. From eqn A.4, for the expected physical behaviour to be obtained, namely

1. At constant volume, an increase in temperature produces an increase in pressure;
2. At constant temperature, an increase in pressure produces a decrease in volume;
3. At constant pressure, an increase in temperature produces an increase in volume,

two conditions are required

$$\overline{\gamma} \geq 1, \tag{A.5}$$

$$C_v^{-1} \geq C_P^{-1}. \tag{A.6}$$

The first result was expected so that $\Gamma \geq 0$ be enforced and the second condition is known to be required for shock stability, an essential property this model must exhibit for physical significance.

A.2 $P - v$ Isentropic Relationship for the Blended SG EOS with $P_r < P_c < P$

From the definition of the blended SG EOS, the pressure integral is

$$C = \int_{P_r}^{P} \frac{\Gamma_1^{-1}W + \Gamma_2^{-1}(1-W) + \left[(P+A_1)\Gamma_1^{-1} - (P+A_2)\Gamma_2^{-1}\right]W'}{P + (P+A_1)\Gamma_1^{-1}W + (P+A_2)\Gamma_2^{-1}(1-W)}dP = \int_{P_r}^{P} f(P)dP. \tag{A.7}$$

The integral is broken into three separate parts,

$$C = \lim_{\epsilon\to 0}\int_{P_r}^{P_c(1-\epsilon)} f(P)dP + \lim_{\epsilon\to 0}\int_{P_c(1-\epsilon)}^{P_c(1+\epsilon)} f(P)dP + \lim_{\epsilon\to 0}\int_{P_c(1+\epsilon)}^{P} f(P)dP = C_1 + C_2 + C_3. \tag{A.8}$$

The first and third integrals are straightforward

$$C_1 = \frac{1}{\Gamma_1 + 1}\ln\frac{(\Gamma_1+1)P_c + A_1}{(\Gamma_1+1)P_r + A_1}, \tag{A.9}$$

$$C_3 = \frac{1}{\Gamma_2 + 1}\ln\frac{(\Gamma_2+1)P + A_2}{(\Gamma_2+1)P_c + A_2}. \tag{A.10}$$

The second integral is solved as follows. For $W(P) = H(1 - P/P_c)$, no contribution comes from

$$\lim_{\epsilon\to 0}\int_{P_c(1-\epsilon)}^{P_c(1+\epsilon)} \frac{W\Gamma_1^{-1} + (1-W)\Gamma_2^{-1}}{P + (P+A_1)\Gamma_1^{-1}W + (P+A_2)\Gamma_2^{-1}(1-W)}dP = 0, \tag{A.11}$$

and the only contribution is from the term involving the derivative of the switch function, a delta function,

$$\lim_{\epsilon\to 0}\int_{P_c(1-\epsilon)}^{P_c(1+\epsilon)}\frac{\left[(P+A_1)\Gamma_1^{-1}-(P+A_2)\Gamma_2^{-1}\right]W'}{P+(P+A_1)\Gamma_1^{-1}W+(P+A_2)\Gamma_2^{-1}(1-W)}dP=\lim_{\epsilon\to 0}\int_{P_c(1-\epsilon)}^{P_c(1+\epsilon)}\Phi(P)dP=\Phi(P_c). \quad (A.12)$$

Assuming a Heaviside function, the integral is evaluated formally

$$\Phi(P_c)=\lim_{\epsilon\to 0}\frac{1}{2\epsilon}\int_{P_c(1-\epsilon)}^{P_c(1+\epsilon)}\Phi(P)dP. \quad (A.13)$$

The result is

$$\begin{aligned}\Phi(P_c) &= \frac{1}{2(\Gamma_1+1)}\left[1+\frac{\Gamma_1 A_1}{A_1+(\Gamma_1+1)P_c}\right]-\frac{\Gamma_1}{\Gamma_2}\frac{1}{2(\Gamma_1+1)}\left[1-\frac{A_1-(\Gamma_1+1)A_2}{A_1+(\Gamma_1+1)P_c}\right]\\ &+ \frac{\Gamma_2}{\Gamma_1}\frac{1}{2(\Gamma_2+1)}\left[1-\frac{A_2-(\Gamma_2+1)A_1}{A_2+(\Gamma_2+1)P_c}\right]-\frac{1}{2(\Gamma_2+1)}\left[1+\frac{\Gamma_2 A_2}{A_2+(\Gamma_2+1)P_c}\right], \quad (A.14)\end{aligned}$$

which gives the second integral

$$C_2=\ln e^{\Phi_g(P_c)}. \quad (A.15)$$

The final relationship between pressure and specific volume is

$$\left[\frac{(\Gamma_1+1)P_c+A_1}{(\Gamma_1+1)P_r+A_1}\right]^{\frac{1}{\Gamma_1+1}}\left[\frac{(\Gamma_2+1)P+A_2}{(\Gamma_2+1)P_c+A_2}\right]^{\frac{1}{\Gamma_2+1}}e^{\Phi_g(P_c)}=\left[\frac{v}{v_r}\right]^{-1}. \quad (A.16)$$

A.3 Derivation of the Tangency Condition for a CJ Wave

The Hugoniot curve and the Rayleigh line are differentiated, in the (P,v)-plane to obtain

$$\left(\frac{dP}{dv}\right)_R = -(\rho_0 D)^2=\frac{P-P_0}{v-v_0}, \quad (A.17)$$

$$\left(\frac{dP}{dv}\right)_H = \frac{2\left(de/dv\right)_H}{v_0-v}+\frac{P+P_0}{v_0-v}. \quad (A.18)$$

The Chapman-Jouguet condition requires that the Rayleigh line and Hugoniot Curve be tangent at the CJ point

$$\left(\frac{dP}{dv}\right)_R=\left(\frac{dP}{dv}\right)_H. \quad (A.19)$$

Equating the previously obtained results yields

$$\left(\frac{de}{dv}\right)_H = -P. \tag{A.20}$$

Using the first law of thermodynamics for a reversible system, $de = Tds - Pdv$, one obtains, for an isentropic process,

$$\left(\frac{de}{dv}\right)_s = -P. \tag{A.21}$$

Equating results A.20 and A.21, one has, at the CJ point

$$\left(\frac{de}{dv}\right)_H = \left(\frac{de}{dv}\right)_s. \tag{A.22}$$

The internal energy state function along the Rayleigh lines and Hugoniot curves is

$$e(P,v) \rightarrow e(P_H(v),v), \tag{A.23}$$

$$e(P,v) \rightarrow e(P_s(v),v). \tag{A.24}$$

$$\tag{A.25}$$

Differentiating the two yields

$$\left(\frac{de}{dv}\right)_H = \frac{\partial e}{\partial v} + \frac{\partial e}{\partial P}\left(\frac{dP}{dv}\right)_H, \tag{A.26}$$

$$\left(\frac{de}{dv}\right)_s = \frac{\partial e}{\partial v} + \frac{\partial e}{\partial P}\left(\frac{dP}{dv}\right)_s. \tag{A.27}$$

Since the partial derivatives of the energy function with respect to the pressure and specific volume are material definitions (i.e. independent of the process), substituting A.26 and A.27 into A.22 implies

$$\left(\frac{dP}{dv}\right)_H = \left(\frac{dP}{dv}\right)_s. \tag{A.28}$$

Hence the isentrope is, like the Rayleigh line, tangent to the Hugoniot at the CJ point and

$$\left(\frac{dP}{dv}\right)_R = \left(\frac{dP}{dv}\right)_H = \left(\frac{dP}{dv}\right)_s = \frac{-(P-P_0)}{v_0 - v}. \tag{A.29}$$

Appendix B

Relative Importance of the Different Heat Transfer Mechanisms in PBX 9502

B.1 Conductive Heat Transfer

A measure of the timescale for conductive heat transfer within the particle, τ_{HC} is obtained by looking at the Fourier number

$$\mathrm{Fo} = \frac{\alpha_{\mathrm{solid}}\tau_{\mathrm{HC}}}{L_{\mathrm{r}}^2}, \tag{B.1}$$

$$\alpha_{\mathrm{solid}} = \frac{K}{\rho C_p}. \tag{B.2}$$

For Fo = 1, the timescale for relevant conduction heat transfer can be calculated.

$$\tau_{\mathrm{HC}} = \frac{\rho C_p L_r^2}{K} \tag{B.3}$$

Very little experimental data is available for the heat capacity and heat conductivity of PBX 9502. The heat conductivity is only available at room temperature and is assumed here to be constant w.r.t. temperature. [55]. The heat capacity was measured over a range of temperatures from -55 to 252°C [120] with linear fits proposed valid at least in this range. The value of the heat capacity is bracketed between the maximum recorded value in the range of measurement and the linear extrapolation at 3000K. The density is assumed to be the initial density of the material, $\rho \simeq 1.890$ g/cc. The actual density of the material in the reaction zone is higher as the material has been shocked, but a higher density would result in a longer time scale and the worst-case scenario is obtained by considering the initial density of the material. The reference lengthscale for heat transfer is taken to be half the grain size of the material, on the order of 25-50μm. The experimental values used for this estimate are reproduced in table B.1.

Using these estimates, the time scale over which heat conduction occurs is $\tau_{\mathrm{HC}} \sim 3.61-81.6$ms. The much longer conduction time scale means that any heat transfer between the product and reactant species will only

K (x10^{-4} cal/s cm °C)	ρ (g/cc)	C_p (cal/g °C)	$2L_r$ (μm)
11 - 13.4	1.890	0.41 - 1.9	50-100

Table B.1: Experimentally obtained values of the different thermal properties used in estimating the importance of heat conduction between the reactants and the products for PBX 9502.

heat the very surface of explosive grains and will not influence the overall reactant species. Alternatively, the maximum grain size for which heat conduction is relevant on the time scale of the detonation zone can be calculated. In this case,$L_{r,max} \sim 0.9 - 5.2$Å, much smaller than a typical grain size. Hence, heat conduction would not become relevant until essentially all of the reactants are consumed.

B.2 Convective Heat Transfer

Convective heat transfer is either forced convection or buoyancy driven convection. Buoyancy driven convection is well known to be relevant on time scales several orders of magnitude larger than the relevant chemical timescales considered here. Looking at the Rayleigh number

$$\mathrm{Ra} = \frac{g\beta(T_s - T_g)L_\mathrm{r}^3}{\nu_\mathrm{gas}\alpha_\mathrm{gas}} \tag{B.4}$$

two conclusions can be drawn. First, the cubic dependence on length scale is likely to reduce the Rayleigh number to very small values. Second, the gas temperature is expected to be higher in the gas than in the solid. For free convection to be a possible mechanism, the reverse must be true and this mechanism can be neglected. Forced convection heat transfer is proportional to the difference of velocity between the solid and gas phases,

$$\delta Q \propto u_{gas} - u_{solid}. \tag{B.5}$$

In most problems involving the reactive solid particle heating by gases, explosive mixtures consisting of reactive particles (e.g. aluminium flakes) are surrounded by a detonating liquid or gas. (See, for example [121].) In such a case, convective heat transfer is relevant because there is an actual velocity discrepancy between both phases. In the particle heating problem referenced above, for example, the lead shock wave of the detonation propagating in the surrounding gas acclerates both low density reactants (the gaseous phase) and high density reactants (the solid reactive particles). The gas is accelerated to higher speeds than the solid particles, resulting in a velocity discrapency. This is not the case in the present model. In the problem explored in this thesis, the lead shock wave of the detonation only accelerates the initially solid reactant phase. The presence of lower density gaseous species occurs as the chemical reaction progresses, after the

passage of the shock. The result is gaseous material moving at the same velocity as the solid material. The assumption of velocity equilibrium, in this case, is justified and forced convection is also negligible.

B.3 Radiative Heat Transfer

The estimate of the radiative heat transfer consists of comparing the total heat transferred to the reactant phase via radiation to the amount of heat generated by the conversion from reactant to products, i.e.

$$\frac{Q_{rad}}{Q_{react}} = \frac{\sigma A(T_g^4 - T_s^4)\tau_R}{\rho\,(\Delta H)_{comb}\,V}, \tag{B.6}$$

where σ is the Stefan-Boltzmann constant, A is the surface area and $(\Delta H)_{comb}$ is the heat of combustion. Assuming spherical particles, the temperature difference between product and reactant can be written, for $Q_{rad} \sim Q_{react}$, as

$$T_g^4 - T_s^4 \sim \frac{\rho\,(\Delta H)_{comb}\,(2L_r)}{6\sigma\tau_R}. \tag{B.7}$$

The heat of combustion is on the order of $(\Delta H)_{comb} = 11.926\text{x}10^3\text{J/g}$ [55], the density is again taken to be the initial density of the solid reactants and all other quantities are estimated as before. The result, for $T_s \sim 0$ (again the worst-case scenario) is a product temperature, $T_g \sim 68556$K. Realistically, one would expect final product temperatures in the range of 3000-6000K. A temperature $T_g \sim 6000$ K yields $Q_{rad}/Q_{react} \sim 0.01\%$. Radiative heat transfer can thus also be neglected.

Appendix C

Experimental Data for the ANFO Rate-Stick Experiments

C.1 Experimental Parameters

Shot #	T_{b} (°C)	T_{m} (°C)	T_{o} (°C)	$\Delta t_{\mathrm{mirror}}$ (μs)
1	22.5	15	14.5	1641.1
2	N/A	23.5	26	1875.5
3	20.5	N/A	25.5	1875.5
4	21.5	21.5	19	1875.5
5	19.5	20.5	10.5	1875.5
6	24.5	16.5	10-15	2612.1
7	19.5	24.5	6-9	2612.2
8	23.5	22.5	19-22	1982.0
9	25	25.5	24.5	1768.8
10	24.5	25.5	26-27	2478.3
11	29.5	28	27-32	2659.9

Shot #	ρ_{charge} (g/cc)	D_{charge} (mm)	$(L/D)_{\mathrm{charge}}$
1	0.897	203.2	6
2	N/A	N/A	N/A
3	0.893	203.2	6
4	0.883	203.2	14
5	0.900	203.2	14
6	0.8967	304.8	14
7	0.9031	304.8	14
8	0.7928	203.2	14
9	1.168 (1.178)	203.2	14
10	1.169	304.8	14
11	X 0.807(0.808) R 0.896	304.8	13

Table C.1: Experimental data from the ANFO rate-stick experiments. T_{b}, T_{m} and T_{o} are respectively the temperatures at the bottom and middle of the charge and the outside temperature. $\Delta t_{\mathrm{mirror}}$ is the streak camera mirror period. ρ_{charge} is the overall density of the charge after filling and packing. D_{charge} is the nominal charge diameter. $(L/D)_{\mathrm{charge}}$ is the charge aspect ratio.

Shot #	ANFO mixing date	Firing Date	Notes	Prill Material	FO Fraction
1	02/23/2009	02/23/2009	Initial Test Shot No Pin data	Regular HE Grade	6%
2	N/A	02/26/2009	PETN Paint Test Shot	N/A	N/A
3	02/26/2009	03/02/2009	Repeat Test Shot	Regular HE Grade	6%
4	03/04/2009	03/04/2009		Regular HE Grade	5%
5	03/03/2009	03/09/2009		Regular HE Grade	6%
6	03/06/2009	03/12/2009		Regular HE Grade	5%
7	03/10/2009	03/13/2009		Regular HE Grade	6%
8	04/27/2009	04/27/2009		expan	6%
9	04/27/2009	04/28/2009	Miscalibrated bucket was probably 2 lbs less	Fragmax	6%
10	04/29/2009	04/29/2009		Fragmax	6%
11	04/30/2009	04/30/2009	Bottom 11ø+3/16in expan, top 2ø+5/16in regular. One bucket of expan probably missing 1/2lbs	expan (HE grade booster)	6%

Table C.2: Experimental data from the ANFO rate-stick experiments.

Shot #	Velocity fit	t–x fit	
		N last points	D_0
4	3.8308	6	3.8363
4		10	3.8228
5	3.8979	6	3.876
5		10	3.8659
6	4.3699	4	4.3294
6		5	4.3192
6		10	4.2753
7	4.309	10	4.308
8	3.8392	10	3.8191
9	4.0672	6	4.014
10	5.0795	6	5.0928
11	4.1244	6	4.1155

Table C.3: Longitudinal detonation propagation velocities at the end of the charges. The Velocity fits (first column) are obtained by calculating the 2-point finite difference velocities between subsequent pin pairs. The "steady" portions of these velocity records are then fitted with a straight line which is extrapolated to the end of the charge. The t–x fits are obtained by linearly fitting the "steady" portions of the t–x diagrams, obtaining a single average velocity over the given region. Different numbers of points were selected (from the end of the charge) for the more problematic experiments.

C.2 Temperature Records for the Different ANFO Shots

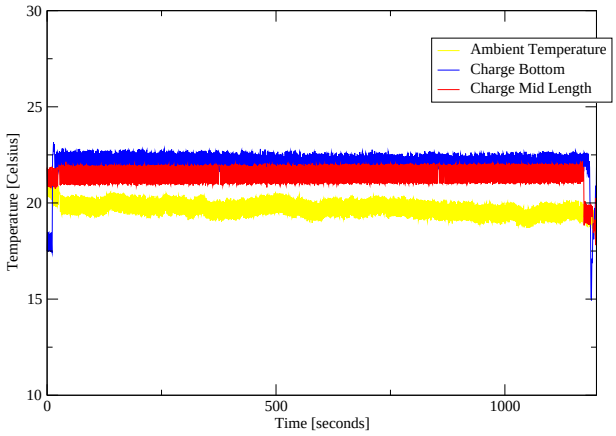

Figure C.1: Temperature record for shot 4.

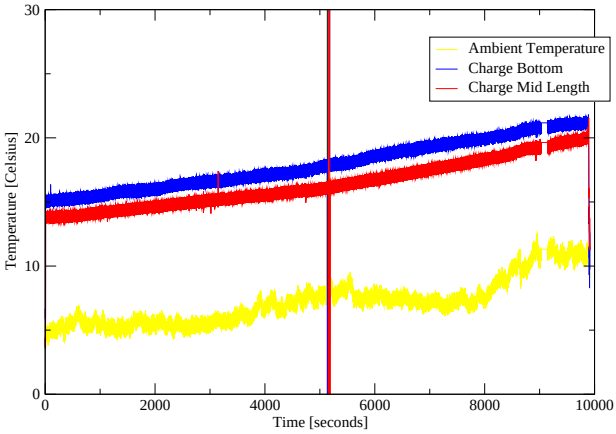

Figure C.2: Temperature record for shot 5.

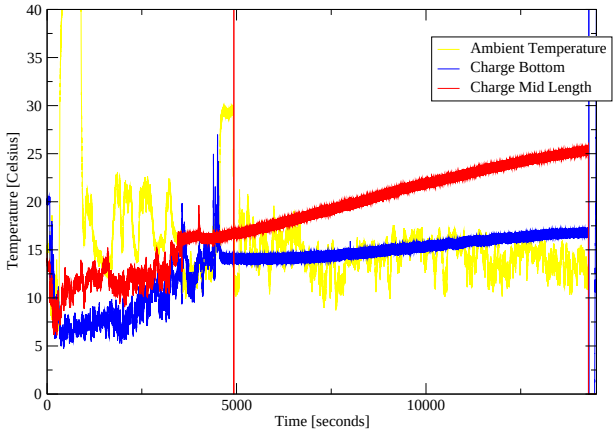

Figure C.3: Temperature record for shot 6.

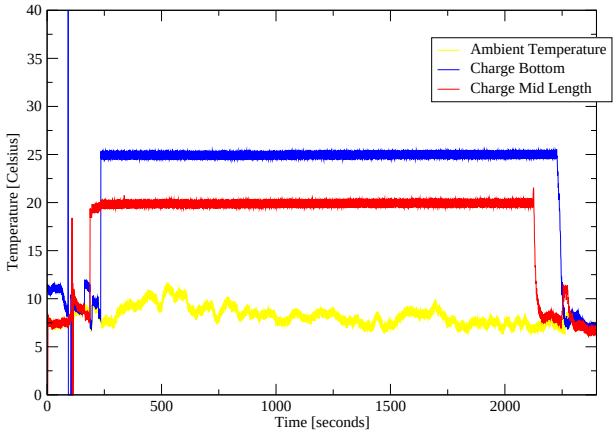

Figure C.4: Temperature record for shot 7.

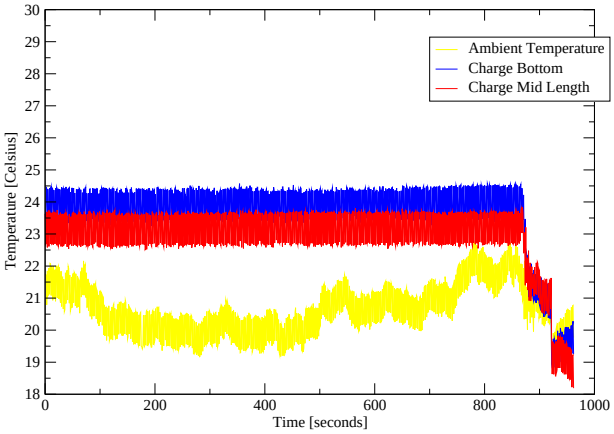

Figure C.5: Temperature record for shot 8.

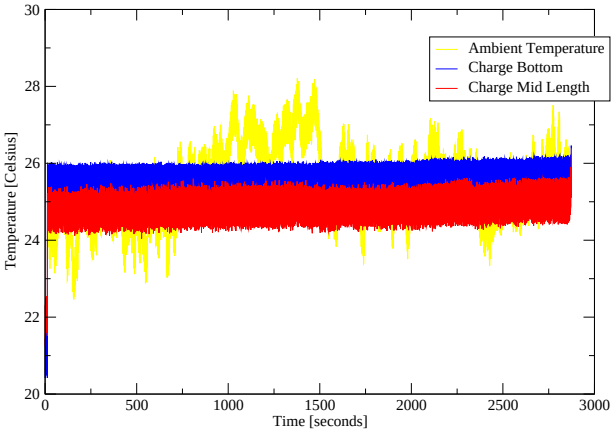

Figure C.6: Temperature record for shot 9.

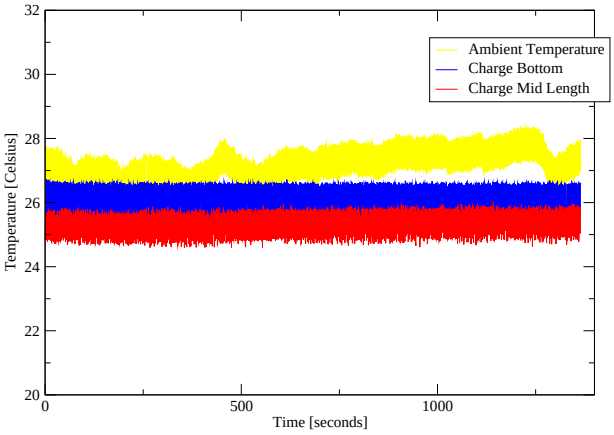

Figure C.7: Temperature record for shot 10.

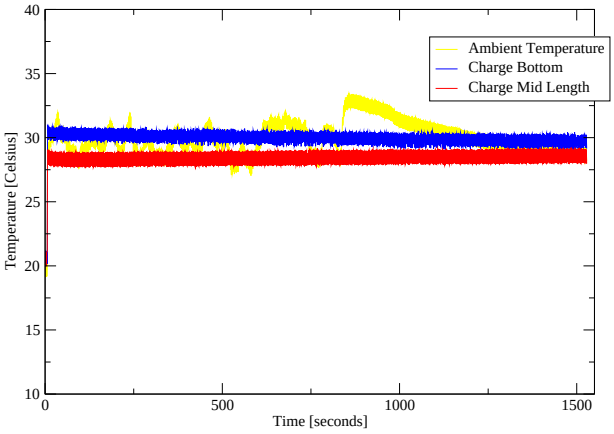

Figure C.8: Temperature record for shot 11.

C.3 Velocity along Charge Length for the Different Charge Types and Diameters

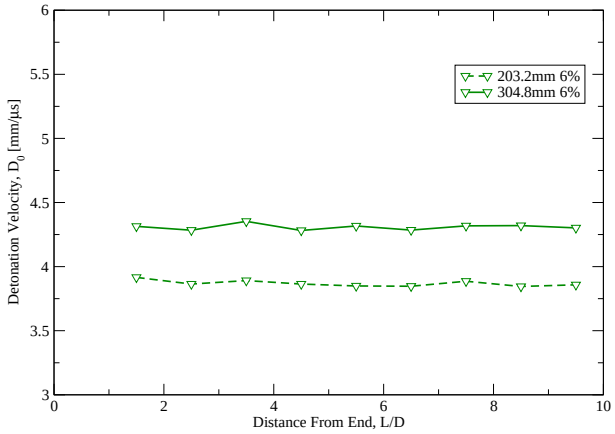

Figure C.9: Velocity along the charge length for the regular HE grade ANFO with 6% FO at both diameters.

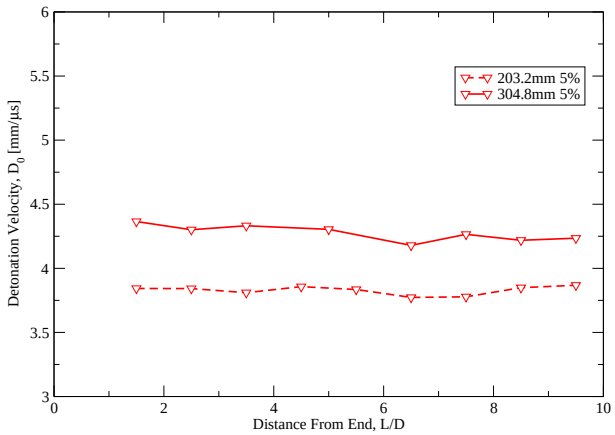

Figure C.10: Velocity along the charge length for the regular HE grade ANFO with 5% FO at both diameters.

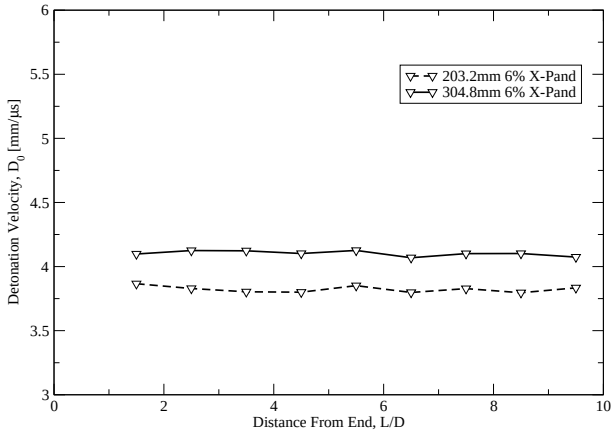

Figure C.11: Velocity along the charge length for the expan based ANFO at both diameters.

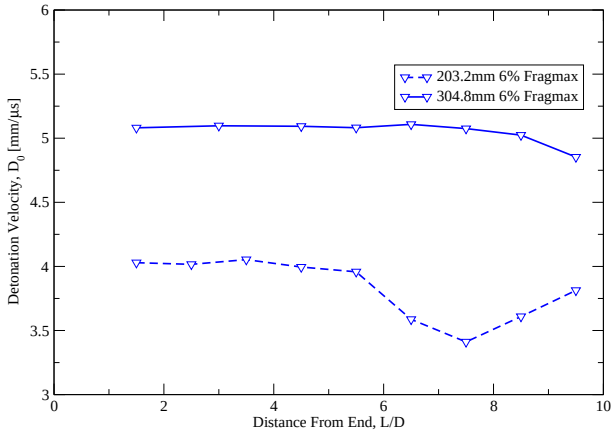

Figure C.12: Velocity along the charge length for the Fragmax based ANFO at both diameters.

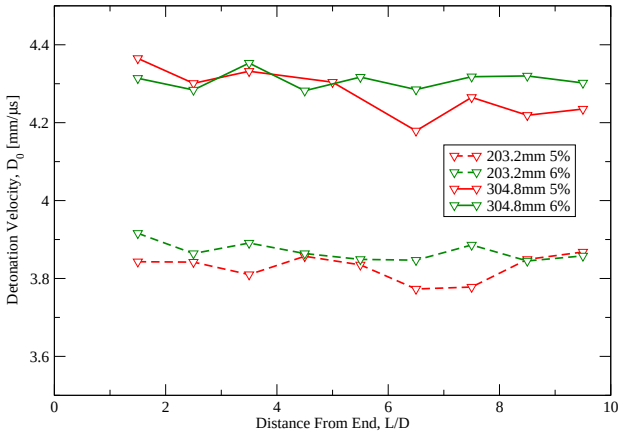

Figure C.13: Velocity along the charge length for the regular HE grade ANFO at both FO fractions and both diameters.

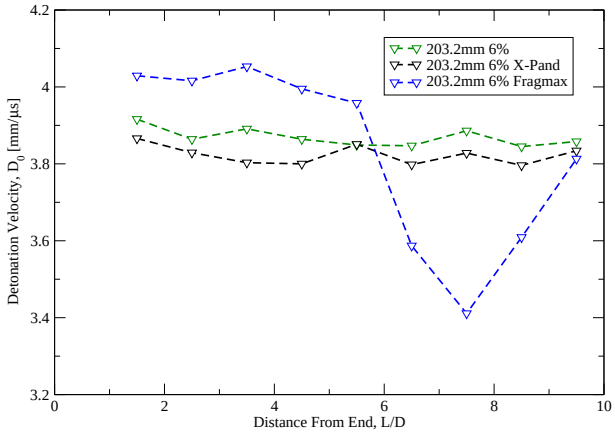

Figure C.14: Velocity along the charge length for the regular HE grade ANFO with 6% FO, the expan based ANFO and the Fragmax based ANFO for the 203.2 mm diameter charges.

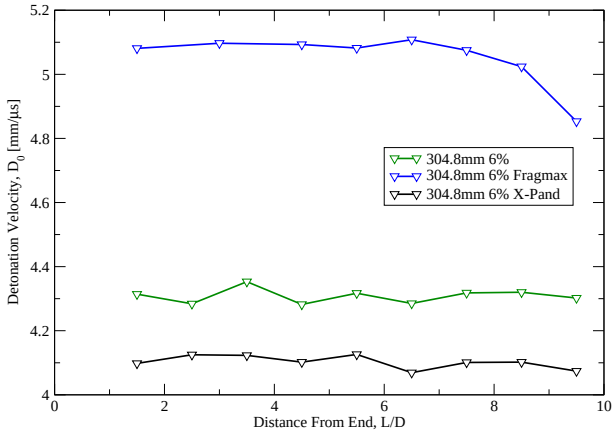

Figure C.15: Velocity along the charge length for the regular HE grade ANFO with 6% FO, the expan based ANFO and the Fragmax based ANFO for the 304.8 mm diameter charges.

C.4 D_n-κ Results from Shock Shape Fitting

Shot #	$\overline{a}_1$	$\overline{b}_1$	Tilt Angle (degrees)	Edge Angle (degrees)
4	26.4853	0.7023	-0.12	29.88
5	33.8170	0.6416	0.17	28.29
6	28.3882	0.7663	-0.17	30.04
7	41.5695	0.6535	-0.65	25.27
8	21.6694	0.7479	-0.52	30.31
9	31.9701	0.6760	0.59	31.11
10	48.3936	0.6711	0.33	30.38
11	31.1602	0.7083	0.032	24.79

Table C.4: Parameters from the shock shape fitting and differentiation.

Appendix D

Conversion of Digitized Streak Records to Wave Shape

Upon digitization of the streak records with a Epson Perfection V700M flatbed scanner, each experiments yields two digital images. One of the front streak record and the other of the still photograph. The goal is to convert the digital images to a wave shape in physical coordinates. Each streak record is "read" using the National Institute of Health software ImageJ. This operation yields a record of pairs of point locations (x,y) along the front in units of pixels.

The streak record yields the arrival time of the detonation front at the bottom of the charge along the charge diameter. The records are recorded on a strip of film and so one must relate two scales. First, the ratio between the horizontal size of objects on the film with the physical size of the experiments, and secondly, the size of objects span wise on the film with the relative time of arrival. As part of the experimental procedures, still photographs of the bottom of the charge were made using the same Cordin Model 136 streak camera. On those photographs, a carefully placed scale is visible making it possible to relate the horizontal size of objects on the film with the physical size of the charge. The film size to time of arrival conversion is slightly more involved, but still relatively simple. From the geometry of the camera,i.e. the relative positions of the film track with the rotating mirror, one can relate the mirror period with a time scale along the length of the film record. This conversion factor is non-linear along the film track, but the nonlinearity factor is given in the camera manual as a function of the position of objects on the film record. The complete equation and writing speed nonlinearity data are given in appendix D. Once the time scale has been obtained, the time of arrival can be converted to a shock shape using the detonation velocity, s.t. $\Delta Y = D_0 \Delta t$, where D_0 is the measured steady detonation velocity at the bottom of the charge, Δt is the relative time of arrival of the wave and ΔY is the relative height coordinate of the detonation wave shape.

D.1 Horizontal (Space) Scale

The horizontal scale is read from the still photograph using a scale that was purposely placed in the image or a shot construction feature. In the present experiment, scribe lines had been marked in the plate surface to

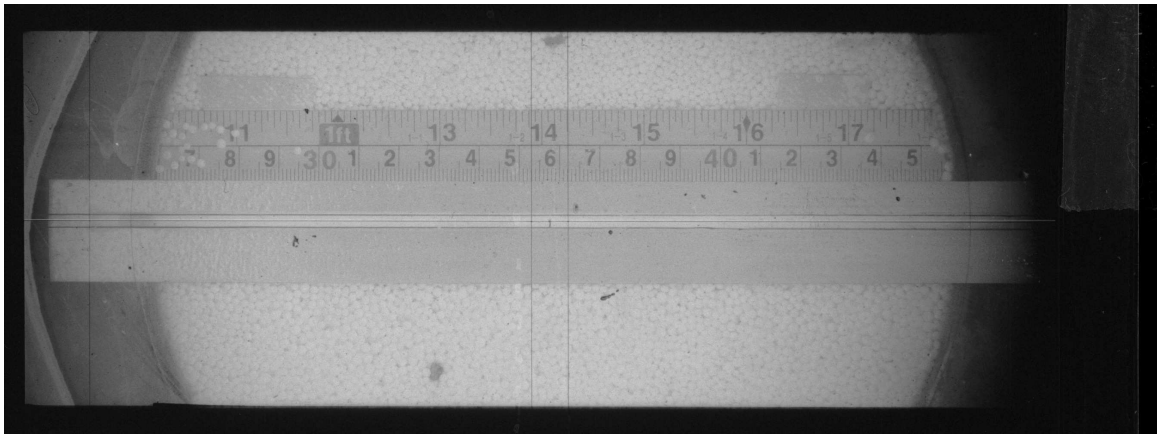

Figure D.1: Sample still photograph of the charge bottom taken with the streak camera.

help with the tube placement and those can be used as an independent check to the scale measurements or as a fall-back scale if the purposefully placed scale had been forgotten. This measurement yields a horizontal scale in mm in physical space/pixels on the image. The x position values are simply multiplied by this scale factor.

D.2 Vertical (Time) Scale

The vertical scale of the streak corresponds to the sweep time of the camera. This sweep time (or write speed) is related to the mirror period, which was recorded for each experiment. Finally, the time of breakout of the wave, assuming a steady wave, is related to the wave shape through the detonation velocity, D_0, measured using the shock pins. The conversion is therefore

$$z_{physical} = \frac{z_{pixels}}{\text{ScanResolution}} \frac{D_0}{W_s} \tag{D.1}$$

The nonlinearity of the Cordin camera write speed, W_s, is given in graphic form in the camera manual. Looking up values of the nonlinearity, W_n, on a graph is a time consuming and approximate process. Given that the streak records were digitized to speed up the data conversion process, it only made sense to digitize the data provided and use a fit of the function. It was found that the quartic fit afforded very little improvement over the cubit fit and so the cubic fit was used in calculating W_n for the different streak records. The non-linearity is a function of the position from the beginning of the film streak, $\overline{L}$, in % of the film track. The write speed at a particular location along the film track can be found using the following:

$$W_s = (1 + \frac{W_n}{100})\frac{4000}{\Delta t_{\text{mirror}}}, \tag{D.2}$$

where T_M is the mirror period.

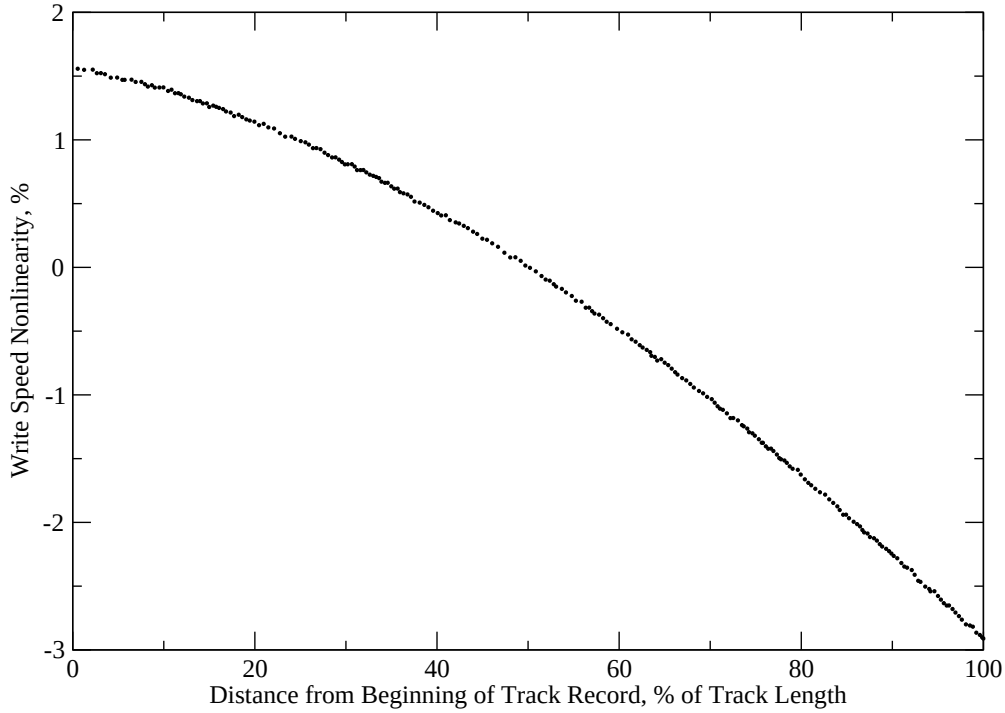

Figure D.2: Nonlinearity of the Cordin model 136 camera write speed scanned from the Cordin manual.

Type	Fit
Quadratic	$W_n = 1.6158 - 0.019032\overline{L} - 0.00026671\overline{L}^2$
Cubic	$W_n = 1.5681 - 0.013862\overline{L} - 0.00039023\overline{L}^2 + 8.0128x10^{-7}\overline{L}^3$
Quartic	$W_n = 1.5770 - 0.015449\overline{L} - 0.00032209\overline{L}^2 - 2.2651x10^{-7}\overline{L}^3 + 5.0215x10^{-9}\overline{L}^4$

Table D.1: Quadratic, cubic and quartic fit equations for the nonlinearity of the Cordin model 136 write speed as obtained from a scan of the cordin manual data.

References

[1] W. Seitz, H. Stacy, R. Engelke, P. Tang, and J. Wackerle, "Detonation reaction-zone structure of pbx 9502," in *9th International Detonation Symposium*, (Portland), pp. 657–669, 1989.

[2] D. Kennedy, "The challenge of non-ideal detonation," *Journal de Physique IV*, vol. 5, pp. 191–207, 1995.

[3] J. Bdzil and D. Stewart, "The dynamics of detonation in explosive systems," *Ann. Rev. Fluid Mech.*, vol. 39, pp. 263–92, 2007.

[4] T. Aslam and L. Hill, "Computing detonation waves in high explosives with material variability," *Nuclear Weapons Journal*, pp. 8–17, 2008.

[5] C. Handley, "The crest reactive burn model," in *13th International Detonation Symposium*, (Norfolk, Virginia), 2006.

[6] T. Aslam and M. Short. private communication, 2009.

[7] P. Souers, R. Garza, and P. Vitello, "Ignition & growth and jwl++ detonation models in coarse zones," *Propellants, Explosives, Pyrotechnics*, vol. 27, pp. 62–71, 2002.

[8] B. Wescott, D. Steward, and W. Davis, "Equation of state and reaction rate for condensed-phase explosives," *Journal of Applied Physics*, vol. 98, p. 053514, 2005.

[9] J. Vorthman, R. Hixson, W. Anderson, J. Fritz, and M. Shaw, "Release isentropes in overdriven pbx 9502," in *Shock Compression of Condensed Matter*, (Snowbird, Utah), pp. 223–226, 1999.

[10] M. Shaw and J. Johnson, "Carbon clustering in detonations," *Journal of Applied Physics*, vol. 62, pp. 2080–2085, 1987.

[11] J. Dick, C. Forest, J. Ramsey, and W. Seitz, "The hugoniot and shock sensitivity of a plastic-bonded tatb explosive pbx9502," *J. Appl. Phys.*, vol. 63, pp. 4881–4888, 1988.

[12] S. Marsh, *LASL Shock and Hugoniot Data*. Berkeley, California: University of California Press, 1980.

[13] J. Dallman and J. Wackerle, "Temperature-dependent shock initiation of tatb-based high explosives," in *10th International Detonation Symposium*, (Boston), pp. 322–332, 1993.

[14] L. Gustavsen. private communication, 2008.

[15] L. Gustavsen, S. Sheffield, and R. Alcon, "Measurements of shock initiation in the tri-amino-tri-nitro-benzene based explosives pbx9502: Wave forms from embedded gauges and comparison from four different material lots," *J. Appl. Phys.*, vol. 99, p. 114907, 2006.

[16] P. Tang, W. Anderson, J. Fritz, R. Hixson, and J. Vorthman, "A study of the overdriven behaviors of pbx9501 and pbx9502," in *11th International Detonation Symposium*, (Snowmass), pp. 1058–1065, 1998.

[17] B. Jensen and M. Byers, "Low-pressure overdriven experiments on pbx 9502," in *APS Topical Conference on Shock Compression of Condensed Matter*, (Nashville, Tennessee), pp. 380–383, 2009.

[18] A. Campbell, "Diameter effect and failure diameter of a tatb-based explosive," *Propellants, Explosives and Pyrotechnics*, vol. 9, pp. 183–187, 1984.

[19] L. Hill, J. Bdzil, and T. Aslam, "Front curvature rate stick measurements and detonation shock dynamics calibration for pbx 9502 over a wide temperature range," in *11th (International) Detonation Symposium*, (Snowmass, Colorado), 1998.

[20] L. Hill, J. Bdzil, W. Davis, and R. Critchfield, "Pbx 9502 front curvature rate stick data: Repeatability and the effects of temperature and material variation," in *13th (International) Detonation Symposium*, (Norfold, Virginia), 2006.

[21] R. Glowinski and P. Neittaanmaki, eds., *The von Neumann Triple Point Paradox*, vol. 16 of *Computational Methods in Applied Sciences*, ch. 6, pp. 113–128. Springer Netherlands, 2008.

[22] E. Vasilev, T. Elperin, and G. Ben-Dor, "Analytical reconsideration of the von neumann paradox in the reflection of a shock wave over a wedge," *Physics of Fluids*, vol. 20, 2008.

[23] R. Catanach and L. Hill, "Diameter effect curve and detonation front curvature measurements for anfo," in *APS Topical Conference on Shock Compression of Condensed matter*, (Atlanta, Georgia), 2001.

[24] J. Bdzil, M. Short, T. Aslam, R. Catanach, and L. Hill, "Dsd front models: Nonideal explosive detonation in anfo," in *12th (International) Detonation Symposium*, (San Diego, California), 2002.

[25] J. Bdzil, "Steady-state two-dimensional detonation," *Journal of Fluid Mechanics*, vol. 108, pp. 195–226, 1981.

[26] P. W. Cooper and S. Kurowski, *Introduction to the Technology of Explosives*. New York: Wiley-VCH, 1996.

[27] J. Bdzil, D. Stewart, and T. Jackson, "Program buurn algorithms based on detonation shock dynamics: Discrete approximations of detonation flows with discontinuous front models," *Journal of Computational Physics*, vol. 174, pp. 870–902, 2001.

[28] J. Bdzil and D. Stewart, "Modeling two-dimensional detonations with detonation shock dynamics," *Physics of Fluids A*.

[29] J. Yao and D. Stewart, "On the dynamics of multi-dimensional detonation," *Journal of Fluid Mechanics*, vol. 309, pp. 225–275, 1996.

[30] T. Aslam and D. Stewart, "Detonation shock dynamics and comparisons with direct numerical simulation," *Combustion, Theory and Modelling*, vol. 3, pp. 77–101, 1999.

[31] W. Davis, "Complete equation of state for unreacted solid explosive," *Combustion and Flame*, vol. 120, pp. 399–403, 2000.

[32] E. Lee and C. Tarver, "Phenomenological model of shock initiation in heterogeneous explosives," *Physics of Fluids*, vol. 23, pp. 2362–2372, 1980.

[33] P. Urtiew and C. Tarver, "Shock initiation of energetic materials at different initial temperatures (review)," *Combustion, Explosion, and Shock Waves*, vol. 41, pp. 766–776, 2005.

[34] C. Tarver, J. Kury, and R. Breithaupt, "Detonation waves in triaminotrinitrobenzene," *Journal of Applied Physics*, vol. 82, pp. 3771–3782, 1997.

[35] C. Tarver and S. Chidester, "On the violence of high explosive reactions," *Journal of Pressure Vessel Technology*, vol. 127, pp. 39–48, 2005.

[36] R. Gustavsen, S. Sheffield, R. Alcon, J. Forbes, C. Tarver, and F. Garcia, "Embedded electromagnetic gauge measurements and modeling of shock initiation in the tatb based explosives lx-17 and pbx 9502," in *Shock Compression of Condensed Matter*, (Seattle, Washington), pp. 1019–1022, 2001.

[37] C. Tarver and E. McGuire, "Reactive flow modeling of the interaction of tatb detonation waves with inert materials," in *12th International Detonation Symposium*, (San Diego, California), 2002.

[38] R. Druce, F. Foeske, P. Souers, C. Tarver, C. Chow, R. Lee, E. McGuire, G. Overturf, and P. Vitello, "Propagation of axially symmetric detonation waves," in *12th International Detonation Symposium*, (San Diego, California), 2002.

[39] T. Tran, C. Tarver, J. Maienschein, P. Lewis, M. Moss, R. Lee, and F. Roeske, "Characterization of detonation wave propagation in lx-17 near the critical diameter," in *12th International Detonation Symposium*, (San Diego, California), 2002.

[40] G. DeOliveira, A. Kapila, D. Schwendeman, J. Bdzil, W. Henshaw, and C. Tarver, "Detonation diffraction, dead zones and the ignition-and-growth model," in *13th International Detonation Symposium*, (Norfolk, Virginia), 2006.

[41] J. Starkenberg, "Modeling detonation propagation and failure using explosive initiation models in a conventional hydrocode," in *12th International Detonation Symposium*, (San Diego, California), 2002.

[42] B. Wescott, *On Detonation Diffraction in Condensed-Phase Explosives*. PhD thesis, University of Illinois at Urbana-Champaign, Urbana, Illinois, 2005.

[43] B. Lambourn, "An improved eos for non-reacted explosives," in *Shock Compression of Condensed Matter*, (Baltimore, Maryland), 2005.

[44] N. Whitworth, "Some issues regarding the hydrocode implementation of the crest reactive burn model," in *13th International Detonation Symposium*, (Norfolk, Virginia), 2006.

[45] R. Menikoff, *Empirical Equations of State for Solids*. Shock Wave Science and Technology Reference Library, Vol 2: Solids I, Springer-Verlag, 2004.

[46] P. Thompson, "A fundamental derivative in gas dynamics," *Physics of Fluids*, vol. 14, 1971.

[47] G. R. Fowles and G. W. Swan, "Stability of plane shock waves," *Phys. Rev. Lett.*, vol. 30, pp. 1023–1025, May 1973.

[48] G. W. Swan and G. R. Fowles, "Shock wave stability," *Physics of Fluids*, vol. 18, no. 1, pp. 28–35, 1975.

[49] G. R. Fowles, "Conditional stability of shock waves—a criterion for detonation," *Physics of Fluids*, vol. 19, no. 2, pp. 227–238, 1976.

[50] G. R. Fowles, "Stimulated and spontaneous emission of acoustic waves from shock fronts," *Physics of Fluids*, vol. 24, no. 2, pp. 220–227, 1981.

[51] R. Menikoff and B. Plohr, "The riemann problem for fluid flow of real materials," *Reviews of Modern Physics*, vol. 61, pp. 75–130, 1989.

[52] L. Stevens, N. Velisavljevic, D. Hooks, and D. Dattelbaum, "Hydrostatic compression curve for triamino-trinitrobenzene determined to 13.0 gpa with powder x-ray diffraction," *Propellantas, Explosives, Pyrotechnics*, vol. 33, no. 4, pp. 286–295, 2008.

[53] M. Shaw. private communication, 2006.

[54] W. Fickett and W. Davis, *Detonation:Theory and Experiment*. Mineola, New York (Berkeley, California): Dover (Originally University of California Press), 1979.

[55] R. Gibbs and A. Popolato, *LASL Explosive Property Data*. Berkeley, California: University of California Press, 1980.

[56] S. Sheffield and D. Bloomquist, "Subnanosecond measurements of detonation fronts in solid high explosives," *Journal of Chemical Physics*, vol. 80, pp. 3831–3844, 1984.

[57] B. Haag, *The Elusive Coefficients of Thermal Expansion in PBX 9502 (internal report)*. Los Alamos National Laboratory, 2003.

[58] C. Kittel, *Elementary Statistical Physics*. New York: John Wiley and Sons, 1958.

[59] F. Ahlers, W. Carlo, C. Fleiner, L. Godwin, M. Keenan, R. Deb Nath, A. Neumaier, J. Phillips, K. Price, R. Storn, P. Turney, F. Wang, J. Van Zandt, H. Geldon, and P. Gauden, "Differential evolution homepage." `http://www.icsi.berkeley.edu/ storn/code.html`.

[60] K. Price, R. Storn, and J. Lampinen, *Differential Evolution: A practical approach to global optimization*. Berlin, Germany: Springer-Verlag, 2005.

[61] D. White, "Turbulent structure of gaseous detonation," *Physics of Fluids*, vol. 4, pp. 465–480, 1961.

[62] D. White and K. Cary, "Structure of gaseous detonation. ii. generation of laminar detonation," *Physics of Fluids*, vol. 6, no. 5, pp. 749–750, 1963.

[63] G. Shott, "Observations of the structure of spinning detonation," *Physics of Fluids*, vol. 8, no. 5, pp. 850–865, 1965.

[64] Voitsekhovskil, V. B.V., Mitrofanov, and M. Topchian, "Investigation of the structure of detonation waves in gases," in *Proceedings of the Symposium (International) on Combustion*, vol. 12, 1969.

[65] J. Erpenbeck, "Stability of idealized one-reaction detonations," *Physics of Fluids*, vol. 7, pp. 684–696, 1964.

[66] J. Buckmaster and J. Neves, "One-dimensional detonation stability: The spectrum for infinite activation energy," *Physics of Fluids*, vol. 31, no. 12, 1988.

[67] H. Lee and D. Stewart, "Calculation of linear detonation instability: One-dimensional instability of plane detonation," *Journal of Fluid Mechanics*, vol. 216, pp. 103–132, 1990.

[68] M. Short and J. Quirk, "On the nonlinear stability and detonability limit of a detonation wave for a model three-step chain-branching reaction," *Journal of Fluid Mechanics*, vol. 339, pp. 89–119, 1997.

[69] M. Short and D. Stewart, "Low-frequency two-dimensional linear instability of plane detonation," *Journal of Fluid Mechanics*, vol. 340, pp. 249–295, 1997.

[70] M. Short, "Multidimensional linear stability of a detonation wave at high activation energy," *SIAM Journal of Applied Mathematics*, vol. 57, no. 2, pp. 307–326, 1997.

[71] M. Short and D. Stewart, "Cellular detonation stability. part 1. a normal-mode linear analysis," *Journal of Fluid Mechanics*, vol. 368, pp. 229–262, 1998.

[72] M. Short and D. Stewart, "The multi-dimensional stability of weak-heat-release detonations," *Journal of Fluid Mechanics*, vol. 382, pp. 109–135, 1999.

[73] M. Short, "A nonlinear evolution equation for pulsating chapman-jouguet detonations with chain-branching kinetics," *Journal of Fluid Mechanics*, vol. 430, pp. 381–400, 2001.

[74] M. Short, J. Bdzil, and I. Anguelova, "Stability of chapman-jouguet detonations for a stiffened-gas model of condensed-phase explosives," *Journal of Fluid Mechanics*, vol. 552, pp. 299–309, 2006.

[75] M. Short, I. Anguelova, A. T.D., J. Bdzil, H. A.K., and S. G.J., "Stability of detonations for an idealized condensed phase model," *Journal of Fluid Mechanics*, vol. 595, pp. 45–82, 2008.

[76] C. Canuto, M. Hussaini, A. Quarteroni, and T. J. Zang, *Spectral Methods: Fundamentals in Single domains*. Berling, Germany: Springer-Verlag, 2006.

[77] C. Canuto, M. Hussaini, A. Quarteroni, and T. J. Zang, *Spectral Methods: Evolution to Complex Geometries and Applications to Fluid Dynamics*. Berlin, Germany: Springer-Verlag, 2007.

[78] A. Tumin, "Multi-domain spectral collocation method for stability analysis of detonations," *AIAA Journal*, vol. 45, no. 9, pp. 2356–2359, 2007.

[79] C. Chiquete and A. Tumin, "Receptivity of plane idealized one-reaction detonations to three-dimensional perturbations," *AIAA paper 2008-1038*, 2008.

[80] J. Boyd, *Chebyshev and Fourier Spectral Methods, 2nd Edition*. Mineola, New York: Dover Publications, 1999.

[81] P. Schmid and D. Henningson, *Stability and Transition in Shear Flows*. Berlin, Germany: Springer-Verlag, 2001.

[82] M. Short. private communication, 2009.

[83] M. Radulescu and J. Lee, "The failure mechanism of gaseous detonations: Experiments in porous wall tubes," *Combustion and Flame*, vol. 131, pp. 29–46, 2002.

[84] J. Austin, *The Role of Instability in Gaseous Detonation*. PhD thesis, California Institute of Technology, Pasadena, California, 2003.

[85] R. Gustavsen, S. Sheffield, and R. Alcon, "Detonation wave profiles in hmx based explosives," in *Shock Compression of Condensed matter*, pp. 739–742, 1998.

[86] S. Sheffield, R. engelke, R. Alcon, R. Gustavsen, D. Robbins, D. Stahl, and H. Stacy, "Particle velocity measurements of the reaction zone in nitromethane," in *12th International Detonatin Symposium*, (San Diego, CA), 2002.

[87] C. Tarver, J. Kury, and R. Breithaupt, "Detonation waves in triaminotrinitrobenzene," *Journal of Applied Physics*, vol. 82, pp. 3771–3782, 1997.

[88] P. Colella and L. Henderson, "The von neumann paradox for the diffraction of weak shock waves," *Journal of Fluid Mechanics*, vol. 213, pp. 71–94, 1990.

[89] G. Ben-Dor, "A reconsideration of the three-shock theory for a pseudo-steady mach reflection," *Journal of Fluid Mechanics*, vol. 181, pp. 467–484, 1987.

[90] G. Ben-Dor, "A state-of-the-knowledge review on pseudo-steady shock-wave reflections and their transition critera," *Shock Waves*, vol. 15, pp. 277–294, 2006.

[91] M. Saad, *Compressible Fluid Flow*. Upper Saddle River, New Jersey: Prentice-Hall, 1993.

[92] J. E. Shepherd, *Detonation Waves and Propulsion*, vol. 1, pp. 373–420. 1994.

[93] S. Xu, T. Aslam, and D. Stewart

[94] A. Henrick, T. Aslam, and J. Powers, "Mapped weighted essentially non-oscillatory schemes: Achieving optimal order near critical points," *Journal of Computational Physics*, vol. 207.

[95] S. Xu, T. Aslam, and D. Stewart, "High resolution numerical simulation of ideal and non-ideal compressible reacting flows with embedded internal boundaries," *Combustion, Theory and Modelling*, vol. 1, pp. 113–142, 1997.

[96] H. Hornung, "On the stability of steady-flow regular and mach reflection," *Shock Waves*, vol. 7, pp. 123–125, 1997.

[97] A. Tesdall and J. Hunter, "Self-similar solutions for weak shock reflection," *SIAM Journal of Applied Mathematics*, vol. 63, no. 1, pp. 42–61, 2002.

[98] A. Tesdall, R. Sanders, and B. Keyfitz, "The triple point paradox for the nonlinear wave system," *SIAM Journal of Applied Mathematics*, vol. 67, no. 2, pp. 321–336, 2006.

[99] A. Tesdall, R. Sanders, and B. Keyfitz, "Self-similar solutions for the triple point paradox in gasdynamics," *SIAM Journal of Applied Mathematics*, vol. 68, no. 5, pp. 1360–1377, 2008.

[100] B. Skews and J. Ashworth, "The physical nature of weak shock wave reflection," *Journal of Fluid Mechanics*, vol. 542, pp. 105–114, 2005.

[101] B. Skews, G. Li, and R. Paton, "Experimetns on guderley mach reflection," *Shock Waves*, vol. 19, pp. 95–102, 2009.

[102] G. Sharpe and J. Bdzil, "Interactions of inert confiners with explosives," *Journal of Engineering Mathemacits*, vol. 54, pp. 279–298, 2006.

[103] T. Aslam and J. Bdzil, "Numerical and theoretical investigations on detonation-inert confinement interactions," in *12th (International) Detonation Symposium*, (San Diego, California), 2002.

[104] J. Yancik, *Some physical, chemical, and thermodynamic parameters of explosive ammonium nitrate-fuel oil mixtures*. PhD thesis, University of Missouri, Columbia, Missouri, 1960.

[105] A. King and A. Bauer, *A review of accidents with ammonium nitrate*. Queen's University, 1977.

[106] A. King, A. Bauer, and R. Heater, *The explosion hazards of ammonium nitrate and ammonium nitrate based fertilizer compositions*. Queen's University, 1982.

[107] A. King and A. Bauer, *A critical review of the EEC detonatiblity test*. Queen's University, 1977.

[108] A. King and A. Bauer, *A critical review of the thermal decomposition mechanisms of ammonium nitrate*. Queen's University, 1977.

[109] A. King and A. Bauer, *Critical shock initiation parameters for molten ammonium nitrate*. Queen's University, 1979.

[110] A. Bauer, R. Heater, and J. Paterson, *The sensitivitiy of ammonium nitrate melts and solutions to projectile impact*. Queen's University, 1981.

[111] A. King, A. Bauer, and R. Heater, *The detonation properties of liquid phase ammonium nitrate*. Queen's University, 1978.

[112] A. Bauer, A. King, and A. Heater, *The deflagration to detonation transitionn characterisitics of molten ammonium nitrate*. Queen's University, 1979.

[113] A. King, A. Bauer, R. Heater, and J. Paterson, *Critical parameters for low amplitude shock initiation of molten ammonium nitrate and ammonoium nitrate fertilizer solutions*. Queen's University, 1982.

[114] A. King, A. Bauer, and R. Heater, *The detonation properties of ammonium nitrate prills*. Queen's University, 1978.

[115] A. King and A. Bauer, *Shock initiation characteristics of ammonium nitrate*. Queen's University, 1980.

[116] A. King, A. Bauer, C. Preston, and G. Dunn, *Priming test data for assorted canadian ammonium nitrate prills*. Queen's University, 1977.

[117] J. Bdzil, W. Davis, and R. Critchfield, "Detonation shock dynamics (dsd) calibration for pbx 9502," in *10th (International) Detonation Symposium*, 1992.

[118] J. Bdzil, W. Davis, and R. Critchfield, "Detonation shock dynamics (dsd) calibration for pbx 9502," in *10th (International) Detonation Symposium*, (Boston, Massachussetts), 1994.

[119] D. Lambert, D. Stewart, S. Yoo, and B. Wescott, "Experimental validation of detonation shock dynamics in condensed explosives," *Journal of Fluid Mechanics*, vol. 546, pp. 227–253, 2005.

[120] J. Billingsley, *Impact Shock Sensitivity of a TATB Based Explosive Relevant to Specific Heat Properties, Technical Report AMR-SS-06-09.* Redstone Arsenal, Alabama: U.S. Army Research, Development, and Engineering Command, 2006.

[121] V. Tanguay, A. Higgins, and F. Zhang, "a simple analytical model for reactive particle ignition in explosives," *Propellants, Explosives, Pyrotechnics*, vol. 32, pp. 371–384.